Politecnico di Milano

MATHEMATICAL MODELS AND METHODS IN ENGINEERING
XXV Cycle

Mechanics of the Heart

Constitutive Issues and Numerical Experiments

Doctoral Dissertation of:
Simone Pezzuto

Supervisor:
Prof. Davide Ambrosi

Tutor:
Prof. Paolo Biscari

The Chair of the Doctoral Program:
Prof. Roberto Lucchetti

Milano — 2013

In questa tesi
ho cercato disperatamente
di far battere dei cuori.

Non so se ci sono riuscito.

Ma conosco una persona
che ha continuato
a far battere il mio,
e continuerà a farlo.

A Naomi,
con tutti i miei cuori ♥.

Acknowledgements

First of all, I wish to deeply acknowledge Prof. Alfio Quarteroni for providing the financial support through the ERC Advanced Grant *Mathcard* (number 227058). The project has given me the opportunity to question and study theories that fascinate me to a great extent. I would like also to express my gratitude to all the people involved in the project I have had the pleasure of meeting.

I'm grateful to Prof. A. McCulloch, Prof. J. Omens, Dr. R. Kerckhoff for giving me the opportunity to join their research group. It has been a great experience.

I would like to thank

Fabio Matt Adarsh Johan Andy Jared Chris Britton Simone^n

Elena^2 Matteo^3 Francesca^{-1} Viola Franco Antonio Alessio Elisabetta Alessia

Stefano Nur Andrea Susanna Nadia Marco Salva Davide Ferra

Ilario Pasquale Chiara Stefano Simona Laura^2 Luca ...

and many others I surely forgot (please refer to MOX and CMRG webpages for a complete list). A special thanks goes to Raimondo, for the fruitful discussion on depression at the microscale, and Kevin and Alessandro, for introducing me to the world of surfing and understanding Hipsters, respectively. Sorry, I failed at both.

Anche se non l'ho mai fatto esplicitamente, forse ora i tempi sono abbastanza maturi per ringraziare i miei genitori affinché continuino a sperare che un giorno anche io riesca finalmente a trovare un vero lavoro. E mio fratello per aver resistito fino all'ultimo nell'occupare la mia stanza durante il mio periodo milanese. I'm also grateful to my off–the–records parents–in–law, for supporting me when their stubborn but loveable daughter wanted to be right (hopefully no Italian translation is required here, isn't it?)

Last but not least, I would like to thank my mentor and advisor Prof. Davide Ambrosi, for being so tolerant of my continuous changes of research plans. But, most importantly, thank you for being less of a boss and more of a marvellous friend!

Contents

Motivations

The functional role of the heart in a living system is to pump the blood throughout the body, so that oxygen and nutrients can be distributed to all the tissues and metabolic waste product can be collected for disposal. This basic physiological job is performed in an extremely sophisticated way, the effectiveness of the mechanical activity as well as its regulation are performed according to rules that exploit the laws of mechanics in service of the needs of the organism.

This thesis deals with the mathematical modelling and numerical simulation of the cardiac activity. We are interested in understanding and reproduce numerically how the heart is able to produce work and regulate its functions. There are at least two motivations behind this work: the first one, is to contribute to advance the human understanding of its functionality by the support of mathematics, shedding some light on the reason why its architecture and physiology make its performance so effective and *stable*. The second motivation, in a long–term vision, is the ambition that a computer–aided medicine, if properly *calibrated*, can provide the clinicians a support to improve their diagnosis and prognosis.

In this work the emphasis is on two keywords: *calibration* and *stability*. A good mathematical model, must be able to reproduce, to a certain extent, some of the peculiarities of the system it has been thought for. In the case of the heart, examples of striking features are the ability to adapt the propulsive force depending on the load, or to torque in order to accommodate the ejection of blood from the ventricle. On the other hand, the introduced complexity possibly with the specific purpose of capturing aspects of the underlying physiology, must not compromise the stability of the model. Secondly, after fixing the properties of the model and its numerical implementation, there is the need to calibrate all the involved parameters.

The first chapter concerns the passive ventricular mechanics, where the chamber is supposed to be an elastic body, without residual stress, that deforms under the action of a pressure difference. The ventricle, which is approximately ellipsoid shaped, has a thick wall composed of, among other things, specifically oriented muscle fibres organised into laminar sheets. This is an essential mechanical characteristic of the myocardium because it determines the ability of the ventricle to twist and swell correctly during the filling phase.

We analyse in detail an hyperelastic model proposed by Holzapfel and Ogden in 2009, to describe the mechanics of the passive myocardium. The model is gaining an increasing popularity because of its simple invariant–based formulation and the small set of material parameters invoked, at least when compared to other models in the literature. It has also already been exploited in patient–specific simulations.

We discuss the sensitivity of the numerical results on the microstructure (which is always known with a large uncertainty) on the basis of various geometries and configurations. We study the influence of different boundary conditions on the solution and the prescriptions to obtain mathematically well–posed problem. While the authors of the model suggest to deactivate the fibres–specific elastic energy contribution when fibres undergo a compressive regime, here we show which problems can occur if this modification is neglected.

In the second and last chapter, we study the contractility of the heart, as a muscle, its ability to spend energy at the microscale to produce work at the macroscale. This interaction between biochemistry and mechanics is usually represented, at the macroscale, by an active stress to be added to the linear momentum balance. The constitutive equation of the passive contribution is usually addressed by standard stress–strain tests *without* electric excitation; conversely the active term can be barely decoupled from the passive contribution at a tissue scale and therefore its constitutive form is usually provided on the basis of the observed cell–scale behaviour.

A less popular biomechanical approach is to introduce just one stress term, while splitting the gradient of deformation into two factors: a passive one and an active one. In this case, standard stress–strain tests are expected to provide the form of the passive (inert) strain–energy function; the determination of the active strain as a function of the activation fields (concentration of ionic species) has to be prescribed on the basis of cell type experiments. From a thermodynamic point of view, the key assumption here is that the *distortion* induced by the active term does not store recoverable energy, so that the strain–energy has to be evaluated with respect to such distortion.

Both the “active stress” and the “active strain” approaches should satisfy due mathematical properties, namely frame indifference and rank–one ellipticity of the total stress. From this point of view, the active strain approach simply inherits these properties from the strain–energy. The rank–one ellipticity of an active stress needs instead to be verified case by case, in particular in the compressive regime. In the first part of the chapter we discuss examples of active stress and active strain laws in terms of precise mathematical and physiological properties.

Constitutive laws deduced from the cell–level dynamics should reproduce the observed physiological behaviour of the specific living tissue at the macroscale, when both active and passive forces contribute. Archetypical requirement in cardiac dynamics is to reproduce the correct pressure–volume relationship and torsion. Intuitively, the heart has to be able to generate the necessary pressure to open the aortic valve and let the blood flow throughout the body. As in the previous chapter, we perform several sensitivity analysis of the model by means of numerical simulations, and we show that the microstructure plays an even more prominent role than the case of a purely passive inflation of the ventricle, since non–physiological orientations of the fibres are not appropriate to produce the expected pressure.

The non–linear mechanical solver has been implemented with the software FEniCS, and a large part of it is going to be ported to LifeV. The meshes for the ventricle have been generated with Gmsh and the solution is post–processed with Paraview and other personal scripts. All the mentioned software are open–source and freely available on the internet, including the GNU/Linux operating system. Some of the source code I developed over the last three years is freely available (or it will soon be) on FEniCS and LifeV repositories.

Chapter 1

Passive mechanics

Introduction

In 1628 William Harvey has been the first physician to describe, on the basis of experiments, the heart as a muscular pump, highlighting in this way the mechanical nature of the organ. He was also aware that there are two distinct phases of the cardiac cycle: systole (from the Greek word συστολή, "contraction"), and diastole (διαστολή, "dilatation"). This distinction holds for every chamber of the heart: ventricles and atria. The systole is the active part of the process, during which an external work is performed.

The diastole starts when the aortic (resp. pulmonary) valve closes, just after ejection of the blood from the left (resp. right) ventricle. At this stage, a constant volume relaxation, due to the deactivation of the contractile units of the myocytes, accompanies a steep drop of blood pressure of about 80 to 100 mmHg. When the ventricle pressure is lower than the atrial one, the mitral (resp. tricuspid) valve opens and the blood rapidly flows into the ventricle. This filling phase is purely passive because no activation is involved. Moreover, at this stage, it becomes important the fluid–structure interaction: the kinetic energy of the fluid is partly stored as elastic strain–energy potential in the cardiac wall.

The very last point of the filling stage (end–diastolic point) is just before the mitral valve[1] closing, when the ventricle reaches its maximum volume. Let's suppose that in the diastolic phase a one–to–one relation exists between volume and mean pressure; by changing the end–diastolic volume, the pressure changes correspondingly: this relationship is called "End–Diastolic Pressure–Volume Relationship" (EDPVR), and it is an intrinsic characteristic of the myocardium.

The EDPVR effectively accounts for the passive properties of the ventricle: the steeper the curve, the stiffer the muscle, so that an extra energy is demanded in order to reach the desired volume or, equivalently, for a fixed work done by the atria, the final volume is lower. On the other hand, it gives only a partial information of underlying mechanical characteristics of the ventricle.

Another important clinical index of heart mechanics is the torsion of the ventricle, defined as the net difference between counter–clockwise and clockwise rotation around the ventricle axis of the apex and the base, respectively, when the deformation is observed from the apex (Sengupta et al., 2008). Besides this "longitudinal" torsion, a "in–plane" or transmural twist is

---

[1] For sake of simplicity, we focus on the left ventricle only, which is responsible for the systemic circulation and it involves the highest stresses and strains in the wall.

also observed during the motion, with a shear deformation occurring between the endocardium and the epicardium (Young and Cowan, 2012).

The torsion is a prominent effect of the complex microstructure of the myocardium. Harvey himself, citing earlier studies of Vesalius, observed that the heart is a bundle of muscular fibres whose orientation could have a significant functional purpose. Stensen in 1664 and then Lower in 1669 (see figure 1.1) pointed out that the fibres describe an helical path, observation also confirmed by the studies of Senac in 1749 and Ludwing in 1849. They state that a transmural specimen of the ventricle, especially from the left one, traversed from the outer side to the inner side, contains fibres that rotate approximately from 60° to −60°. This means that at the mid–wall section fibres are almost circumferential.

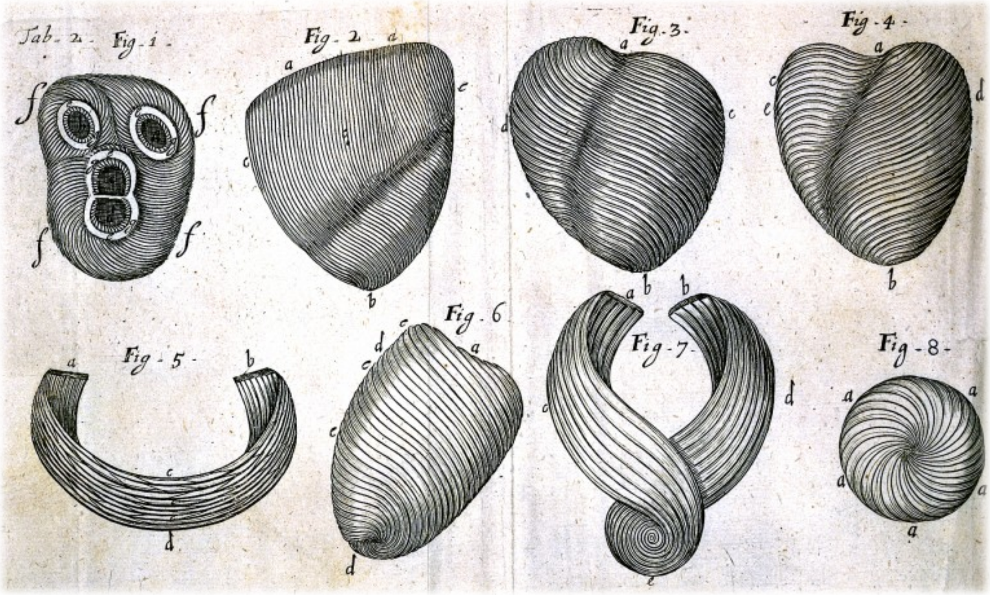

Figure 1.1 Fibres and sheets distribution sketched by R. Lower in *Tractatus de Corde* (1669).

Recent histological studies of the myocardium show that the fibres are organised into laminar sheets, each one composed by an ensemble of 3 to 4 cells tightly bounded together by endomysial collagen (LeGrice et al., 2001; Gilbert et al., 2007). The orientation of these sheets varies through the myocardium, but not as much as the fibres orientation; a rough approximation is to consider the normal direction of the sheets parallel to the longitudinal direction of the ventricle.

A physiological insight comes from mathematical models of the passive behaviour of the myocardium when considered as a continuum body that undergoes large deformations (Hunter et al., 2003). The mechanical properties of the tissue strongly depend on the microstructure which plays a prominent role on the EDPVR curve, on the torsion and on the distribution of the stresses through the wall.

Several models for the passive mechanics of the ventricle have been proposed over the last three decades, starting from simple isotropic model (Demiray, 1976), to more realistic transversely isotropic models (Chadwick, 1982; Humphrey et al., 1990; Taber, 1991; Guccione et al., 1995), where the microstructure is taken into account. In more recent years it has become evident that the myocardium should be considered an inhomogeneous orthotropic model, and several authors proposed new models in this respect (Hunter et al., 1997; Costa et al., 2001; Schmid et al., 2006). Recently, a review by Holzapfel and Ogden (2009) resumes many of them in the framework of hyperelasticity. In their work the microstructure of the cardiac tissue is encoded in the mathematical model in terms of strain–energy dependency on generalised invariants, and the parameters are eventually fitted on shear tests on pig myocardium (Dokos et al., 2002) by means of an optimisation process.

Aim of the present chapter is to investigate the passive mechanical properties of the left ventricle, by means of a numerical implementation of the Holzapfel–Odgen model. The first part concerns mathematical aspects and implementation issues, and it is basically a review of a classical framework of computational mechanics. A non–standard point of our tractation is the enforcement of boundary conditions: the common practice to fix a portion of the base surface of the ventricle dictates the deformation far from physiology. Here we analyse possible weaker choices in terms of the effect they have on the solution of the mechanical problem.

In second part of the chapter we simulate the passive inflation of an idealised ventricle with a physiological fibres microstructure (Streeter et al., 1969). We study the sensitivity of the solution on several parameters in terms of stress distribution, torsion and EDPVR. As expected (Nielsen et al., 1991; Bovendeerd et al., 1992; Vendelin et al., 2002; Nardinocchi et al., 2012), the fibres play a fundamental role in this respect, and a different distribution of them, for instance by changing their orientation, can dramatically affect the deformation and the stress distribution. Moreover, we have found a not entirely negligible role in accounting for the sheets. We conclude that the overall microstructure of the myocardium is the most important parameter of the mechanical model proposed by Holzapfel and Ogden.

1.1 The continuum model

1.1.1 Background notation

A *configuration* of a continuum body $\mathfrak{B}$ is a function $\chi\colon \mathbb{R}^3 \supseteq \mathfrak{B} \to \mathbb{R}^3$. We consider a given *reference configuration* χ_0 and a generally unknown *actual configuration* χ. Moreover, the reference and actual placements of the body in $\mathbb{R}^3$ are defined as follows:

$$\Omega_0 := \chi_0(\mathfrak{B}), \qquad \text{and} \qquad \Omega := \chi(\mathfrak{B}).$$

In continuum mechanics, the standard notation for a point $\mathfrak{p} \in \mathfrak{B}$ is denoted by $\mathbf{X} = \chi_0(\mathfrak{p}) \in \Omega_0$ in the reference configuration, and $\mathbf{x} = \chi(\mathfrak{p}) \in \Omega$ in the actual configuration.

A *deformation* is a map from the reference to the actual configuration:

$$\boldsymbol{\varphi} = \chi \circ \chi_0^{-1}, \qquad \boldsymbol{\varphi}\colon \Omega_0 \ni \mathbf{X} \mapsto \mathbf{x} = \chi\big(\chi_0^{-1}(\mathbf{X})\big) \in \Omega.$$

We suppose that $\boldsymbol{\varphi}$ is a diffeomorphism from Ω_0 to Ω, and its derivative

$$\mathsf{F}(\mathbf{X}) := \frac{\partial \boldsymbol{\varphi}}{\partial \mathbf{X}}, \qquad [\mathsf{F}_{ij}] = \frac{\partial \psi_i}{\partial X_j}, \qquad i, j \in \{1, 2, 3\},$$

is the *deformation gradient tensor.*

Denoting by $\mathrm{Lin}(\mathbb{R}^3)$, or just Lin, the vector space of all linear transformation from $\mathbb{R}^3$ to $\mathbb{R}^3$, we define the following subsets:

$$\begin{aligned}
\mathrm{Lin}^+(\mathbb{R}^3) &= \Big\{ \mathsf{F} \in \mathrm{Lin}(\mathbb{R}^3)\colon\ \det \mathsf{F} > 0 \Big\}, \\
\mathrm{Sym}^+(\mathbb{R}^3) &= \Big\{ \mathsf{C} \in \mathrm{Lin}^+(\mathbb{R}^3)\colon\ \mathsf{C}^\mathsf{T} = \mathsf{C} \Big\}, \\
\mathrm{Orth}^+(\mathbb{R}^3) &= \Big\{ \mathsf{Q} \in \mathrm{Lin}^+(\mathbb{R}^3)\colon\ \mathsf{Q}^{-1} = \mathsf{Q}^\mathsf{T} \Big\}.
\end{aligned}$$

A configuration is admissible if $J := \det \mathsf{F} > 0$, so if $\mathsf{F} \in \mathrm{Lin}^+$. Furthermore, let $\partial\Omega_0$ be the boundary of Ω_0, and two distinct subsets of it, namely $\partial_{\mathrm{D}}\Omega_0$, on which essential boundary conditions are considered, and $\partial_{\mathrm{N}}\Omega_0$, for the natural one. We also require that

$$\partial\Omega_0 = \overline{\partial_{\mathrm{D}}\Omega_0 \cup \partial_{\mathrm{N}}\Omega_0}, \qquad \text{and} \qquad \partial_{\mathrm{D}}\Omega_0 \cap \partial_{\mathrm{N}}\Omega_0 = \varnothing.$$

Then the admissible configurations $\mathscr{C}$ of our body $\mathfrak{B}$ belong to the space

$$\mathscr{C} = \Big\{ \boldsymbol{\varphi} \colon \Omega_0 \to \Omega \text{ such that } \mathsf{F} \in \mathrm{Lin}^+ \text{ and } \boldsymbol{\varphi}|_{\partial_{\mathrm{D}}\Omega_0} = \mathbf{g} \Big\}, \tag{1.1}$$

where $\mathbf{g}(\mathbf{X})$ is a given displacement of the boundary $\partial_{\mathrm{D}}\Omega_0$.

As usual, we define the left and right Cauchy–Green and Green strain tensors as follows:

$$\mathsf{C} := \mathsf{F}^{\mathsf{T}}\mathsf{F}, \qquad \mathsf{B} := \mathsf{F}\mathsf{F}^{\mathsf{T}}, \qquad \text{and} \qquad \mathsf{E} := \frac{1}{2}(\mathsf{C} - \mathsf{I}),$$

respectively.

The stress state of the body is described, on the actual configuration, by the Cauchy stress tensor T; thanks to the Piola transformation, we can also write first and second Piola–Kirchhoff tensors:

$$\mathsf{P} := J\mathsf{T}\mathsf{F}^{-\mathsf{T}}, \qquad \mathsf{S} := \mathsf{F}^{-1}\mathsf{P} = J\mathsf{F}^{-1}\mathsf{T}\mathsf{F}^{-\mathsf{T}}. \tag{1.2}$$

The balance of the linear momentum, in material coordinates, reads as follows:

$$-\operatorname{Div} \mathsf{P} = \rho_0 \mathbf{b}_0, \qquad \text{in } \Omega_0, \tag{1.3}$$

where ρ_0 is the density of the body on the reference configuration while $\mathbf{b}_0$ represents an external bulk force per unit volume. Natural boundary conditions, such as traction forces, are applied on the surface $\partial_{\mathrm{N}}\Omega_0$.

The constitutive relationship that relates stress T and strain F is prescribed within the hyperelasticity framework; this means that it exists a function $\mathcal{W} \colon \Omega_0 \times \mathrm{Lin}^+ \to \mathbb{R}$, called strain–energy density function, such that:

$$\mathsf{P} = \frac{\partial \mathcal{W}}{\partial \mathsf{F}}, \qquad \text{or, equivalently} \qquad \mathsf{S} = 2\frac{\partial \widehat{\mathcal{W}}}{\partial \mathsf{C}}, \tag{1.4}$$

where $\widehat{\mathcal{W}}(\mathbf{X}, \mathsf{C}) = \widehat{\mathcal{W}}(\mathbf{X}, \mathsf{F}^{\mathsf{T}}\mathsf{F}) = \mathcal{W}(\mathbf{X}, \mathsf{F})$. As usual, $\mathcal{W}$ must be objective, which implies that:

$$\mathcal{W}(\mathbf{X}, \mathsf{F}) = \mathcal{W}(\mathbf{X}, \mathsf{Q}\mathsf{F}), \qquad \text{for all } \mathsf{Q} \in \mathrm{Orth}.$$

The *polar decomposition theorem* states that there always exist two tensors $\mathsf{R} \in \mathrm{Orth}$ and U unitary such that $\mathsf{F} = \mathsf{R}\mathsf{U}$ and such a decomposition is unique; because of this, the objectivity of $\mathcal{W}$ is equivalent to state that $\mathcal{W}$ depends on F only through U. In this respect, because $\mathsf{C} = \mathsf{U}^2$, we can directly use $\widehat{\mathcal{W}}$ in order to automatically satisfy the objectivity.

Remark 1. Equation (1.3) underlies a *quasi–static* approximation, so that inertial terms are neglected. This is a common hypothesis in cardiac mechanics, also supported by the literature: Tallarida et al. (1970) shows that inertia represents less that 1% of the total energy balance.

Remark 2. For sake of simplicity, we fix a unique orthonormal reference system for both reference and actual configurations. This simplifies considerably the tensor notation, because there is no metric to deal with. On the other hand, it is worth mentioning that several authors consider a curvilinear system aligned with the microstructure of the myocardium, i.e. the three axes are the local fibre, sheet and normal direction, respectively: see Smith et al. (2004).

1.1.2 Invariant–based formulation

Given an hyperelastic material with strain–energy function $\widehat{\mathcal{W}}(\mathbf{X}, \mathsf{C})$, we suppose that, for a fixed point $\mathbf{X} \in \Omega_0$, the following local invariance property is verified:

$$\widehat{\mathcal{W}}(\mathsf{C}) = \widehat{\mathcal{W}}(\mathsf{QCQ}^\mathsf{T}), \qquad \text{for every } \mathsf{Q} \in \mathscr{G} \subseteq \text{Orth}.$$

The relation means that the strain–energy is the same if we change the reference configuration through the rotation Q, for any given deformation C (and so is the elastic response of the considered material). It is possible to show that $\mathscr{G}$ is a subgroup of Orth, with respect to the usual composition law. In particular, if $\mathscr{G} \equiv$ Orth, the material is *isotropic*; on the other hand, if $\mathscr{G}$ is a proper subgroup of Orth, the material is *anisotropic*.

A generic scalar function $\Psi(s_1, \dots, s_p, \mathbf{v}_1, \dots, \mathbf{v}_n, \mathsf{A}_1, \dots, \mathsf{A}_m)$ of p scalar fields, n vector fields and m tensor fields, is said isotropic with respect to these fields if for every $\mathsf{Q} \in$ Orth we have:

$$\Psi(s_1, \dots, s_p, \mathbf{v}_1, \dots, \mathbf{v}_n, \mathsf{A}_1, \dots, \mathsf{A}_m) = \Psi(s_1, \dots, s_p, \mathsf{Q}\mathbf{v}_1, \dots, \mathsf{Q}\mathbf{v}_n, \mathsf{QA}_1\mathsf{Q}^\mathsf{T}, \dots, \mathsf{QA}_m\mathsf{Q}^\mathsf{T}).$$

If a function Ψ is invariant with respect to a group of the form:

$$\mathcal{H} = \Big\{\mathsf{Q} \in \text{Orth}\colon \mathsf{Q}\mathbf{v}_i = \mathbf{v}_i,\ \mathsf{QA}_j\mathsf{Q}^\mathsf{T} = \mathsf{A}_j, \text{ for } i \in \{1, \dots, n\} \text{ and } j \in \{1, \dots, m\}\Big\},$$

then it is possible to show that it always exists an isotropic function $\widetilde{\Psi}$ of the fields $\mathbf{v}_i$, A_j and s_k, and also of the former arguments of Ψ, such that $\Psi = \widetilde{\Psi}$; this function is a isotropic representation of the former function Ψ, and automatically encodes for the invariant group $\mathcal{H}$.

The next step is the representation of Ψ, which is an isotropic function of its arguments, as a function of scalar quantities. For instance, if a scalar function $\Psi(\mathsf{A})$, with A symmetric, is isotropic, then, because of the *spectral theorem*, it takes the same values if in place of A we apply a matrix similar to A. So Ψ depends on A only through its eigenvalues, which are scalar quantities or, more generally, on a set of scalar functions of the eigenvalues. We denote this *invariant set* with the symbol Υ (Liu, 2002).

If Ψ is an isotropic function of more than one tensor field, the set of the invariants Υ can be built as follows: we consider every possible scalar quantity obtained as a trace of the tensors A_j, or any multiplication of them, like $\mathsf{A}_1^2\mathsf{A}_2$ or $\mathsf{A}_1^3\mathsf{A}_2\mathsf{A}_3$; moreover, as a consequence of *Cayley–Hamilton theorem*, the set of monomials of degree less than four is enough to represent all the others, and so the function. On the other hand, many of them can be redundant, for instance because of their particular form. We say that Υ is *irreducible* when it is the smallest one that represents the function.

Given an orthonormal ternary $\{\mathbf{f}_\circ, \mathbf{s}_\circ, \mathbf{n}_\circ\}$, in the reference configuration, for an *orthotropic* material the strain–energy is invariant with respect to rotations around any versor of the triplet. This defines:

$$\mathscr{G}_{\mathsf{orth}} = \Big\{\mathsf{Q} \in \text{Orth}\colon \mathsf{Q}(\mathbf{m} \otimes \mathbf{m})\mathsf{Q}^\mathsf{T} = \mathbf{m} \otimes \mathbf{m}, \text{ for } \mathbf{m} \in \{\mathbf{f}_\circ, \mathbf{s}_\circ, \mathbf{n}_\circ\}\Big\}.$$

On the other hand, if the material is invariant for any rotation around a given vector, say for instance $\mathbf{f}_\circ$, then the material is *transversely isotropic*, and the corresponding material symmetry group is:

$$\mathscr{G}_{\mathsf{tr}} = \Big\{\mathsf{Q} \in \text{Orth}\colon \mathsf{Q}\mathbf{f}_\circ = \mathbf{f}_\circ\Big\}.$$

If a function $\widehat{\mathcal{W}}(\mathsf{C})$, with $\mathsf{C} \in \text{Sym}^+$, is invariant with respect to $\mathscr{G}_{\mathsf{orth}}$, then there exists a representation $\widehat{\mathcal{W}}_{\mathsf{orth}}$ such that:

$$\widehat{\mathcal{W}}(\mathsf{C}) = \widehat{\mathcal{W}}_{\mathsf{orth}}(\mathsf{C}, \mathbf{f}_\circ \otimes \mathbf{f}_\circ, \mathbf{s}_\circ \otimes \mathbf{s}_\circ, \mathbf{n}_\circ \otimes \mathbf{n}_\circ),$$

for every $\mathsf{C} \in \mathrm{Sym}^+$ and with $\widehat{\mathcal{W}}_{\mathsf{orth}}$ isotropic with respect to its arguments. As a matter of fact, the dependency on $\mathbf{n}_\circ \otimes \mathbf{n}_\circ$ is redundant, because:

$$\mathbf{f}_\circ \otimes \mathbf{f}_\circ + \mathbf{s}_\circ \otimes \mathbf{s}_\circ + \mathbf{n}_\circ \otimes \mathbf{n}_\circ = \mathsf{I}.$$

The function $\widehat{\mathcal{W}}_{\mathsf{orth}}$ depends on four tensors, so several possible combinations exist however many of them will be redundant as

$$(\mathbf{a} \otimes \mathbf{b})^k = (\mathbf{a} \cdot \mathbf{b})^{k-1} \mathbf{a} \otimes \mathbf{b}, \qquad \text{with } k > 0.$$

This observation, and the fact that $\mathbf{n}_\circ$ is redundant and $\mathbf{f}_\circ$ and $\mathbf{s}_\circ$ are orthogonal, we have that the invariant set for an orthotropic material is defined as follows:

$$\Upsilon_{\mathsf{orth}} = \Big\{ \operatorname{tr} \mathsf{C},\ \operatorname{tr} \mathsf{C}^2,\ \operatorname{tr} \mathsf{C}^3,\ \mathbf{f}_\circ \cdot \mathsf{C} \mathbf{f}_\circ,\ \mathbf{s}_\circ \cdot \mathsf{C} \mathbf{s}_\circ,\ \mathbf{f}_\circ \cdot \mathsf{C}^2 \mathbf{f}_\circ,\ \mathbf{s}_\circ \cdot \mathsf{C}^2 \mathbf{s}_\circ \Big\}. \tag{1.5}$$

It's actually possible to prove that only six of these seven invariants are independent, so the set is not irreducible (Shariff, 2012).

In a perfect analogy, we can define a transversely isotropic version of $\widehat{\mathcal{W}}$ if we suppose that the function is invariant with respect to $\mathscr{G}_{\mathsf{tr}}$. In this case, we have:

$$\widehat{\mathcal{W}}(\mathsf{C}) = \widehat{\mathcal{W}}_{\mathsf{tr}}(\mathsf{C}, \mathbf{f}_\circ).$$

In this case, the argument is slightly different, because $\widehat{\mathcal{W}}_{\mathsf{tr}}$ depends on a vector $\mathbf{f}_\circ$ and not on the rank–one tensor $\mathbf{f}_\circ \otimes \mathbf{f}_\circ$; there are differences between the two cases, although not relevant for our problem (Liu, 1982). The final set is:

$$\Upsilon_{\mathsf{tr}} = \Big\{ \operatorname{tr} \mathsf{C},\ \operatorname{tr} \mathsf{C}^2,\ \operatorname{tr} \mathsf{C}^3,\ \mathbf{f}_\circ \cdot \mathsf{C} \mathbf{f}_\circ,\ \mathbf{f}_\circ \cdot \mathsf{C}^2 \mathbf{f}_\circ \Big\}. \tag{1.6}$$

It's worth mentioning that in principle one could use an arbitrary set of invariant: the only requirement is that it should be irreducible or equivalent to an irreducible set of invariants.

Remark 3. If $\mathbf{f}_\circ$ and $\mathbf{s}_\circ$ are not orthogonal, then Υ_{orth} is not sufficient to describe the symmetries of the material. In this case there are two additional invariants

$$(\mathbf{f}_\circ \cdot \mathbf{s}_\circ)\, \mathbf{f}_\circ \cdot \mathsf{C} \mathbf{s}_\circ, \qquad \text{and} \qquad (\mathbf{f}_\circ \cdot \mathbf{s}_\circ)^2,$$

which accounts for the angle between $\mathbf{f}_\circ$ and $\mathbf{s}_\circ$ in the actual and in the reference configuration. Observe that it is necessary to multiply both by $\mathbf{f}_\circ \cdot \mathbf{s}_\circ$, since the invariants should not change their sign if one of the two unit vector is reversed (but not both).

1.1.3 Holzapfel–Ogden model

Given the orthogonal versors $\mathbf{a}$ and $\mathbf{b}$, we define the following scalar functions of the right Cauchy–Green strain tensor:

$$\begin{aligned}
\mathcal{I}_1(\mathsf{C}) &= \operatorname{tr} \mathsf{C}, \\
\mathcal{I}_2(\mathsf{C}) &= \frac{1}{2} \Big[(\operatorname{tr} \mathsf{C})^2 - \operatorname{tr} \mathsf{C}^2 \Big], \\
\mathcal{I}_3(\mathsf{C}) &= \det \mathsf{C}, \\
\mathcal{I}_{4,\mathbf{a}}(\mathsf{C}) &= \mathbf{a} \cdot \mathsf{C} \mathbf{a}, \\
\mathcal{I}_{5,\mathbf{a}}(\mathsf{C}) &= \mathbf{a} \cdot \mathsf{C}^2 \mathbf{a}, \\
\mathcal{I}_{8,\mathbf{ab}}(\mathsf{C}) &= \mathbf{a} \cdot \mathsf{C} \mathbf{b}.
\end{aligned}$$

The first 3, with $\mathcal{I}_{4,\mathbf{f}_\circ}$, $\mathcal{I}_{5,\mathbf{f}_\circ}$, $\mathcal{I}_{4,\mathbf{s}_\circ}$ and $\mathcal{I}_{5,\mathbf{s}_\circ}$ form a set of invariants for the symmetry group $\mathscr{G}_{\mathsf{orth}}$, equivalent to Υ_{orth}. All of them have a clear kinematic interpretation: for instance, $\mathcal{I}_{4,\mathbf{a}}$ is the square of the local stretch along the direction $\mathbf{a}$, while $\mathcal{I}_{5,\mathbf{a}}$ is related to the variation of the infinitesimal cross–area orthogonal to the direction $\mathbf{a}$. To prove the second statement, first recall that the cofactor of a tensor F is the unique tensor $\operatorname{cof}\mathsf{F}$ such that

$$\mathsf{F}\mathbf{u} \wedge \mathsf{F}\mathbf{v} \cdot \mathbf{w} = (\operatorname{cof}\mathsf{F})\,\mathbf{u} \wedge \mathbf{v} \cdot \mathbf{w} \qquad \text{for every } \mathbf{u}, \mathbf{v}, \mathbf{w} \in \mathbb{R}^3.$$

Thanks to this definition, it is straightforward to see that any infinitesimal area $\mathrm{d}A$ in the reference configuration, with normal $\mathbf{a}$, is transformed into the infinitesimal area $\mathrm{d}a$ in the actual configuration in a such a way that

$$\mathrm{d}a^2 = |(\operatorname{cof}\mathsf{F})\,\mathbf{a}|^2 \mathrm{d}A^2.$$

Now, the Cayley–Hamilton theorem implies that

$$\mathsf{C}^3 - \mathcal{I}_1\mathsf{C}^2 + \mathcal{I}_2\mathsf{C} - \mathcal{I}_3\mathsf{I} = 0,$$

or, equivalently,

$$\mathsf{C}^2 - \mathcal{I}_1\mathsf{C} + \mathcal{I}_2\mathsf{I} - \mathcal{I}_3\mathsf{C}^{-1} = 0. \tag{†}$$

Multiplying both sides of (†) by $\mathbf{a}\,\mathrm{d}A$, we have that

$$(\mathbf{a} \cdot \mathsf{C}^2\mathbf{a} - \mathcal{I}_1\,\mathbf{a} \cdot \mathsf{C}\mathbf{a} + \mathcal{I}_2 - \mathcal{I}_3\,\mathbf{a} \cdot \mathsf{C}^{-1}\mathbf{a})\,\mathrm{d}A^2 = 0.$$

Observe that $\mathbf{a} \cdot \mathsf{C}^2\mathbf{a} = \mathcal{I}_{5,\mathbf{a}}$, $\mathbf{a} \cdot \mathsf{C}\mathbf{a} = \mathcal{I}_{4,\mathbf{a}}$ and

$$\mathcal{I}_3\mathbf{a} \cdot \mathsf{C}^{-1}\mathbf{a} = J\mathsf{F}^{-\mathsf{T}}\mathbf{a} \cdot J\mathsf{F}^{-\mathsf{T}}\mathbf{a} = (\operatorname{cof}\mathsf{F})\mathbf{a} \cdot (\operatorname{cof}\mathsf{F})\mathbf{a}.$$

Putting all the terms together, it is now clear that

$$\mathcal{I}_{5,\mathbf{a}}\mathrm{d}A^2 = \mathrm{d}a^2 - \mathcal{I}_2\mathrm{d}A^2 + \mathcal{I}_1\mathcal{I}_{4,\mathbf{a}}\mathrm{d}A^2.$$

The last invariant $\mathcal{I}_{8,\mathbf{ab}}$ is instead redundant, because if $\mathbf{a} \cdot \mathbf{b} = 0$ then we have the following result (cited in Merodio and Ogden (2006) without proof):

$$\mathcal{I}_{8,\mathbf{ab}}^2 = \mathcal{I}_2 + \mathcal{I}_{4,\mathbf{a}}\mathcal{I}_{4,\mathbf{b}} + \mathcal{I}_{5,\mathbf{a}} + \mathcal{I}_{5,\mathbf{b}} - \mathcal{I}_1(\mathcal{I}_{4,\mathbf{a}} + \mathcal{I}_{4,\mathbf{b}}). \tag{1.7}$$

In order to prove this, first observe that given a orthonormal set $\{\mathbf{a}, \mathbf{b}, \mathbf{c}\}$, we have

$$\mathsf{C}\mathbf{a} = (\mathbf{a} \cdot \mathsf{C}\mathbf{a})\mathbf{a} + (\mathbf{b} \cdot \mathsf{C}\mathbf{a})\mathbf{b} + (\mathbf{c} \cdot \mathsf{C}\mathbf{a})\mathbf{c},$$

so we can multiply both sides by $\mathsf{C}\mathbf{a}$ in order to recover the quadratic invariants:

❶ $\mathcal{I}_{5,\mathbf{a}} = \mathbf{a} \cdot \mathsf{C}^2\mathbf{a} = \mathsf{C}\mathbf{a} \cdot \mathsf{C}\mathbf{a} = (\mathbf{a} \cdot \mathsf{C}\mathbf{a})^2 + (\mathbf{b} \cdot \mathsf{C}\mathbf{a})^2 + (\mathbf{c} \cdot \mathsf{C}\mathbf{a})^2 = \mathcal{I}_{4,\mathbf{a}}^2 + \mathcal{I}_{8,\mathbf{ab}}^2 + \mathcal{I}_{8,\mathbf{ac}}^2.$

Analogously, with $\mathsf{C}\mathbf{b}$ and $\mathsf{C}\mathbf{c}$ we have:

❷ $\mathcal{I}_{5,\mathbf{b}} = \mathcal{I}_{8,\mathbf{ab}}^2 + \mathcal{I}_{4,\mathbf{b}}^2 + \mathcal{I}_{8,\mathbf{bc}}^2,$ and ❸ $\mathcal{I}_{5,\mathbf{c}} = \mathcal{I}_{8,\mathbf{ac}}^2 + \mathcal{I}_{8,\mathbf{bc}}^2 + \mathcal{I}_{4,\mathbf{c}}^2.$

Substituting $\mathcal{I}_{8,\mathbf{ac}}^2$ of ❶ and $\mathcal{I}_{8,\mathbf{bc}}^2$ of ❷ into ❸ it follows that

❹ $\mathcal{I}_{5,\mathbf{c}} = \mathcal{I}_{5,\mathbf{a}} - \mathcal{I}_{4,\mathbf{a}}^2 - \mathcal{I}_{8,\mathbf{ab}}^2 + \mathcal{I}_{5,\mathbf{b}} - \mathcal{I}_{4,\mathbf{b}}^2 - \mathcal{I}_{8,\mathbf{ab}}^2 + \mathcal{I}_{4,\mathbf{c}}^2$

In order to remove $\mathcal{I}_{4,\mathbf{c}}^2$ and $\mathcal{I}_{5,\mathbf{c}}$, we recall that:

$$\begin{aligned} \mathcal{I}_1 = \operatorname{tr}\mathsf{C} \ &= \mathcal{I}_{4,\mathbf{a}} + \mathcal{I}_{4,\mathbf{b}} + \mathcal{I}_{4,\mathbf{c}}, \\ \mathcal{I}_1^2 - 2\,\mathcal{I}_2 = \operatorname{tr}\mathsf{C}^2 &= \mathcal{I}_{5,\mathbf{a}} + \mathcal{I}_{5,\mathbf{b}} + \mathcal{I}_{5,\mathbf{c}}, \end{aligned}$$

so we obtain equation (1.7) substituting the following expressions into ❹:

$$\begin{aligned} &\mathcal{I}_{4,\mathbf{c}}^2 = (\mathcal{I}_1 - \mathcal{I}_{4,\mathbf{a}} - \mathcal{I}_{4,\mathbf{b}})^2 = \mathcal{I}_1^2 + 2\,\mathcal{I}_{4,\mathbf{a}}\mathcal{I}_{4,\mathbf{b}} - 2\,\mathcal{I}_1(\mathcal{I}_{4,\mathbf{a}} + \mathcal{I}_{4,\mathbf{b}}), \\ &\mathcal{I}_{5,\mathbf{c}} = \mathcal{I}_1^2 - 2\mathcal{I}_2 - \mathcal{I}_{5,\mathbf{a}} - \mathcal{I}_{5,\mathbf{b}}. \end{aligned}$$

From a kinematic viewpoint, the invariant $\mathcal{I}_{8,\mathbf{ab}}$ represents an important quantity: it is in fact related to the angle spanned by the vectors $\mathsf{F}\mathbf{a}$ and $\mathsf{F}\mathbf{b}$, in the actual configuration, supposing that $\mathbf{a}$ and $\mathbf{b}$ are initially orthogonal. The model proposed by Holzapfel and Ogden (2009) utilises this measure in place of $\mathcal{I}_{5,\cdot}$ and $\mathcal{I}_2$, reducing the total number of invariants to 5.

The Holzapfel–Ogden model is for an incompressible material, so $\det\mathsf{F} = 1$ and thus also $\mathcal{I}_3$ cancels, with strain–energy density function of the form:

$$\begin{aligned} \widehat{\mathcal{W}}(\mathsf{C}) &= \widetilde{\mathcal{W}}(\mathcal{I}_1, \mathcal{I}_{4,\mathbf{f}_\circ}, \mathcal{I}_{4,\mathbf{s}_\circ}, \mathcal{I}_{8\mathbf{f}_\circ\mathbf{s}_\circ}) \\ &= \widetilde{\mathcal{W}}_1(\mathcal{I}_1) + \widetilde{\mathcal{W}}_{4,\mathbf{f}_\circ}(\mathcal{I}_{4,\mathbf{f}_\circ}) + \widetilde{\mathcal{W}}_{4,\mathbf{s}_\circ}(\mathcal{I}_{4,\mathbf{s}_\circ}) + \widetilde{\mathcal{W}}_{8,\mathbf{f}_\circ\mathbf{s}_\circ}(\mathcal{I}_{8,\mathbf{f}_\circ\mathbf{s}_\circ}), \end{aligned} \tag{1.8}$$

which is considerably simplified either thanks to the additive splitting of the strain–energy and the dropping of quadratic invariants. Besides the mathematical reasons behind this simplification, there is also an experimental argument: it is particularly easy to identify the corresponding material parameters from an experiment, because each term has its precise physical meaning (this of course doesn't mean that in principle this model performs better than the others.)

The specific form of each term is of exponential type, in order to accommodate the typical response of a biological tissue, where the greater is the strain, the greater is the apparent stiffness:

$$\begin{aligned} \widetilde{\mathcal{W}}_1(\mathcal{I}_1) &= \frac{a}{2b}\left[e^{b(\mathcal{I}_1-3)} - 1\right], \\ \widetilde{\mathcal{W}}_{4,\mathbf{f}_\circ}(\mathcal{I}_{4,\mathbf{f}_\circ}) &= \frac{a_\mathsf{f}}{2b_\mathsf{f}}\left[e^{b_\mathsf{f}(\mathcal{I}_{4,\mathbf{f}_\circ}-1)^2} - 1\right], \\ \widetilde{\mathcal{W}}_{4,\mathbf{s}_\circ}(\mathcal{I}_{4,\mathbf{s}_\circ}) &= \frac{a_\mathsf{s}}{2b_\mathsf{s}}\left[e^{b_\mathsf{s}(\mathcal{I}_{4,\mathbf{s}_\circ}-1)^2} - 1\right], \\ \widetilde{\mathcal{W}}_{8,\mathbf{f}_\circ\mathbf{s}_\circ}(\mathcal{I}_{8,\mathbf{f}_\circ\mathbf{s}_\circ}) &= \frac{a_\mathsf{fs}}{2b_\mathsf{fs}}\left[e^{b_\mathsf{fs}\mathcal{I}_{8,\mathbf{f}_\circ\mathbf{s}_\circ}^2} - 1\right]. \end{aligned}$$

Thanks to equations (1.2) and (1.4) we can compute the explicit form of the Cauchy stress tensor T. We only have to pay attention to the incompressibility constraint, because the variations of deformations must be tangent to the manifold $\{\mathsf{F} \in \mathrm{Lin}^+ \colon \det\mathsf{F} = 1\}$. This means that it exists a scalar function $p\colon \Omega_0 \to \mathbb{R}$ (pressure) such that:

$$\mathsf{P} - \frac{\partial\mathcal{W}}{\partial\mathsf{F}} = -p\,\frac{\partial\det}{\partial\mathsf{F}} = -p\,\operatorname{cof}\mathsf{F}.$$

Now we can compute the derivative of $\mathcal{W}$:

$$\begin{aligned} \mathsf{P} &= \frac{\partial\mathcal{W}}{\partial\mathsf{F}} - p\operatorname{cof}\mathsf{F} = 2\mathsf{F}\frac{\partial\widehat{\mathcal{W}}}{\partial\mathsf{C}} - p\operatorname{cof}\mathsf{F} \\ &= 2\mathsf{F}\left[\frac{\partial\widetilde{\mathcal{W}}_1}{\partial\mathcal{I}_1}\frac{\partial\mathcal{I}_1}{\partial\mathsf{C}} + \frac{\partial\widetilde{\mathcal{W}}_{4,\mathbf{f}_\circ}}{\partial\mathcal{I}_{4,\mathbf{f}_\circ}}\frac{\partial\mathcal{I}_{4,\mathbf{f}_\circ}}{\partial\mathsf{C}} + \frac{\partial\widetilde{\mathcal{W}}_{4,\mathbf{s}_\circ}}{\partial\mathcal{I}_{4,\mathbf{s}_\circ}}\frac{\partial\mathcal{I}_{4,\mathbf{s}_\circ}}{\partial\mathsf{C}} + \frac{\partial\widetilde{\mathcal{W}}_{8,\mathbf{f}_\circ\mathbf{s}_\circ}}{\partial\mathcal{I}_{8,\mathbf{f}_\circ\mathbf{s}_\circ}}\frac{\partial\mathcal{I}_{8,\mathbf{f}_\circ\mathbf{s}_\circ}}{\partial\mathsf{C}}\right] - p\operatorname{cof}\mathsf{F}. \end{aligned}$$

The derivatives of the invariants are easy to compute:

$$\frac{\partial \mathcal{I}_1}{\partial \mathsf{C}} = \mathsf{I}, \quad \frac{\partial \mathcal{I}_{4,\mathbf{f}_\circ}}{\partial \mathsf{C}} = \mathbf{f}_\circ \otimes \mathbf{f}_\circ, \quad \frac{\partial \mathcal{I}_{4,\mathbf{s}_\circ}}{\partial \mathsf{C}} = \mathbf{s}_\circ \otimes \mathbf{s}_\circ, \quad \frac{\partial \mathcal{I}_{8,\mathbf{f}_\circ\mathbf{s}_\circ}}{\partial \mathsf{C}} = \frac{1}{2}\big(\mathbf{f}_\circ \otimes \mathbf{s}_\circ + \mathbf{s}_\circ \otimes \mathbf{f}_\circ\big),$$

and so the derivatives of the additive terms of the energy function. The final form reads as follows:

$$\begin{aligned} \mathsf{T} &= a e^{b(\mathcal{I}_1 - 3)}\mathsf{B} - p\mathsf{I} \\ &\quad + 2\, a_{\mathsf{f}}(\mathcal{I}_{4,\mathbf{f}_\circ} - 1) e^{b_{\mathsf{f}}(\mathcal{I}_{4,\mathbf{f}_\circ} - 1)^2}\, \mathbf{f} \otimes \mathbf{f} + 2\, a_{\mathsf{s}}(\mathcal{I}_{4,\mathbf{s}_\circ} - 1) e^{b_{\mathsf{s}}(\mathcal{I}_{4,\mathbf{s}_\circ} - 1)^2}\, \mathbf{s} \otimes \mathbf{s} \\ &\quad + a_{\mathsf{fs}} \mathcal{I}_{8,\mathbf{f}_\circ\mathbf{s}_\circ} e^{b_{\mathsf{fs}}\mathcal{I}^2_{8,\mathbf{f}_\circ\mathbf{s}_\circ}}\, (\mathbf{f} \otimes \mathbf{s} + \mathbf{s} \otimes \mathbf{f}), \end{aligned} \tag{1.9}$$

where $\mathbf{f} = \mathsf{F}\mathbf{f}_\circ$ and $\mathbf{s} = \mathsf{F}\mathbf{s}_\circ$. The transversely isotropic version of the model can be formally obtained taking $a_{\mathsf{s}} = b_{\mathsf{s}} = a_{\mathsf{fs}} = b_{\mathsf{fs}} = 0$, while the isotropic one corresponds to assume also $a_{\mathsf{f}} = b_{\mathsf{f}} = 0$; furthermore, in these two cases the set of invariants is smaller then the irreducible one, always because the quadratic terms are not considered.

It's interesting to observe that the assumptions made on the symmetry of the material, and in particular on its microstructure, reflect in the tensorial form of the Cauchy stress tensor: the isotropic contribution can be thought as due to the extracellular matrix, while the anisotropic terms play a role along the fibres and the sheets, or when the deformation changes the angle between the two.

Remark 4. The predictions of the model in the compressive regime are not satisfactory, because it is well known that a fibre (one may think to a rod) behaves very differently in compressive vs. tensile regime. For this reason Holzapfel and Odgen suggest that the anisotropic terms associated to $\mathcal{I}_{4,\mathbf{f}_\circ}$ and $\mathcal{I}_{4,\mathbf{s}_\circ}$ should be turned off under compression, i.e. when $\mathcal{I}_{4,\mathbf{f}_\circ} < 1$, or $\mathcal{I}_{4,\mathbf{s}_\circ} < 1$, respectively.

A mathematical advantage of this formulation, is that strong ellipticity of $\widetilde{\mathcal{W}}_{4,\cdot}$ can be proved. On the other hand, loss of strong ellipticity for soft biological tissues has been studied in literature in relation to formation and rupture of aneurysms (Destrade et al., 2008). In the case of the heart, fibres are almost always loaded, even during the diastolic phase, because of the residual stress.

1.1.4 Quasi–incompressible formulation

Biological tissues are mostly made of water, which is an incompressible fluid. Because of this, it is usual to include in the hyperelastic models the incompressibility constraint, as it has been done in the previous sections. Nonetheless, a living tissue is not just a vesicle filled with water, it is rather an intricate bundle of vessels of different scales, collagen, elastin, other substances that compose the extracellular matrix, and perfused blood; the latter in particular plays a fundamental role, because it is responsible for the large volume variation (up to 30%) observed in the ventricle (Yin et al., 1996). Concluding, even neglecting the role of perfused blood, an extra degree of freedom that takes into the account very moderate volumetric changes, is not forbidden by experimental evidence. Moreover, there are some numerical advantages in a quasi–incompressible formulation over an incompressible one (Simo and Taylor, 1991).

For a given incompressible model, such us the Holzapfel–Ogden's one, it is possible to write a quasi–incompressible version introducing the following multiplicative decomposition of the deformation gradient tensor:

$$\mathsf{F} = \mathsf{F}_{\mathsf{iso}}\mathsf{F}_{\mathsf{vol}}, \tag{1.10}$$

that is, the local deformation is the composition of purely volumetric deformation, followed by an isochoric one. In particular, we would like to have that $\det \mathsf{F}_{\mathsf{iso}} = 1$ and $\mathsf{F}_{\mathsf{vol}} = \alpha \mathsf{I}$, so:

$$J = \det \mathsf{F} = \det \mathsf{F}_{\mathsf{iso}} \cdot \det \mathsf{F}_{\mathsf{vol}} = \alpha^3, \qquad \text{so} \qquad \alpha = J^{\frac{1}{3}}.$$

This decomposition perfectly fits with the volumetric–deviatoric additive decomposition of the infinitesimal strain, as usually done in linear elasticity. In fact, define the following strain tensors:

$$\mathsf{C}_{\mathsf{iso}} := \mathsf{F}_{\mathsf{iso}}^{\mathsf{T}} \mathsf{F}_{\mathsf{iso}} = J^{-\frac{2}{3}} \mathsf{C}, \qquad \text{and} \qquad \mathsf{E}_{\mathsf{iso}} := \frac{1}{2}\big(\mathsf{C}_{\mathsf{iso}} - \mathsf{I}\big).$$

Then the infinitesimal strain is computed as follows:

$$\begin{aligned} \delta \mathsf{F}_{\mathsf{iso}}\big|_{\mathsf{F}=\mathsf{I}} &= J^{-\frac{1}{3}} \delta \mathsf{F} + \delta(J^{-\frac{1}{3}}) : \mathsf{F}\,\Big|_{\mathsf{F}=\mathsf{I}} = \delta \mathsf{F} - \frac{1}{3} \delta \mathsf{F} : \mathsf{I} = \operatorname{dev} \delta \mathsf{F}, \\ \delta \mathsf{E}_{\mathsf{iso}}\big|_{\mathsf{F}=\mathsf{I}} &= \operatorname{sym} \delta \mathsf{F}_{\mathsf{iso}} = \operatorname{dev} \varepsilon, \end{aligned}$$

so we recover the splitting $\varepsilon = \operatorname{dev} \varepsilon + \frac{1}{3} \operatorname{tr} \varepsilon$.

Within this context, the two deformations $\mathsf{F}_{\mathsf{iso}}$ and $\mathsf{F}_{\mathsf{vol}}$ (which is just J) contribute additively to the strain–energy, so:

$$\mathcal{W}(\mathsf{F}) = \mathcal{W}_{\mathsf{iso}}(\mathsf{F}_{\mathsf{iso}}) + \mathcal{W}_{\mathsf{vol}}(J). \tag{1.11}$$

The term $\mathcal{W}_{\mathsf{iso}}$ can be any strain–energy for an incompressible material, so we can choose the Holzapfel–Ogdgen material, keeping in mind that now the argument of the functional is $\mathsf{F}_{\mathsf{iso}}$ and not F. In this respect, let's define the isochoric (or reduced) version of the invariants:

$$\begin{aligned} \mathcal{I}_1(\mathsf{C}_{\mathsf{iso}}) &= \operatorname{tr} \mathsf{C}_{\mathsf{iso}} = J^{-\frac{2}{3}} \mathcal{I}_1(\mathsf{C}), \\ \mathcal{I}_{4,\mathbf{a}}(\mathsf{C}_{\mathsf{iso}}) &= \mathbf{a} \cdot \mathsf{C}_{\mathsf{iso}} \mathbf{a} = J^{-\frac{2}{3}} \mathcal{I}_{4,\mathbf{a}}(\mathsf{C}), \\ \mathcal{I}_{8,\mathbf{ab}}(\mathsf{C}_{\mathsf{iso}}) &= \frac{1}{2}\Big[\mathbf{a} \cdot \mathsf{C}_{\mathsf{iso}} \mathbf{b} + \mathbf{b} \cdot \mathsf{C}_{\mathsf{iso}} \mathbf{a}\Big] = J^{-\frac{2}{3}} \mathcal{I}_{8,\mathbf{ab}}(\mathsf{C}). \end{aligned}$$

The second term of the r.h.s. of equation (1.11) is the volumetric energy, and it increases when $J \neq 1$. Several forms for $\mathcal{W}_{\mathsf{vol}}$ can be found in the literature: as a rule of thumb, a good choice would be a function bounded from below, convex and whose derivative is zero for $J = 1$.

Figure 1.2 shows some possibile choices: as one can observe all the functions are very similar around $J = 1$, while they substantially differ for $J < 1$, and the limit $J \to 0$ is approached in different ways. The scaling factor κ is the *bulk modulus* for the linearised version, and formally the material is incompressible for $\kappa \to \infty$. Generally one would expect that $\mathcal{W}_{\mathsf{iso}} \to \infty$ as $J \to 0$ and $J \to \infty$, because from a physical viewpoint we are compressing the body down to a point or dilating it indefinitely. Nevertheless, we are considering quasi–incompressible model, and we expect to keep $J \approx 1$, so practically there is no difference between the models from a pratical viewpoint; at the mathematical level instead, the well–posedness of the problem can be compromised in some cases (Schröder and Neff, 2003).

In order to compute the stress tensors, first we observe that:

$$\mathcal{W}(\mathsf{F}) = \widehat{\mathcal{W}}(\mathsf{F}^{\mathsf{T}}\mathsf{F}) = \widehat{\mathcal{W}}(\mathsf{C}) = \widehat{\mathcal{W}}_{\mathsf{iso}}(\mathsf{C}_{\mathsf{iso}}) + \mathcal{W}_{\mathsf{vol}}(J).$$

The second Piola–Kirchhoff tensor is:

$$\mathsf{S} = 2\frac{\partial \widehat{\mathcal{W}}}{\partial \mathsf{C}} = 2\frac{\partial \widehat{\mathcal{W}}_{\mathsf{iso}}}{\partial \mathsf{C}} + 2\frac{\partial \mathcal{W}_{\mathsf{vol}}}{\partial \mathsf{C}} = 2\frac{\partial \widehat{\mathcal{W}}_{\mathsf{iso}}}{\partial \mathsf{C}_{\mathsf{iso}}}\frac{\partial \mathsf{C}_{\mathsf{iso}}}{\partial \mathsf{C}} + 2\frac{\partial \mathcal{W}_{\mathsf{vol}}}{\partial J}\frac{\partial J}{\partial \mathsf{C}} = \mathsf{S}_{\mathsf{iso}} + \mathsf{S}_{\mathsf{vol}}.$$

Explicit relations for the derivatives with respect to C can be easily established as follows:

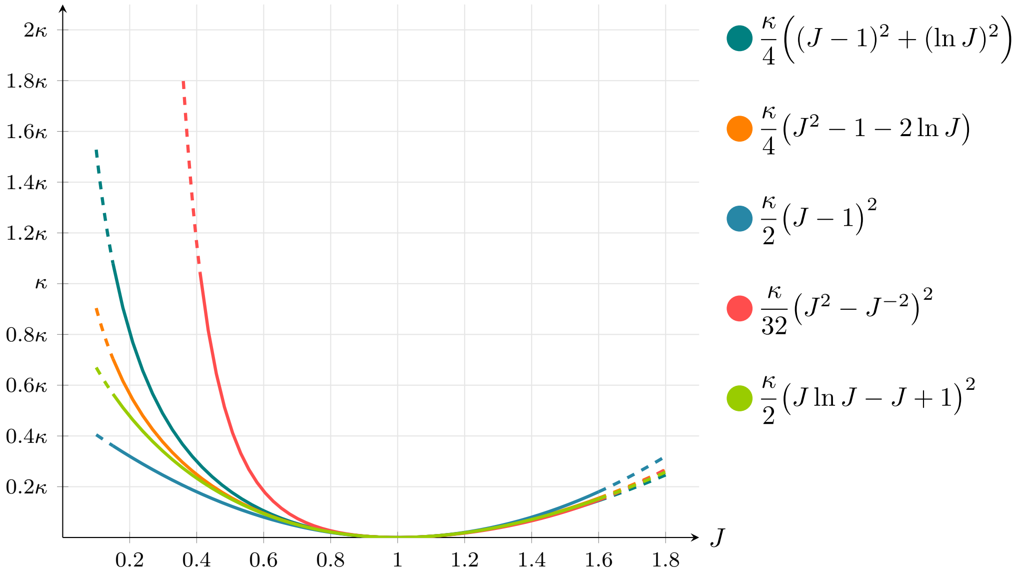

Figure 1.2 Examples of $\mathcal{W}_{\mathsf{iso}}(J)$.

❶ Notice that $\det(\mathsf{C}) = J^2$, so we have

$$2J\frac{\partial J}{\partial \mathsf{C}} = \frac{\partial \det \mathsf{C}}{\partial \mathsf{C}} = (\det \mathsf{C})\mathsf{C}^{-1} = J^2\mathsf{C}^{-1} \qquad \Rightarrow \qquad \mathsf{S}_{\mathsf{vol}} = \mathcal{W}'_{\mathsf{vol}}(J)J\mathsf{C}^{-1},$$

where we have exploited also the simmetry of C.

❷ By definition $\mathsf{C}_{\mathsf{iso}} = J^{-\frac{2}{3}}\mathsf{C}$, thanks to the previous relation and the chain–rule:

$$\frac{\partial \mathsf{C}_{\mathsf{iso}}}{\partial \mathsf{C}} = J^{-\frac{2}{3}}\mathbb{I} - \frac{2}{3}J^{-\frac{5}{3}}\mathsf{C}\otimes\frac{\partial J}{\partial \mathsf{C}} = J^{-\frac{2}{3}}\left(\mathbb{I} - \frac{1}{3}\mathsf{C}\otimes\mathsf{C}^{-1}\right), \tag{1.12}$$

where $\mathbb{I}$ is the fourth–order tensor such that $\mathbb{I}\mathsf{A} = \mathsf{A}$ for every second–order tensor A, while $\otimes$ denotes the tensor product. Many authors refer to the tensorial part of the expression in equation (1.12) as the material deviatoric operator Dev:

$$\mathrm{D{\small EV}}\colon \mathrm{Sym}^+ \ni \mathsf{S} \mapsto \mathrm{D{\small EV}}\,\mathsf{S} := \mathsf{S} - \frac{1}{3}(\mathsf{S}:\mathsf{C})\mathsf{C}^{-1} \in \mathrm{Sym}^+.$$

The isochoric part of the second Piola–Kirchhoff tensor is then:

$$\mathsf{S}_{\mathsf{iso}} = J^{-\frac{2}{3}}\,\mathrm{D{\small EV}}\,\overline{\mathsf{S}}_{\mathsf{iso}}, \qquad \text{with } \overline{\mathsf{S}}_{\mathsf{iso}} := 2\frac{\partial \widehat{\mathcal{W}}_{\mathsf{iso}}}{\partial \mathsf{C}_{\mathsf{iso}}}.$$

Observe that $\overline{\mathsf{S}}_{\mathsf{iso}}$ is the fictitious second Piola–Kirchhoff tensor of $\widehat{\mathcal{W}}_{\mathsf{iso}}$, and is a function of $\mathsf{C}_{\mathsf{iso}}$.

The Cauchy stress tensor is obtained by means of a Piola transformation:

$$\begin{aligned} \mathsf{T} = J^{-1}\mathsf{F}\mathsf{S}\mathsf{F}^{\mathsf{T}} &= J^{-1}J^{-\frac{1}{3}}\mathsf{F}\mathsf{S}_{\mathsf{iso}}J^{-\frac{1}{3}}\mathsf{F}^{\mathsf{T}} + \mathcal{W}'_{\mathsf{vol}}(J)\mathsf{I} \\ &= J^{-1}\left(\mathsf{F}_{\mathsf{iso}}\mathsf{S}_{\mathsf{iso}}\mathsf{F}_{\mathsf{iso}}^{\mathsf{T}} - \frac{1}{3}(\mathsf{S}_{\mathsf{iso}}:\mathsf{C})\mathsf{I}\right) + \mathcal{W}'_{\mathsf{vol}}(J)\mathsf{I} \\ &= \left(\overline{\mathsf{T}}_{\mathsf{iso}} - \frac{1}{3}(\mathrm{tr}\,\overline{\mathsf{T}}_{\mathsf{iso}})\mathsf{I}\right) + \mathcal{W}'_{\mathsf{vol}}(J)\mathsf{I} = \mathsf{T}_{\mathsf{iso}} + \mathsf{T}_{\mathsf{vol}}. \end{aligned} \tag{1.13}$$

where $\mathsf{T}_{\mathsf{iso}} = \operatorname{dev} \overline{\mathsf{T}}_{\mathsf{iso}}$ and $\overline{\mathsf{T}}_{\mathsf{iso}} := J^{-1} \mathsf{F}_{\mathsf{iso}} \overline{\mathsf{S}}_{\mathsf{iso}} \mathsf{F}_{\mathsf{iso}}^{\mathsf{T}}$ is the fictitious Cauchy stress tensor associated to the strain–energy $\mathcal{W}_{\mathsf{iso}}$. In particular, for the Holzapfel–Ogden model, we can just substitute equation (1.9) with $J\overline{\mathsf{T}}_{\mathsf{iso}}$, so:

$$\begin{aligned} J\overline{\mathsf{T}}_{\mathsf{iso}} &= a e^{b(\mathcal{I}_1 - 3)} \mathsf{B}_{\mathsf{iso}} \\ &\quad + 2\, a_{\mathsf{f}} (\mathcal{I}^{\mathsf{iso}}_{4,\mathbf{f}_\circ} - 1) e^{b_{\mathsf{f}}(\mathcal{I}^{\mathsf{iso}}_{4,\mathbf{f}_\circ} - 1)^2}\, \mathbf{f}_{\mathsf{iso}} \otimes \mathbf{f}_{\mathsf{iso}} + 2\, a_{\mathsf{s}} (\mathcal{I}^{\mathsf{iso}}_{4,\mathbf{s}_\circ} - 1) e^{b_{\mathsf{s}}(\mathcal{I}^{\mathsf{iso}}_{4,\mathbf{s}_\circ} - 1)^2}\, \mathbf{s}_{\mathsf{iso}} \otimes \mathbf{s}_{\mathsf{iso}} \\ &\quad + a_{\mathsf{fs}} \mathcal{I}^{\mathsf{iso}}_{8,\mathbf{f}_\circ \mathbf{s}_\circ} e^{b_{\mathsf{fs}}(\mathcal{I}^{\mathsf{iso}}_{8,\mathbf{f}_\circ \mathbf{s}_\circ})^2}\, (\mathbf{f}_{\mathsf{iso}} \otimes \mathbf{s}_{\mathsf{iso}} + \mathbf{s}_{\mathsf{iso}} \otimes \mathbf{f}_{\mathsf{iso}}), \end{aligned}$$

where all the quantities marked with $(\circ)^{\mathsf{iso}}$ or $(\circ)_{\mathsf{iso}}$ have to be computed with respect to $\mathsf{F}_{\mathsf{iso}}$ instead of F. Observe also that the pressure is exactly $-\mathcal{W}'_{\mathsf{vol}}(J)$.

Remark 5. The multiplicative splitting in equation (1.10) of the deformation tensor F is critical in order to have a stress–free reference configuration. Indeed, when $\mathsf{F} = \mathsf{I}$, the Cauchy stress tensor is a multiple of the identity, and because $\operatorname{dev} \mathsf{I} = 0$ the only requirement is $\mathcal{W}'_{\mathsf{vol}}(1) = 0$.

1.2 Numerical approximation

1.2.1 Variational formulation

The equation (1.3) can be reformulated as minimum problem under specific regularity conditions. Consider the following functional of the deformation $\boldsymbol{\varphi}$:

$$\mathcal{F}(\boldsymbol{\varphi}) := \int_{\Omega_0} \mathcal{W}(\mathbf{X}, \mathsf{F})\, \mathrm{d}V - \int_{\Omega_0} \rho_0 \mathbf{b}_0 \cdot \boldsymbol{\varphi}\, \mathrm{d}V - \int_{\partial_{\mathrm{N}} \Omega_0} \mathbf{t}_0 \cdot \boldsymbol{\varphi}\, \mathrm{d}A, \tag{1.14}$$

where $\rho_0 \colon \Omega_0 \to \mathbb{R}^+$ is the density mass of the body in the material configuration, $\mathbf{b}_0 \colon \Omega_0 \to \mathbb{R}^3$ is a body force and $\mathbf{t}_0 \colon \partial_{\mathrm{N}} \Omega_0 \to \mathbb{R}^3$ the traction at the boundary, with $\mathbf{t}_0 = \mathsf{P}\mathbf{n}_0$ for $\mathbf{n}_0$ the normal to the boundary. The functional is essentially the balance between the potential energy of the internal stresses and the external loads.

We look for the minimum of the functional defined in equation (1.14). First of all, the minimum has to be admissible, i.e. it has to belong to

$$\mathscr{C} := \Big\{ \boldsymbol{\varphi} \colon \Omega_0 \to \Omega \text{ such that } \mathsf{F} \in \operatorname{Lin}^+ \text{ and } \boldsymbol{\varphi}|_{\partial_{\mathrm{D}} \Omega_0} = \mathbf{g} \Big\}.$$

Secondly, we need some extra restriction on the deformations and the functional itself, in order to establish that at least a minimum exists. A typical choice of the functional space is $V := \mathscr{C} \cap \mathrm{W}^{1,s}(\Omega_0; \mathbb{R}^3)$.

The theory behind the minimization problem is sophisticate and uses tools of the calculus of variation, and in particular the direct method. Indeed, under certain continuity conditions on the functional and compactness properties of the space, it is possible to prove that at least one minimum exists. If also the functional and the space are convex, then the minimum is unique.

Unfortunately this is not the case for an hyperelastic material, because even if the strain–energy function is convex with respect to F, the set Lin^+ is not. There are also other reason on why we cannot rely on convexity, such as the fact that is not compatible with the frame–invariance or the fact that uniqueness forbids bifurcations (for instance buckling). In this respect, polyconvexity has been a key idea over the last four decades: a function $\mathcal{W} \colon \operatorname{Lin}^+ \to \mathbb{R}$ is polyconvex if it exists a convex function $g \colon \operatorname{Lin}^+ \times \operatorname{Lin}^+ \times \mathbb{R}^+ \to \mathbb{R}$ such that

$$\mathcal{W}(\mathsf{F}) = g(\mathsf{F}, \operatorname{cof} \mathsf{F}, \det \mathsf{F}), \qquad \text{for every } \mathsf{F} \in \operatorname{Lin}^+.$$

Observe for instance that a function $\mathcal{W}(\mathsf{F}) = \mathcal{W}(\det \mathsf{F})$, such as the volumetric contribution in the quasi–incompressible formulation, convex with respect to $\det \mathsf{F}$, cannot be convex with respect to F because Lin^+ is not; but it is polyconvex, because $\mathcal{W}(J)$ is convex on $\mathbb{R}^+$.

It's possible to prove that if $\mathcal{W}$ is polyconvex and coercive then it exists at least one minimum in $\mathrm{W}^{1,s}(\Omega_0;\mathbb{R}^3)$, $s > \frac{3}{2}$ and $\frac{1}{s} + \frac{1}{q} < \frac{4}{3}$, with q such that $\operatorname{cof} \mathsf{F} \in \mathrm{L}^q(\Omega_0;\mathrm{Lin}^+)$. For an extensive treatise see Antman (2005) and Marsden and Hughes (1983).

Suppose now that there is a minimizing deformation $\boldsymbol{\varphi} \in \mathscr{C}$: then, under regularity hypothesis, it must be a stationary point of $\mathcal{F}$. A variation $\boldsymbol{\eta}$ about $\boldsymbol{\varphi}$ must be admissible, so it belongs to the tangent space of $\mathscr{C}$ at $\boldsymbol{\varphi}$:

$$\mathscr{T}_{\boldsymbol{\varphi}}\mathscr{C} := \left\{\boldsymbol{\eta}\colon \Omega \to \mathbb{R}^3 \text{ such that } \boldsymbol{\eta} \circ \boldsymbol{\varphi}|_{\partial_{\mathrm{D}}\Omega_0} = \mathbf{0}\right\}$$

that is, we fix a deformation $\boldsymbol{\varphi}$ and we "slightly" change it while keeping the essential boundary fixed. If we define $\boldsymbol{\eta}_0 := \boldsymbol{\eta} \circ \boldsymbol{\varphi}$ as the material version of $\boldsymbol{\eta}$, the variation computed along a curve starting at $\boldsymbol{\varphi}$ and tangent to $\boldsymbol{\eta}_0$ reads:

$$\varepsilon \mapsto \boldsymbol{\varphi} + \varepsilon\boldsymbol{\eta}_0 \in \mathscr{C},$$

so we can define the Gâteaux derivative of $\mathcal{F}\colon V \to \mathbb{R}$ as follows:

$$\langle \mathrm{D}\mathcal{F}(\boldsymbol{\varphi}), \boldsymbol{\eta}_0\rangle := \left.\frac{\mathrm{d}}{\mathrm{d}\varepsilon}\mathcal{F}(\boldsymbol{\varphi} + \varepsilon\boldsymbol{\eta}_0)\right|_{\varepsilon=0}.$$

The minimum of $\mathcal{F}$ is such that $\langle \mathrm{D}\mathcal{F}(\boldsymbol{\varphi}), \boldsymbol{\eta}_0\rangle = 0$ for every $\boldsymbol{\eta}_0 \in V$.

With the aid of the latter formula, we have:

$$\begin{aligned}
\left.\frac{\mathrm{d}}{\mathrm{d}\varepsilon}\mathsf{F}(\boldsymbol{\varphi} + \varepsilon\boldsymbol{\eta} \circ \boldsymbol{\varphi})\right|_{\varepsilon=0} &= \textsc{Grad}\,\boldsymbol{\eta}_0 := (\nabla\boldsymbol{\eta} \circ \boldsymbol{\varphi})\mathsf{F}(\boldsymbol{\varphi}),\\
\left.\frac{\mathrm{d}}{\mathrm{d}\varepsilon}\int_{\Omega_0} \mathcal{W}\big(\mathsf{F}(\boldsymbol{\varphi} + \varepsilon\boldsymbol{\eta} \circ \boldsymbol{\varphi})\big)\mathrm{d}V\right|_{\varepsilon=0} &= \int_{\Omega_0} \frac{\partial\mathcal{W}}{\partial\mathsf{F}}\big(\mathsf{F}(\boldsymbol{\varphi})\big) : (\nabla\boldsymbol{\eta} \circ \boldsymbol{\varphi})\mathsf{F}(\boldsymbol{\varphi})\,\mathrm{d}V.
\end{aligned}$$

The other two terms in equation (1.14) are linear with respect to $\boldsymbol{\varphi}$, so recalling also that the first Piola–Kirchhoff tensor is by definition $\frac{\partial\mathcal{W}}{\partial\mathsf{F}}$, the final form of the variational problem is as follows:

$$\left\|\;\begin{aligned}
&\text{Find } \boldsymbol{\varphi} \in V \text{ such that}\\
&\int_{\Omega_0} \mathsf{P} : \textsc{Grad}\,\boldsymbol{\eta}_0\,\mathrm{d}V - \int_{\Omega_0} \rho_0\mathbf{b}_0 \cdot \boldsymbol{\eta}_0\,\mathrm{d}V - \int_{\partial_{\mathrm{N}}\Omega_0} \mathbf{t}_0 \cdot \boldsymbol{\eta}_0\,\mathrm{d}A = 0, \qquad \forall\boldsymbol{\eta}_0 \in V.
\end{aligned}\right. \tag{1.15}$$

The same problem can also be stated in the actual configuration, exploiting that $\mathbf{x} = \boldsymbol{\varphi}(\mathbf{X})$:

$$\begin{aligned}
\int_{\Omega_0} \mathsf{P} : \textsc{Grad}\,\eta_0\,\mathrm{d}V &= \int_{\Omega} \mathsf{P} : \nabla\eta\mathsf{F}\,J^{-1}\mathrm{d}V = \int_{\Omega} J^{-1}\mathsf{P}\mathsf{F}^{\mathsf{T}} : \nabla\eta\,\mathrm{d}v = \int_{\Omega} \mathsf{T} : \nabla\eta\,\mathrm{d}v,\\
\int_{\Omega_0} \rho_0\mathbf{b}_0 \cdot \boldsymbol{\eta}_0\,\mathrm{d}V &= \int_{\Omega} (J^{-1}\rho_0\mathbf{b}_0) \circ \boldsymbol{\varphi}^{-1} \cdot \boldsymbol{\eta}\,\mathrm{d}v = \int_{\Omega} \rho\mathbf{b} \cdot \boldsymbol{\eta}\,\mathrm{d}v,
\end{aligned}$$

where $\rho = (J^{-1}\rho_0) \circ \boldsymbol{\varphi}^{-1}$ and $\mathbf{b} = \mathbf{b}_0 \circ \boldsymbol{\varphi}$. Regarding the term on boundary $\partial_{\mathrm{N}}\Omega_0$, we can use the Piola transformation:

$$\int_{\partial_{\mathrm{N}}\Omega_0} \mathbf{t}_0 \cdot \boldsymbol{\eta}_0\,\mathrm{d}A = \int_{\partial_{\mathrm{N}}\Omega_0} \mathsf{P}\mathbf{n}_0 \cdot \boldsymbol{\eta}_0\,\mathrm{d}A = \int_{\partial_{\mathrm{N}}\Omega} \mathsf{T}\mathbf{n} \cdot \boldsymbol{\eta}\,\mathrm{d}a = \int_{\partial_{\mathrm{N}}\Omega} \mathbf{t} \cdot \boldsymbol{\eta}\,\mathrm{d}a.$$

Thus, the equation (1.15) in the actual coordinates reads:

$$\left\|\begin{array}{l}\text{Find } \boldsymbol{\varphi} \in V \text{ such that}\\ \displaystyle\int_{\Omega} \mathsf{T} : \nabla\boldsymbol{\eta}\, \mathrm{d}v - \int_{\Omega} \rho\mathbf{b}\cdot\boldsymbol{\eta}\, \mathrm{d}v - \int_{\partial_{\mathrm{N}}\Omega} \mathbf{t}\cdot\boldsymbol{\eta}\, \mathrm{d}a = 0, \qquad \forall\boldsymbol{\eta} \in V.\end{array}\right. \tag{1.16}$$

The quasi–incompressible formulation can be straightforwardly obtained by substitution of equation (1.13) into equation (1.16) and observing that $\operatorname{dev}\mathsf{A}_1 : \mathsf{A}_2 = \operatorname{dev}\mathsf{A}_1 : \operatorname{dev}\mathsf{A}_2$. In fact, $\mathsf{A} = \operatorname{dev}\mathsf{A} + \operatorname{vol}\mathsf{A}$ and

$$\operatorname{dev}\mathsf{A}_1 : \operatorname{vol}\mathsf{A}_2 = \mathsf{A}_1 : \frac{1}{3}(\operatorname{tr}\mathsf{A}_2)\mathsf{I} - \frac{1}{9}(\operatorname{tr}\mathsf{A}_1)(\operatorname{tr}\mathsf{A}_2)\mathsf{I} : \mathsf{I} = 0.$$

The equation (1.16) becomes:

$$\left\|\begin{array}{l}\text{Find } \boldsymbol{\varphi} \in V \text{ such that}\\ \displaystyle\int_{\Omega} \Big(\operatorname{dev}\bar{\mathsf{T}}_{\mathsf{iso}} : \operatorname{dev}\nabla\boldsymbol{\eta} + \mathcal{W}'_{\mathsf{vol}}(J)\operatorname{div}\boldsymbol{\eta}\Big)\, \mathrm{d}v - \int_{\Omega} \rho\mathbf{b}\cdot\boldsymbol{\eta}\, \mathrm{d}v - \int_{\partial_{\mathrm{N}}\Omega} \mathbf{t}\cdot\boldsymbol{\eta}\, \mathrm{d}a = 0, \qquad \forall\boldsymbol{\eta} \in V.\end{array}\right.$$

Remark 6. It's often simpler to introduce the displacement $\mathbf{u}\colon \Omega_0 \to \mathbb{R}^3$ as the vector field $\mathbf{u}(\mathbf{X}) = \mathbf{x}(\mathbf{X}) - \mathbf{X}$. In particular its gradient is just $\mathsf{F} - \mathsf{I}$. But the definition of $\mathbf{u}$ makes sense only if $\mathbf{x}$ can be pulled back to the reference configuration: this is not possible in general if a curvilinear coordinate system is used, or more generally if the metric on Ω differs from the metric on Ω_0. On the other hand, the displacement will arise naturally after linearisation.

1.2.2 Three–field variational principle

The variational formulation as minimisation of the functional of equation (1.14) is not satisfactory when κ is very large, i.e. when we try to enforce incompressibility: in this case the *locking* phenomenon might be observed. In such a regime a valid possibility is to go back to the full incompressible formulation, with the pressure as a Lagrangian multiplier. The resulting formulation of the tangent problem, required by Newton method, rereads as a Stokes type problem, which introduces various difficulties from a computational viewpoint.

A widely accepted alternative, that preserves quasi–incompressibility is the so called "three–field" or "Hu–Washitzu" formulation. The general idea, inherited from linear elasticity, is to split the infinitesimal strain ε and the stress σ into dilational and parts:

$$\begin{aligned}\varepsilon &= \operatorname{dev}\varepsilon + \operatorname{vol}\varepsilon = \operatorname{dev}\varepsilon + \frac{1}{3}\theta\mathsf{I},\\ \sigma &= \operatorname{dev}\sigma + \operatorname{vol}\sigma = \operatorname{dev}\sigma + p\mathsf{I},\end{aligned}$$

so there are two new variables: θ, which measures volume variations, and p, which is the pressure. The final step is to introduce two independent constitutive laws for $\operatorname{dev}\sigma$ and p, the former depending on $\operatorname{dev}\varepsilon$ and the latter on θ only.

It is possible to do something similar for finite deformations. Consider the following factorization of the deformation gradient tensor:

$$\tilde{\mathsf{F}}(\boldsymbol{\varphi}, \Theta) := \Theta^{\frac{1}{3}}(\det\mathsf{F})^{-\frac{1}{3}}\mathsf{F},$$

which is now a function of the new variable $\Theta \in Q := \mathrm{L}^2(\Omega_0)$, with $\Theta > 0$. The strain–energy density function will be a function $\mathcal{W}$ of $\bar{\mathsf{F}}$, so in particular of Θ and F.

In a similar way done for the isochoric–volumetric decomposition, we define:

$$\tilde{\mathsf{C}}(\boldsymbol{\varphi},\Theta) := \tilde{\mathsf{F}}(\boldsymbol{\varphi},\Theta)^{\mathsf{T}}\tilde{\mathsf{F}}(\boldsymbol{\varphi},\Theta), \qquad \text{and} \qquad \tilde{\mathsf{E}}(\boldsymbol{\varphi},\Theta) := \frac{1}{2}\big(\tilde{\mathsf{C}} - \mathsf{I}\big),$$

and we observe that this choice is consistent with linear elasticity:

$$\begin{aligned} \delta\tilde{\mathsf{F}}\big|_{\mathsf{F}=\mathsf{I},\Theta=1} &= \delta\mathsf{F} - \frac{1}{3}\delta\mathsf{F} : \mathsf{I} + \frac{1}{3}\delta\Theta\mathsf{I}, = \operatorname{dev}\delta\mathsf{F} + \frac{1}{3}\delta\Theta\mathsf{I}, \\ \delta\tilde{\mathsf{E}}\big|_{\mathsf{F}=\mathsf{I},\Theta=1} &= \operatorname{sym}\delta\tilde{\mathsf{F}} = \operatorname{dev}\varepsilon + \frac{1}{3}\theta\mathsf{I}. \end{aligned}$$

Now consider a quasi–incompressible formulation for $\mathcal{W}$. The first step is the splitting of $\bar{\mathsf{F}}$ into the isochoric and volumetric parts:

$$\begin{aligned} (\tilde{\mathsf{F}}(\boldsymbol{\varphi},\Theta))_{\mathsf{vol}} &:= \det(\tilde{\mathsf{F}}(\boldsymbol{\varphi},\Theta)) = \Theta, \\ (\tilde{\mathsf{F}}(\boldsymbol{\varphi},\Theta))_{\mathsf{iso}} &:= (\tilde{\mathsf{F}}(\boldsymbol{\varphi},\Theta))_{\mathsf{vol}}^{-\frac{1}{3}}\tilde{\mathsf{F}}(\boldsymbol{\varphi},\Theta) = (\det\mathsf{F})^{-\frac{1}{3}}\mathsf{F} = \mathsf{F}_{\mathsf{iso}} \end{aligned}$$

The second step is the additive splitting of the energy:

$$\mathcal{W}(\tilde{\mathsf{F}}) = \mathcal{W}_{\mathsf{iso}}(\mathsf{F}_{\mathsf{iso}}) + \mathcal{W}_{\mathsf{vol}}(\Theta).$$

The last ingredient we need is a variational principle: consider the following functional $\mathcal{F}_{\mathsf{HW}}$ of the variables $(\boldsymbol{\varphi},\Theta,p) \in V \times Q \times Q$:

$$\mathcal{F}_{\mathsf{HW}}(\boldsymbol{\varphi},\Theta,p) := \int_{\Omega_0} \Big(\mathcal{W}_{\mathsf{iso}}(\mathbf{X},\mathsf{F}_{\mathsf{iso}}) + \mathcal{W}_{\mathsf{vol}}(\mathbf{X},\Theta) + p(J-\Theta)\Big)\,\mathrm{d}V - \mathcal{F}^{\mathsf{ext}}(\boldsymbol{\varphi}), \tag{1.17}$$

where $\mathcal{F}^{\mathsf{ext}}$ is the external work due to $\mathbf{b}_0$ and $\mathbf{t}_0$. $\mathcal{F}_{\mathsf{HW}}$ mimics the functional in equation (1.14) with the additional term $p(J-\Theta)$ that enforces the constraint $\Theta = J$. In this respect, p is the pressure.

Denoting with $\mathrm{D}_{\boldsymbol{\varphi}}$ the partial Gâteaux derivative with respect to $\boldsymbol{\varphi}$, we have

$$\begin{aligned} \langle \mathrm{D}_{\boldsymbol{\varphi}}\mathcal{F}_{\mathsf{HW}}, \boldsymbol{\eta}_0\rangle &= \int_{\Omega_0} \frac{\partial\mathcal{W}_{\mathsf{iso}}}{\partial\mathsf{F}} : \textsc{Grad}\,\boldsymbol{\eta}_0\,\mathrm{d}V + \int_{\Omega_0} p\operatorname{cof}\mathsf{F} : \textsc{Grad}\,\boldsymbol{\eta}_0\,\mathrm{d}V - \big\langle \mathrm{D}_{\boldsymbol{\varphi}}\mathcal{F}^{\mathsf{ext}}, \boldsymbol{\eta}_0\big\rangle \\ &= \int_{\Omega} \operatorname{dev}\overline{\mathsf{T}}_{\mathsf{iso}} : \operatorname{dev}\nabla\boldsymbol{\eta}\,\mathrm{d}v + \int_{\Omega} p\operatorname{div}\boldsymbol{\eta}\,\mathrm{d}v - \big\langle \mathbf{f}^{\mathsf{ext}}, \boldsymbol{\eta}\big\rangle\,, \end{aligned}$$

where $\mathbf{f}^{\mathsf{ext}}$ is the linear functional in the actual configuration that encapsulates $\mathbf{b}$ and $\mathbf{t}$. The corresponding Cauchy stress tensor is simply as follows:

$$\mathsf{T} = \operatorname{dev}\overline{\mathsf{T}}_{\mathsf{iso}} + p\mathsf{I}.$$

In order to fully characterize the minimum, we have two more derivatives to consider, one with respect to Θ and the other for p:

$$\begin{aligned} \langle \mathrm{D}_{\Theta}\mathcal{F}_{\mathsf{HW}}, \Xi\rangle &= \int_{\Omega_0} \big(\mathcal{W}'_{\mathsf{vol}}(\Theta) - p\big)\Xi\,\mathrm{d}V = \int_{\Omega} \big(\mathcal{W}'_{\mathsf{vol}}(\Theta) - p\big)\Xi\,J^{-1}\mathrm{d}v, \\ \langle \mathrm{D}_{p}\mathcal{F}_{\mathsf{HW}}, q\rangle &= \int_{\Omega_0} q(J-\Theta)\,\mathrm{d}V = \int_{\Omega} q(J-\Theta)\,J^{-1}\mathrm{d}v. \end{aligned}$$

The final variational problem reads as follows:

$$\left\| \begin{aligned} &\text{Find } (\boldsymbol{\varphi},\Theta,p) \in V \times Q \times Q \text{ such that} \\ &\int_{\Omega} \Big(\operatorname{dev}\overline{\mathsf{T}}_{\mathsf{iso}} : \operatorname{dev}\nabla\boldsymbol{\eta} + p\operatorname{div}\boldsymbol{\eta}\Big)\,\mathrm{d}v - \big\langle \mathbf{f}^{\mathsf{ext}}, \boldsymbol{\eta}\big\rangle \\ &+ \int_{\Omega} \big(\mathcal{W}'_{\mathsf{vol}}(\Theta) - p\big)\Xi\,J^{-1}\mathrm{d}v + \int_{\Omega} q(J-\Theta)\,J^{-1}\mathrm{d}v = 0, \quad \forall(\boldsymbol{\eta},\Xi,q) \in V \times Q \times Q. \end{aligned} \right. \tag{1.18}$$

1.2.3 The tangent problem

The variational formulation (1.18) is a non–linear problem in the unknowns $(\boldsymbol{\varphi}, \Theta, p)$. We can highlight two non–linearities: the first one is the constitutive equation, because $\mathsf{T}_{\mathsf{iso}}$ depends on the deformation $\boldsymbol{\varphi}$, as well as $\mathcal{W}_{\mathsf{vol}}$ depends on Θ; the second one is geometrical, because also the integration domain $\Omega = \boldsymbol{\varphi}(\Omega_0)$ is unknown.

The Newton's method is a classical iterative algorithm to find the solution of a non–linear problem. Given a generic operator $\mathcal{G}\colon W \to W^*$, where W is a Banach space and W^* its dual, the Newton's method reads as follows:

$$
\begin{aligned}
&1.\ \textbf{Given } x^0 \in W;\\
&2.\ \textbf{Until } \langle\text{convergence criteria}\rangle \text{ is satisfied:}\\
&3.\ \quad \textbf{Solve for } \delta x \text{ such that } \mathrm{D}\mathcal{G}(x^k)\,\delta x = -\mathcal{G}(x^k);\\
&4.\ \quad \textbf{Let } x^{k+1} = x^k + \delta x.
\end{aligned}
\tag{1.19}
$$

The linear operator $\mathrm{D}\mathcal{G} \in \mathcal{L}(W, W^*)$ is the Gâteaux derivative of $\mathcal{G}$. As a convergence test, typically one checks that both δx and the residual $\mathcal{G}(x_k)$ are smaller than a given tolerance, with respect to a suitable norm.

For our variational problem (1.18) we have $W = V \times Q \times Q$, $x = (\boldsymbol{\varphi}, \Theta, p)$ and $\delta x = (\delta\boldsymbol{\varphi}, \delta\Theta, \delta p)$. The computation of $\mathrm{D}\mathcal{G}(x_k)$ is particularly tedious, but it is just an application of the chain–rule, so we simply report the final result:

$$
\begin{aligned}
\langle \mathrm{D}\mathcal{G}(x)\,\delta x, (\boldsymbol{\eta}, \Xi, p)\rangle = &\int_\Omega \Big(\nabla\delta\boldsymbol{\varphi}\mathsf{T} + \big(\mathfrak{c}_{\mathsf{iso}} + p(\mathsf{I}\otimes\mathsf{I} - 2\mathbb{I})\big)\nabla\delta\boldsymbol{\varphi} + \delta p\,\mathsf{I}\Big) : \nabla\boldsymbol{\eta}\,\mathrm{d}v\\
&+ \int_\Omega \Xi\,\big(\mathcal{W}''_{\mathsf{vol}}(\Theta)\delta\Theta - \delta p\big) J^{-1}\mathrm{d}v\\
&+ \int_\Omega q\,\big(\operatorname{div}\delta\boldsymbol{\varphi} - J^{-1}\delta\Theta\big)\mathrm{d}v,
\end{aligned}
\tag{1.20}
$$

where $\mathsf{T} = \operatorname{dev}\overline{\mathsf{T}}_{\mathsf{iso}} + p\mathsf{I}$ and $\mathfrak{c}_{\mathsf{iso}}$ is the spatial elasticity tensor of the isochoric term:

$$
\mathfrak{c}_{\mathsf{iso}} = \mathbb{P} : \bar{\mathfrak{c}}_{\mathsf{iso}} : \mathbb{P} + \frac{2}{3}J^{-1}\big(\operatorname{tr}\overline{\mathsf{T}}_{\mathsf{iso}}\big)\mathbb{P} - \frac{2}{3}\left(\operatorname{dev}\mathsf{T}_{\mathsf{iso}}\otimes\mathsf{I} + \mathsf{I}\otimes\operatorname{dev}\mathsf{T}_{\mathsf{iso}}\right),
$$

$$
\begin{aligned}
\bar{\mathfrak{c}}_{\mathsf{iso}} = {}& 4\widehat{\mathcal{W}}''_1(\mathcal{I}_1^{\mathsf{iso}})\,\mathsf{B}_{\mathsf{iso}}\otimes\mathsf{B}_{\mathsf{iso}}\\
&+ 4\widehat{\mathcal{W}}''_{4,\mathbf{f}_\circ}(\mathcal{I}_{4,\mathbf{f}_\circ}^{\mathsf{iso}})\,\mathbf{f}_{\mathsf{iso}}\otimes\mathbf{f}_{\mathsf{iso}}\otimes\mathbf{f}_{\mathsf{iso}}\otimes\mathbf{f}_{\mathsf{iso}}\\
&+ 4\widehat{\mathcal{W}}''_{4,\mathbf{s}_\circ}(\mathcal{I}_{4,\mathbf{s}_\circ}^{\mathsf{iso}})\,\mathbf{s}_{\mathsf{iso}}\otimes\mathbf{s}_{\mathsf{iso}}\otimes\mathbf{s}_{\mathsf{iso}}\otimes\mathbf{s}_{\mathsf{iso}}\\
&+ 4\widehat{\mathcal{W}}''_{8,\mathbf{f}_\circ\mathbf{s}_\circ}(\mathcal{I}_{8,\mathbf{f}_\circ\mathbf{s}_\circ}^{\mathsf{iso}})\,\operatorname{sym}(\mathbf{f}_{\mathsf{iso}}\otimes\mathbf{s}_{\mathsf{iso}})\otimes\operatorname{sym}(\mathbf{f}_{\mathsf{iso}}\otimes\mathbf{s}_{\mathsf{iso}}).
\end{aligned}
$$

We have introduced the fourth–order tensor $\mathbb{P}$ as the linear application such that $\mathbb{P}\colon \mathsf{A}\mapsto\operatorname{dev}\mathsf{A}$:

$$
\mathbb{P} := \mathbb{I} - \frac{1}{3}\mathsf{I}\otimes\mathsf{I}.
$$

The expression obtained above contains several terms, but the mathematical structure is particularly simple. We can identify two contributions:

$$
\begin{aligned}
\int_\Omega \nabla\delta\boldsymbol{\varphi}\mathsf{T} : \nabla\delta\boldsymbol{\eta}\,\mathrm{d}v \quad &= \quad \text{residual geometrical contribution},\\
\int_\Omega (\mathfrak{c}_{\mathsf{iso}} + \mathfrak{c}_{\mathsf{vol}})\nabla\delta\boldsymbol{\varphi} : \nabla\delta\boldsymbol{\eta}\,\mathrm{d}v \quad &= \quad \text{constitutive contribution},
\end{aligned}
$$

where $\mathfrak{c}_{\mathsf{vol}} = p(\mathsf{I}\otimes\mathsf{I} - 2\mathbb{I})$ is spatial elasticity tensor associated to the volumetric part.

Remark 7. From an algorithmic viewpoint it is not worth to write equation (1.20) in the reference configuration, because the integration domain is fixed during the Newton's iterations: one can formally keep the same integrand and put Ω_0 in place of Ω and $J\,\mathrm{d}V$ at any occurence of $\mathrm{d}v$. Given $\boldsymbol{\varphi}$, one can directly compute F, C and then the invariants, in order to form the stress tensor, and the same applies to the elasticity tensors. Finally, concerning the unknowns $(\delta\boldsymbol{\varphi}, \delta\Theta, \delta p)$ and the test functions $(\boldsymbol{\eta}, \Xi, q)$, it is enough to observe that the application of the spatial gradient, denoted by $\nabla(\circ)$, is equivalent to $\textsc{Grad}(\circ)\mathsf{F}^{-1}$.

1.2.4 Galerkin formulation

Consider a finite dimensional subspace V_h of V and another finite dimensional subspace Q_h of Q, where h stands for any discretisation parameter (typically the size of the mesh). Then the Galerkin problem associated to the tangent problem reads as follows:

$$\left\|\begin{aligned}
&\text{Find } (\delta\boldsymbol{\varphi}_h, \delta\Theta_h, \delta p_h) \in V_h \times Q_h \times Q_h \text{ such that}\\
&\int_\Omega \Big(\nabla\delta\boldsymbol{\varphi}_h \mathsf{T} + \big(\mathfrak{c}_{\mathsf{iso}} + \mathfrak{c}_{\mathsf{vol}}\big)\nabla\delta\boldsymbol{\varphi}_h + \delta p_h \mathsf{I}\Big) : \nabla\boldsymbol{\eta}_h \,\mathrm{d}v = \big\langle \mathbf{f}^{\mathsf{ext}}, \boldsymbol{\eta}_h\big\rangle - \int_\Omega \mathsf{T} : \nabla\boldsymbol{\eta}_h \,\mathrm{d}v,\\
&\int_\Omega \Xi_h \,\big(\mathcal{W}''_{\mathsf{vol}}(\Theta)\delta\Theta_h - \delta p_h\big) J^{-1}\mathrm{d}v = \int_\Omega \Xi_h \,\big(p - \mathcal{W}'_{\mathsf{vol}}(\Theta)\big) J^{-1}\mathrm{d}v,\\
&\int_\Omega q_h \,\big(\operatorname{div}\delta\boldsymbol{\varphi}_h - J^{-1}\delta\Theta_h\big)\mathrm{d}v = \int_\Omega q_h \,\big(1 - J^{-1}\Theta\big)\mathrm{d}v, \quad \forall(\boldsymbol{\eta}_h, \Xi_h, q_h) \in V_h \times Q_h \times Q_h.
\end{aligned}\right.$$

The discrete tangent problem can be rewritten in matrix form after introducing a basis $\{\Phi_i\}_{i=1}^{N_{\mathsf{v}}}$ for the space V_h, of cardinality N_{v}, and another basis $\{\Psi_i\}_{i=1}^{N_{\mathsf{q}}}$ for the space Q_h, whose cardinality is instead N_{q}. In fact we have that:

$$\delta\boldsymbol{\varphi}_h(\mathbf{X}) = \sum_{i=1}^{N_{\mathsf{v}}} \delta\boldsymbol{\varphi}_h^i \,\Phi_i(\mathbf{X}), \quad \delta\Theta_h(\mathbf{X}) = \sum_{i=1}^{N_{\mathsf{q}}} \delta\Theta_h^i \,\Psi_i(\mathbf{X}), \quad \delta p_h(\mathbf{X}) = \sum_{i=1}^{N_{\mathsf{q}}} \delta p_h^i \,\Psi_i(\mathbf{X}),$$

where the Fourier coefficients form the vectors of the unknown $(\delta\boldsymbol{\varphi}, \delta\boldsymbol{\Theta}, \delta\mathbf{p})$ with components

$$\big[\delta\boldsymbol{\varphi}_h\big]_i = \delta\boldsymbol{\varphi}_h^i, \qquad \big[\delta\boldsymbol{\Theta}_h\big]_i = \delta\Theta_h^i, \qquad \big[\delta\mathbf{p}_h\big]_i = \delta p_h^i.$$

The algebraic form of the tangent problem is then:

$$\left\|\begin{aligned}
&\text{Find } (\delta\boldsymbol{\varphi}, \delta\boldsymbol{\Theta}, \delta\mathbf{p}) \in \mathbb{R}^{N_{\mathsf{v}}} \times \mathbb{R}^{N_{\mathsf{q}}} \times \mathbb{R}^{N_{\mathsf{q}}} \text{ such that:}\\
&\begin{bmatrix} \mathsf{K}_{\varphi\varphi} & \mathsf{O} & \mathsf{K}_{\varphi\mathsf{p}} \\ \mathsf{O} & \mathsf{K}_{\theta\theta} & -\mathsf{K}_{\theta\mathsf{p}} \\ \mathsf{K}_{\mathsf{p}\varphi} & -\mathsf{K}_{\mathsf{p}\theta} & \mathsf{O} \end{bmatrix} \begin{bmatrix} \delta\boldsymbol{\varphi} \\ \delta\boldsymbol{\Theta} \\ \delta\mathbf{p} \end{bmatrix} = \begin{bmatrix} \mathbf{f}_\varphi \\ \mathbf{f}_\theta \\ \mathbf{f}_{\mathsf{p}} \end{bmatrix}
\end{aligned}\right. \tag{1.21}$$

The matrix in equation (1.21) is symmetric, because we have $\mathsf{K}_{\varphi\varphi}^{\mathsf{T}} = \mathsf{K}_{\varphi\varphi}$, $\mathsf{K}_{\theta\theta}^{\mathsf{T}} = \mathsf{K}_{\theta\theta}$, $\mathsf{K}_{\varphi\mathsf{p}}^{\mathsf{T}} = \mathsf{K}_{\mathsf{p}\varphi}$ and $\mathsf{K}_{\theta\mathsf{p}}^{\mathsf{T}} = \mathsf{K}_{\mathsf{p}\theta}$. The explicit definitions are:

$$\begin{aligned}
\big[\mathsf{K}_{\varphi\varphi}\big]_{ij} &:= \int_\Omega \Big(\nabla\delta\Phi_j \mathsf{T} + \big(\mathfrak{c}_{\mathsf{iso}} + p(\mathsf{I}\otimes\mathsf{I} - 2\mathbb{I})\big)\nabla\delta\Phi_j\Big) : \nabla\Phi_i \,\mathrm{d}v,\\
\big[\mathsf{K}_{\theta\theta}\big]_{ij} &:= \int_\Omega \mathcal{W}''_{\mathsf{vol}}(\Theta)\;\Psi_j\Psi_i\; J^{-1}\mathrm{d}v,\\
\big[\mathsf{K}_{\varphi\mathsf{p}}\big]_{ij} &:= \int_\Omega \Psi_j \operatorname{div}\Phi_i \,\mathrm{d}v,
\end{aligned}$$

$$\begin{aligned}
\big[\mathsf{K}_{\theta\mathsf{p}}\big]_{ij} &:= \int_\Omega \Psi_j \Psi_i \, J^{-1} \mathrm{d}v, \\
\big[\mathbf{f}_{\varphi}\big]_i &:= \big\langle \mathbf{f}^{\mathsf{ext}}, \Phi_i \big\rangle - \int_\Omega \mathsf{T} : \nabla \Phi_i \, \mathrm{d}v, \\
\big[\mathbf{f}_{\theta}\big]_i &:= \int_\Omega \Psi_i \, \big(p - \mathcal{W}'_{\mathsf{vol}}(\Theta)\big) J^{-1} \mathrm{d}v, \\
\big[\mathbf{f}_{\mathsf{p}}\big]_i &:= \int_\Omega \Psi_i \, \big(1 - J^{-1}\Theta\big) \mathrm{d}v,
\end{aligned}$$

A proper choice of the discrete spaces V_h and Q_h enables us to reduce the problem in size by the elimination of $\delta\boldsymbol{\Theta}$ and $\delta\mathbf{p}$ (*static condensation*). First, observe that $\mathsf{K}_{\theta\theta}$ is the mass matrix associated to the space Q_h, so it is invertible; this means that we can solve for $\delta\boldsymbol{\Theta}$ in equation (1.21):

$$\delta\boldsymbol{\Theta} = \mathsf{K}_{\theta\theta}^{-1} \left(\mathbf{f}_\theta + \mathsf{K}_{\theta\mathsf{p}} \delta\mathbf{p}\right).$$

But now we are in conditions to solve for $\delta\mathbf{p}$, because we can substitute $\delta\boldsymbol{\Theta}$ in the third equation of the problem:

$$\mathsf{K}_{\mathsf{p}\theta} \mathsf{K}_{\theta\theta}^{-1} \mathsf{K}_{\theta\mathsf{p}} \, \delta\mathbf{p} = \mathsf{K}_{\mathsf{p}\varphi} \delta\boldsymbol{\varphi} + \mathsf{K}_{\mathsf{p}\theta} \mathsf{K}_{\theta\theta}^{-1} \mathbf{f}_\theta - \mathbf{f}_{\mathsf{p}}. \tag{1.22}$$

The last step consists in another substitution of $\delta\mathbf{p}$ inside the first equation; if we define the matrix $\mathsf{K}_{\mathsf{pp}} := \mathsf{K}_{\mathsf{p}\theta} \mathsf{K}_{\theta\theta}^{-1} \mathsf{K}_{\theta\mathsf{p}}$, then we have a reduced form for the $\delta\boldsymbol{\varphi}$ problem:

$$\left(\mathsf{K}_{\varphi\varphi} + \mathsf{K}_{\varphi\mathsf{p}} \mathsf{K}_{\mathsf{pp}}^{-1} \mathsf{K}_{\mathsf{p}\varphi}\right) \delta\boldsymbol{\varphi} = \mathbf{f}_\varphi - \mathsf{K}_{\varphi\mathsf{p}} \left(\mathsf{K}_{\mathsf{p}\theta}^{-1} \mathbf{f}_\theta - \mathsf{K}_{\mathsf{pp}}^{-1} \mathbf{f}_{\mathsf{p}}\right). \tag{1.23}$$

The formulation we have just found sheds light on the locking phenomenon: suppose for a moment that $\mathsf{F} = \mathsf{I}$, $\Theta = 1$ and $p = 0$, in order to recover linear elasticity. Then $\mathbf{f}_{\mathsf{p}} = 0$ and $\mathbf{f}_\theta = 0$, and the equation (1.22) becomes:

$$\mathsf{K}_{\mathsf{pp}} \delta\mathbf{p} = \mathsf{K}_{\mathsf{p}\varphi} \delta\boldsymbol{\varphi}.$$

If $\mathcal{W}''_{\mathsf{vol}}(1) = \kappa$, where κ is the bulk modulus, then the matrix K_{pp} is κ^{-1} times the mass matrix of the space Q_h. Recalling also the definition of $\mathsf{K}_{\mathsf{p}\varphi}$ we have:

$$\kappa^{-1} \int_\Omega \delta p_h \Psi_i \, \mathrm{d}v = \int_\Omega \Psi_i \operatorname{div} \delta\boldsymbol{\varphi}_h \, \mathrm{d}v,$$

that is, δp_h is the L^2–projection of $\operatorname{div} \delta\boldsymbol{\varphi}_h$. In principle, as soon as $\kappa \to \infty$, the solution $\delta\boldsymbol{\varphi}_h$ is constrained to have L^2–projection, denoted with $\mathbb{P}_{\mathrm{L}^2}$, of its divergence equal to zero or, equivalently, to lie in the space:

$$\bar{V}_h = \Big\{ \eta_h \in V_h : \mathbb{P}_{\mathrm{L}^2}(\operatorname{div} \eta_h) = 0 \Big\}.$$

First, Q_h cannot be larger than V_h, because otherwise the space $\bar{V}_h$ would contain only the trivial solution, i.e. $\delta\boldsymbol{\varphi}_h \equiv \mathbf{0}$ (no displacement at all, which explains the word "locking"). On the other hand, if Q_h is very small with respect to V_h, then the projection is poor so the incompressibility is loosely enforced, so we lose accuracy.

Here we use a very common choice for the spaces V_h and Q_h. Let first introduce a triangulation $\mathscr{T}_h$ of a polygonal approximation $\tilde{\Omega}_0$ of the domain Ω_0, such that:

1. every element $K \in \mathscr{T}_h$ is closed;
2. $\bigcup_{K \in \mathscr{T}_h} K = \tilde{\Omega}_0$;

3. for every $K_i,\ K_j \in \mathscr{T}_h$, $K_i \cap K_j$ is either an empty set or a shared point, edge or face among the two.

The finite element spaces we are going to use are defined as follows:

$$\begin{aligned}
\mathbb{CG}_p(\tilde{\Omega}_0) &:= \Big\{ u \in \mathcal{C}(\tilde{\Omega}_0) \colon\ u\big|_K \text{ is a polynomial of degree } p, \text{ for } K \in \mathscr{T}_h \Big\},\\
\mathbb{DG}_p(\tilde{\Omega}_0) &:= \Big\{ u \colon\ u\big|_K \text{ is a polynomial of degree } p, \text{ for } K \in \mathscr{T}_h \Big\},\\
\mathbb{B}_p(\tilde{\Omega}_0) &:= \Big\{ b \colon\ b\big|_K \text{ is a polynomial of degree } p, \text{ with } b\big|_{\partial K} = 0, \text{ for } K \in \mathscr{T}_h \Big\}.
\end{aligned}$$

On tetrahedral meshes we select $V_h = \big(\mathbb{CG}_1 \oplus \mathbb{B}_4\big)^3$ or $V_h = \big[\mathbb{CG}_2\big]^3$, and two different Q_h for the other two fields: $\mathbb{CG}_1$ for the pressure and $\mathbb{DG}_0$ for the dilatations. These choices avoid locking and also keep a good accuracy of the solution. The discontinuous Galerkin approximation for the dilational variable makes possible to easily invert the matrix $\mathsf{K}_{\theta\theta}$ element–wise.

1.2.5 Boundary conditions

If $\partial_{\mathrm{D}}\Omega_0 = \varnothing$, or if essential boundary conditions are applied only on some components of the deformation, the solution might not be unique: any rigid motion that satisfy the boundary conditions can be superimposed to the solution of the elastic problem. In this case, the problem is actually more subtle, because the tangent operator is singular (its kernel contains the allowed rigid motions): given a problem $\mathsf{L}\mathbf{u} = \mathbf{f}$, the *Fredholm's alternative theorem* assures that at least one solution exists if and only if the right hand side $\mathbf{f}$ is orthogonal to the kernel of the adjoint tangent operator L^{T}. It follows, for instance, that the linear and angular momentum of the external loads (body force and surface traction) should balance, because otherwise the deformation cannot be static. On the other hand, even if a small[2] portion of the boundary is fixed, any force or momentum can be balanced by the constraint reaction.

As we shall see, it is not easy to constrain in a physiologically correct way the left ventricle, even taking into account the surrounding anatomy of the heart, because the organ slightly moves and rotates during the heartbeat. Our approach is then to constrain at a minimum the load free boundary conditions by two possible strategies: introduce a “small” portion of essential boundary or require zero mean rotation and mean displacement.

The latter approach can be formulated as follows: a global constraint on the solution is enforced in order to avoid any rigid motion, such as

$$\int_{\Omega_0} \delta\boldsymbol{\varphi}_h \,\mathrm{d}V = 0,$$

for the zero mean translation and, in a similar fashion, the condition

$$\int_{\Omega_0} \mathbf{X} \wedge \delta\boldsymbol{\varphi}_h \,\mathrm{d}V = 0$$

for a zero mean rotation. For instance, a Lagrangian formulation of problem (1.17) accounting for these constraints should be

$$\mathscr{L}(\boldsymbol{\varphi}, \theta, p, \mathbf{c}_1, \mathbf{c}_2) := \mathcal{F}_{\mathrm{HW}}(\boldsymbol{\varphi}, \theta, p) - \mathbf{c}_1 \cdot \int_{\Omega_0} \boldsymbol{\varphi} \,\mathrm{d}V - \mathbf{c}_2 \cdot \int_{\Omega_0} \mathbf{X} \wedge \boldsymbol{\varphi} \,\mathrm{d}V,$$

---

[2] From a mathematical standpoint this means that the capacity of the portion of the boundary is not zero.

where we have two new unknowns $\mathbf{c}_1, \mathbf{c}_2 \in \mathbb{R}^3$ to be appended to the former set $(\boldsymbol{\varphi}, \theta, p)$. If we prefer to remove only a particular rigid motion, such as the rotation around a fixed axis, we just set $\mathbf{c}_1 = \mathbf{0}$ and $\mathbf{c}_2 = c\,\mathbf{a}$, where $\mathbf{a}$ is the direction of the axis and $c \in \mathbb{R}$ is the only extra unknown.

The numerical implementation of these constraints can be obtained in different ways:

- Consider the constraints as an essential boundary condition that, after discretisation, can be written in the form

  $$\mathsf{H}\,\delta\boldsymbol{\varphi}_h = \mathbf{g},$$

  for some matrix H and vector $\mathbf{g}$. Some software can handle this kind of generalised Dirichlet boundary condition, for instance by means of a penalisation technique.

- Try to solve the linear system even if singular. As mentioned before, if the a solution exists, then there are infinitely many: the solver returns one of them, therefore the solution must be post–processed removing spurious rigid motions.

  When a Krylov method is exploited, it is a good idea to inform the solver on the null eigenvalues, prescribing the null space: in particular, we have to prescribe six vectors, three translations and three rotations. However, the convergence rate might be affected, and some preconditioners could not properly work.

  A direct solver, on the other hand, typically based on LU or Cholesky factorisation, with a good pivoting strategy is able to find one solution. The idea is to replace the entries of the matrix corresponding to the null pivots with a "smart" choice performed by the software.

- Fix some vertex point of the mesh of the domain. This strategy is not always viable, because it strongly depends on the geometry and the deformation, so if the vertices are not carefully selected the resulting algebraic problem could lead to unexpected results.

In our simulation, if necessary and no further specified, we will always adopt the "Lagrangian multipliers" strategy.

Another important issue is the correct application of a pressure loading p_{ext} at the boundary $\partial_{\mathrm{N}}\Omega$, which yields to a boundary term of the form

$$\left\langle \mathbf{f}^{\mathsf{ext}}, \boldsymbol{\eta} \right\rangle = \int_{\partial_{\mathrm{N}}\Omega} p_{\mathsf{ext}}\, \mathbf{n} \cdot \boldsymbol{\eta} \,\mathrm{d}a.$$

This term *depends geometrically* on the deformation, because, pulling back on the reference configuration, the expression reads as follows

$$\left\langle \mathbf{f}_0^{\mathsf{ext}}(\boldsymbol{\varphi}), \boldsymbol{\eta}_0 \right\rangle = \int_{\partial_{\mathrm{N}}\Omega_0} p_{\mathsf{ext}}\, (\operatorname{cof} \mathsf{F})\, \mathbf{n}_0 \cdot \boldsymbol{\eta}_0 \,\mathrm{d}A, \tag{1.24}$$

which is clearly non–linear with respect to F. This leads to the introduction of a new term, to be added to the stiffness matrix $\mathsf{K}_{\varphi\varphi}$, that some authors (Hibbitt et al., 1970) indicate as *correction matrix* $\mathsf{K}_{\varphi\varphi}^{\mathsf{load}}$, which reads as follows:

$$[\mathsf{K}_{\varphi\varphi}^{\mathsf{load}}]_{ij} := \int_{\partial_{\mathrm{N}}\Omega} p_{\mathsf{ext}} \Big[(\operatorname{div} \Phi_j)\mathsf{I} - \nabla\Phi_j \Big] \mathbf{n} \cdot \Phi_i \,\mathrm{d}a,$$

resulting from the differentiation of expression (1.24).

1.2.6 Implementation aspects

There are at least three important issues concerning the implementation of the numerical algorithm: non–linear iteration solver, tangent problem solver, and assembly.

The Newton's method is a basic prototype for solving non–linear problems. In general, convergence is quadratic and the method becomes particularly effective when the starting point gets very close to the solution thus it is fundamental to correctly choose the initial guess.

A good strategy, very easy to implement, is the *incremental loads* technique: we start from the stress–free solution, with zero displacement as initial guess, and we add a small percentage of the external load (e.g. boundary traction). If the solution depends continuously on the data, then distance between the solution and the initial guess can be controlled by the increment of the external load.

This strategy works well but it is not optimal if the increment in load is kept constant during the whole simulation. In fact, a soft tissue generally becomes stiffer with the strain, so the same increment of the stress yields a smaller increment on the strain; this can be noticed by the fact that the Newton solver performs less iterations to reach convergence. It is then advantageous to adapt the incremental load, increasing it when the number of iterations is low and decreasing it when the Newton solver fails.

An even better strategy we adopted here for some specific simulations is the use of a *continuation method*, such as the Moore–Penrose continuation (Kuznetsov, 1998). Given a non–linear problem of the form

$$f(u, p) = 0,$$

where u is the unknown (e.g. the displacement) and p the parameter (e.g. the external pressure), the *implicit function Theorem* asserts that, under suitable conditions, given a pair (u_0, p_0) it is possible to find a curve $u = u(p)$ such that $f(u(p), p) = 0$ and $u(p_0) = u_0$, at least locally. A continuation method aims to reconstruct such a curve in a smart way, trying to follow the tangent. With this method it is also possible to overtake a turning–point (or limit–point): a typical example is the inflation of a thin–walled rubber balloon (Needleman, 1977). From our point of view the main advantage is that the increments are automatically selected and they can be significantly larger with respect to the ones provided by the incremental load strategy.

The second implementation issue is the linear solver for the tangent problem. The size of the linear systems is generally not very big, but the sparsity pattern is dense if compared to the discretisation of other operators such as the vector Laplacian. An iterative solver needs a good preconditioner to converge: a basic choice is a Jacobi preconditioner, which is most of the times mandatory.

A valid alternative, very suitable in our case, is a direct solver. The usage is discouraged for large and sparse systems, because its tendency to fill the memory. However, as mentioned before, the tangent problem is not very large and the sparsity is low. It can also be very effective when constraints are enforced by means of Lagrangian multipliers (e.g. boundary conditions).

Last but not least, the assembly of the tangent problem, it is performed several times during each Newton iterations, can take most of computational time (up to 80%, depending of the implementation). A common strategy that aims to reduce the disparity between assembly and linear system solving time is to invest a good amount of memory to store frequently used quantities, such as F or J. Ideally, the best strategy is to store both Cauchy stress and elasticity tensors, but it could be very expensive from the memory viewpoint. Indeed, it is not enough to store the values at the vertices, rather it is preferable to store them for each quadrature node of each cell of the mesh.

Another good practice is to compute only once the sparsity pattern of the matrices, at the first iteration: this helps the solver to optimize the memory usage in order to reduce the matrix–vector product time. Moreover, if a direct solver is exploited, then also the symbolic factorisation can be performed only once, while updating the numerical factorisation at each iteration.

1.3 Numerical assessment

Consider an unit cube $[-0.5, 0.5]^3$ as a reference configuration, and select $\mathbf{f}_\circ$, $\mathbf{s}_\circ$ and $\mathbf{n}_\circ$ aligned with the x, y and z axes, respectively, so that $\mathbf{f}_\circ = \mathbf{e}_1$ and $\mathbf{s}_\circ = \mathbf{e}_2$. Regarding the material parameters (see table 1.1), two sets are given by Holzapfel and Ogden (2009): one for the orthotropic material and the other for the transversely isotropic version. A third and a fourth set has been proposed in Göktepe et al. (2011) and Wang et al. (2013), respectively, for the orthotropic material only.

		a (kPa)	b	a_f (kPa)	b_f	a_s (kPa)	b_s	a_fs (kPa)	b_fs
Orth.	Holzapfel–Ogden	0.059	8.023	18.472	16.026	2.481	11.120	0.216	11.436
	Göktepe et al.	0.496	7.209	15.193	20.417	3.283	11.176	0.662	9.466
	Wang et al.	0.2362	10.810	20.037	14.154	3.7245	5.1645	0.4108	11.300
Tr. iso	Holzapfel–Ogden	2.280	9.726	1.685	15.779	—	—	—	—

Table 1.1 Material parameters.

As explained in section 1.1.3, the Holzapfel–Ogden material considers an anisotropic contributions $\mathcal{W}_{4,\cdot}$ to be switched off in compression. In this respect, out of its physical motivations, it may be numerically interesting to see what happens if this correction is taken into account or not: in the following we will refer to this with the label no–fix, while the standard will be referred as fix.

Concerning the bulk modulus κ, we consider a value of about 10^5 kPa in order to ensure a local volume change smaller than 1%. As a rule of thumb, κ should be $3 \div 6$ order of magnitude higher that the highest stiffness of the material (the fibres' one, in our case). On the other hand, with large strains, it should be considered an higher value of κ, or even an adaptive strategy, because the exponential form of the stiffness: see Simo and Taylor (1991).

1.3.1 Uni–axial and bi–axial tests

The first tests are uni–axial and a bi–axial stretch along the directions $\mathbf{f}_\circ$, $\mathbf{s}_\circ$ and $\mathbf{n}_\circ$, respectively with a traction stress ranging from 0 N/cm^2 to 20 N/cm^2, with increments of 0.2 N/cm^2. The external traction is applied symmetrically to the two faces; the other four faces of the cube are free. In order to avoid rigid motions, the solution is constrained to have zero mean displacement and zero mean rotation, as explained in section 1.2.5. We also consider all the different combinations of parameters listed in table 1.1.

Results of the unixial tests are presented in figures 1.3 and 1.4 for the fix and no–fix, respectively, whereas figures 1.5 and 1.6 refer to the biaxial tests, again for fix and no–fix version of the model. The expected deformation is uniform in all the three directions, and so the stress, thus a very coarse mesh is sufficient to have an excellent agreement with the solution obtained from (1.13).

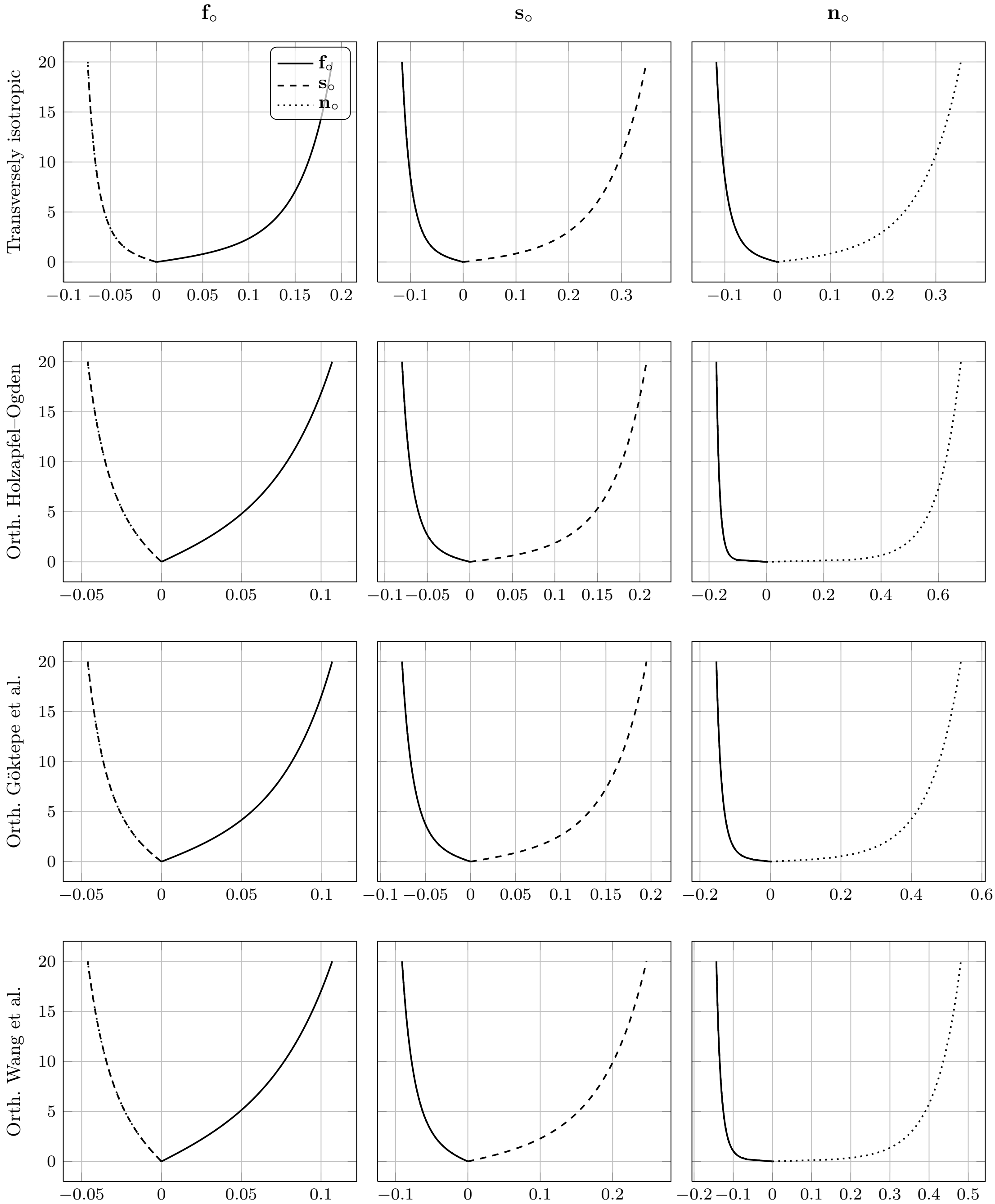

Figure 1.3 Uni–axial test with $\boxed{\mathsf{fix}}$. The table consists in tests along $\mathbf{f}_\circ$, $\mathbf{s}_\circ$ and $\mathbf{n}_\circ$, respectively, for every set of material parameter. For each plot, the curves indicate the Cauchy stress T, in $\mathrm{N/cm^2}$, with respect to the strain E.

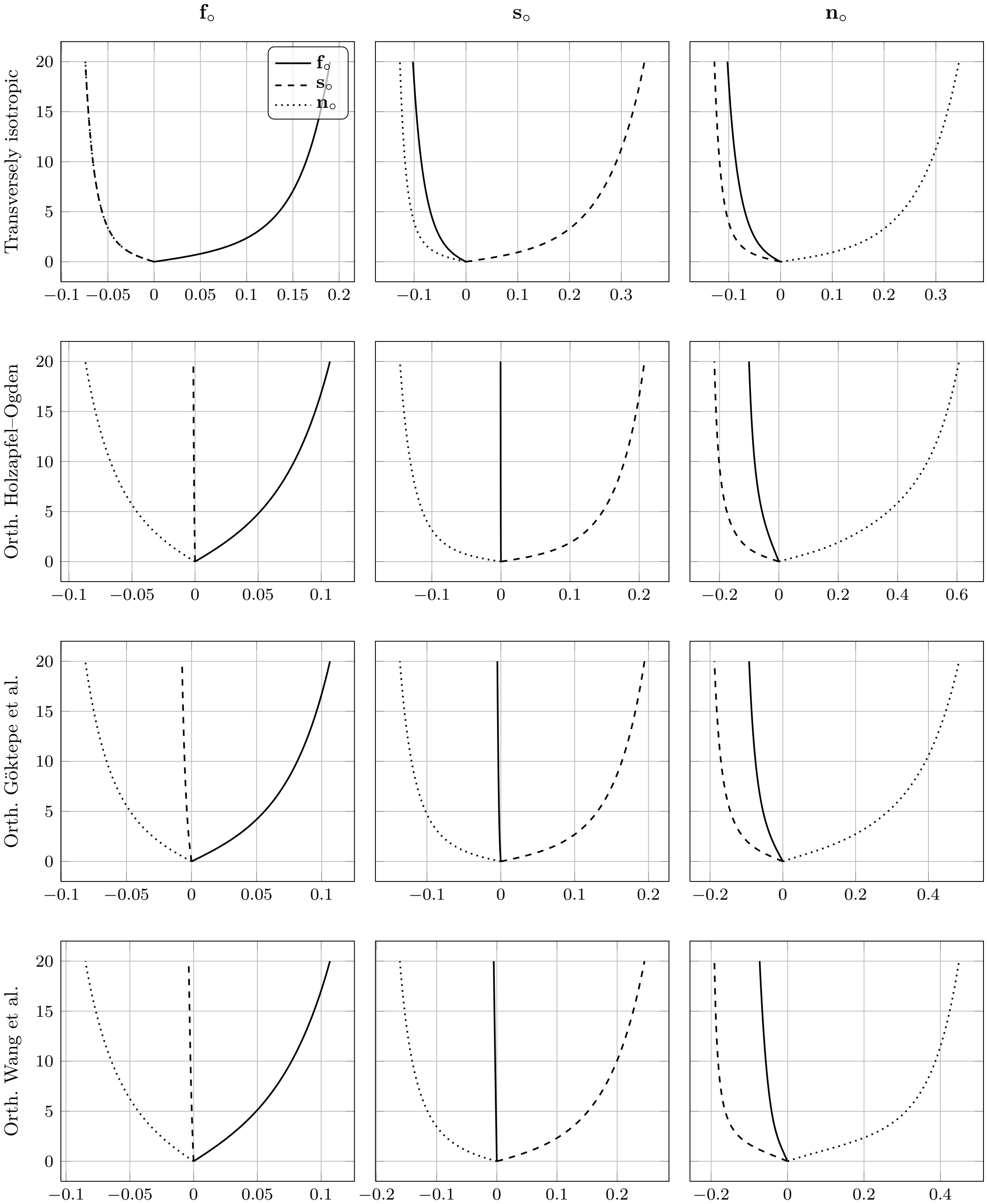

Figure 1.4 Uni–axial test with $\boxed{\textsf{no–fix}}$. The table consists in tests along $\mathbf{f}_\circ$, $\mathbf{s}_\circ$ and $\mathbf{n}_\circ$, respectively, for every set of material parameter. For each plot, the curves indicate the Cauchy stress T, in $\mathrm{N/cm^2}$, with respect to the strain E.

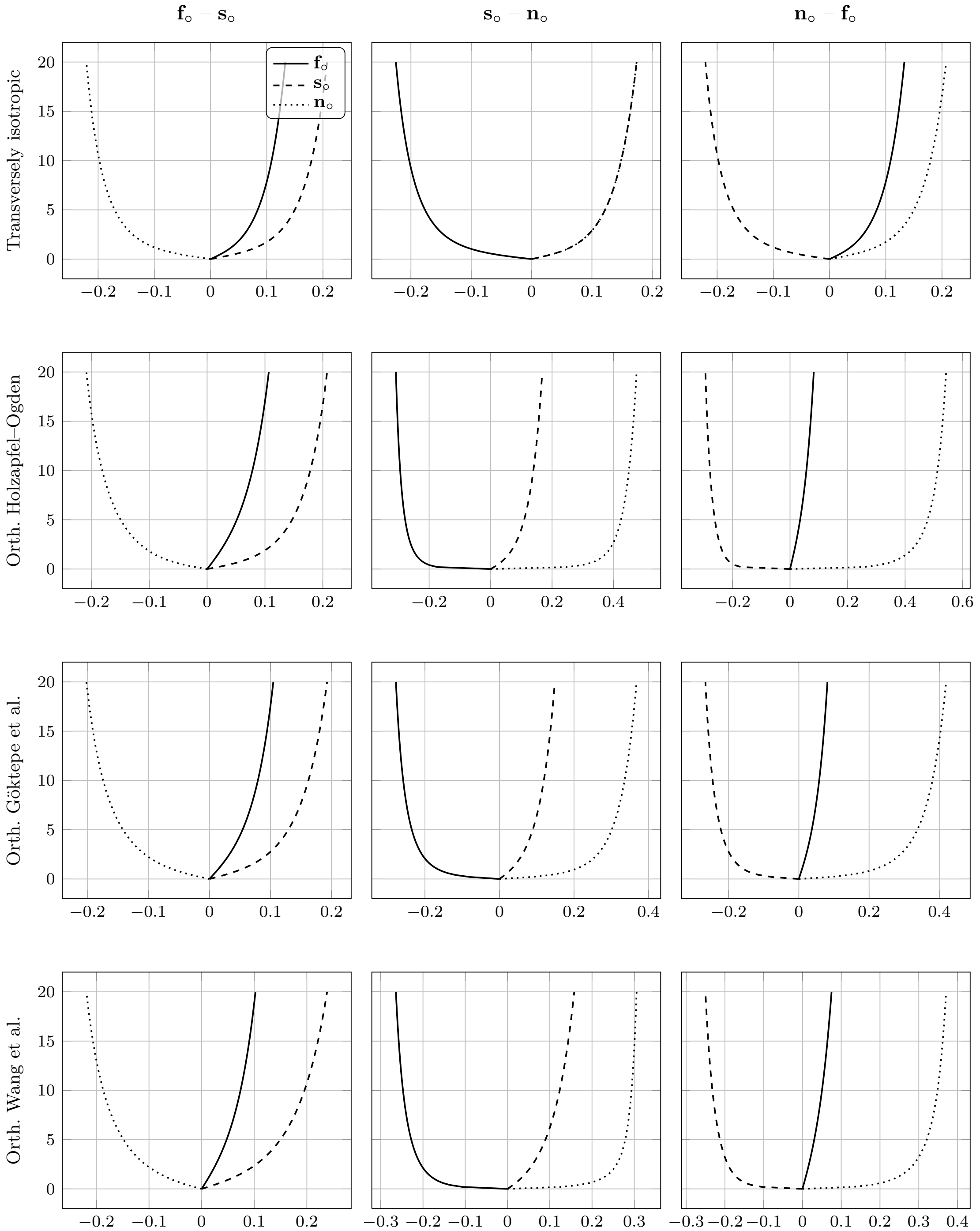

Figure 1.5 Bi–axial test with $\boxed{\mathsf{fix}}$. The table consists in tests along $\mathbf{f}_\circ$–$\mathbf{s}_\circ$, $\mathbf{s}_\circ$–$\mathbf{n}_\circ$ and $\mathbf{f}_\circ$–$\mathbf{n}_\circ$, respectively, for every set of material parameter. For each plot, the curves indicate the Cauchy stress T, in N/cm^2, with respect to E.

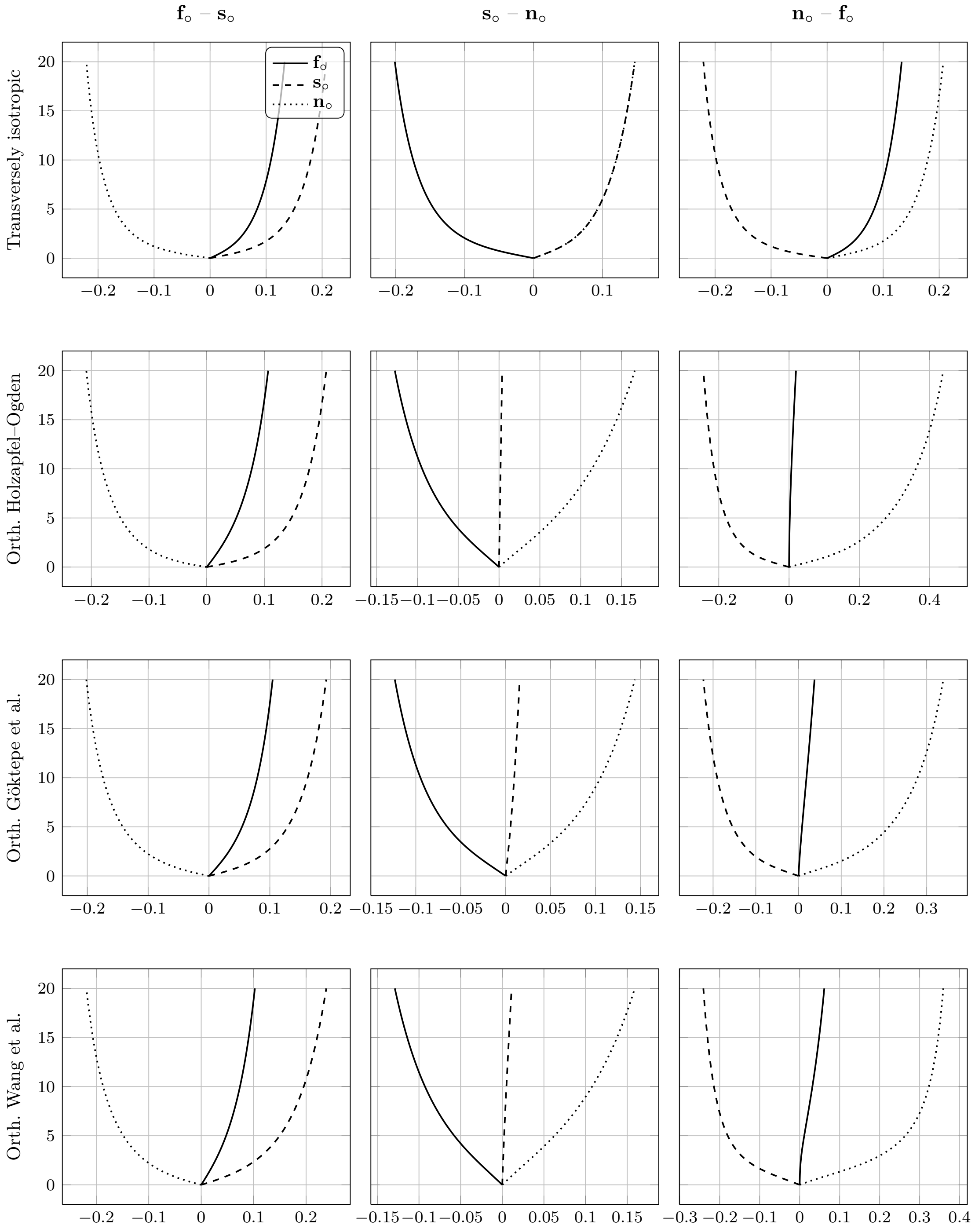

Figure 1.6 Bi–axial test with $\boxed{\text{no–fix}}$. The table consists in tests along $\mathbf{f}_\circ$–$\mathbf{s}_\circ$, $\mathbf{s}_\circ$–$\mathbf{n}_\circ$ and $\mathbf{f}_\circ$–$\mathbf{n}_\circ$, respectively, for every set of material parameter. For each plot, the curves indicate the Cauchy stress T, in N/cm^2, with respect to E.

Discussion

- The transversely isotropic model behaves quite differently (in all the directions) with respect to the orthotropic case: for instance, when this material is loaded along the fibres, its elongation is almost twice the elongation of the corresponding orthotropic version. Such a big discrepancy is in the fitting of the parameters, which has not been done on the same data. In particular, the transversely isotropic model has been fitted using the bi–axial test data provided by Yin et al. (1987), for a canine myocardium while the orthotropic models are instead calibrated on the shear data for pig myocardium provided by Dokos et al. (2002). Observe that none of them is based on human data, which is obviously difficult to obtain.
- The difference between the values of the parameters in the table 1.1 for the orthotropic models is remarkable when considering that the fitting has been done on the basis of the same experimental data. Focusing on the uni–axial results, the difference can be especially appreciated in the normal direction in the stiffness associated to the isotropic term: from table 1.1, we observe that the parameter a provided by Göktepe et al. (2011) and Wang et al. (2013) is one order of magnitude higher that the one provided by Holzapfel and Ogden (2009). This highlights a very interesting fact: it seems that there is no unique choice of the parameters that explains the experiments from Dokos et al. (2002), even if the set of parameters is not particularly large, compared to previous models such as the "pole–zero" model from Humphrey et al. (1990).

  There could be several explanations:

  1. the optimisation procedure exploited during the fitting could have several local minima, due to the highly non–linear nature of the problem, and so the result depends on the initial guess;
  2. the strain–energy is over–parametrised so the global minimum of the fitting procedure in not unique;
  3. the simple shear experiments couldn't unequivocally determine all the parameters, but they can only restrict their range. Moreover, it is worth mentioning that simple shear is very difficult to obtain in finite deformations (Destrade et al., 2012), so the parameters could be particularly sensitive to the experimental data (Horgan and Murphy, 2011).
- We didn't observe numerical issues during the tests for the `no–fix` version, such as loss of ellipticity, typically associated to a singular tangent problem during the Newton iterations (see section 2.2.2). Also the number of non–linear iterations is always very low, about 3 with a tolerance of 10^{-10} for both residual and increment, but this might be related to the incremental strategy, with small loading steps, here adopted.

The eighth invariant remains constant and provides no contribution to the strain–energy in these tests, because fibres and sheets remain orthogonal. We conclude that this specific test is not sufficient to calibrate all the parameters and shear tests are needed.

1.3.2 Shear induced by compression: constant fibre direction case

It is well known that simple shear is particularly difficult to obtain in large deformation regimes Destrade et al. (2012), because of the so–called *Poynting effect*: no simple shear in deformation can be produced by a simple shear in boundary conditions. In this specific test we produce simple shear by applying pure pressure on a cube of orthotropic material.

In this section we address the compression of a cube whose microstructure, in Cartesian coordinates, reads as follows:

$$\mathbf{f}_\circ = \cos\alpha\,\mathbf{e}_1 + \sin\alpha\,\mathbf{e}_2, \qquad \mathbf{s}_\circ = \mathbf{e}_3.$$

The fibres lie on planes orthogonal to $\mathbf{e}_3$, which is also the sheets direction, and they form an angle α with respect to the horizontal direction $\mathbf{e}_1$. An uniform compressive normal pressure p_{load} is applied to the faces orthogonal to $\mathbf{e}_3$ (see figure 1.7).

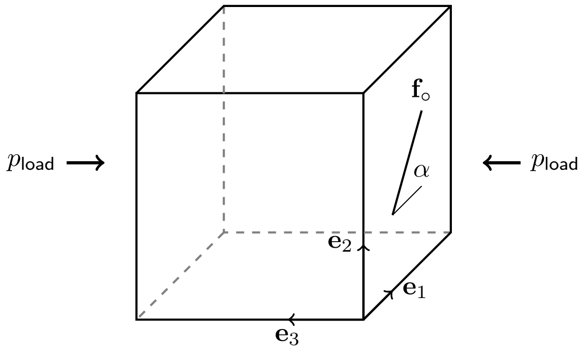

Figure 1.7 Geometry of the pressure induced shear test with constant microstructure.

The idea behind this test is to mimic the behaviour of a small portion of the wall of the left ventricle when passively inflated (see section 1.4). From a numerical viewpoint we want to establish whether our implementation correctly captures rotations, which is an important and not trivial expected result considering complexity of the model. It is also a good benchmark for boundary conditions imposed by means of Lagrangian multipliers (see section 1.2.5).

Analytical solution

Consider the following deformation of the unit cube (we follow Liu (2002)):

$$x = \lambda_1 X + \kappa\lambda_2 Y, \qquad y = \lambda_2 Y, \qquad z = \lambda_3 Z, \tag{1.25}$$

which is an homogeneous stretch followed by a simple shear. The associated deformation gradient tensor, with respect to the Cartesian coordinate system is given by

$$\mathsf{F} = \begin{bmatrix} \lambda_1 & \kappa\lambda_2 & 0 \\ 0 & \lambda_2 & 0 \\ 0 & 0 & \lambda_3 \end{bmatrix} = \begin{bmatrix} 1 & \kappa & 0 \\ 0 & 1 & 0 \\ 0 & 0 & 1 \end{bmatrix} \cdot \begin{bmatrix} \lambda_1 & 0 & 0 \\ 0 & \lambda_2 & 0 \\ 0 & 0 & \lambda_3 \end{bmatrix}.$$

For a fixed value of κ, it is possible to determine the three constants λ_1, λ_2 and λ_3 in such a way that the three normal stresses vanish on the surface of the cube. We restrict our attention to the incompressible case, thus the unknowns two stretch components and the pressure p.

The left and right Cauchy–Green tensors are given by

$$\mathsf{B} = \begin{bmatrix} \lambda_1^2 + \kappa^2\lambda_2^2 & \kappa\lambda_2^2 & 0 \\ \kappa\lambda_2^2 & \lambda_2^2 & 0 \\ 0 & 0 & \lambda_3^2 \end{bmatrix}, \qquad \mathsf{C} = \begin{bmatrix} \lambda_1^2 & \kappa\lambda_1\lambda_2 & 0 \\ \kappa\lambda_1\lambda_2 & (\kappa^2+1)\lambda_2^2 & 0 \\ 0 & 0 & \lambda_3^2 \end{bmatrix},$$

and the corresponding invariants are

$$\begin{aligned}
\mathcal{I}_1 &= \operatorname{tr}\mathsf{C} = \lambda_1^2 + (\kappa^2+1)\lambda_2^2 + \lambda_3^2,\\
\mathcal{I}_{4,\mathbf{f}_\circ} &= \mathbf{f}_\circ \cdot \mathsf{C}\mathbf{f}_\circ = (\lambda_1 \cos\alpha + \kappa\lambda_2 \sin\alpha)^2 + \lambda_2^2 \sin\alpha,\\
\mathcal{I}_{4,\mathbf{s}_\circ} &= \mathbf{s}_\circ \cdot \mathsf{C}\mathbf{f}_\circ = \lambda_3^2,\\
\mathcal{I}_{8,\mathbf{f}_\circ\mathbf{s}_\circ} &= \mathbf{s}_\circ \cdot \mathsf{C}\mathbf{f}_\circ = 0.
\end{aligned}$$

From the incompressibility constrain we have $\lambda_1\lambda_2\lambda_3 = 1$, thus $\lambda_3 = (\lambda_1\lambda_2)^{-1}$.

The Cauchy stress tensor (1.9) has 5 non–trivial components, that reads as follows:

$$\begin{aligned}
\mathsf{T}_{11} &= a e^{b(\mathcal{I}_1-3)}(\lambda_1^2+\kappa^2\lambda_2^2) + 2a_{\mathsf{f}}(\mathcal{I}_{4,\mathbf{f}_\circ}-1)_+ e^{b_{\mathsf{f}}(\mathcal{I}_{4,\mathbf{f}_\circ}-1)^2}(\lambda_1\cos\alpha+\kappa\lambda_2\sin\alpha)^2 - p,\\
\mathsf{T}_{22} &= a e^{b(\mathcal{I}_1-3)}\lambda_2^2 + 2a_{\mathsf{f}}(\mathcal{I}_{4,\mathbf{f}_\circ}-1)_+ e^{b_{\mathsf{f}}(\mathcal{I}_{4,\mathbf{f}_\circ}-1)^2}\lambda_2^2\sin^2\alpha - p,\\
\mathsf{T}_{33} &= a e^{b(\mathcal{I}_1-3)}\lambda_3^2 + 2a_{\mathsf{s}}(\mathcal{I}_{4,\mathbf{s}_\circ}-1)_+ e^{b_{\mathsf{s}}(\mathcal{I}_{4,\mathbf{s}_\circ}-1)^2}\lambda_3^2 - p,\\
\mathsf{T}_{12} = \mathsf{T}_{21} &= a e^{b(\mathcal{I}_1-3)}\kappa\lambda_2^2 + 2a_{\mathsf{f}}(\mathcal{I}_{4,\mathbf{f}_\circ}-1)_+ e^{b_{\mathsf{f}}(\mathcal{I}_{4,\mathbf{f}_\circ}-1)^2}(\lambda_1\cos\alpha+\kappa\lambda_2\sin\alpha)\lambda_2\sin\alpha.
\end{aligned}$$

The trace of T suggests that the pressure p is positive, because it is the sum of positive terms; in order to have $\mathsf{T}_{33} = -p_{\mathsf{load}}$ the only possibility is $\lambda_3 \le 1$, which yields to $\mathcal{I}_{4,\mathbf{s}_\circ} \le 1$. This also means that

$$(\mathcal{I}_{4,\mathbf{s}_\circ} - 1)_+ = 0,$$

thus the terms in T depending on $\mathbf{s}_\circ$ vanish and the constant pressure in the material is

$$p = p_{\mathsf{load}} + a e^{b(\mathcal{I}_1-3)}(\lambda_1\lambda_2)^{-2}.$$

There still remain the unknowns κ, λ_1 and λ_2. One condition is $\mathsf{T}_{12} = 0$, while the other two are that the normal stress at each unloaded face is zero. The deformation (1.25) preserves the orientation of the faces in figure 1.7 orthogonal to $\mathbf{e}_2$, while the faces originally orthogonal to $\mathbf{e}_1$ will become orthogonal to the vector $(1, \kappa, 0)^{\mathsf{T}}$. This yields to

$$\mathsf{T}_{22} = 0, \qquad \text{and} \qquad \mathsf{T}_{11} + 2\kappa\mathsf{T}_{12} + \kappa^2\mathsf{T}_{22} = 0.$$

The non–linear form of the Cauchy stress tensor prevents an explicit determination of the unknowns, but the algebraic system can be easily solved numerically. Nonetheless, it is possible to observe that κ and α have opposite sign, because, for condition $\mathsf{T}_{12} = 0$, we have

$$\kappa \underbrace{\lambda_2\left(\mathcal{W}_1'(\mathcal{I}_1) + \mathcal{W}_{4,\mathbf{f}_\circ}'(\mathcal{I}_{4,\mathbf{f}_\circ})\sin^2\alpha\right)}_{\geq 0} = -\mathcal{W}_{4,\mathbf{f}_\circ}'(\mathcal{I}_{4,\mathbf{f}_\circ})\lambda_1\cos\alpha\sin\alpha.$$

In particular is zero for $\alpha \in \left\{-\frac{\pi}{2}, 0, \frac{\pi}{2}\right\}$, and it is maximum (resp. minimum) for $\alpha = \mp\frac{\pi}{4}$, which also follows from a symmetry arguments.

Numerical results and discussion

In this test case the stress is constant in space and we can use again a very coarse mesh. Nevertheless, for sake of completeness we report in table 1.2 the convergence results for a geometry with $\alpha = \frac{\pi}{3}$.

- Simulations reproduce the expected deformation, which is the composition of an uniform stretch and a simple shear. Moreover, the correct values of λ_1, λ_2, λ_3, p and κ are captured even with the coarsest mesh.

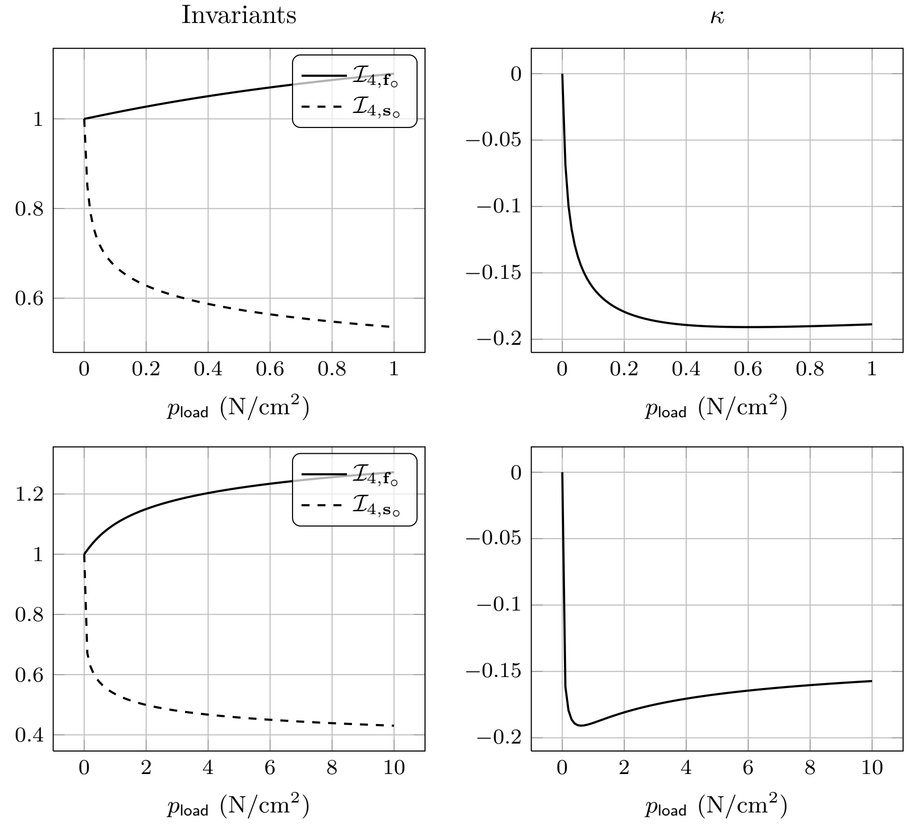

Figure 1.8 Invariants and shear vs. applied pressure, with constant fibre angle $\alpha = \frac{\pi}{3}$. On the bottom row, we have extended the maximum pressure load in order to highlight the shear behaviour. Material parameters from Wang et al. (2013).

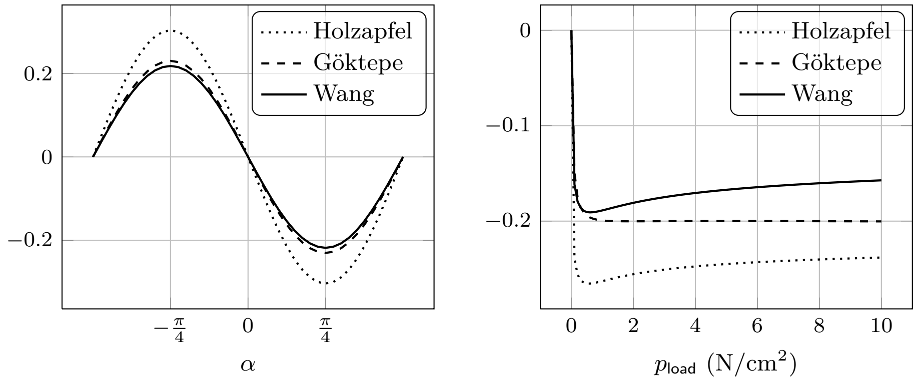

Figure 1.9 Trend of the shear with respect to the material parameters set, the fibre angle α (on the left) and the pressure load (on the right, with $\alpha = \frac{\pi}{3}$).

Side subdivisions	$\lvert\mathcal{I}_{4,\mathbf{f}_\circ}\rvert_2$	$\lvert\mathcal{I}_{4,\mathbf{s}_\circ}\rvert_2$	$\lvert\mathcal{I}_{8,\mathbf{f}_\circ\mathbf{s}_\circ}\rvert_2$	κ	$\lvert\mathsf{T}\mathbf{f}\cdot\mathbf{f}\rvert_2$	$\lvert\mathsf{T}\mathbf{s}\cdot\mathbf{s}\rvert_2$
2	1.101	0.5355	0.	-0.1888	0.	1.
4	1.101	0.5355	0.	-0.1888	0.	1.

Table 1.2 Convergence results for pressure induced shear with constant fibre angle $\alpha = \frac{\pi}{3}$ and pressure $p_{\mathsf{load}} = 1.0$ N/cm^2 with parameters from Wang et al. (2013). Units of stresses are N/cm^2.

- The first important observation, confirmed by the table 1.2, is that

  $$\mathcal{I}_{8,\mathbf{f}_\circ\mathbf{s}_\circ} = 0, \qquad \text{and} \qquad \mathcal{I}_{4,\mathbf{s}_\circ} \leq 1,$$

  which implies that in this test the model behaves as an transversely isotropic one, so that the deformation is essentially dictated by the fibres elongation.

- The right panel of figure 1.8 shows that the shear κ increases rapidly in absolute value with respect to p_{load}, until the maximum value of about -0.19 around $p_{\mathsf{load}} \approx -0.64$ N/cm^2, and eventually decreases reaching a limit value approximatively equal to -0.15. It is worth mentioning that at this point the pressure is particularly high, clearly outside the physiological range.

  The occurrence of the maximum shear cannot be easily deduced from the analysis of the deformation and it is not a property of the specific form of the strain energy, it instead occurs depending on the material parameters. Indeed, with a different set of material parameters, such as the one from Göktepe et al. (2011), the curve doesn't present any maximum: see the right panel of figure 1.9.

- The axial tests of the previous section have shown a significant discrepancy in the results for different parameter sets of table 1.1 especially in the normal direction. Here, results of figure 1.9 point out a difference especially on the maximum shear. For instance, according to Holzapfel and Ogden (2009) the isotropic shear modulus a has a very low value, with respect to the other two sets; the difference shows up here because the stresses associated to the invariants $\mathcal{I}_{4,\mathbf{s}_\circ}$ and $\mathcal{I}_{8,\mathbf{f}_\circ\mathbf{s}_\circ}$ are deactivated.

- The deformation is stable for all the values of $p_{\mathsf{load}} \in [0, 10.0]$, meaning that the equilibrium of the function $\mathcal{W}(\mathsf{F})$ is actually a minimum. In this respect, we consider the reduced strain–energy

  $$\mathcal{W}(\mathsf{F}) = \overline{\mathcal{W}}(\lambda_1, \lambda_2, \kappa),$$

  and we have numerically verified that the corresponding Hessian is positive–definite at equilibrium. Because the eigenvalues depend continuously on p_{load}, we conclude that the equilibrium is stable. This result is not surprising because the Holzapfel–Ogden model is rank–one convex when restricted to the set of deformations given by equation (1.25): indeed, the $\mathcal{W}_{8,\mathbf{f}_\circ\mathbf{s}_\circ}$ and $\mathcal{W}_{4,\mathbf{s}_\circ}$ are always zero.

  On the hand, if we consider the $\boxed{\textsf{no--fix}}$ version of the model, rank–one convexity is not guaranteed even if we restrict our attention on deformations of the form (1.25), because $\mathcal{W}'_{4,\mathbf{s}_\circ} < 0$. Nonetheless, after checking the eigenvalues of the Hessian matrix we do not observe any loss of stability for this specific problem.

1.3.3 Shear induced by compression: variable fibre direction case

An interesting aspect of cardiac mechanics is that the fibre angle α (we use the notation of the previous section) is not fixed across the wall, and it significantly varies between the two sides ($-60°$ and $+60°$, for instance). Consider the following microstructure (see figure 1.10):

$$\mathbf{f}_\circ = \cos\alpha(Z)\,\mathbf{e}_1 + \sin\alpha(Z)\,\mathbf{e}_2, \qquad \mathbf{s}_\circ = \mathbf{e}_3,$$

where, in this case, α depends on the Z (transmural) coordinate as follows:

$$\alpha(Z) = \alpha_0\,(0.5 - Z) + \alpha_1\,(0.5 + Z),$$

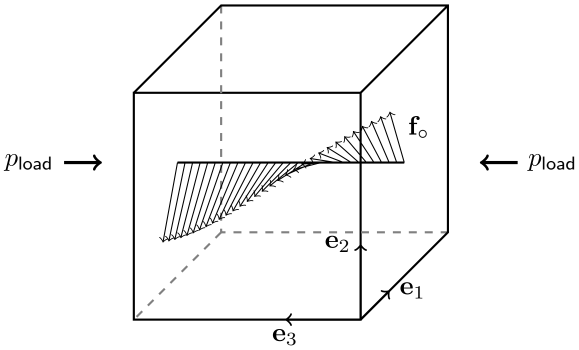

Figure 1.10 Geometry of the pressure induced shear test with variable microstructure.

A fundamental difference between this test and the previous one, with constant fibre direction, is that now the expected deformation gradient is not uniform but spatially dependent, especially in the Z–direction. In this respect, it is geometrically simple but kinematically complex benchmark to test the numerical convergence. The geometry of the problem is very simple, but we intentionally make use of a tetrahedral mesh (and not hexahedral), in order to better understand the effect of the mesh on the solution, in terms of error on the strain and the stress. This is done keeping in mind that is rather easy to produce a tetrahedral mesh for a patient–specific geometry of the ventricle (or possibly of both ventricles), as opposed to an hexahedral one.

We perform a large number of tests with different combinations of material parameters, boundary conditions, and fibres distribution, plotting some quantities of interest, such as the invariants and the stress, along the segment $(x, 0, 0)$, with $x \in [-0.5, 0.5]$. We also measure the torsion as the angle between the projection on the $\mathbf{e}_1$–$\mathbf{e}_2$ plane of $\mathbf{X}$ and $\mathbf{x} = \mathbf{X} + \mathbf{u}$:

$$\sin\tau = \frac{\overline{\mathbf{X}} \wedge \overline{\mathbf{x}}}{\|\overline{\mathbf{X}}\|\,\|\overline{\mathbf{x}}\|} \cdot \mathbf{e}_1, \qquad \overline{\mathbf{X}} = \mathbf{X} - (\mathbf{X}\cdot\mathbf{e}_1)\,\mathbf{e}_1, \quad \overline{\mathbf{x}} = \mathbf{x} - (\mathbf{x}\cdot\mathbf{e}_1)\,\mathbf{e}_1.$$

The torsion is sampled along the segment $(x, 0.5, 0)$.

Results and discussion

As usual, table 1.3 reports the L^2–norm of the invariants and the corresponding Cauchy stress component with respect to meshes of different resolution.

Figure 1.11 shows the solution at $p_{\mathsf{load}} = 1.0$ N/cm^2 for two possible choices of the boundary conditions: “fixed y–component”, which means that faces orthogonal to $\mathbf{e}_2$ cannot move in the

Side subdivisions	$\|\mathcal{I}_{4,\mathbf{f}_\circ}\|_2$	$\|\mathcal{I}_{4,\mathbf{s}_\circ}\|_2$	$\|\mathcal{I}_{8,\mathbf{f}_\circ\mathbf{s}_\circ}\|_2$	$\|\mathsf{T}\mathbf{f}\cdot\mathbf{f}\|_2$	$\|\mathsf{T}\mathbf{s}\cdot\mathbf{s}\|_2$	$\|\mathsf{T}\mathbf{f}\cdot\mathbf{s}\|_2$
2	1.1343	0.5635	0.0870	0.2815	0.9623	0.0788
4	1.1335	0.5620	0.0829	0.2712	0.9625	0.0785
8	1.1331	0.5615	0.0802	0.2745	0.9625	0.0772
16	1.1333	0.5611	0.0788	0.2860	0.9632	0.0764

Table 1.3 Convergence results for pressure induced shear with fibre angle $\alpha_{0,1} = \pm\frac{\pi}{3}$ and pressure $p_{\mathsf{load}} = 1.0$ N/cm^2 with parameters from Wang et al. (2013). Units of stresses are N/cm^2.

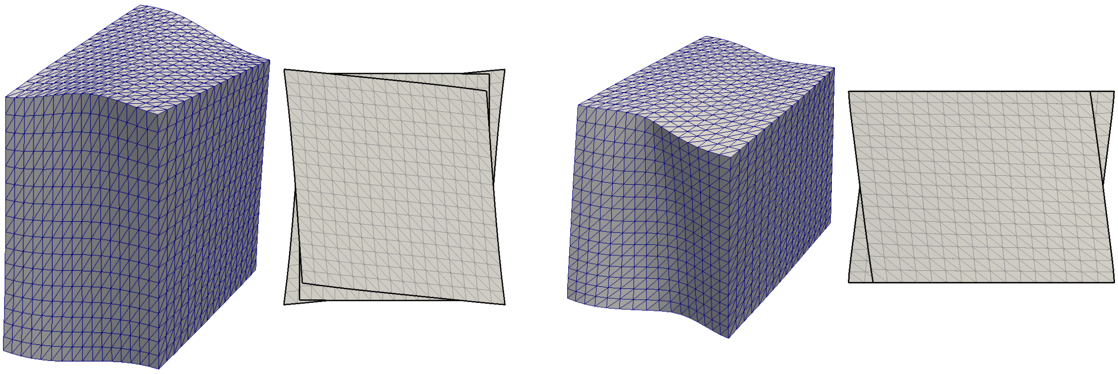

Figure 1.11 Shear induced by compression for an orthotropic cube, at $p_{\mathsf{load}} = 1.0$ N/cm^2, for different "free" boundary conditions (on the left) and "fixed y–component" (on the right).

normal direction, and "free", which instead refer to the stress free condition for all the faces except for the ones on which the traction is applied.

The final deformation can be pictorially understood as a superposition of different in–plane shear deformations. Indeed, we know from the previous section that when the fibre angle is constant, the whole cube is deformed into a prism with rhomboid section; in the present case, we can suppose that every section, which has its own fibre direction, is deformed into a rhombus as well, but with an opening angle that depends on the fibre angle. The whole deformation is approximatively obtained gluing together all these sections.

This intuitive sketch is confirmed by the fact that $\mathcal{I}_{8,\mathbf{f}_\circ\mathbf{s}_\circ}$ is very small, so the sections orthogonal to $\mathbf{e}_1$ do not change orientation and $\mathcal{I}_{4,\mathbf{s}_\circ}$ doesn't vary that much across the cube, and its value is comparable to the one obtained with constant fibre direction (see table 1.2). Also the torsion smoothly varies from $-5°$ to $5°$, in a similar fashion to the left panel of figure 1.9.

Convergence analysis The convergence rate, extrapolated from table 1.3 and the top panel of figure 1.12, is quadratic for the displacement and the torsion, because these quantities are directly related to the unknown $\boldsymbol{\varphi}_h$, which is a quadratic finite element approximation of $\boldsymbol{\varphi}$. On the other hand, all the quantities related to F, and so to the gradient of the displacement, converge linearly with respect to mesh size; actually, there is also a projection error, in fact F is cell–wise linear, but not continuous across the elements, and during the post–processing phase we need to project it on the vertices.

A minimum number of layers for accuracy is eight or even four. The invariant $\mathcal{I}_{4,\mathbf{f}_\circ}$ and the associated stress exhibit a slower convergence especially near the boundaries. In our opinion, this could be due to the projection error on F, magnified by the exponential form of the stress components, because it is also present for $\mathsf{T}\mathbf{s}\cdot\mathbf{s}$ and $\mathsf{T}\mathbf{f}\cdot\mathbf{s}$. This suggests

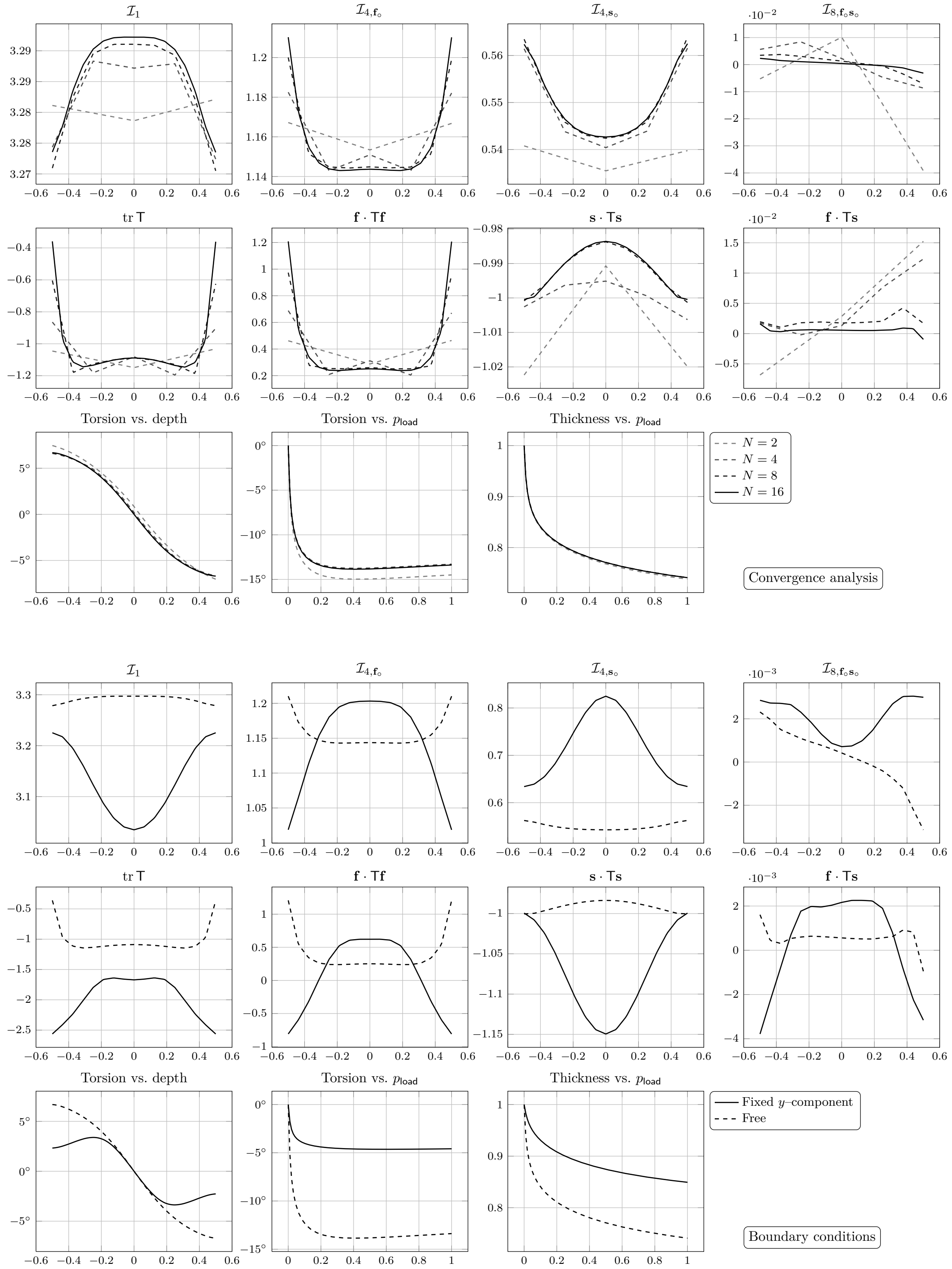

Figure 1.12 Convergence analysis and boundary sensitivity of the shear test with variable fibre angle. The external pressure is $p_{\mathsf{load}} = 1.0$ N/cm^2, and parameters from Wang et al. (2013).

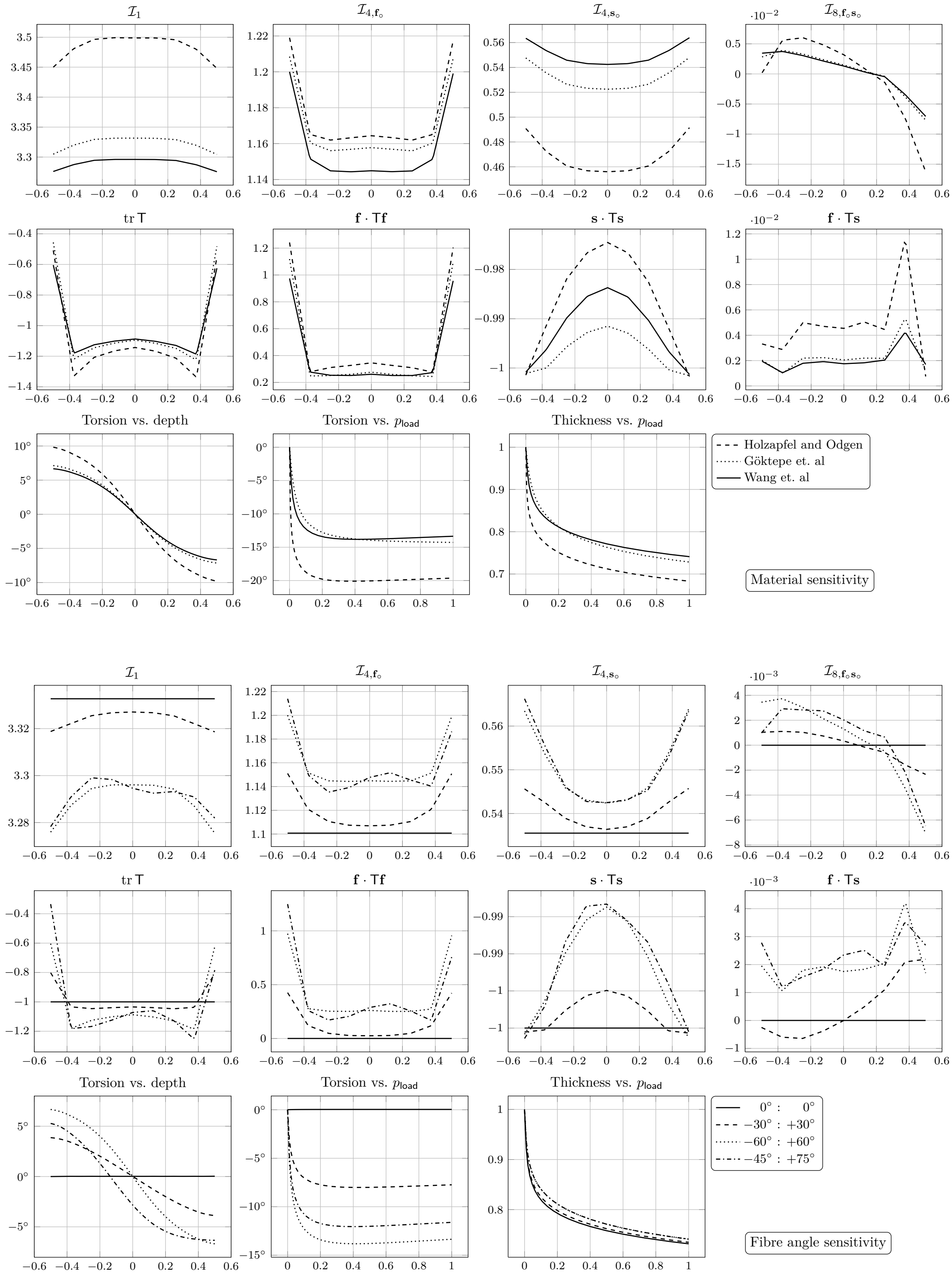

Figure 1.13 Material and fibre angle sensitivity of the shear test with variable fibre angle. The external pressure is $p_{\mathsf{load}} = 1.0\ \mathrm{N/cm^2}$, and parameters from Wang et al. (2013).

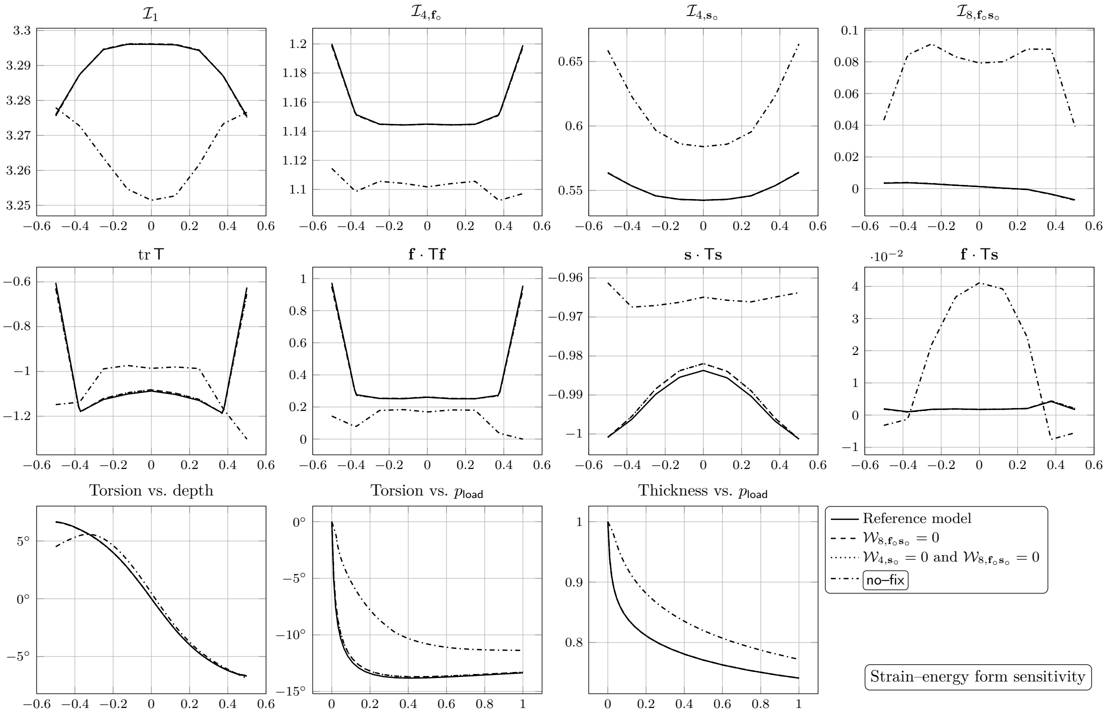

Figure 1.14 Effect of the strain–energy form of the shear test with variable fibre angle. The external pressure is $p_{\mathsf{load}} = 1.0$ N/cm^2, and parameters from Wang et al. (2013).

that the stress measurements, in the forthcoming simulations, should be always generally considered as a rough approximation of the real ones.

Material parameters The top panel of Figure 1.13 confirms that the Holzapfel–Ogden material parameters set performs quite differently from the other two considered here. In fact, both the displacement and the torsion are higher, because $\mathcal{I}_{4,\mathbf{s}_\circ}$ is significantly lower than the others. The reason is again that the sheet–specific term of the strain–energy is deactivated during the deformation, so the dominant term in the cross–fibre direction is the isotropic contribution, which has a shear modulus a about an order of magnitude lower for the Holzapfel–Ogden parameters set with respect to the one obtained by Wang and Göktepe.

Boundary conditions When the “fixed y–component” boundary condition is enforced, faces orthogonal to $\mathbf{e}_2$ experience an evident shear deformation: this is also observed in the simulations regarding the left ventricle (see next section), but as a circumferential shear, where the innermost boundary rotates in the opposite direction with respect to the outermost layer. Moreover, the invariants, and so the stresses, are totally different with respect to the “free” boundary condition case, as deduced from the bottom panel of figure 1.12. For instance, $\mathcal{I}_{4,\mathbf{f}_\circ}$ and $\mathcal{I}_{4,\mathbf{s}_\circ}$ have opposite concavity, with the maximum value attained at the centre of the cube.

Another interesting aspect is the torsion: the “fixed y–component” case presents two local extrema around $x = \pm 0.3$; this can be explained by the stress component $\mathsf{T}\mathbf{f}\cdot\mathbf{s}$, because around these points it changes its sign. For $x > 0.3$ (resp. $x < -0.3$), also the stress along the fibres changes the sign, even if the invariant $\mathcal{I}_{4,\mathbf{f}_\circ}$ is (slightly) greater than one; in particular, for $p_{\mathsf{load}} \approx 0.3$ N/cm^2, $\mathcal{I}_{4,\mathbf{f}_\circ}$ becomes greater than one around $x = \pm 0.5$, and it keeps increasing with p_{load}.

Microstructure The last set of simulations inspect different choices of fibres distribution: see the bottom panel of figure 1.13. The reference case is a constant fibre direction parallel to $\mathbf{e}_1$, which is an uniform axial compression along $\mathbf{e}_3$. Surprisingly, the displacement in the $\mathbf{e}_3$ direction is not significantly affected by the fibre distribution while, as expected, the most prominent dissimilarity is in the torsion, absent in the reference case. Concerning the stress, the component along $\mathbf{f}$ significantly increases with the fibre angle variability, especially at the boundaries.

Finally, we also considered an asymmetric distribution of the fibres, because some authors consider this case for the left ventricle. The loss of symmetry is highlighted also by the fibres invariant and the corresponding stress, but the mean values is comparable to the $\pm\frac{\pi}{3}$ case. On the other hand, the torsion is quite different: in this case the one side rotates less than the other one, and the total variation is less than the $\pm\frac{\pi}{3}$ case.

From this results there is no clear difference in a variable fibres distribution over a constant one, in terms of strain and stress. The most significant difference, as already noticed, is in the torsion, which is a major indicator of functionality in cardiovascular physiology.

Strain–energy form The analysis of the deformation clearly suggests that the sheet–specific strain–energy contribution $\mathcal{W}_{4,\mathbf{s}_\circ}$ is always zero and $\mathcal{W}_{8,\mathbf{f}_\circ\mathbf{s}_\circ}$ is negligible, because $\mathcal{I}_{8,\mathbf{f}_\circ\mathbf{s}_\circ} \approx 0$. To prove this point, we consider a modified model where these two terms are explicitly removed, going from an orthotropic model to a transversely isotropic one. Results, presented in figure 1.14, confirm the hypothesis: indeed, all the measures are almost identical, except for $\mathsf{T}\mathbf{s}\cdot\mathbf{s}$, but the difference is probably numerical approximation error.

The conclusion we draw is that under these conditions it is not worth using an orthotropic model because a transversely isotropic one is enough to capture the essential mechanics. This is also implicitly stated by the model itself, because the condition

$$\mathcal{W}_{4,\mathbf{s}_\circ} > 0 \qquad \Leftrightarrow \qquad \mathcal{I}_{4,\mathbf{s}_\circ} > 1$$

behaves as a switch that reduces the model under specific deformation regimes.

After removing the switch, the Newton solver fails and reduces the timestep several times, and eventually stops at $p_{\mathsf{load}} \approx 0.365$ N/cm^2, while the axial tests and the shear with constant fibre angle didn't show any stability issue. Surprisingly, after removing also the switch

$$\mathcal{W}_{4,\mathbf{f}_\circ} > 0 \qquad \Leftrightarrow \qquad \mathcal{I}_{4,\mathbf{f}_\circ} > 1,$$

the Newton solver has been able to load the cube until the final pressure, but only after a meandering selection of the timestep: the result can be found in figure 1.14 under the no–fix label.

1.4 Inflation of an idealized ventricle

1.4.1 Geometry and microstructure

The left ventricular–cavity geometry is generally approximated by a truncated ellipsoid, where the major axis is roughly two–fold the minor one. The actual size widely varies among individuals, and it substantially differs under pathological condition, such as hypertrophy: $7 \div 8$ cm for the major axis of the ventricle during the diastolic phase is a average value of a normal heart, with a corresponding volume between $80 \div 120$ ml.

It is common in the literature the adopt of the *prolate coordinate system* to describe the geometry of the ventricle, because it is a convenient starting point to fit patient–specific geometries from medical images (LeGrice et al., 2001). With this coordinate system, the position of a generic point is given by a triplet (λ, μ, θ) in such a way that

$$\begin{cases} x = d \sinh\lambda \sin\mu \cos\theta, \\ y = d \sinh\lambda \sin\mu \sin\theta, \\ z = d \cosh\lambda \cos\mu, \end{cases}$$

where d is the *focal length*, $\lambda \geq 0$, and $\mu, \theta \in (0, 2\pi]$. The coordinate λ measures the distance of a point from the major axis along an hyperbola; thus, for a fixed value of λ, the other two variables μ and θ describe the position of the point on a ellipsoidal surface with major and minor axes equal to $d\cosh\lambda$ and $d\sinh\lambda$, respectively. In fact with have:

$$\frac{x^2+y^2}{d^2\sinh^2\lambda} + \frac{z^2}{d^2\cosh^2\lambda} = \sin^2\mu + \cos^2\mu = 1. \tag{1.26}$$

For instance, the apex of the ventricle is the point having $\mu = 0$.

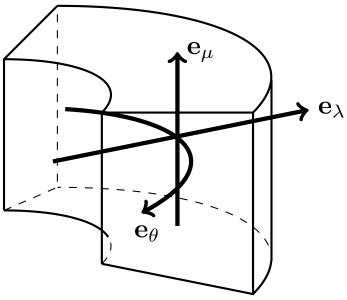

Figure 1.15 Prolate ellipsoidal curvilinear coordinate system.

The focal length d is a scaling factor, and for the human left ventricle is about 3.5 cm to 4.5 cm. Figure 1.16 shows two different geometries and the corresponding parameters: the first one, labeled "canine", is similar to the one considered by Guccione et al. (1995), while the second one is closer to the one by Wang et al. (2013).

The computational domain (i.e. the ventricle) reads as follows:

$$\Omega_0 := \Big\{(\lambda, \mu, \theta) \colon \lambda_{\mathsf{endo}} < \lambda < \lambda_{\mathsf{epi}},\ \mu_{\mathsf{base}} < \mu < 0,\ 0 \leq \theta < 2\pi\Big\}. \tag{1.27}$$

The prolate coordinate system is curvilinear, because the associated metric tensor is not constant; suppose that $\{\mathbf{e}_\lambda, \mathbf{e}_\mu, \mathbf{e}_\theta\}$ is the local basis of the tangent space at a given point (λ, μ, θ). Each component has a precise geometrical meaning (see also figure 1.15):

- $\mathbf{e}_\lambda$ defines the radial direction or, more precisely, is always tangent to the hyperboloid defined by
$$\frac{x^2+y^2}{d^2\sin^2\mu} - \frac{z^2}{d^2\cos^2\mu} = \sinh^2\lambda - \cosh^2\lambda = 1;$$
- $\mathbf{e}_\mu$ defines the longitudinal direction, because it is tangent to the ellipsoid implicitely defined by equation (1.26);

- $\mathbf{e}_\theta$ is the circumferential direction.

Fibres and sheets are defined by means of a linear combination of $\mathbf{e}_\lambda$, $\mathbf{e}_\mu$ and $\mathbf{e}_\theta$ as follows:

$$\mathbf{f}_\circ = \cos\alpha(\lambda_*)\,\mathbf{e}_\theta + \sin\alpha(\lambda_*)\,\mathbf{e}_\mu, \qquad \mathbf{s}_\circ = \mathbf{e}_\lambda, \tag{1.28}$$

where $\alpha\colon [0,1] \to \left[-\frac{\pi}{2}, \frac{\pi}{2}\right]$ is the fibre angle and $\lambda_* \in [0,1]$ measures the wall depth: $\lambda_* = 0$ refers to the endocardium while $\lambda_* = 1$ identifies the epicardium. More precisely, we use the following definition

$$\lambda_* := \frac{\lambda - \lambda_{\mathsf{endo}}}{\lambda_{\mathsf{epi}} - \lambda_{\mathsf{endo}}}, \qquad \alpha(\lambda_*) = \alpha_{\mathsf{endo}}(1 - \lambda_*) + \alpha_{\mathsf{epi}}\,\lambda_*.$$

The last panel of figure 1.16 shows an example of microstructure.

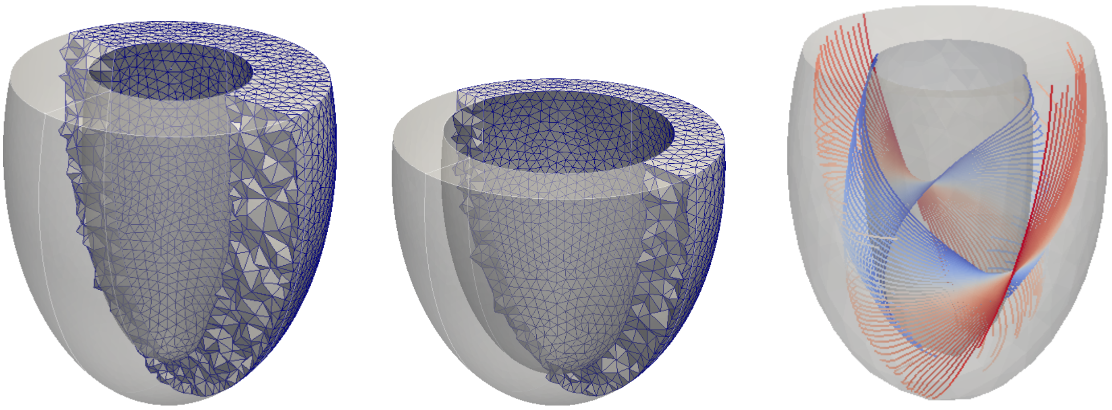

d	λ_{endo}	λ_{epi}	μ_{base}
3.7 cm	0.4	0.7	120°

(a) Canine ventricle.

d	λ_{endo}	λ_{epi}	μ_{base}
4.5 cm	0.6	0.8	110°

(b) Human ventricle.

α_{endo}	α_{epi}
-45°	75°

(c) Fibres distribution.

Figure 1.16 Geometries considered during the simulations. The mesh spacing is purely indicative, but generally the number of elements ranges from 5 000 to 25 000. The fibres distribution also varies among the simulations.

1.4.2 Computational aspects

For a given value of μ_{base}, λ_{endo} and λ_{epi}, the domain Ω_0 defined by equation (1.27) is uniformly triangulated with the software GMSH. For sake of simplicity, we cut the base by a planar face orthogonal to $\mathbf{e}_3$ because it is easier to apply normal boundary conditions. The mesh is precomputed at different resolutions, giving a total number of quadratic tetrahedra that ranges from 5 000 to 25 000 and more (the finest mesh, only used to test convergence, has 71 931 cells and 15 231 vertices).

The microstructure is computed at each Gauss point of the computational domain only once, and then stored into the memory. Indeed, the computation of the basis $\{\mathbf{e}_\lambda, \mathbf{e}_\mu, \mathbf{e}_\theta\}$ is not straightforward to obtain, because we work with Cartesian coordinates. We procede as follows:

1. For a given triplet (x, y, z), we compute the corresponding triplet (λ, μ, θ), which is uniquely defined for our computational domain;

2. We compute the metric tensor such that

$$\begin{bmatrix} \mathrm{d}x \\ \mathrm{d}y \\ \mathrm{d}z \end{bmatrix} = \begin{bmatrix} d\cosh\lambda\sin\mu\cos\theta & d\sinh\lambda\cos\mu\cos\theta & -d\sinh\lambda\sin\mu\sin\theta \\ d\cosh\lambda\sin\mu\sin\theta & d\sinh\lambda\cos\mu\cos\theta & d\sinh\lambda\sin\mu\sin\theta \\ d\sinh\lambda\cos\mu & -d\cosh\lambda\sin\mu & 0 \end{bmatrix} \begin{bmatrix} \mathrm{d}\lambda \\ \mathrm{d}\mu \\ \mathrm{d}\theta \end{bmatrix}.$$

   Inverting the matrix we can compute $\mathbf{e}_\lambda$, $\mathbf{e}_\mu$ and $\mathbf{e}_\theta$ as a linear combination of orthonormal basis given by $\mathbf{e}_1$, $\mathbf{e}_2$ and $\mathbf{e}_3$;

3. The microstructure is obtained by means of equation (1.28), and then normalised.

An important physiological quantity is the cavity (or inner) volume of the ellipsoid. We don't generate a mesh for this region but calculate the volume using the following identity:

$$|\Omega_{\mathsf{inner}}| = \int_{\Omega_{\mathsf{inner}}} 1\,\mathrm{d}V = \frac{1}{3}\int_{\Omega_{\mathsf{inner}}} \operatorname{div}\mathbf{X}\,\mathrm{d}V = \frac{1}{3}\int_{\partial\Omega_{\mathsf{inner}}} \mathbf{X}\cdot\mathbf{n}_0\,\mathrm{d}A.$$

Part of the boundary $\partial\Omega_{\mathsf{inner}}$ is shared with $\partial\Omega_0$, and defines the endocardium:

$$\Gamma_{\mathsf{endo}} := \partial\Omega_{\mathsf{inner}} \cap \partial\Omega_0.$$

We can also define the "cap" of the inner domain as follows:

$$\Gamma_{\mathsf{cap}} := \partial\Omega_{\mathsf{inner}} \setminus \Gamma_{\mathsf{endo}}.$$

Suppose that Γ_{cap} is planar, normal to $\mathbf{e}_3$ and such that each of its points has $z = 0$; then we have the following formula for the volume:

$$\begin{aligned} |\Omega_{\mathsf{inner}}| &= \frac{1}{3}\int_{\partial\Omega_{\mathsf{inner}}} \mathbf{X}\cdot\mathbf{n}_0\,\mathrm{d}A = -\frac{1}{3}\int_{\Gamma_{\mathsf{endo}}} \mathbf{X}\cdot\mathbf{n}_0\,\mathrm{d}A + \frac{1}{3}\int_{\Gamma_{\mathsf{cap}}} \mathbf{X}\cdot\mathbf{e}_3\,\mathrm{d}A \\ &= -\frac{1}{3}\int_{\Gamma_{\mathsf{endo}}} \mathbf{X}\cdot\mathbf{n}_0\,\mathrm{d}A + \underbrace{\frac{1}{3}|\Gamma_{\mathsf{cap}}|\,z}_{=0}. \end{aligned}$$

Notice that the sign is reversed because the outer normal of $\partial\Omega_{\mathsf{inner}}$ is the opposite of the outer normal of $\partial\Omega_0$. The deformed volume is computed in a similar way, in fact:

$$\begin{aligned} |\boldsymbol{\varphi}(\Omega_{\mathsf{inner}})| &= \int_{\boldsymbol{\varphi}(\Omega_{\mathsf{inner}})} 1\,\mathrm{d}v = \frac{1}{3}\int_{\partial\boldsymbol{\varphi}(\Omega_{\mathsf{inner}})} \mathbf{x}\cdot\mathbf{n}\,\mathrm{d}a = \frac{1}{3}\int_{\partial\Omega_{\mathsf{inner}}} \boldsymbol{\varphi}(\mathbf{X})\cdot(\operatorname{cof}\mathsf{F})\mathbf{n}_0\,\mathrm{d}A \\ &= -\frac{1}{3}\int_{\Gamma_{\mathsf{endo}}} \boldsymbol{\varphi}(\mathbf{X})\cdot(\operatorname{cof}\mathsf{F})\mathbf{n}_0\,\mathrm{d}A. \end{aligned}$$

The internal pressure p_{inner}, which is uniform in the space variable, is applied to the endocardium Γ_{endo} in the *actual* normal direction, so that

$$\mathsf{T}\mathbf{n} = -p_{\mathsf{inner}}\mathbf{n}.$$

As explained in section 1.2.5, this boundary term depends on the deformation, indeed

$$\mathsf{T}\mathbf{n}\,\mathrm{d}a = -p_{\mathsf{inner}}\mathbf{n}\,\mathrm{d}a = -p_{\mathsf{inner}}(\operatorname{cof}\mathsf{F})\mathbf{n}_0\,\mathrm{d}A.$$

Finally, the torsion is evaluated from the formula:

$$\sin\tau = \frac{\overline{\mathbf{X}}\wedge\overline{\mathbf{x}}}{\|\overline{\mathbf{X}}\|\,\|\overline{\mathbf{x}}\|}\cdot\mathbf{e}_3, \qquad \overline{\mathbf{X}} = \mathbf{X} - (\mathbf{X}\cdot\mathbf{e}_3)\,\mathbf{e}_3, \quad \overline{\mathbf{x}} = \mathbf{x} - (\mathbf{x}\cdot\mathbf{e}_3)\,\mathbf{e}_3,$$

which is exactly the same we used in the previous sections, except for the plane of rotation, here orthogonal to $\mathbf{e}_3$.

1.4.3 Results

The forthcoming simulations consist in a passive inflation of an idealised left ventricle, with typical physiological size. The inner pressure p_{inner} is uniform and is increased from zero up to 6 kPa, which is about 45 mmHg. Moreover, at 1 kPa (or about 7.5 mmHg) we measure the invariants and the stress along specific transmural sections of the myocardium; the choice of this particular pressure is dictated by the fact that 8 mmHg is a physiological value for the end–diastolic pressure, so it provides a representative snapshot of the mechanical status of the ventricle.

Like in the previous section, we compare and discuss different combinations of material parameters (see table 1.1), boundary conditions, strain–energy forms and fibres distributions. The results are presented in the subsequent figures.

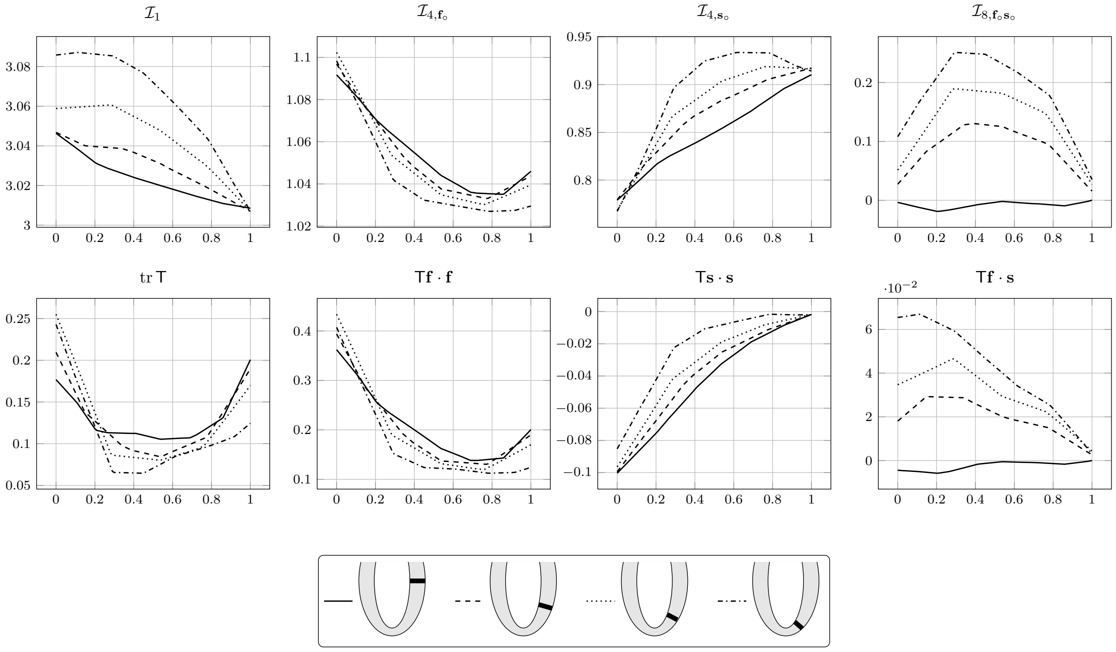

Figure 1.17 Transmural variation of the invariants and the stress components for the passive inflation of the canine geometry. Sections are indicated by the legend, and the abscissa indicates the wall depth. The pressure is 0.1 N/cm^2. Stresses are measured in N/cm^2.

Figures 1.17 and 1.18 show the result of the simulation for a canine and a human geometry, respectively. The most prominent difference with respect to the tests on the cube illustrated in the previous section is that $\mathcal{I}_{8,\mathbf{f}_\circ\mathbf{s}_\circ}$ is significantly different from 0, especially at the apical sections. The corresponding stress is small, but comparable with the radial stress as order of magnitude.

As expected, fibres are under traction everywhere, while sheets are compressed: thus the $\mathcal{W}_{4,\mathbf{s}_\circ}$ term is largely deactivated. The stress projected in the fibre direction is quite uniform across the sections, but it is at least an order of magnitude higher then the radial stress, while it is comparable with the stress in the axial direction $\mathbf{n}_\circ$.

Comparing the two geometries, we don't notice any significant difference on the trends of the invariants and the stress; also the values are similar. We conclude that the geometry doesn't play a prominent role in passive inflation.

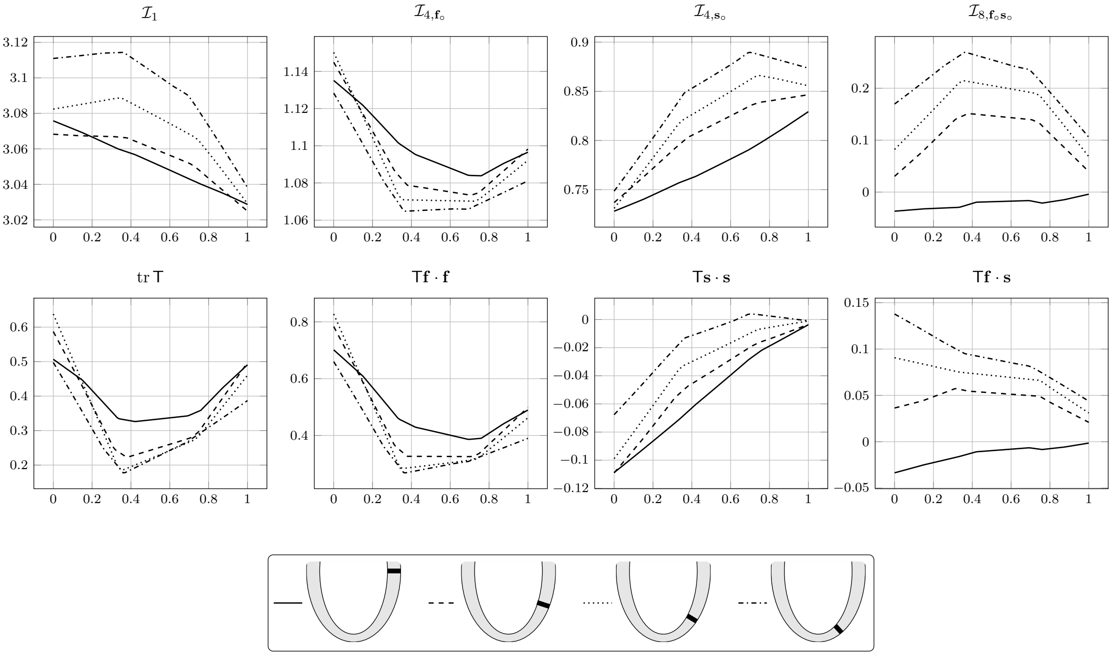

Figure 1.18 Transmural variation of the invariants and the stress components for the passive inflation of the human geometry. Sections are indicated by the legend, and the abscissa indicates the wall depth. The pressure is 0.1 N/cm^2. Stresses are measured in N/cm^2.

Pressure–Volume relationship

Focusing on the canine ventricle, we have an initial volume of 32.19 ml, that becomes 39.62 ml (+23% of the initial one) at 7.5 mmHg and 52.65 ml (+64%) at the final step, with $p_{\mathsf{inner}} = 45$ mmHg. The increase of volume is due both to an increase of the inner radius and a downward elongation towards the apex, with no other significant change of the shape. The human geometry behaves similarly, with the volume that increases from 136 ml to 172 ml (+26%) at 7.5 mmHg and to 221 ml (+62%) at 45 mmHg. It is remarkable the small discrepancy between the two geometries in terms of relative increase of the volume.

Klotz et al. (2006) reports the EDPVR for several *ex–vivo* hearts, both healthy and with some pathologies: they suggest that the pressure–volume curve is very well fitted by the relation

$$\mathrm{EDP} = A \cdot \left(\frac{\mathrm{EDV} - \mathrm{EDV}_0}{\mathrm{EDV}_{30} - \mathrm{EDV}_0} \right)^B ,$$

where EDP is the end–diastolic pressure and EDV is the end–diastolic volume; the parameters A and B describe the curve, and are fitted on the experimental data. In particular

$$A = 28.2 \text{ mmHg}, \qquad \text{and} \qquad B = 2.79.$$

Finally, EDV_{30} and EDV_0 are the end–diastolic volume values for a pressure equal to 30 mmHg and 0 mmHg, respectively. In our case, $\mathrm{EDV}_{30} = 49$ ml for the canine geometry and 209 ml for the human one.

Figure 1.19 shows the computed EDPVR with respect to the prediction of Klotz et al. (2006). There is more or less good agreement for the human geometry, but both the computed curves

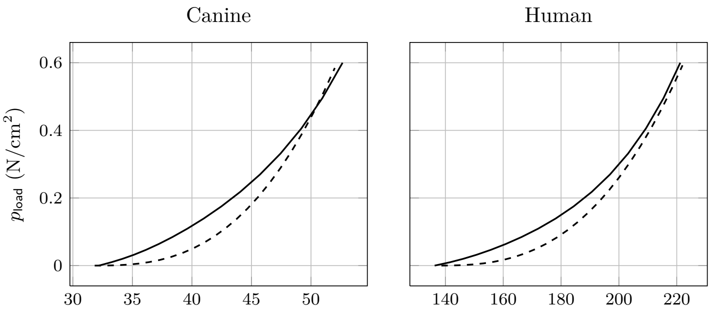

Figure 1.19 EDPVR (solid line) and Klotz formula (dashed line). Volume is in millilitres.

are somewhat stiffer at lower pressures. This could be due to several reasons: in particular, as we will see in the next sections, the EDPVR strongly depends on the fibres distribution and on the material parameters.

Torsion of the ventricle

During an heartbeat, the heart noticeably experiences a torsion, with the apex that rotates counter–clockwise in the opposite direction of the base. The torsion is an important clinical index, that can be evaluated by the CMR tissue tagging, which is the gold standard or, more recently, with a non–invasive techniques like echocardiographic speckle tracking (Takeuchi et al., 2009). It provides important insights on the pump functionality of the heart, because the torsion is sensitive to changes in the microstructure (fibres distribution), or in concentric remodelling: see Young and Cowan (2012).

There are two torsional deformations observed during the simulation: a rotation of the apex with respect to the base (say *axial* torsion), as explained before, and a rotation of the endocardium with respect to the epicardium (*transmural* torsion)[3]. Both are associated to the shear stress generated by the asymmetric distribution of the fibres. Indeed, the traction of the left handed epicardial fibres induces a rotation which is opposite to the right handed endocardial fibres. Moreover, the force balance is generally in favor of the epicardial fibres because of the longer arm of their torque. Torsion therefore provides useful information about the mechanical functionality of the fibres.

Figure 1.20 highlights that significant axial and transmural torsion are produced. Axial torsion is more pronounced at the endocardial surface where the fibres are much more elongated than the epicardial ones. Moreover, the different sign suggests that also a transverse torsion is present as confirmed by the right plot of figure 1.20. It is worth noticing that the axial rotation of the epicardium is small (less than 2°), at least towards the apex.

Sensitivity analysis

The tests on the cube of section 1.3.3 clarify several aspects on the role of the microstructure or the material parameters set of the deformation. Here we discuss similar tests performed on a prototype geometry, with the aim to understand the physiological implications of the aforementioned results.

Boundary conditions The base of the ventricle is a crude approximation of the real anatomy, where two valves, aortic and mitral with their own compliance, connect the ventricle to

---

[3] There is no stardard definition of these two kind of torsions.

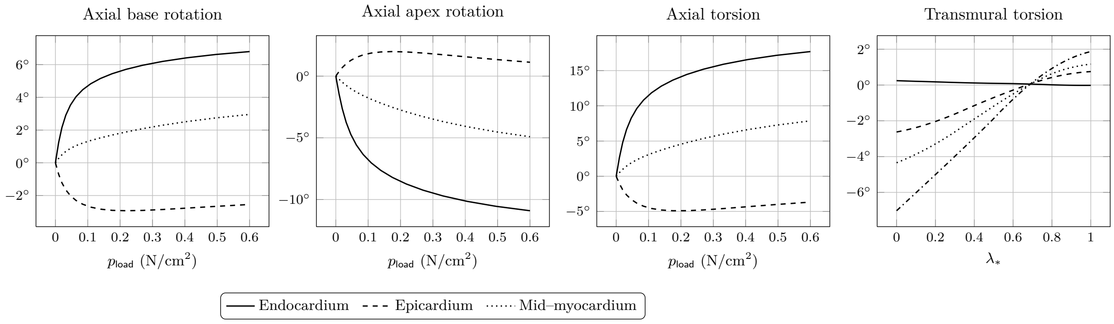

Figure 1.20 Torsion of the canine ventricle. The first three plots show the axial rotation with respect to the inner pressure. The last plot shows the transmural rotation for a fixed pressure (0.1 N/cm^2) and for different sections: please refer to figure 1.17 for the legend.

the aorta and the left atrium, respectively. Moreover, the epicardial ring of the base is surrounded by big coronary vessels. This complex anatomy clearly affects the kinematics of the left ventricle in a more complex way than the one adopted here either in terms of translations and rotations. If such kind of geometry is not available, like in this specific case, a possibility is to specify some boundary conditions at the base. A common choice is to fix a small area, for instance the epicardial ring; on the other hand, this area acts also as a fulcrum, so the resulting torsion might be compromised. As an alternative, fixing the whole base would considerably reduce the end–diastolic volume, because the constraint induces the ventricle to change its shape.

Here we adopted a completely different choice, which consists in keeping the base free to move circumferentially and, possibly, longitudinally. This choice, as explained in section 1.2.5, can lead to numerical issue, so we fixed the axis of the ventricle by means of Lagrangian multipliers, in order to have zero mean axial rotation. A typical deformation is presented in figure 1.21.

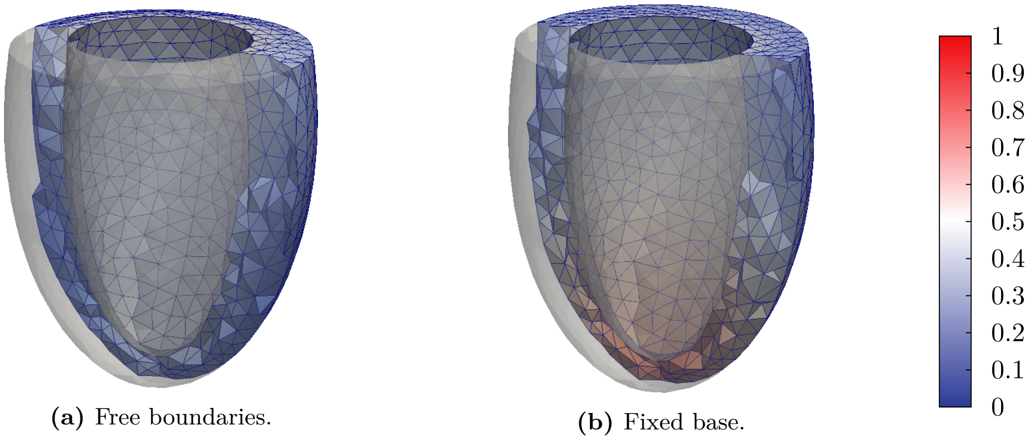

(a) Free boundaries.

(b) Fixed base.

Figure 1.21 Effect of the base boundary condition of the deformation. The colour bar represents the magnitude of the displacement, in centimetre.

For fixed z–component of the base, no vertical movements are allowed. In this case, the

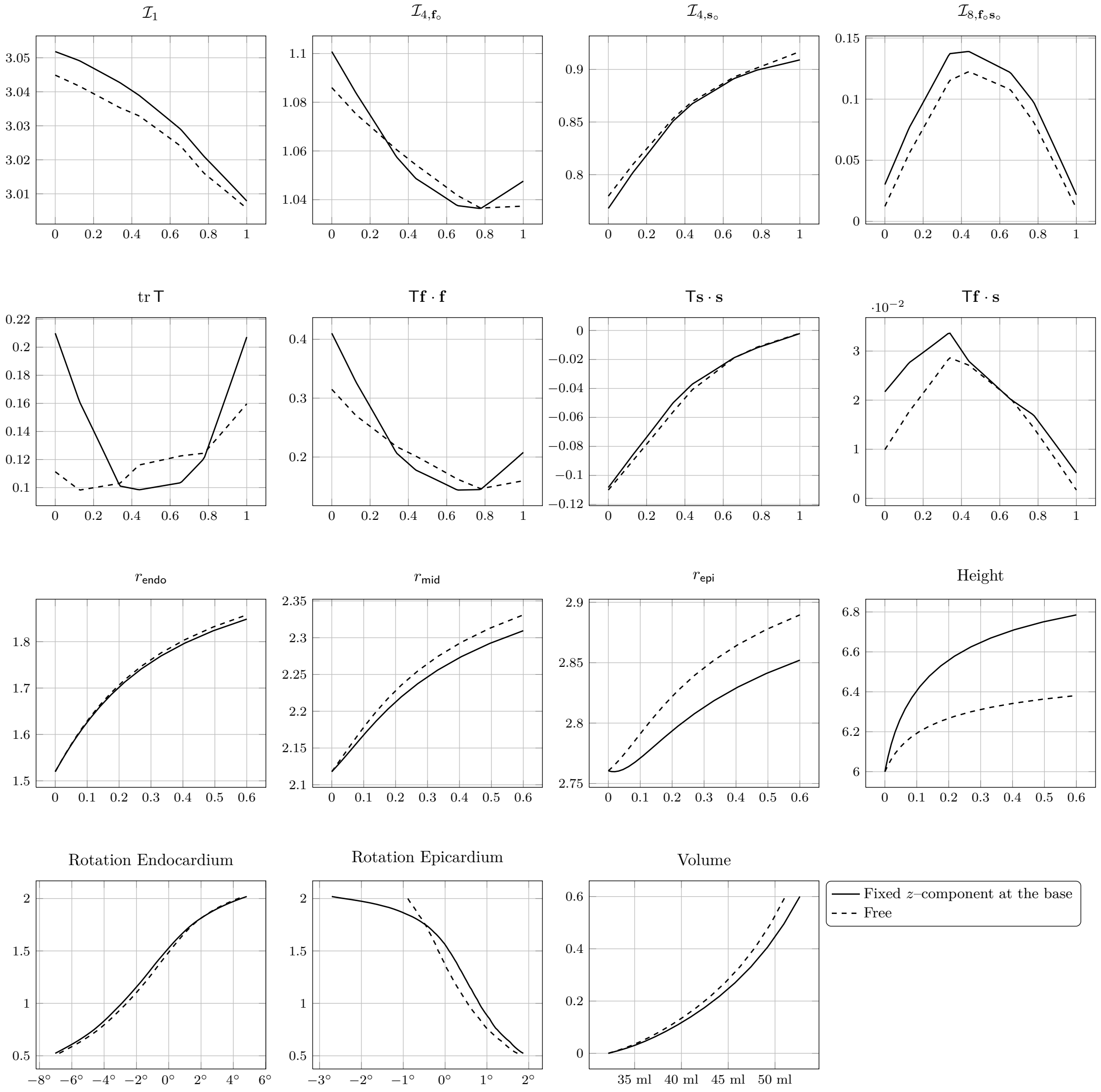

Figure 1.22 Effect of different boundary conditions at the ventricle base for the passive inflation test of the canine geometry of the left ventricle. The first two rows show the invariants and the stresses (in N/cm^2) vs. wall thickness λ_* at the height $\mu = \pi/3$ at $p_{\mathsf{inner}} = 0.1$ N/cm^2. The third row shows the radius at different wall depths for $\mu = \pi/2$ and the height (base–apex distance) vs. the inner pressure. The last row consists of the torsion vs. the longitudinal coordinate μ and the volume vs. the inner pressure.

deformed ventricle has a more elongated shape than the case of no restriction at the base. This latter case, on the other hand, yields a deformation which has an higher inner radius; indeed, the final volume is comparable, as showed in figure 1.22.

The overall distribution of the invariants and the stress in similar across the selected sections. Except for the displacement, the other noticeable difference is the epicardial rotation, which is significantly smaller at the base for the free boundary case.

Microstructure The fibres distribution has a tremendous effect on the solution of the inflation problem, as confirmed by figure 1.24. Here we have considered a couple of common choices, namely the range ±60°, utilised also in all the other test cases, and $-45°:+75°$, which is an example of asymmetric fibre distribution. There is no substantial difference between the two cases, except for the volume, that for the asymmetric case is slightly lower, and the torsion.

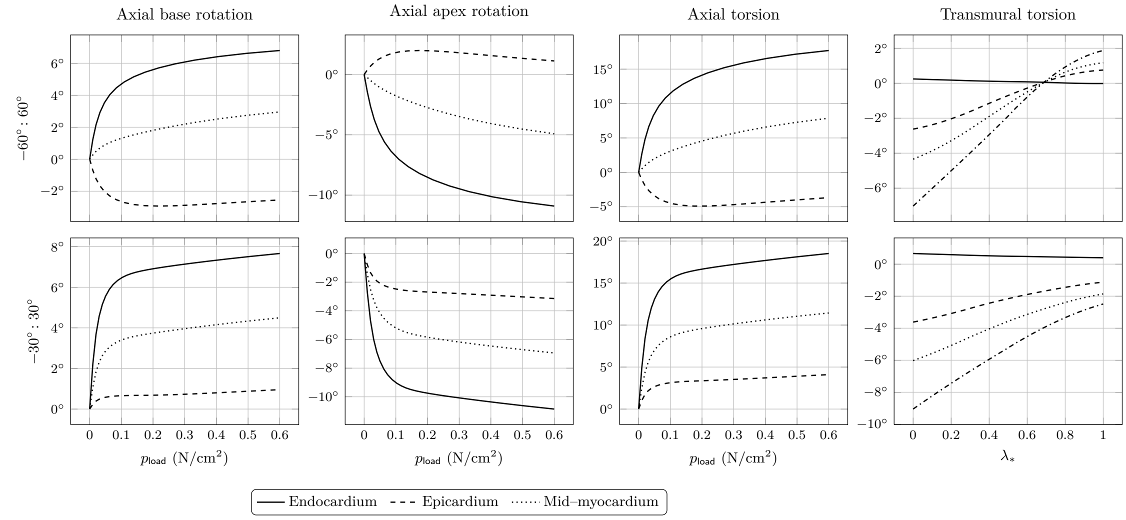

Figure 1.23 Torsion of the canine ventricle. The first three plots show the axial rotation with respect to the inner pressure. The last plot shows the transmural rotation for a fixed pressure (0.1 N/cm^2): please refer to figure 1.17 for the legend.

More interesting is the comparison of the reference case with a less variable distribution, such as $-30°: 30°$ or the case of circumferential fibres (0°). The deformation is completely different in this case, because the ventricle becomes much more elongated while the outer radius is lower. This explains why the volume is higher than the reference case: at a first sight, one would expect to have a stiffer ventricle, because fibres, which have an higher shear modulus, are more effective when circumferentially distributed. On the other hand, there is no longitudinal reinforcement, so the inner pressure tends to deform the structure downwards. Moreover, epicardium and endocardium rotate in the same direction with $-30°: 30°$ fibres (see figure 1.23), while the torsion is absent in the circumferential case, for symmetry reasons.

The circumferential distribution yields a deformation that keeps fibres and sheets orthogonal, which means that the invariant $\mathcal{I}_{8,\mathbf{f}_\circ\mathbf{s}_\circ} = 0$, and whose stresses along the fibres and sheets monotonically decreases from the endocardium to the epicardium.

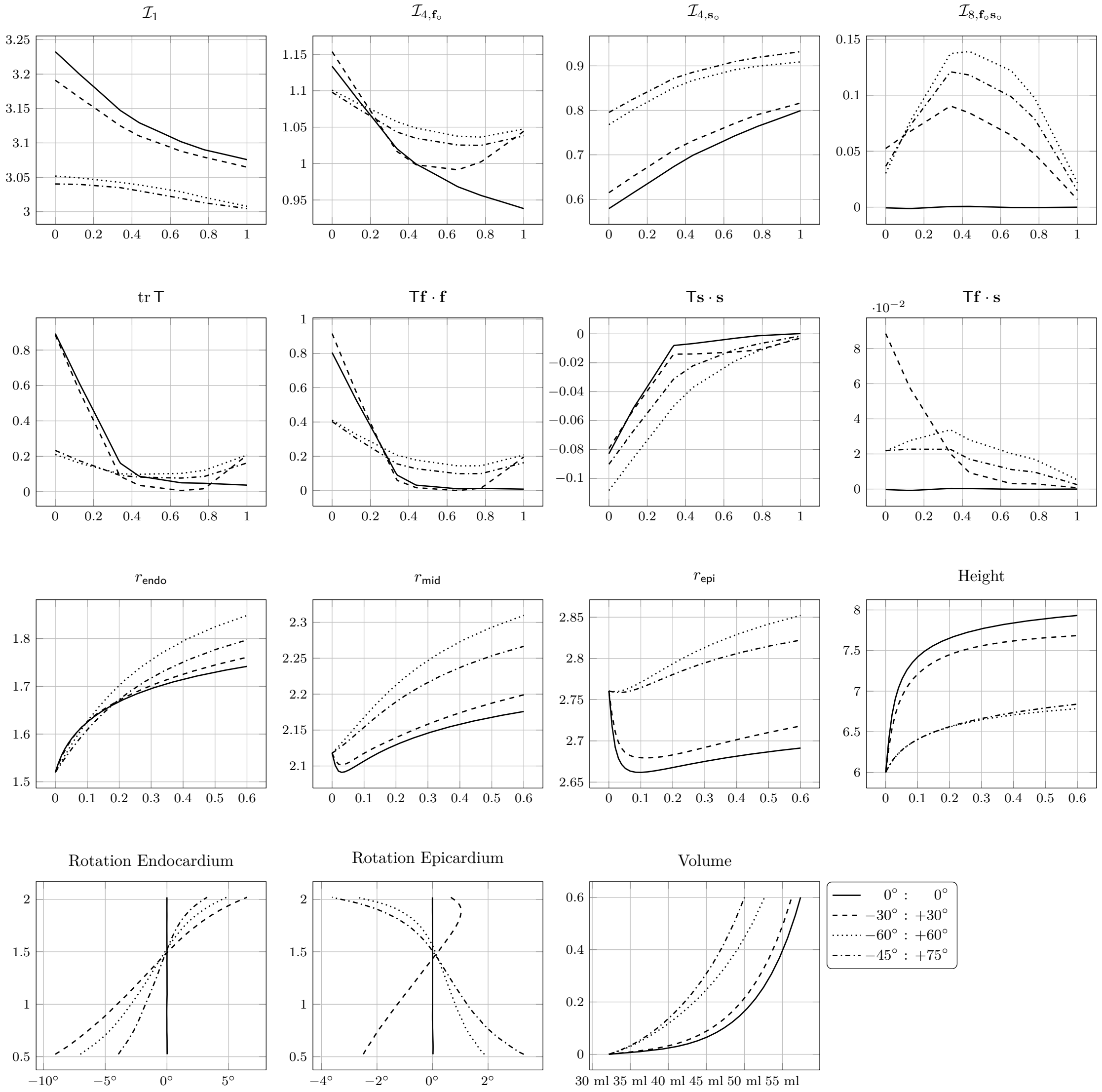

Figure 1.24 Sensitivity of the results to the fibres distribution during the fibre distribution on the passive inflation test of the canine geometry of the left ventricle. The first two rows show the invariants and the stresses (in N/cm^2) vs. wall thickness λ_* at the height $\mu = \pi/3$ at $p_{\mathsf{inner}} = 0.1$ N/cm^2. The third row shows the radius at different wall depths for $\mu = \pi/2$ and the height (base–apex distance) vs. the inner pressure. The last row consists of the torsion vs. the longitudinal coordinate μ and the volume vs. the inner pressure.

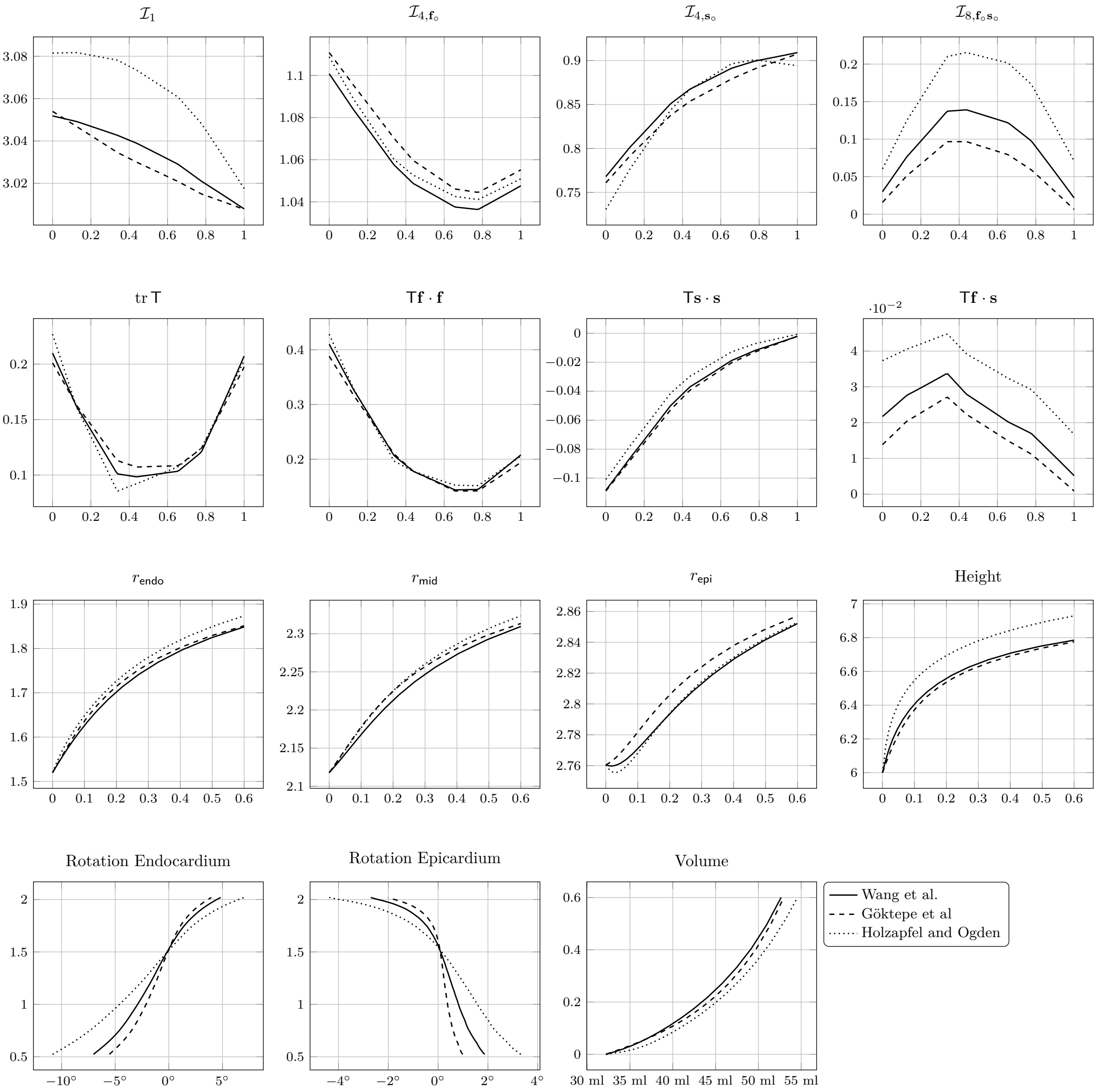

Figure 1.25 Numerical results produced by different material parameters sets on the passive inflation test of the canine geometry of the left ventricle. The first two rows show the invariants and the stresses (in N/cm^2) vs. wall thickness λ_* at the height $\mu = \pi/3$ at $p_{\mathsf{inner}} = 0.1$ N/cm^2. The third row shows the radius at different wall depths for $\mu = \pi/2$ and the height (base–apex distance) vs. the inner pressure. The last row consists of the torsion vs. the longitudinal coordinate μ and the volume vs. the inner pressure.

Material parameters The material parameters set, for this particular test case, influences especially the first and the eighth invariants. Indeed, the Holzapfel–Ogden parameters set has a much lower shear modulus of the isotropic contribution to the strain–energy, as observed in all the previous tests, and this yields to a lower radial stiffness of the ventricle, that can be deduced also from the slope of the EDPVR curve.

The rotation is comparable for Wang and Göktepe parameters sets, while it is almost two times higher (in absolute value) for the Holzapfel–Ogden set, probably for the same reason discussed above.

Strain–energy form The eighth invariant is here significantly different from zero, so it is interesting to investigate whether $\mathcal{W}_{8,\mathbf{f}_\circ\mathbf{s}_\circ}$ provides an important contribution to the strain–energy contribution. To answer this, we removed this term during the simulation: results can be found in figure 1.26. There is no substantial difference of the deformation in terms of displacement, because volume, torsion, radii and height are the same. On the other hand, the stress distribution is slightly different between the two cases in all the components, especially for the trace of the Cauchy stress and its components along the fibres.

If we remove also the sheet–specific contribution $\mathcal{W}_{4,\mathbf{s}_\circ}$, there is no significant disparity, either for the displacement and the stress. This supports again the hypothesis that sheets work in compressive regime during the inflation, so the specific contribution doesn't show up.

The last test is performed removing the deactivation of fibres and sheets for compressive regime (no–fix case). With this model the solver is not able to complete the simulation, and it stops around $p_{\mathsf{load}} \approx 1.2$ kPa. This remarks the importance to introduce the deactivation.

Effect of a non–radial sheets distribution So far the sheets have been placed in the radial direction $\mathbf{e}_\lambda$. Simulations showed that in this particular case the sheet–specific strain–energy term doesn't contribute to the elastic energy, since the sheets are in a compressive regime. In this respect, an interesting issue is whether or not this happens also when sheets are not radially distributed.

Several authors pointed out a significant variability of the laminar structure of the myocardium, both supported by the histology (LeGrice et al., 2001) and by means diffusion tensor magnetic resonance imaging (DT–MRI) analysis (Helm et al., 2005) of the heart. Unfortunately, the distribution of the sheets doesn't seem to be as regular as for the fibres so the solution of mechanical model shouldn't be particularly sensitive on the variability of the sheets: if this was not the case, we would conclude that also a correct description of the laminar structure is fundamental to correctly describe the mechanics of the ventricle, at least when the Holzapfel–Odgen model is exploited.

Given the fibres field

$$\mathbf{f}_\circ = \cos\alpha(\lambda_*)\,\mathbf{e}_\theta + \sin\alpha(\lambda_*)\,\mathbf{e}_\mu,$$

we select $\mathbf{s}_\circ$ lying in the plane orthogonal to $\mathbf{f}_\circ$ and spanning an angle β with respect to the radial direction:

$$\mathbf{s}_\circ = \cos\beta(\lambda_*)\Big(\sin\alpha(\lambda_*)\,\mathbf{e}_\theta - \cos\alpha(\lambda_*)\,\mathbf{e}_\mu\Big) + \sin\beta(\lambda_*)\,\mathbf{e}_\lambda.$$

The angle $\beta(\lambda_*)$ varies across the myocardial wall similarly to $\alpha(\lambda_*)$, linearly spanning the angles between β_{endo} and β_{epi}. An mentioned before, there is no accordance on which choice would be more physiologically motivated, so we tested three different variants and we compared them to the reference case, where sheets are radially distributed and so $\beta \equiv 0$.

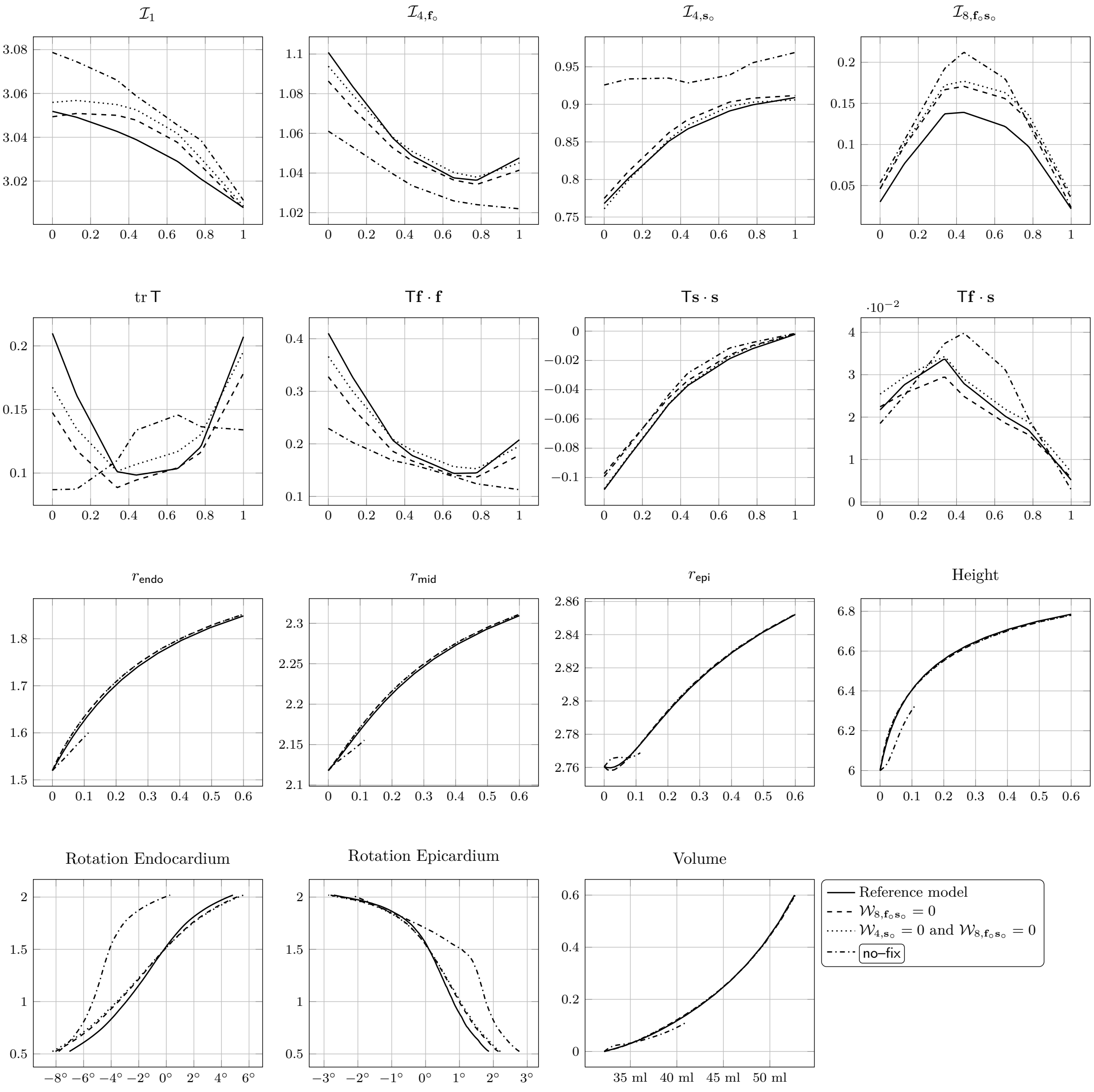

Figure 1.26 Effect of the activation/deactivation of some specific contributions of the strain–energy for the passive inflation test of the canine geometry of the left ventricle. The first two rows show the invariants and the stresses (in $\mathrm{N/cm^2}$) vs. wall thickness λ_* at the height $\mu = \pi/3$ at $p_{\mathsf{inner}} = 0.1\ \mathrm{N/cm^2}$. The third row shows the radius at different wall depths for $\mu = \pi/2$ and the height (base–apex distance) vs. the inner pressure. The last row consists of the torsion vs. the longitudinal coordinate μ and the volume vs. the inner pressure.

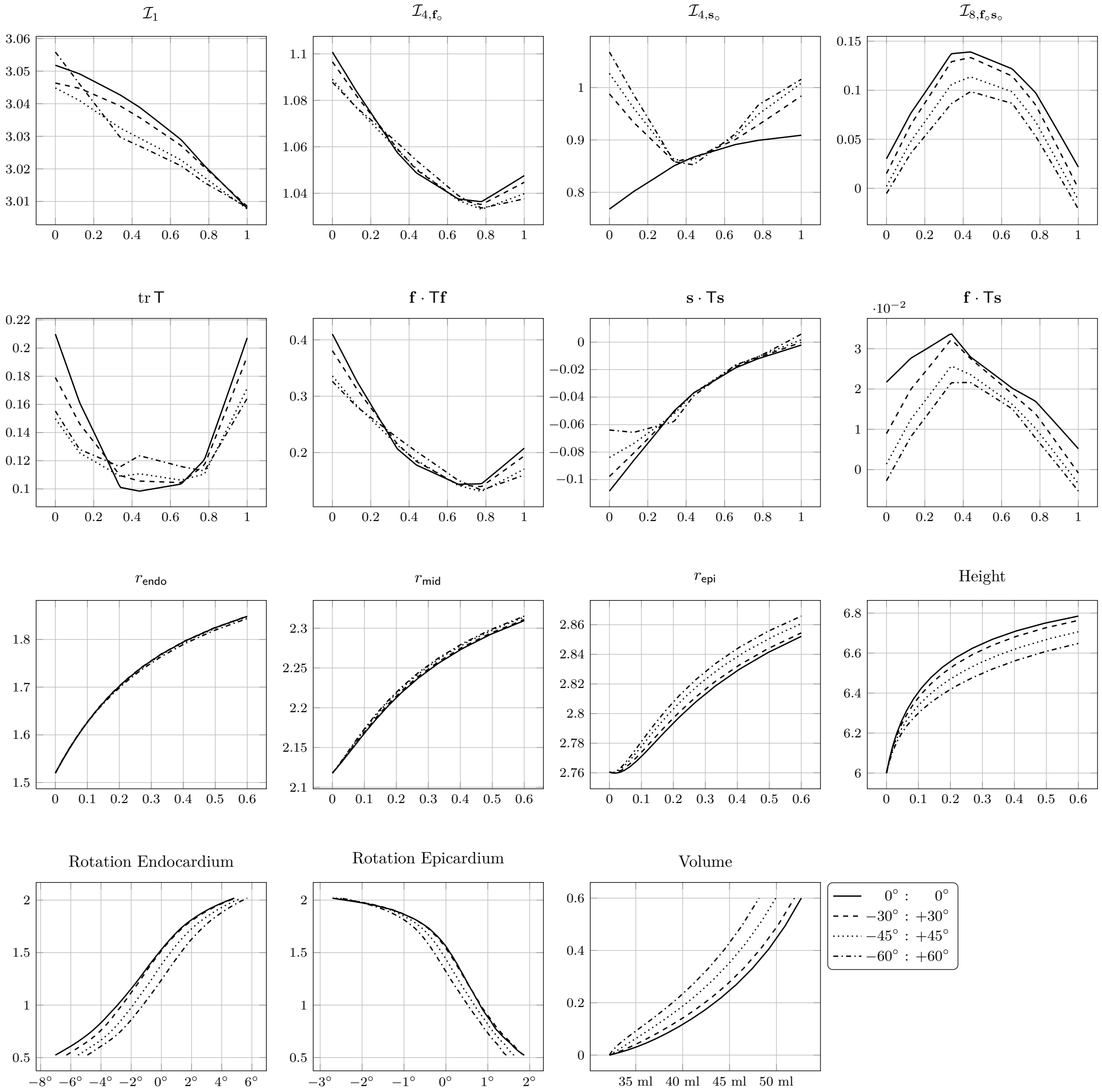

Figure 1.27 Sensitivity of the results on the sheets distribution for the passive inflation test of the canine geometry of the left ventricle. Sheets form a non–zero angle with respect the radial direction $\mathbf{e}_\lambda$, as indicated by the legend. The first two rows show the invariants and the stresses (in N/cm^2) vs. wall thickness λ_* at the height $\mu = \pi/3$ at $p_{\mathsf{inner}} = 0.1$ N/cm^2. The third row shows the radius at different wall depths for $\mu = \pi/2$ and the height (base–apex distance) vs. the inner pressure. The last row consists of the torsion vs. the longitudinal coordinate μ and the volume vs. the inner pressure.

It is important to remark that with this definition fibres and sheets are always orthogonal, for any choice of $\alpha(\lambda_*)$ and $\beta(\lambda_*)$. As showed in section 1.1.2, the symmetry group of an orthotropic material is defined through an orthonormal basis $\{\mathbf{f}_\circ, \mathbf{s}_\circ, \mathbf{n}_\circ\}$, where $\mathbf{n}_\circ = \mathbf{f}_\circ \wedge \mathbf{s}_\circ$, so the orthogonality condition is necessary.

Results are presented in figure 1.27. The most important quantity is $\mathcal{I}_{4,\mathbf{s}_\circ}$, which indicates whether or not sheets are contributing to the elastic energy. There is an evident difference of this quantity when compared to the reference case, since the sheets towards the endocardium and epicardium are less compressed than the ones in the midwall, and in the "$-60°:+60°$" case are even under traction. This is a consequence of the longitudinal elongation of the ventricle, which now contributes to stretch also the sheets.

Another effect of a non–uniform laminar structure is an overall volume stiffening, as suggested by the EDPVR curve. The reason is the same as before, since the longitudinal deformation is less pronounced (height vs. pressure plot).

These observations yields to the conclusion that the Holzapfel–Ogden model effectively accounts for the laminar structure of the myocardium. On the other hand, the sensitivity in accounting for the sheets is secondary with respect to the sensitivity on the fibres structure.

Conclusions

In the present chapter we have implemented a finite element solver in the framework of the non–linear and anisotropic hyperelasticity to study the passive inflation of the left ventricle. Following Holzapfel and Ogden (2009), it has been adopted an invariant–based strain–energy function that accounts for the orthotropic and inhomogeneous microstructure. The enforcement of the correct boundary conditions for the left ventricle has been discussed, proposing a couple possible solution based on Lagrangian multipliers.

The implementation of the specific strain–energy in a three–dimensional numerical code enabled us to test the proposed model from different points of view. The pressure induced shear on a cube, whose microstructure mimics the one from the myocardium, highlighted several interesting aspects of the model. In this respect, we found that the distribution of the fibres can dramatically change the expected deformation, more than other like the material parameters set or presence or not of the sheets.

The simulation of an idealised but physiological geometry of the left ventricle confirmed that the description of the fibres distribution is crucial to correctly capture the desired deformation. Indeed, simulations highlight that a transversely isotropic model, with exponential stiffening of the shear moduli, is sufficient to describe the strain and, at some measure, also the stress. When the diastolic phase is considered, the orthotropic the model from Holzapfel and Ogden (2009), behaves exactly like a transversely isotropic model, because the sheet–specific strain–energy term is deactivated in compressive regime. On the other hand, this is due to the particular choice of considering the sheets radially distributed: indeed, a variable laminar structure yields to a moderately different deformation.

Another interesting characteristic of the model is the presence of the cross fibre–sheet invariant, that takes into the account the different shear property of myocardium. The associated strain–energy term is not strongly elliptic, but we haven't found any numerical issues in this respect. On the other hand, the presence of this term doesn't affect significantly the solution, so its role is negligible in this context.

Unfortunately, the activation of the sheet–specific term also when the corresponding invariant is less then one, highly destabilises the mechanical deformation. This is probably due to the loss of ellipticity of the elasticity tensor, which is not desirable in this context.

We conclude that the model by Holzapfel and Ogden (2009) is suitable to describe the passive inflation of the left ventricle, accounting for the fibres and laminar structure of the myocardium. Some authors suggest that this laminar structure could facilitate the torsion of the ventricle, but from the simulations the effect of the sheet–specific contribution is negligible in this respect, a result confirmed also by Wang et al. (2013). This aspect needs further investigations: the microstructure by itself only suggests the involved invariants at the macroscopic scale, but it doesn't say anything regarding the specific form of the strain–energy. It might be more effective to fit the parameters on the basis of macroscopic *in–vivo* quantities such as the torsion or the EDPVR, instead of fitting them on tests of *ex–vivo* animal myocardium specimen, such as in Dokos et al. (2002).

Chapter 2

Active mechanics

Introduction

Mechanobiology is an area of increasing interest in continuum mechanics. The impressive improvements of experimental techniques offer to scientists a huge number of data, at several spatial scales, ranging from cells to big mammals. The accuracy of experimental measures and the novelty of the observed phenomena make the mathematical modelling of biological phenomena a very attractive field. Molecular biology currently plays a major role, but there is quite a consensus that mechanics, and in particular continuum mechanics, is the correct tool for an insight of several open questions as, for instance, mechanotrasduction (Taber, 2009).

One of the non–standard characteristics of living matter, that poses intriguing questions in continuum mechanics, is the ability of a body to change its own placement, without external loads. This property is shared with several other mechanical systems: a few examples are thermally–induced strain in metals, swelling gels, phase transitions. In the present context the internal dynamics is due to the action of muscles, who spend energy at the microscale in order to produce a deformation at the macroscale. Our main interest is in modelling specifically the cardiac muscle, which is probably the most important example of “active biological material”. Some mathematical issues to be addressed in the chapter have general validity, while the modelling aspects are dictated by our specific interest in heart physiology.

The cardiac functionality can be sketched as follows (see also figure 2.1). The electric signal, produced by self–excitable cells specifically located, triggers the release of intracellular calcium ions, which starts the mechanical activity. A voltage wave then travels along the conduction fibres, depolarizes the cardiac cells, dictates the shortening of cardiomyocytes and the corresponding contraction of the cardiac muscle, that pumps the blood through the arteries and in the whole body. It is worth noting that the contraction also acts as a feedback to the other compartments of the myocyte (dashed paths in figure 2.1), since it has a positive and/or negative impact on the eletrophysiology (Winfree, 1989; Trayanova et al., 2004; Mesin and Ambrosi, 2011; Weise and Panfilov, 2013).

The mathematical description of such a process faces a number of difficulties. Restricting to the solid mechanics issues only, the passive behaviour of the cardiac wall is quite complex. The material is non–homogeneous, composed by several layers; in each layer the fibres have a specific orientation and their direction rotates for tens of degrees across the wall thickness, giving rise to a complex mechanical characterization, as it has been shown in chapter 1. Boundary conditions

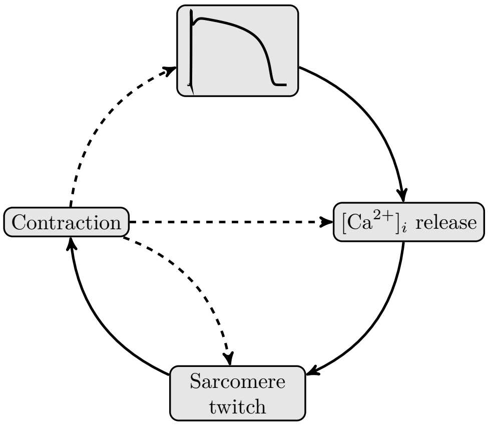

Figure 2.1 Sketch of the electromechanical coupling.

are not a trivial issue, as they are externally due to the traction exerted by other organs, while internally the blood, an incompressible fluid, prevents contraction until the valves open up. Boundary traction and elastic moduli are typically known with a severe uncertainty.

Another fundamental characteristic of a biological tissue is the possibility to adapt its properties to the surrounding environment: for instance, the greater is the blood volume entering the ventricle, the more powerful is the contraction exerted by the muscle. This simple fact, discussed in section 2.1.2, considerably complicates the mathematical modelling of the heart, because it requires the description of a mechanical feedback which tells the cell how to set up the contraction accordingly to the requested extra effort.

The focus of this chapter is on a specific aspect involved in the mathematical modelling of active biological tissues and cardiac mechanics, in particular: we describe the heart as a continuum body and our question is how to include the active tension, due to the contraction of cardiomyocytes, in the force balance that determines its deformation. Two possible strategies are available in the literature. The most popular approach is to add an active contribution to the stress of the material, as done by Smith et al. (2004), Panfilov et al. (2005), Göktepe and Kuhl (2010), and Pathmanathan et al. (2010). In principle, one first characterizes the passive mechanical properties of a specimen, provided that experiments are carried out in physiological conditions, and obtains a standard strain–energy. Then an additive stress contribution is to be included in the force balance, typically dependent on fibre orientation, so that the observed contraction and torsion is reproduced (Redaelli and Pietrabissa, 1997).

A different point of view, inspired by the theory of active materials, has been introduced by Taber and Perucchio (2000) and then deeply explored by others: Nardinocchi and Teresi (2007), Cherubini et al. (2008), Ambrosi et al. (2011), Nardinocchi et al. (2011), Nobile et al. (2012), Sharifimajd and Stålhand (2012), and Rossi et al. (2012). They adopt a multiplicative decomposition of the tensor gradient of deformation, reminiscent of the theory of plasticity and, in biology, volumetric growth (Rodriguez et al., 1994). The deformation gradient rewrites then $\mathsf{F} = \mathsf{F}_\mathsf{e}\mathsf{F}_\mathsf{a}$, where the active contribution F_a has to be constitutively provided. The active strain F_a stores no energy, and it could be pictorially understood as a distortion of the microstructure, that forms a kind of watermark defined in the whole body. The elastic deformation F_e must accommodate the material in order to preserve the compatibility of the deformation F, possibly undermined by the distortion F_a.

In section 2.2 we examine some mathematical and biological instances of these two approaches:

frame invariance, ellipticity of the stress tensor and compatibility with the expected physiological behaviour. In section 2.2.1, elementary monotonicity arguments applied to a contractile rod illustrates the very difference in the two approaches and how different models can ensure existence and uniqueness of the solution or not. In section 2.2.2 are resumed the basic definitions of ellipticity and convexity that are to be applied to active tension models taken from the literature in sections 2.2.3 and 2.2.4. A physiological characterization of the stress–strain curve of cardiomyocytes under pre–stretch and pressure–volume curves in the cardiac muscle is illustrated in section 2.1.2.

The second part of the chapter is dedicated to the numerical approximation of the systolic phase of the cardiac cycle. This stage is characterised by the active contraction of the muscle fibres, which can be mathematically described by means of one of two aforementioned strategies: active stress and active strain. After an in–depth study of both approaches, in this work, we deepen the active strain ideas. Besides standard benchmark problems, such as the contraction of a cube with different fibres patterns, provided in section 2.3.2, we apply the methodology to an interesting engineering application of cardiac stem cells, namely the muscular thin films (MTFs) obtained from the maturation of seeded muscle cells on an elastic polymer sheet. These "myocytes–powered" micro–actuators, firstly proposed by Feinberg et al. (2007), provides a very controlled cellular experimental set up (Feinberg et al., 2012), that accompanies the increasing design of contractile bio–hybrid materials created in the engineered tissues context (Nawroth et al., 2012). These thin films, in fact, can be used to repair damaged body parts as patches, for example, for cardiac repair (Iyer et al., 2011), or can be used to test new drugs, or to test the effect of the drugs on contractility and potentially decrease the high failure rate of cardiovascular ones (Alford et al., 2010).

The myocytes, during their systolic phase, are able to bend, to some extent, the elastic substrate they were seeded on. As the mechanical parameters of the elastic substrate are known with high accuracy, in this system it is possible to quantify the active properties of the cells directly from the measurement of the curvature of the deformed actuator, as shown in section 2.4. The numerical experiments on MTFs will naturally provide a physiological range for the activation parameters of the cardiac cells that can be used during the simulations of the systolic phase of the ventricle, subject of section 2.5. In this way we reproduce numerically the MTF test to support the later simulations and validate this model and the produced results.

The systole is composed by two distinct phases: an isovolumic contraction, where the blood is constrained to remain inside the ventricle since both the valves are closed, and an ejection phase, when the blood flows through the aortic valve leaving the chamber. We propose a physically motivated Lagrangian strategy to account for the isovolumic contraction, in section 2.5.2. Then, in a similar fashion to the previous chapter, we perform several numerical tests in order to establish the sensitivity of the model on the parameters, in terms of strain, stress, and the torsion. The ejection phase (section 2.5.1), on the other hand, is approximated by a free contraction, where the inner pressure is constant and the volume varies due to active contraction of the fibres. Finally, the last section is dedicated to a full simulation of the passive inflation and the subsequent systole, for a canine and a human geometries.

2.1 Electromechanical coupling

2.1.1 Active contraction

During an isometric test, an electrically stimulated cardiomyocyte produces a reaction constraint that can be associated to the active force. On the other hand, this constraint reaction is naturally present also when the cell is stretched over its resting length and no electric stimulus is applied, as an elastic response: this is just a passive force. It is therefore natural to assume that the total Cauchy stress exerted by the cell can be decomposed into two distinct contributions (Wakatsuki et al., 2000): a passive one, that represents the elastic response of the material to external loads, when no active contraction is involved, and an active contribution that encodes for the forces generated at the microscale:

$$f_{\mathsf{total}} = f_{\mathsf{active}} + f_{\mathsf{passive}}. \tag{2.1}$$

Suppose now that the mechanical properties of the myocyte can be described by an hyperelastic material with strain–energy density function $\mathcal{W}\colon \mathrm{Lin}^+ \to \mathbb{R}^+$. By definition, the first Piola–Kirchhoff tensor is

$$\mathsf{P} = \frac{\partial \mathcal{W}}{\partial \mathsf{F}},$$

which means that, thanks to the Piola transformation, the Cauchy stress tensor reads as follows:

$$\mathsf{T} = (\det \mathsf{F})^{-1} \frac{\partial \mathcal{W}}{\partial \mathsf{F}} \mathsf{F}^{\mathsf{T}}. \tag{2.2}$$

This stress is purely passive, so it accounts for f_{passive}. When the activation is involved, an extra term shows up, associated to f_{active}:

$$\mathsf{T}(\mathsf{F}, \xi) = \mathsf{T}_{\mathsf{e}}(\mathsf{F}) + \mathsf{T}_{\mathsf{a}}(\mathsf{F}, \xi) = (\det \mathsf{F})^{-1} \frac{\partial \mathcal{W}}{\partial \mathsf{F}} \mathsf{F}^{\mathsf{T}} + \mathsf{T}_{\mathsf{a}}(\mathsf{F}, \xi).$$

The active stress T_{a} depends on some internal variable ξ, that synthesizes the biochemical status of the cell and, in general, is also a function of the deformation gradient F. In fact the stress T_{a} is a force per unit area, so we cannot trivially match it with the force f_{active}; even if then latter had no dependence on the strain (which is actually not true, cfr. section 2.1.2), the corresponding stress would depend on F for *geometrical* reasons, as we shall see in a moment.

In absence of active contraction, say for $\xi = \xi_{\mathsf{ref}}$, the active vanishes:

$$\mathsf{T}_{\mathsf{a}}(\mathsf{F}, \xi_{\mathsf{ref}}) = \mathsf{O}, \qquad \text{for every } \mathsf{F} \in \mathrm{Lin}^+.$$

The specific tensorial form of T_{a} can be deduced enforcing the correct symmetries from the microstructure. The 2nd Piola–Kirchhoff tensor associated to T_{a} reads:

$$\mathsf{S}_{\mathsf{a}}(\mathsf{F}, \xi) = (\det \mathsf{F}) \mathsf{F}^{-1} \mathsf{T}_{\mathsf{a}}(\mathsf{F}, \xi) \mathsf{F}^{-\mathsf{T}}.$$

The first requirement is objectivity, which means that S_{a} depends on F only through U, with U such that $\mathsf{F} = \mathsf{R}\mathsf{U}$. For instance, a possibility is to consider

$$\widehat{\mathsf{S}}_{\mathsf{a}}(\mathsf{C}, \xi) = \widehat{\mathsf{S}}_{\mathsf{a}}(\mathsf{F}^{\mathsf{T}}\mathsf{F}, \xi) = \mathsf{S}_{\mathsf{a}}(\mathsf{F}, \xi).$$

The second ingredient is that the active stress acts in the fibre direction $\mathbf{f}_\circ$, so we look for a transversely isotropic tensor $\widehat{\mathsf{S}}_{\mathsf{a}}$ of its arguments C and ξ. Using the arguments exposed in section 1.1.2, we obtain that

$$\widehat{\mathsf{S}}_{\mathsf{a}}(\mathsf{C}, \xi) = s_1 \, \mathsf{I} + s_2 \, \mathsf{C} + s_4 \, \mathbf{f}_\circ \otimes \mathbf{f}_\circ + s_5 \, \mathrm{sym}(\mathsf{C}\mathbf{f}_\circ \otimes \mathbf{f}_\circ), \tag{2.3}$$

where s_1, s_2, s_4 and s_5 are scalar functions of ξ of the invariants

$$\Upsilon = \Big\{ \mathrm{tr}\, \mathsf{C}, \mathrm{tr}\, \mathsf{C}^2, \mathbf{f}_\circ \cdot \mathsf{C}\mathbf{f}_\circ, \mathbf{f}_\circ \cdot \mathsf{C}^2 \mathbf{f}_\circ \Big\},$$

where $\det \mathsf{C} = 1$ and $\mathbf{f}_\circ \cdot \mathbf{f}_\circ = 1$. The general structure of (2.3) can be very complex; a popular mathematical simplification is to neglect the quadratic invariants, so that

$$\widehat{\mathsf{S}}_{\mathsf{a}}(\mathsf{C}, \xi) = s_1(\mathcal{I}_1, \mathcal{I}_{4,\mathbf{f}_\circ}, \xi) \, \mathsf{I} + s_4(\mathcal{I}_1, \mathcal{I}_{4,\mathbf{f}_\circ}, \xi) \, \mathbf{f}_\circ \otimes \mathbf{f}_\circ.$$

This form is however much more complicated than what has been proposed over the last decades in the literature: the invariant $\mathcal{I}_1$ is usually not considered and, most of the time, also s_1 is neglected:

$$\widehat{\mathsf{S}}_{\mathsf{a}}(\mathsf{C},\xi) = s_{\mathsf{a}}(\mathcal{I}_{4,\mathbf{f}_\circ},\xi)\,\mathbf{f}_\circ \otimes \mathbf{f}_\circ$$

or, in terms of physical stress

$$\mathsf{T}_{\mathsf{a}}(\mathsf{F},\xi) = s_{\mathsf{a}}(\mathcal{I}_{4,\mathbf{f}_\circ},\xi)\,\mathsf{F}\mathbf{f}_\circ \otimes \mathsf{F}\mathbf{f}_\circ \tag{2.4}$$

so that the active stress acts in the deformed fibre direction, with a magnitude that nonlinearly depends on the current stretch of the fibres. Some authors (Usyk et al., 2000; Aguado–Sierra et al., 2011) adopt an orthotropic active stress, which actually is a transversely isotropic activation of the form

$$\widehat{\mathsf{S}}_{\mathsf{a}}(\mathsf{C},\xi) = s_{\mathsf{a}}(\mathcal{I}_{4,\mathbf{f}_\circ},\xi)\,\mathbf{f}_\circ \otimes \mathbf{f}_\circ + r\,s_{\mathsf{a}}(\mathcal{I}_{4,\mathbf{f}_\circ},\xi)\,(\mathsf{I} - \mathbf{f}_\circ \otimes \mathbf{f}_\circ) \tag{2.5}$$

for some factor $r \geq 0$ (usually $0.2 \div 0.4$).

The scalar factor s_{a}, which is a force per unit area, has to be related to the active force f_{active}, in order to fit the experimental data. A possibility is to analyse a specific test case such as the homogeneous contraction of a rod along its $\mathbf{f}_\circ$ axis:

$$\mathsf{F} = \lambda \mathbf{f}_\circ \otimes \mathbf{f}_\circ + \frac{1}{\sqrt{\lambda}}(\mathsf{I} - \mathbf{f}_\circ \otimes \mathbf{f}_\circ).$$

Substituting the latter into equation (2.4) we have

$$\mathsf{T}_{\mathsf{a}}(\lambda,\xi) = s_{\mathsf{a}}(\lambda^2,\xi)\lambda^2 = f_{\mathsf{active}}\,A_0\lambda,$$

where A_0 is the initial cross area, so that $A_0\mathsf{C}^{-1}\mathbf{f}_\circ \cdot \mathbf{f}_\circ = A_0\lambda$ is the deformed area. Simplifying we get

$$f_{\mathsf{active}}(\lambda,\xi) = \frac{\lambda}{A_0} s_{\mathsf{a}}(\lambda^2,\xi). \tag{2.6}$$

Therefore the force is independent from λ if (observe that $\lambda^2 = \mathcal{I}_{4,\mathbf{f}_\circ}$):

$$s_{\mathsf{a}}(\mathcal{I}_{4,\mathbf{f}_\circ},\xi) = A_0 \frac{f_{\mathsf{active}}(\xi)}{\sqrt{\mathcal{I}_{4,\mathbf{f}_\circ}}}.$$

More physiologically motivated choices of s_{a} (see section 2.1.2) are linearly dependent on λ, in order to recover the Frank–Starling effect for moderate values of the strain. Another options is a nonlinear function like $\lambda\exp(-\lambda^2)$ (or a quadratic approximation of it) which captures an optimal value of the sarcomere stretch and the descending limb of Frank–Starling relationship (Weiwad et al., 2000).

The construction of a specific form for the active stress term T_{a} is delicate, because it should account for the geometry of the deformation, which changes considerably in finite strain. Moreover, an important property of a stress–strain relationship, *an increase of the strain is accompanied by an increase of the stress, and vice–versa* (Baker and Ericksen, 1954; Marsden and Hughes, 1983), translates in the positiveness of the derivative of f_{active} of equation (2.6)

$$A_0\,\frac{\partial f_{\mathsf{active}}}{\partial \lambda} = s_{\mathsf{a}}(\mathcal{I}_{4,\mathbf{f}_\circ},\xi) + 2\mathcal{I}_{4,\mathbf{f}_\circ}\frac{\partial s_{\mathsf{a}}(\mathcal{I}_{4,\mathbf{f}_\circ},\xi)}{\partial \mathcal{I}_{4,\mathbf{f}_\circ}} > 0, \tag{2.7}$$

here doesn't seems to apply: the *active* nature of the material clearly violates this basic principle. This lack of monotonicity (or strong–ellipticity), is critical for the well–posedness of the mathematical model: in section 2.2.3 we show that the inequality (2.7) is general and provides a necessary and sufficient condition for the strong–ellipticity.

An alternative approach, the so–called active strain, consists in a multiplicative decomposition of the deformation gradient tensor

$$\mathsf{F} = \mathsf{F}_{\mathsf{e}}\mathsf{F}_{\mathsf{a}}$$

in an elastic deformation F_{e} and an active distortion F_{a}.

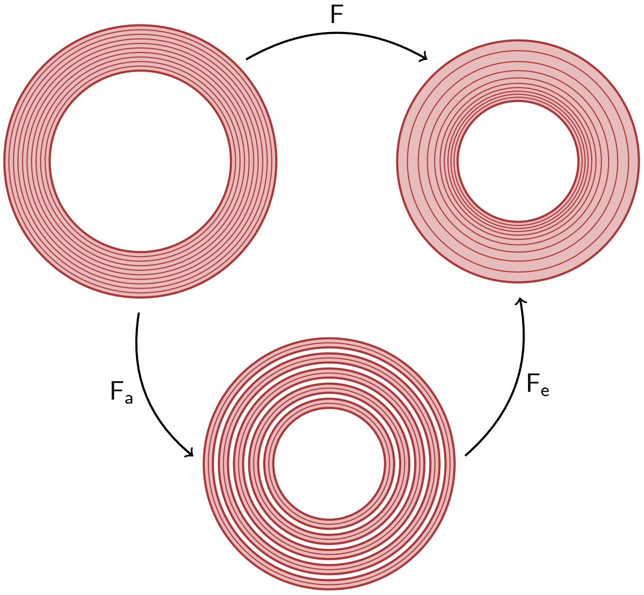

Figure 2.2 Pictorial view of the active strain approach.

The idea, sketched in figure 2.2 is the following: an inelastic process, dictated by the biochemistry, locally changes the length and the shape of the fibres; then, an elastic deformation accommodates the active strain distortion F_{a} in order to preserve the compatibility. The physiological basis of the approach resides in the contractile units of the myocytes: the sarcomeres shorten because of the sliding filaments of the actin–myosin molecular motor, and this shortening is encoded by F_{a}, and the fictitious intermediate placement determined by F_{a} is the new reference configuration for the elastic deformation.

The strain–energy density is a function of F_{e} only, the active deformation F_{a} being a fully dissipative process; the objective is to minimise the total elastic energy with respect to all the admissible configuration:

$$\min_{\boldsymbol{\varphi}\in\mathscr{C}} \int_{\Omega_0} \mathcal{W}(\mathsf{F}\mathsf{F}_{\mathsf{a}}^{-1})\,(\det\mathsf{F}_{\mathsf{a}})\,\mathrm{d}V - \left\langle \mathbf{f}^{\mathsf{ext}}, \boldsymbol{\varphi} \right\rangle . \tag{2.8}$$

If no dead–load is applied, so $\mathbf{f}^{\mathsf{ext}} = 0$, it would be reasonable to argue that $\mathsf{F} = \mathsf{F}_{\mathsf{a}}$, since $\mathsf{F}_{\mathsf{e}} = \mathsf{I}$ is a local minimum of $\mathcal{W}$ (actually, if $\mathcal{W}$ and $\mathscr{C}$ are convex, the minimum global and hence unique). However, there is no guarantee that there exists a deformation $\boldsymbol{\varphi}$ such that $\textsc{Grad}\,\boldsymbol{\varphi} = \mathsf{F}_{\mathsf{a}}$. This restricts the set of possible solutions among which the minimisation problem makes sense from a geometric viewpoint, and it yields a residual stress in the body, even if there is no body force or surface traction.

Suppose that a minimum exists; then, the first variation of the functional in equation (2.8) must be null:

$$\int_{\Omega_0} (\det \mathsf{F_a}) \frac{\partial \mathcal{W}(\mathsf{F_e})}{\partial \mathsf{F_e}} \mathsf{F_a^{-T}} : \textsc{Grad}\, \boldsymbol{\eta}_0 \, \mathrm{d}V - \left\langle \mathbf{f}^{\mathsf{ext}}, \boldsymbol{\eta}_0 \right\rangle = 0.$$

The 1^{st} Piola–Kirchhoff and the Cauchy stress tensors are, respectively:

$$\mathsf{P} = (\det \mathsf{F_a}) \frac{\partial \mathcal{W}(\mathsf{F_e})}{\partial \mathsf{F_e}} \mathsf{F_a^{-T}}, \qquad \mathsf{T} = (\det \mathsf{F_e})^{-1} \frac{\partial \mathcal{W}(\mathsf{F_e})}{\partial \mathsf{F_e}} \mathsf{F_e^{T}}.$$

If no activation is involved, then $\mathsf{F_a} = \mathsf{I}$ and $\mathsf{F_e} = \mathsf{F}$, thus the passive behaviour of the material is recovered. On the other hand, if $\mathsf{F} = \mathsf{I}$ and $\mathsf{F_e} = \mathsf{F_a^{-1}}$, the Cauchy stress tensor can be interpreted as a purely active response:

$$\mathsf{T} = (\det \mathsf{F_a}) \left. \frac{\partial \mathcal{W}}{\partial \mathsf{F_e}} \right|_{\mathsf{F_e} = \mathsf{F_a^{-1}}} \mathsf{F_a^{-T}}.$$

The tensorial form of the active Cauchy stress in dictated by $\mathsf{F_a}$ and the strain–energy form as well. A transversely isotropic choice might be

$$\mathsf{F_a} = \gamma_1 \mathbf{f}_\circ \otimes \mathbf{f}_\circ + \gamma_2 (\mathsf{I} - \mathbf{f}_\circ \otimes \mathbf{f}_\circ).$$

If $\gamma_2 = \gamma_1^{-1/2} = \gamma^{-1/2}$, the deformation is isochoric, which is a physiological choice since during a contraction myocytes don't change their volume significantly (Boyett et al., 1991). The coefficient γ, which depends on the internal dynamics described by a variable ξ, doesn't depends on F, so the question if it captures or not the Frank–Starling relationship is open at this stage. We investigate on this issue in section 2.2.4.

Concluding, an interesting point of view of this multiplicative decomposition approach, widely exploited in finite strain theories, in the concept of evolving metric (Yavari and Goriely, 2012). The body is considered as a manifold whose metric is prescribed; the elastic problem, derived by the minimisation of the strain–energy, is written through the metric, which dictates the local curvilinear coordinate system. Since the metric evolves because of some inelastic process, also the manifold is locally changing. Observe that there is no intermediate configuration.

2.1.2 Physiological facts

While the mathematical results illustrated in the next sections may apply to any active material, the modelling issues specifically refer to the problem that we have in mind, namely the heart contraction. A milestone of the physiological literature in this respect is that a mathematical model designed to predict the solid mechanics behaviour of the cardiac muscle should be able to reproduce the active tension according to the Frank–Starling law. Its qualitative statement is the following: *"the greater the volume of blood entering the heart during diastole (end–diastolic volume), the greater the volume of blood ejected during systolic contraction (stroke volume) and vice-versa"*. In dynamic terms, this means that the larger the passive strain of the cardiac muscle originated by the venous pressure before contraction, the larger the active stress. This relation has a clear functional motivation: the muscle applies a bigger force when a greater work has to be performed, thus pumping a larger volume of blood.

This self–regulation mechanism at a tissue level has a striking counterpart at a cellular level, where a quantitative evidence is offered by several experiments. Cardiomyocytes stretched up to 1.3 times of their original length apply an active force, after electric stimulus, that grows linearly with the pre–stretch (Iribe et al., 2007). This relation is apparent in the plot of figure 2.3 (a sketch of the results reported by Iribe et al. (2007)). A cardiomyocyte undergoes isometric

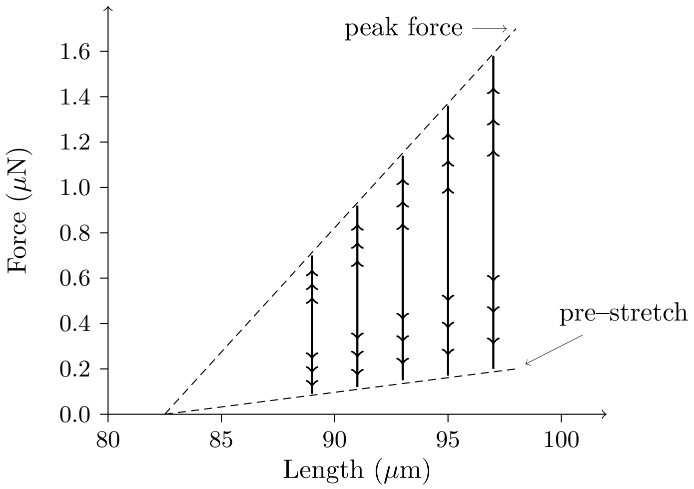

Figure 2.3 Cardiomyocytes electrically stimulated under isometric conditions: the produced force grows linearly with the pre-stretch [sketch from Figure 5A of Iribe et al. (2007)].

contractions after pre–stretch at different ratios (lower straight line). The cell is activated by a voltage difference while kept at a constant length. The produced force depends linearly on the pre–stretch (difference between the value of the two lines) at fixed length.

While the active–passive stress–strain relations are well understood at a cellular level, to our knowledge a quantitative Frank–Starling law at a tissue scale has not been stated yet. The prototypical set up to state a force–strain relation at the macroscale is the pressure–volume curve that occurs in the heart during its cycle. Figure 2.4 shows the different pressure–volume loops that can be obtained in a ventricle by tuning the aortic pressure. This plot provides the quantitative dependence of the active stress on the deformation (Campbell et al., 2008; Nardinocchi et al., 2011): the upper and lower dashed lines denote the pressure of the fluid, i.e. the radial stress at the inner wall, both when the stress is purely passive (lower curve) and when the stress is actively produced (upper curve).

In this thesis we do not enter further physiological details and the reader interested in cardiac physiology may refer to the cited literature. We just point out that it is not trivial to match the cellular and tissutal experiments in order to state a macroscopic constitutive equation. At the macroscale, the curves reported in the literature clearly show a strongly nonlinear dependence of the active stress (measured by the pressure of the fluid) and the strain (represented by the change in volume). In fact, the hoop stress in a hollow elastic sphere filled by a fluid at pressure p obeys the Laplace formula:

$$\mathsf{T}_{\Theta\Theta} = \frac{rp}{2h},$$

where r is the radius, h the thickness of the wall and $T_{\Theta\Theta}$ is an averaged hoop stress (basically the active stress, in our case). For an incompressible material, the constant volume of the solid body is $\simeq r^2 h$ and therefore, as a rule of thumb,

$$\mathsf{T}_{\Theta\Theta} = \frac{rp}{2h} \simeq r^3 p \simeq r^6, \tag{2.9}$$

where the dependence of the pressure on the volume has been exported by the curve in Figure 2.3. As the hoop strain is proportional to r, it follows from equation (2.9) that the active stress grows very nonlinearly with the deformation. Quoting Downey: *“increasing end–diastolic*

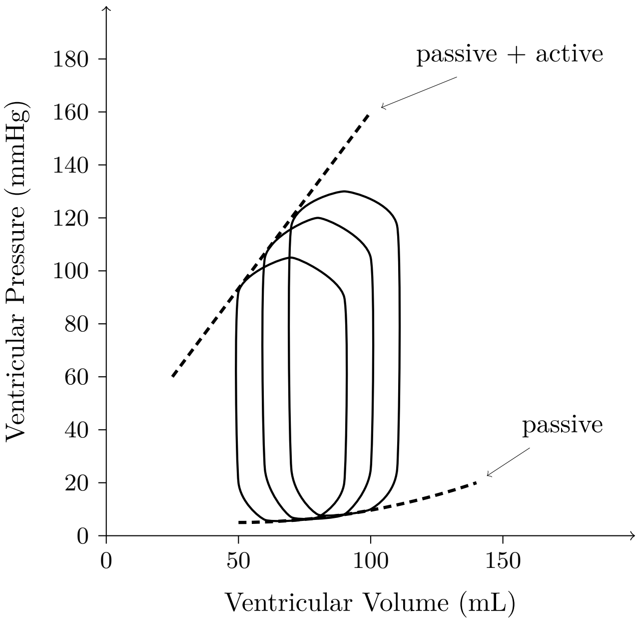

Figure 2.4 Pressure–volume loops in a ventricle allow to determine the curve of the passive and active normal stress at the cardiac wall [sketch from Figure 12 of (Downey, 2003)].

volume actually diminishes the heart's ability to convert its fibre tension into pressure. In the physiological range, this disadvantage is greatly overshadowed by the increase in force generation that results from the longer fibre length". As a matter of fact, Teresi and co–workers reproduce the plot of Figure 2.4 in an active strain framework choosing a constitutive law for the stress that grows with the sixth power of the strain (Nardinocchi et al., 2011).

We close this section mentioning that active stress models reported in the literature are sometimes inspired by experimental evidence at a cell–scale, sometimes they account for a macroscopic behaviour directly. The first approach is clearly more satisfactory from a methodological point of view and the efficacy of the active constitutive relation at a tissue scale is to be verified *a posteriori*, typically on the basis of numerical simulations.

2.2 Active stress vs. active strain: constitutive issues

2.2.1 An elementary argument

Some elementary arguments on the active deformation of an elastic rod can turn useful to point out the essence of the active stress and active strain approaches. Consider the active stress model first. In an idealized experiment, we load a one dimensional elastic rod, characterized by the homogeneous deformation λ and a convex strain energy $\mathcal{W}(\lambda)$. The balance of standard and active force reads:

$$\frac{\mathrm{d}\mathcal{W}}{\mathrm{d}\lambda} + \tau + \sigma = 0, \tag{2.10}$$

where τ is the active tension, and σ the external force. We are interested in an active tension able to produce shortening ($\lambda < 1$, $\mathcal{W}' < 0$), in absence of external load ($\sigma = 0$), i.e. $\tau > 0$. For reasons discussed in previous sections, the models presented in the literature typically assume that the active tension depends on the stretch: $\tau = \tau(\lambda)$. The non–trivial case we are interested in is when $\tau|_{\lambda=1} \neq 0$ so that the relaxed state is not of equilibrium.

Equation (2.10) provides the equilibrium strain; its existence and uniqueness are ensured if

$$\frac{\mathrm{d}^2\mathcal{W}}{\mathrm{d}\lambda^2} + \frac{\mathrm{d}\tau}{\lambda} \geq 0, \qquad \forall\lambda > 0. \tag{2.11}$$

Notice that convexity of $\mathcal{W}(\lambda)$ would be sufficient for our purposes if τ does not depend on λ, but this case is not of much interest.

Depending on the specific functional forms $\mathcal{W}(\lambda)$ and $\tau(\lambda)$, the condition in equation (2.11) may be satisfied or not. Consider the following examples of active tension:

$$\tau = \tau_{\mathsf{ref}}\,\lambda, \tag{2.12a}$$

$$\tau = \tau_{\mathsf{ref}}\,\lambda^2, \tag{2.12b}$$

$$\tau = \tau_{\mathsf{ref}}\,\lambda^{-1}, \tag{2.12c}$$

where $\tau_{\mathsf{ref}} > 0$. It is an elementary calculation to check if the condition equation (2.11) is verified:

$$\frac{\mathrm{d}\mathcal{W}}{\mathrm{d}\lambda} + \tau_{\mathsf{ref}} > 0, \tag{2.13a}$$

$$\frac{\mathrm{d}\mathcal{W}}{\mathrm{d}\lambda} + 2\tau_{\mathsf{ref}}\,\lambda > 0, \tag{2.13b}$$

$$\frac{\mathrm{d}\mathcal{W}}{\mathrm{d}\lambda} - \tau_{\mathsf{ref}}\,\lambda^{-2} > 0. \tag{2.13c}$$

Relations (2.13a) and (2.13b) always apply. For a given strain energy, (2.13c) reads as a restriction on the strain range that can be spanned; in particular, it might be not satisfied for large compression.

Consider the same problem illustrated above in terms of active strain: now we set $\mathcal{W} = \mathcal{W}(\lambda/\lambda_{\mathsf{a}})$, where λ_{a}, the active shortening, is given, and $\tau = 0$. The force balance equation reads

$$\frac{\mathrm{d}\mathcal{W}}{\mathrm{d}\lambda}\frac{1}{\lambda_{\mathsf{a}}} + \sigma = 0.$$

The convexity condition at equilibrium state is:

$$\frac{\mathrm{d}^2\mathcal{W}}{\mathrm{d}\lambda^2}\frac{1}{\lambda_{\mathsf{a}}^2} > 0.$$

In this case, existence and uniqueness of equilibrium are ensured by the mere convexity of the strain energy function.

The elementary argument sketched above illustrates the motivation of next sections: to point out the mathematical properties and physiological characteristics that a model for active contraction should possess and possibly propose new approaches that fulfil such requirements.

2.2.2 Convexity and strong–ellipticity

The constitutive relation for an elastic material $\mathsf{P} = \mathsf{P}(\mathsf{F})$ is strictly monotone if

$$\Big(\mathsf{P}(\mathsf{F} + \alpha\mathsf{H}) - \mathsf{P}(\mathsf{F})\Big) : \mathsf{H} > 0,$$

$$\text{for each } \mathsf{F} \in \mathrm{Lin}^+,\ \mathsf{H} \neq 0 \text{ and } \alpha \in (0,1] \text{ such that } \det(\mathsf{F} + \alpha\mathsf{H}) > 0. \tag{2.14}$$

In case of hyperelastic material, the definition (2.14) corresponds to the strict convexity of the strain energy function:

$$\alpha\mathcal{W}(\mathsf{F}) + (1-\alpha)\mathcal{W}(\mathsf{F}+\mathsf{H}) > \mathcal{W}\big(\mathsf{F}+(1-\alpha)\mathsf{H}\big),$$
$$\text{for each } \mathsf{F}\in \mathrm{Lin}^+,\ \mathsf{H}\neq 0 \text{ and } \alpha\in(0,1) \text{ such that } \det\big(\mathsf{F}+(1-\alpha)\mathsf{H}\big) > 0. \quad (2.15)$$

If $\mathsf{P}(\mathsf{F})$ is differentiable, the condition (2.14) is equivalent to say that the second derivative of the energy is a positive definite linear operator:

$$\mathsf{H} : \frac{\partial \mathsf{P}(\mathsf{F})}{\partial \mathsf{F}} : \mathsf{H} > 0, \qquad \text{for each } \mathsf{F}\in\mathrm{Lin}^+ \text{ and } \mathsf{H}\neq 0. \quad (2.16)$$

Despite its appeal, strict convexity is a too restrictive condition for several reasons (Antman, 2005). A well established weaker characterization is the strong ellipticity condition: inequality (2.16) must hold for any increment H of rank–one. Analogously, a strain energy is rank–one convex if (2.16) holds for any increment H of rank–one. Notice that the set of the rank–one tensors is represented by the dyads $\mathbf{a}\otimes\mathbf{b}$ where $\mathbf{a},\mathbf{b}\in\mathbb{R}^3$.

Finally, if the material is incompressible, the condition $\det(\mathsf{F}+\alpha\mathsf{H}) = 1$ should be added in (2.14) and, for a smooth enough strain energy function, this condition translates into $\mathsf{F}^{\mathsf{T}} : \mathsf{H} = 0$ in inequality (2.16). If the increment is a rank–one tensor, i.e. $\mathsf{H} = \mathbf{a}\otimes\mathbf{b}$, then it must be $\mathsf{F}^{-\mathsf{T}} : \mathsf{H} = \mathbf{a}\cdot\mathsf{F}^{-1}\mathbf{b} = 0$.

2.2.3 Active stress

We address first the question whether ellipticity of the Piola stress tensor is ensured when adopting an active stress approach. The aim is to investigate the mathematical characteristics of the equilibrium predicted by models currently adopted in numerical codes, as well as to discuss their physiological basis.

In general there is no reason why the active stress tensor should arise from a potential, and in fact it is not a conservative force. We therefore investigate ellipticity by direct derivation of the total stress. If now $\mathcal{W} = \mathcal{W}(\mathsf{F})$, the total Piola stress reads

$$\mathsf{P} = \frac{\partial\mathcal{W}}{\partial\mathsf{F}} + \mathsf{P}_{\mathsf{a}}$$

where $\mathsf{P}_{\mathsf{a}} = \mathsf{F}\mathsf{S}_{\mathsf{a}}$ is the active Piola stress to be prescribed, possibly depending on F.

If the material is hyperelastic in its passive mechanical behaviour, the condition equation (2.16) rewrites now

$$\mathsf{H} : \frac{\partial^2\mathcal{W}}{\partial\mathsf{F}\partial\mathsf{F}} : \mathsf{H} + \mathsf{H} : \frac{\partial\mathsf{P}_{\mathsf{a}}}{\partial\mathsf{F}} : \mathsf{H} > 0, \qquad \forall\mathsf{F}\in\mathrm{Lin}^+,\ \mathsf{H}\neq 0, \quad (2.17)$$

with the additional constraint $\mathsf{F}^{-\mathsf{T}} : \mathsf{H} = 0$ in the case of incompressible material.

Given for granted that $\mathcal{W} = \mathcal{W}(\mathsf{F})$ is a rank–one convex function, inequality of equation (2.17) reads as a condition on the functional form of the active stress. In this section we address the ellipticity of the total stress P by checking the positivity of the second term at the right hand side of equation (2.17) for some specific models taken from the literature. If the active term in equation (2.17) is not positive, the inequality can still hold, depending on the specific strain energy $\mathcal{W}(\mathsf{F})$, but conditions can apply on the admissible strain range.

Notice that possible strong mathematical properties of the active stress P_{a} (as strict monotonicity) are not to be deprecated, because the sum of two functions retains the (good) properties of the weaker one. Conversely, if P_{a} is not at least rank–one elliptic, the existence of the solution might be not ensured.

Examples from the literature

One possible form of the active tension that does not involve an active role for the fibres is proposed by Panfilov et al. (2005) in terms of second Piola–Kirchhoff active stress tensor:

$$\mathsf{S}_\mathsf{a} = s_\mathsf{a} \mathsf{C}^{-1} \tag{2.18}$$

where $\mathsf{C} = \mathsf{F}^\mathsf{T}\mathsf{F}$. In an electromechanical model, the scalar quantity s_a depends on the activated state of the material, possibly thanks a delay equation; however such a dependence is not of interest herein, where balance of forces applies in static form, and we take it constant.

Notice that the Cauchy stress corresponding to (2.18) is spherical. Here the first Piola stress reads

$$\mathsf{P} = \frac{\partial \mathcal{W}}{\partial \mathsf{F}} + s_\mathsf{a}\, \mathsf{F}^{-\mathsf{T}},$$

where $\mathcal{W}$ is a strain energy of a compressible material. The ellipticity can be checked by further derivation:

$$\mathsf{H} : \frac{\partial^2 \mathcal{W}}{\partial \mathsf{F} \partial \mathsf{F}} : \mathsf{H} - s_\mathsf{a}\, \mathsf{F}^{-\mathsf{T}}\mathsf{H}^\mathsf{T}\mathsf{F}^{-\mathsf{T}} : \mathsf{H} > 0. \tag{2.19}$$

The last term at the left hand side can be negative (take, for instance, $\mathsf{H} = \mathbf{a} \otimes \mathbf{a}$) and, depending on the specific form of the strain energy, the total stress might not be unconditionally strongly elliptic. In particular the condition (2.19) may be not satisfied for large compressions.

A constitutive equation for active stress that accounts for the orientation of the fibres can be written in a general form as follows (see section 2.1.1):

$$\mathsf{P}_\mathsf{a} = s_\mathsf{a}(\mathcal{I}_{4,\mathbf{f}_\circ})\, \mathsf{F}\mathbf{f}_\circ \otimes \mathbf{f}_\circ \tag{2.20}$$

where s_a is a positive function of $\mathcal{I}_{4,\mathbf{f}_\circ} = \mathsf{F}\mathbf{f}_\circ \cdot \mathsf{F}\mathbf{f}_\circ$ (in the range of interest). A popular choice, firstly proposed by Smith et al. (2004) and then adopted by other groups, is a dependence of the following type:

$$s_\mathsf{a}(\mathcal{I}_{4,\mathbf{f}_\circ}) = \alpha \frac{1 + \beta \left(\sqrt{\mathcal{I}_{4,\mathbf{f}_\circ}} - 1 \right)}{\mathcal{I}_{4,\mathbf{f}_\circ}}, \tag{2.21}$$

where β and α are constant in this context and the active stress works only when the fibres are elongated ($\mathcal{I}_{4,\mathbf{f}_\circ} > 1$). The numerator of the r.h.s. term encodes the Frank–Starling effect while the denominator can be interpreted as a normalization factor accounting that s_a is a Cauchy stress per unit fibre length.

Böl et al. (2012) propose

$$s_\mathsf{a}(\mathcal{I}_{4,\mathbf{f}_\circ}) = \alpha_0 + \alpha_1 \left(1 - e^{-\eta\left(\sqrt{\mathcal{I}_{4,\mathbf{f}_\circ}} - 1\right)} \right), \tag{2.22}$$

which accounts for the Frank–Starling effect directly at a macroscopic level.

Finally Pathmanathan et al. (2010) adopt a form of the active stress tensor that can be obtained deriving a scalar function:

$$\mathsf{P}_\mathsf{a} = \alpha \frac{\partial}{\partial \mathsf{F}} \left(\log \left(\mathsf{F}\mathbf{f}_\circ \cdot \mathsf{F}\mathbf{f}_\circ \right) \right) = \frac{2\alpha}{\mathcal{I}_{4,\mathbf{f}_\circ}}\, \mathsf{F}\mathbf{f}_\circ \otimes \mathbf{f}_\circ. \tag{2.23}$$

Such a scalar function should not be understood as a strain energy, as no conservation applies: the possibility to derive the stress from a scalar is just a technical tool that simplifies the analysis. As a matter of fact, the Piola stress (2.23) is not even rank–one elliptic and therefore, for a given generic passive strain function, strong ellipticity of the total stress holds under condition.

Irrespective of the specific form at hand, the strong ellipticity of the active stress forms illustrated above can be checked by direct derivation of (2.20). In fact, strong ellipticity for a given deformation $\mathsf{F}_\circ$, with $\mathsf{H} = \mathbf{a} \otimes \mathbf{b}$ reads as follows:

$$\mathsf{H} : \left.\frac{\partial \mathsf{P}_\mathsf{a}}{\partial \mathsf{F}}\right|_{\mathsf{F}_\circ} : \mathsf{H} = \left[2 \left.\frac{\partial s_\mathsf{a}}{\partial \mathcal{I}_{4,\mathbf{f}_\circ}}\right|_{\mathsf{F}_\circ} (\mathsf{F}_\circ \mathbf{f}_\circ \cdot \mathbf{a})^2 + s_\mathsf{a}|_{\mathsf{F}_\circ} (\mathbf{a} \cdot \mathbf{a}) \right] (\mathbf{b} \cdot \mathbf{f}_\circ)^2 \geq 0, \tag{2.24}$$

with the condition $\mathsf{F}_\circ^{-1}\mathbf{a} \cdot \mathbf{b} = 0$ on the admissible virtual displacements dictated by the incompressibility constraint. Take $\mathbf{a} = \mathsf{F}_\circ \mathbf{m}$, with $\mathbf{m}$ such that $\mathbf{m} \cdot \mathbf{b} = 0$. Observe first that strict inequality is not satisfied if $\mathbf{b} \cdot \mathbf{f}_\circ = 0$, i.e. $\{\mathbf{f}_\circ, \mathbf{m}, \mathbf{b}\}$ is an orthogonal basis. In other cases the last factor can be dropped:

$$2 \left.\frac{\partial s_\mathsf{a}}{\partial \mathcal{I}_{4,\mathbf{f}_\circ}}\right|_{\mathsf{F}_\circ} (\mathsf{F}_\circ \mathbf{f}_\circ \cdot \mathsf{F}_\circ \mathbf{m})^2 + s_\mathsf{a}|_{\mathsf{F}_\circ} (\mathsf{F}_\circ \mathbf{m} \cdot \mathsf{F}_\circ \mathbf{m}) \geq 0. \tag{2.25}$$

If $\mathbf{b} = \mathbf{f}_\circ$ and $\mathsf{F}_\circ$ is an homogeneous deformation in direction $\mathbf{m}$ and $\mathbf{f}_\circ$, then the first term is always zero, and the second one is non–negative if and only if

$$s_\mathsf{a}(\mathcal{I}_{4,\mathbf{f}_\circ}, \xi) \geq 0,$$

which might be not true for large fibres compression.

In general, using Cauchy–Schwartz inequality on the first term of (2.24)

$$(\mathsf{F}_\circ \mathbf{f}_\circ \cdot \mathbf{a})^2 \leq (\mathsf{F}_\circ \mathbf{f}_\circ \cdot \mathsf{F}_\circ \mathbf{f}_\circ)^2 (\mathbf{a} \cdot \mathbf{a})^2 = \mathcal{I}_{4,\mathbf{f}_\circ} (\mathbf{a} \cdot \mathbf{a})^2,$$

a necessary and sufficient condition on $s_\mathsf{a}(\mathcal{I}_{4,\mathbf{f}_\circ}, \xi)$ can be found and reads (cfr. section 2.1.1):

$$s_\mathsf{a}(\mathcal{I}_{4,\mathbf{f}_\circ}, \xi) + 2\mathcal{I}_{4,\mathbf{f}_\circ} \frac{\partial s_\mathsf{a}(\mathcal{I}_{4,\mathbf{f}_\circ}, \xi)}{\partial \mathcal{I}_{4,\mathbf{f}_\circ}} \geq 0, \qquad \text{for all } \mathbf{a} \neq 0.$$

Remark If an active stress model is not rank–one elliptic, an equilibrium solution of the force balance equation may not exist, at least for some range of the strain. In the numerical approximation of the momentum equation, the absence of equilibrium configurations might be interpreted as a numerical instability to be addressed by a more careful numerical discretisation. However, no numerical strategy can cure an ellipticity loss of the differential equations.

Boundary conditions

The active stress is originated by fibre contraction, their orientation being $\mathbf{f}_\circ$ in the reference configuration and $\mathsf{F}\mathbf{f}_\circ$ in the current one. As the fibres are tangential to the surface at the boundary, a reasonable requirement is that they do not contribute to the traction balance at the boundary itself, i.e.

$$\mathsf{P}_\mathsf{a} \mathbf{m} = 0,$$

where $\mathbf{m}$ is the normal to the boundary in the reference configuration. The reader can notice that such a characterization is satisfied by the active stress tensors (2.20).

2.2.4 Active strain

Consider now a modified convex energy of the form $\mathcal{W} = \mathcal{W}(\mathsf{F}_\mathsf{e})$, where $\mathsf{F} = \mathsf{F}_\mathsf{e}\mathsf{F}_\mathsf{a}$. The meaning of this assumption is as follows: in absence of external forces the minimum of energy (the relaxed configuration) is shifted by the internal active forces to the configuration $\mathsf{F} = \mathsf{F}_\mathsf{a}^{-1}$ and no energy is stored by the action of the internal active forces (DiCarlo and Quiligotti, 2002). The corresponding Piola stress, evaluated in the reference configuration, is obtained by a pull back of the Fréchet derivative of the strain energy:

$$\mathsf{P}(\mathsf{F}) = \det(\mathsf{F}_\mathsf{a}) \frac{\partial \mathcal{W}}{\partial \mathsf{F}_\mathsf{e}} \mathsf{F}_\mathsf{a}^{-\mathsf{T}}.$$

We start checking if convexity is preserved. The answer is positive: $\forall \mathsf{H} \neq 0$ it holds

$$\mathsf{H} : \frac{\partial \mathcal{W}}{\partial \mathsf{F} \partial \mathsf{F}} : \mathsf{H} = \mathsf{H} : \frac{\partial \mathcal{W}(\mathsf{F}\mathsf{F}_\mathsf{a}^{-1})}{\partial \mathsf{F} \partial \mathsf{F}} : \mathsf{H} = \mathsf{H}\mathsf{F}_\mathsf{a}^{-1} : \frac{\partial \mathcal{W}}{\partial \mathsf{F}_\mathsf{e} \partial \mathsf{F}_\mathsf{e}} : \mathsf{H}\mathsf{F}_\mathsf{a}^{-1} > 0.$$

Rank–one convexity is granted by the properties of $\mathcal{W}$; in fact if H is a rank–one tensor, also $\mathsf{H}\mathsf{F}_\mathsf{a}^{-1}$ is a rank–one tensor.

For a frame invariant strain–energy, here the principle of material indifference for change in observer is abided if the gradient of deformation in its factorial representation transforms correctly:

$$\mathsf{F}^* = \mathsf{Q}\mathsf{F} \quad \Rightarrow \quad \mathsf{F}_\mathsf{e}^* \mathsf{F}_\mathsf{a}^* = \mathsf{Q}\mathsf{F}_\mathsf{e}\mathsf{F}_\mathsf{a},$$

for any rotation Q. The simplest way to obey this prescription is to choose F_a invariant: $\mathsf{F}_\mathsf{a}^* = \mathsf{F}_\mathsf{a}$. It follows that

$$\mathsf{F}_\mathsf{e}^* = \mathsf{F}^*(\mathsf{F}_\mathsf{a}^*)^{-1} = \mathsf{Q}\mathsf{F}(\mathsf{F}_\mathsf{a})^{-1} = \mathsf{Q}\mathsf{F}_\mathsf{e}.$$

The Cauchy stress is,

$$\mathsf{T} = \mathsf{P}\mathsf{F}^\mathsf{T} = \frac{\partial \mathcal{W}}{\partial \mathsf{F}} \mathsf{F}^\mathsf{T} = (\det \mathsf{F}_\mathsf{a})\, \mathcal{W}'\, \mathsf{F}_\mathsf{a}^{-\mathsf{T}} \mathsf{F}^\mathsf{T} \tag{2.26}$$

where $\mathcal{W}'$ denotes differentiation of $\mathcal{W}$ with respect to its argument.

Since, in general, there are no apparent passive and active stress herein, it is not immediate to argue the physiological admissibility of the model in terms of "Cauchy stress growing with strain", along the same lines exposed in the previous sections. However specific constitutive forms allow to outline an analogy.

A frame invariant constitutive equation for the active strain F_a that naturally accounts for the contraction of the fibres is

$$\mathsf{F}_\mathsf{a} = \gamma\, \mathbf{f}_\circ \otimes \mathbf{f}_\circ + \gamma^{-1/2}\, (\mathsf{I} - \mathbf{f}_\circ \otimes \mathbf{f}_\circ). \tag{2.27}$$

where γ is a positive constant, $0 < \gamma < 1$.

The inverse of F_a can be explicitly calculated: introduce $\mathbf{e}_1 = (1, 0, 0)^\mathsf{T}$ and let Q be the rotation such that $\mathsf{Q}\mathbf{e}_1 = \mathbf{f}_\circ$. The following identity holds:

$$\begin{aligned} \mathsf{F}_\mathsf{a}^{-1} = \gamma\, \mathbf{f}_\circ \otimes \mathbf{f}_\circ + \gamma^{-1/2}\, (\mathsf{I} - \mathbf{f}_\circ \otimes \mathbf{f}_\circ) &= \Big(\gamma\, \mathsf{Q}\mathbf{e}_1 \otimes \mathsf{Q}\mathbf{e}_1 + \gamma^{-1/2}\, (\mathsf{Q}\mathsf{Q}^\mathsf{T} - \mathsf{Q}\mathbf{e}_1 \otimes \mathsf{Q}\mathbf{e}_1)\Big)^{-1} \\ &= \mathsf{Q}\Big(\gamma\, \mathbf{e}_1 \otimes \mathbf{e}_1 + \gamma^{-1/2}\, (\mathsf{I} - \mathbf{e}_1 \otimes \mathbf{e}_1)\Big)^{-1} \mathsf{Q}^\mathsf{T} = \gamma^{-1}\, \mathbf{f}_\circ \otimes \mathbf{f}_\circ + \gamma^{1/2}\, (\mathsf{I} - \mathbf{f}_\circ \otimes \mathbf{f}_\circ). \end{aligned}$$

Let us suppose that the strain energy of the inert material be neo–Hookean isotropic, as follows:

$$\mathcal{W}(\mathsf{F}_\mathsf{e}) = \frac{\mu}{2}\, \mathsf{F}_\mathsf{e} : \mathsf{F}_\mathsf{e}.$$

According to (2.26), the corresponding Cauchy (total) stress is[1]:

$$\begin{aligned}\mathsf{T} &= \mu\,\mathsf{F_e}\mathsf{F_a}^{-\mathsf{T}}\mathsf{F}^{\mathsf{T}} = \mu\,\mathsf{F}\mathsf{F_a}^{-1}\mathsf{F_a}^{-\mathsf{T}}\mathsf{F}^{\mathsf{T}} = \mu\,\mathsf{F}\Big(\gamma^{-2}\mathbf{f}_\circ\otimes\mathbf{f}_\circ + \gamma\,(\mathsf{I}-\mathbf{f}_\circ\otimes\mathbf{f}_\circ)\Big)\mathsf{F}^{\mathsf{T}} \\ &= \mu\gamma\,\mathsf{B} + \mu\frac{1-\gamma^3}{\gamma^2}\,\mathsf{F}\mathbf{f}_\circ\otimes\mathsf{F}\mathbf{f}_\circ.\end{aligned} \tag{2.28}$$

The polynomial strain energy allows here to recover an interpretation of the active strain in terms of active stress. We devise in (2.28) a standard passive Cauchy stress plus an extra one: all the terms depending on γ can be understood as active dynamic contribution. The same comment would not apply for a non–polynomial energy and, as a matter of fact, exponential strain energies are common in biomechanics. Notice that all the active contributions (2.28) are quadratic in the deformation, a direct consequence of the quadratic form of the neo–Hookean Cauchy stress.

2.3 Numerical approximation

2.3.1 Implementation aspects

Given an hyperelastic law $\mathcal{W}(\mathsf{F})$ for the passive behaviour of the material, the variational formulation for the active strain model is formally obtained substituting F with $\mathsf{F_e}$: this can be understood as a rescaling of the strain metrics. For instance, the Cauchy–Green tensors of $\mathsf{F_e}$ are

$$\mathsf{B_e} = \mathsf{F_e}\mathsf{F_e}^{\mathsf{T}} = \mathsf{F}\mathsf{F_a}^{-1}\mathsf{F_a}^{-\mathsf{T}}\mathsf{F}^{\mathsf{T}}, \qquad \mathsf{C_e} = \mathsf{F_e}^{\mathsf{T}}\mathsf{F_e} = \mathsf{F_a}^{-\mathsf{T}}\mathsf{F}^{\mathsf{T}}\mathsf{F}\mathsf{F_a}^{-1}.$$

If we consider an explicit form for $\mathsf{F_a}$ such as equation (2.27), the above expressions take a more precise physical meaning:

$$\begin{aligned}\mathsf{B_e} &= \gamma\mathsf{B} + \frac{1-\gamma^3}{\gamma^2}\,\mathsf{F}\mathbf{f}_\circ\otimes\mathsf{F}\mathbf{f}_\circ, \\ \mathsf{C_e} &= \gamma\mathsf{C} + (\gamma^{-2} - 2\gamma^{-1/2} + \gamma)\mathcal{I}_{4,\mathbf{f}_\circ}\,\mathbf{f}_\circ\otimes\mathbf{f}_\circ + 2(\gamma^{-1/2} - \gamma)\mathsf{F}\mathbf{f}_\circ\otimes\mathsf{F}\mathbf{f}_\circ.\end{aligned}$$

From these it is straightforward to compute the invariants and all the necessary quantities to build the residual and the tangent matrix of the Newton problem of section 1.2.3.

The convergence of the Newton scheme can be compromised if the initial guess is not carefully selected. As explained in section 1.2.6, a simple strategy to address this issue is to solve the problem for incremental steps of γ: given γ_k and the corresponding solution $\boldsymbol{\varphi}_k$, the idea is to solve for $\gamma_k + \delta$ starting from $\boldsymbol{\varphi}_k$. If there is no convergence, then one can reduce δ and start again. On the other hand, if the convergence is obtained in few iterations, δ could be increased in order to reduce the total computational time.

2.3.2 Basic experiments

As already done for passive mechanics (see section 1.3), we consider an unit cube $[-0.5, 0.5]^3$ as a reference configuration, and we select fibres and sheets as follows:

$$\mathbf{f}_\circ = \cos\alpha(Z)\,\mathbf{e}_1 + \sin\alpha(Z)\,\mathbf{e}_2, \qquad \mathbf{s}_\circ = \mathbf{e}_3,$$

---

[1] A neo–Hookean hyperelastic material is incompressible and the Lagrange multiplier corresponding to such a constrain should appear in the Cauchy stress (2.28). However, we are here interested in investigating the rank–one ellipticity of the stress tensor, the pressure does not perform any work because $-p\mathsf{F}^{\mathsf{T}} : \mathsf{H} = 0$ and we omit such a term for the sake of simplicity. The same argument applies for possible incompressible materials of the previous sections.

where the angle $\alpha(Z)$ depends linearly on the depth Z:

$$\alpha(Z) = \alpha_0 \left(\tfrac{1}{2} - Z\right) + \alpha_1 \left(\tfrac{1}{2} + Z\right), \tag{2.29}$$

for given angles α_0, $\alpha_1 \in [-\frac{\pi}{2}, \frac{\pi}{2})$.

Concerning the material parameters, the boundary conditions, and the specific form of the strain–energy density function, we refer to chapter 1: in the forthcoming sections we repeat some of the tests performed in the passive mechanics context, introducing the active behaviour.

We consider the following active deformation:

$$\mathsf{F_a} = \gamma \mathbf{f}_\circ \otimes \mathbf{f}_\circ + \frac{1}{\sqrt{\gamma}}(\mathsf{I} - \mathbf{f}_\circ \otimes \mathbf{f}_\circ), \tag{2.30}$$

which corresponds to a shortening of a factor $\gamma \in (0, 1]$ in the fibre direction $\mathbf{f}_\circ$. In order to have an isochoric deformation, such that $\det \mathsf{F_a} = 1$, we consider also a cross–fibre elongation of magnitude $\frac{1}{\sqrt{\gamma}}$.

Concerning numerical aspects, we start from $\gamma = 1.0$ and we decrease it of an initial decrement equal to 0.01, which is then adapted if the number of Newton iterations is low.

Constant microstructure

The first test is the active deformation of a traction–free elastic cube with homogeneous microstructure, hence $\alpha_0 = \alpha_1$. The distortion $\mathsf{F_a}$ is compatible, i.e. there exists a deformation $\boldsymbol{\varphi}$ such that $\textsc{Grad}\,\boldsymbol{\varphi} = \mathsf{F_a}$, thus $\mathsf{F_e} = \mathsf{I}$ and the actual configuration is stress–free: the numerical test is passed if the computed stress is zero.

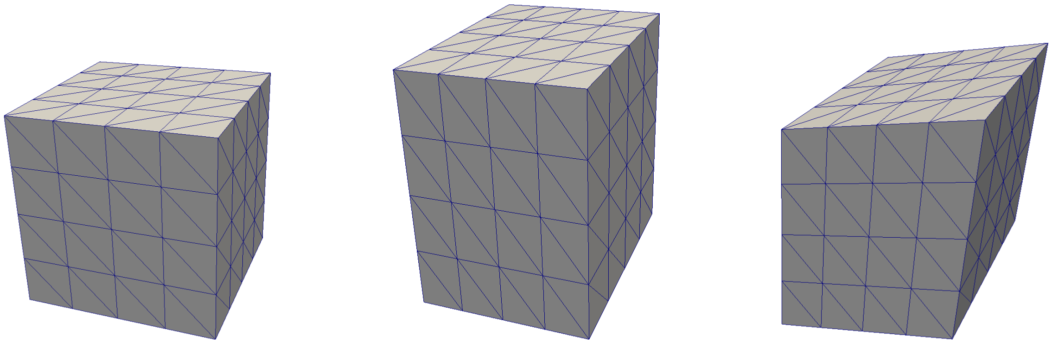

(a) Initial geometry. **(b)** $\alpha = 0°$. **(c)** $\alpha = +30°$.

Figure 2.5 Activation of a cube with constant fibre direction, with $\gamma = 0.8$, traction–free boundary conditions and material parameters from Wang et al. (2013).

Figure 2.5 shows the result of two simulation with different orientation of the fibres. Both deformed configurations are stress–free, hence they are only dictated by $\mathsf{F_a}$. With $\gamma = 0.8$, which corresponds to a shortening of 20%, and $\alpha = 0°$, invariants take the following values

$$\mathcal{I}_1 = 2\gamma^{-1} + \gamma^2 = 3.14, \qquad \mathcal{I}_{4,\mathbf{f}_\circ} = \gamma^2 = 0.64, \qquad \mathcal{I}_{4,\mathbf{s}_\circ} = \gamma^{-1} = 1.25, \qquad \mathcal{I}_{8,\mathbf{f}_\circ\mathbf{s}_\circ} = 0.$$

We infer that fibres and sheets remain orthogonal, and the cube is stretched of about 12% in direction orthogonal to $\mathbf{f}_\circ$. The case $\alpha = 30°$ is analogous, but with a shear of about $-9°$.

If the top and the bottom faces are fixed in their vertical component of the displacement, the deformation is not stress–free any more, but it can explicitly calculated. Indeed, we look for a scalar λ such that (we make use of the coordinates $\{\mathbf{f}_\circ, \mathbf{s}_\circ, \mathbf{n}_\circ\}$):

$$\mathsf{F}_\mathsf{e} = \begin{bmatrix} \frac{\lambda}{\gamma} & & \\ & \frac{\sqrt{\gamma}}{\lambda} & \\ & & \sqrt{\gamma} \end{bmatrix} = \begin{bmatrix} \lambda & & \\ & \frac{1}{\lambda} & \\ & & 1 \end{bmatrix} \begin{bmatrix} \frac{1}{\gamma} & & \\ & \sqrt{\gamma} & \\ & & \sqrt{\gamma} \end{bmatrix} = \mathsf{F}\mathsf{F}_\mathsf{a}^{-1}.$$

Invariants associated to F_e are:

$$\mathcal{I}_1^\mathsf{e} = \frac{\lambda^2}{\gamma^2} + \frac{\gamma}{\lambda^2} + \gamma, \qquad \mathcal{I}_{4,\mathbf{f}_\circ}^\mathsf{e} = \frac{\lambda^2}{\gamma^2}, \qquad \mathcal{I}_{4,\mathbf{s}_\circ}^\mathsf{e} = \frac{\gamma}{\lambda}, \qquad \mathcal{I}_{8,\mathbf{f}_\circ\mathbf{s}_\circ}^\mathsf{e} = 0,$$

which can be substituted into the Holzapfel–Odgen hyperelastic model $\mathcal{W}$. This function, for different values of γ, is sketched in figure 2.6.

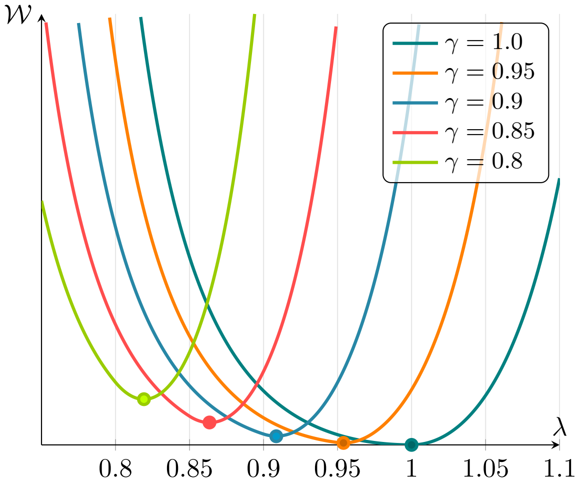

Figure 2.6 Strain–energy of active cube with constant fibre direction and fixed z–component.

For instance, if $\gamma = 0.8$, then $\lambda \approx 0.82$, which corresponds to a slightly lower strain: pictorially, we could imagine that γ is the microstructurally dictated shortening, while λ is the actual one. Since the geometrical constraint, here represented by the boundary condition, forbids the expected deformation $\mathsf{F}_\mathsf{a}^{-1}$, the actual deformation minimises the strain–energy with respect to the metric $\mathsf{F}_\mathsf{a}^\mathsf{T}\mathsf{F}_\mathsf{a}$.

Variable microstructure

The second set of tests consists in the active deformation of a traction–free elastic cube with variable fibre direction, accordingly to the law in equation (2.29). The gross deformation is that every slice of the cube with a fixed fibre angle undergoes a shear deformation depending on the fibre direction; since the variation of the angle is smooth, also the shear varies smoothly across the slices. On the other hand, it is not possible in general to glue together of these slices without a further elastic deformation: this translates into a residual–stress. Figure 2.7 shows the final deformation for different values of γ (no shortening, 10% and 20%).

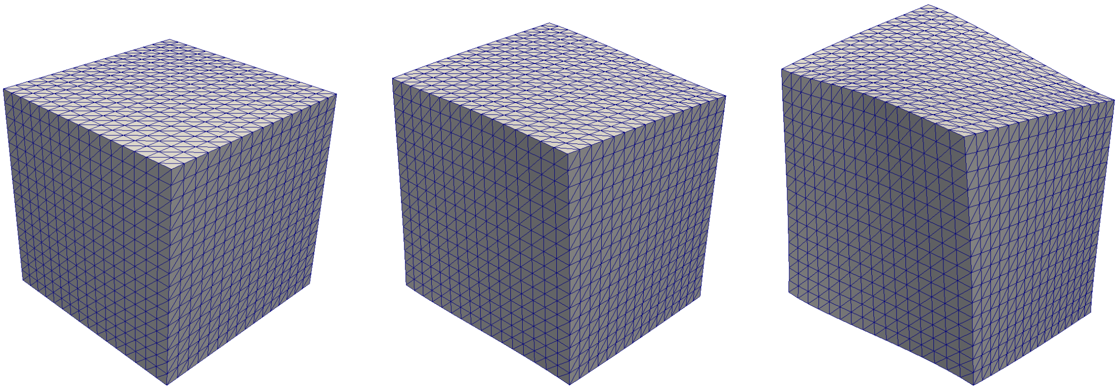

(a) $\gamma = 1.0$. **(b)** $\gamma = 0.9$. **(c)** $\gamma = 0.8$.

Figure 2.7 Activation of a cube with variable fibre direction (±60°), with traction–free boundary conditions and material parameters from Wang et al. (2013).

- The convergence analysis (top panel of figure 2.8), is very similar to the one obtained for the passively compressed cube of chapter 1. With $N = 4$ subdivisions of the side of the cube we have convergence of the displacement and the torsion, and a reasonable approximation of the stress, expect for $\mathcal{I}_{8,\mathbf{f}_\circ\mathbf{s}_\circ}$.

- The invariants, and so the stresses, are particularly steep close to the boundary: we already observed this phenomenon in the previous chapter, and it might be related to a projection error. Indeed, if the displacement if a continuous finite element function of degree r, then the deformation gradient (and so the invariants and the stress) is discontinuous finite element function of degree $r - 1$ (cell–wise constant if $r = 1$). In order to have a continuous representation of it, a L^2–projection is exploited, but this can lead to spurious oscillations around the jumps. More sophisticate procedures are available (Zienkiewicz et al., 2005), for instance a weighted–average recovery at the vertices (not adopted here).

- The residual–stress in very small: the order of magnitude of its highest component is 10^{-2} N/cm^2. This suggests that the final configuration is only slightly incompatible, hence $\mathsf{F} \approx \mathsf{F}_\mathsf{a}^{-1}$. While fibre and isotropic stresses would suggest that the incompatibility is only due to numerical error (except for the boundaries, see above), it is clear that the stress along $\mathbf{s}_\circ$ converges towards a non–zero asymptotic value, although very small. This fact is also supported by the bottom panel of figure 2.8, where the greater the angle span, the greater the residual stress in the sheet direction.

- The thickness of the deformed cube, which is measured in the direction of the sheets, is not sensible to any of the tested variations of figures 2.8 and 2.9. Since fibres and sheets remain orthogonal during the activation process, the invariant $\mathcal{I}_{4,\mathbf{s}_\circ}$ simply compensates the cross–area variation due to the fibres contraction, which is proportional to γ^{-1}, whether the fibre distribution.

- In contrast with the results of section 1.3.3, here the contribution to the strain–energy provided by the elongation of the sheets $\mathcal{W}_{4,\mathbf{s}_\circ}$, is not null since $\mathcal{I}^\mathsf{e}_{4,\mathbf{s}_\circ} > 1$. This can be deduced also from the bottom panel of figure 2.9: when $\mathcal{W}_{4,\mathbf{s}_\circ}$ is removed from the strain–energy, several components of the strain take totally different values. On the other hand, the influence of the eighth–invariant $\mathcal{I}_{8,\mathbf{f}_\circ\mathbf{s}_\circ}$ is on minor relevance.

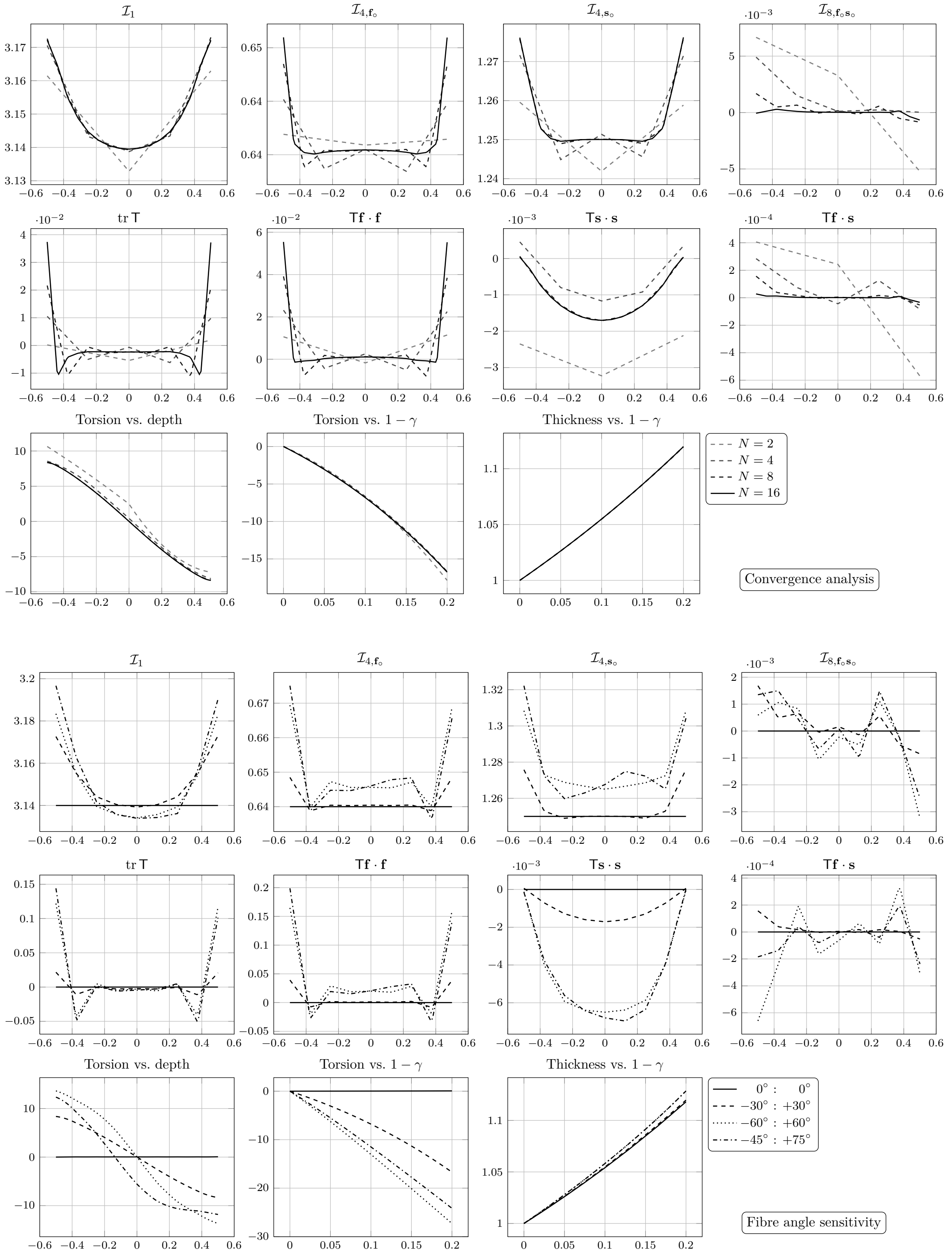

Figure 2.8 Convergence analysis and fibre angle sensitivity of the activated cube with variable fibre structure. Material parameters from Wang et al. (2013). Stress are in N/cm^2.

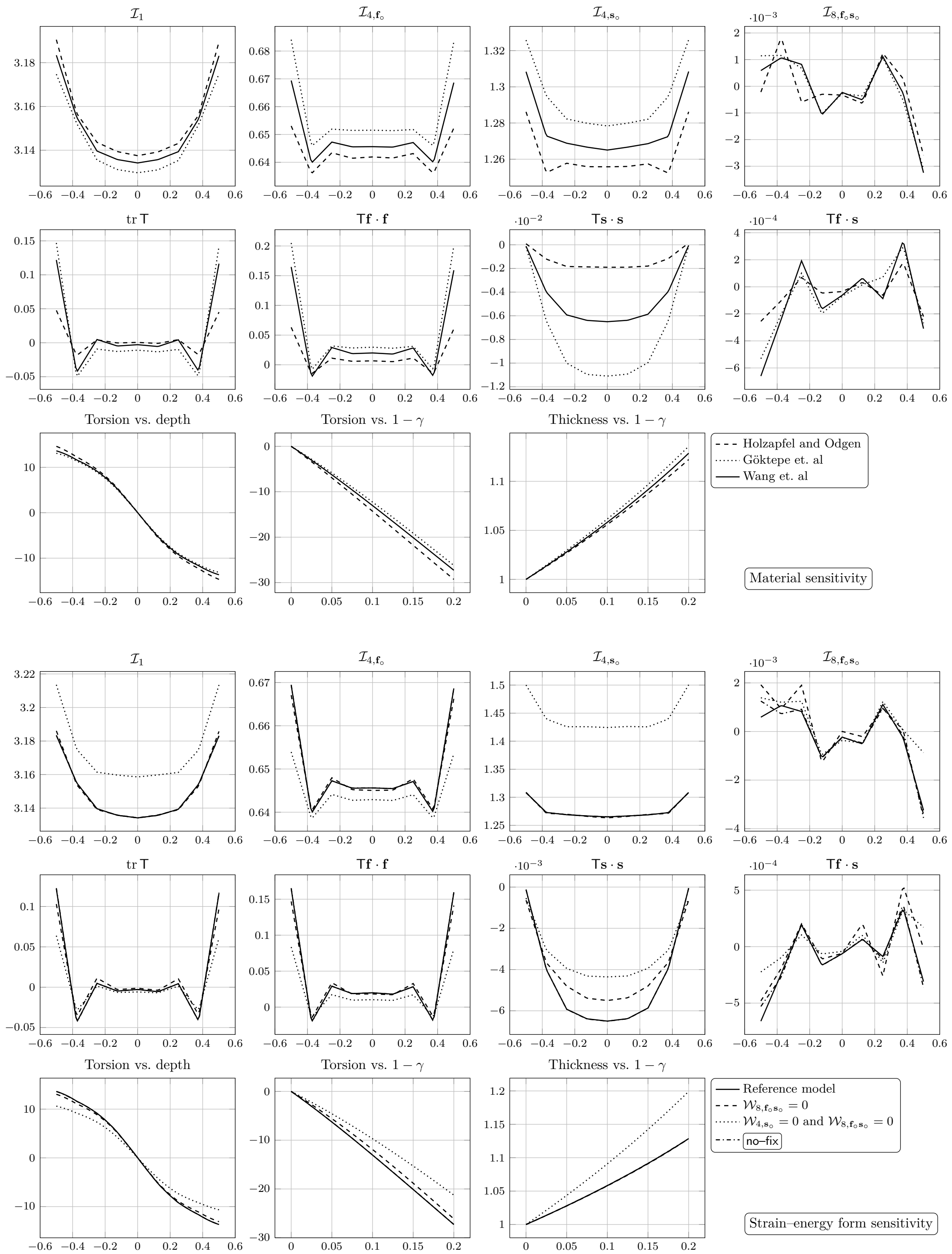

Figure 2.9 Material parameters and strain–energy form sensitivity of the active cube with variable fibre structure. Stress are in N/cm^2.

- The convergence of the Newton scheme is strongly affected by several aspect of the simulation: with the Holzapfel–Ogden material parameters set, the increment must be reduced by an order of magnitude, increasing by ten the total number of steps (146 instead of 20 for the Wang et al. material). This is due to the strong difference in the isotropic shear modulus, take makes the material is particularly soft in the fibre direction, since these are under compression ($\mathcal{I}^{\mathsf{e}}_{4,\mathbf{f}_\circ} < 1$) and therefore $\mathcal{W}_{4,\mathbf{f}_\circ} = 0$.

  Concerning the Newton sub–iterations, we found that the $\boxed{\mathsf{fix}}$ strategy, which consider fibre– and sheet–specific strain–energy terms deactivated in contractile regime, has a negative impact on the convergence rate. This is also pointed out by the number of iterations, always from 6 to 10. Since the second derivative of the strain–energy function is not continuous at $\mathsf{F} = \mathsf{I}$, the quadratic convergence of the Newton solver could be compromised, especially when the elastic deformation $\mathsf{F_e}$ is close to the identity, such as this case. This can be partially addressed by means of a mollifier, smoothing down the discontinuity.

2.4 Muscular Thin Films

2.4.1 Introduction

In the previous sections we showed the performance of the active strain approach from a mathematical and a numerical viewpoint. While the theoretical and numerical results are quite convincing, it remains to prescribe a rationale to fix the parameter γ, that dictates the contraction. As already observed, this parameter can be understood as a target shortening of the fibres, because when the deformation is stress–free, they exactly take that value. However, we cannot consider γ as an universal value that can be used without changing it case by case. In fact, the cell is a living being, so it modifies its properties depending on the surrounding environment; for instance, it is becoming evident that cells are able to sense, to some extent, the mechanical stress they bear (Ambrosi and Guana, 2007; Taber, 2008).

Recently, Feinberg et al. (2007), were able to build micro–actuators with myocytes, providing experimental data that perfectly fit for our purpose, to evaluate γ in a controlled system with a collective dynamics of cells. These actuators, called muscular thin films (MTFs), are a combination of a polydimethylsiloxane substrate (PDMS) and rat ventricular cardiomyocytes, cultured on top of the former. The seeding face of the substrate can be engineered in order to have high/low nutrients density strips, aligned in a particular direction. During the maturation, this external matrix induces a strong anisotropy in the tissue (cfr. figure 2.10).

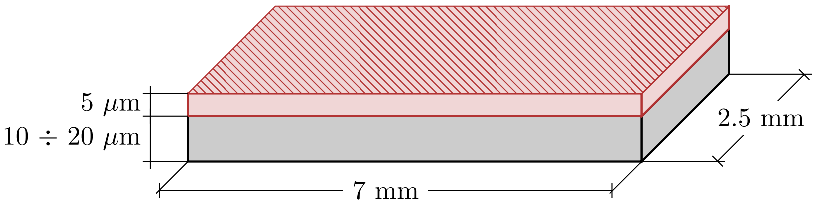

Figure 2.10 Sketch of a Muscular Thin Film (MTF).

The substrate is a thin sample of elastic material, and its mechanical properties are known with high accuracy (Shim et al., 2012). After the maturation, the myocytes are able to produce a visible (and easily measurable) bending of the substrate during the contraction (systole), thanks to the active force exerted by the cells. The maximum observed curvature is therefore a function of few physical parameters. In our active strain hyperelastic framework the only unknown of the system is the contractility γ, which can therefore be evaluated by solution of an inverse problem.

Aim of this section is to find a physiological range for γ. The main difference from an isotonic or isometric test on a single myocyte is that here the distinction between "passive" and "active" is clear, since only the tissue is activated while bearing the stiffness of the purely passive substrate. Moreover, the geometry of the MTF is very simple, and its fibres are uniformly distributed in the tissue.

2.4.2 A specific model

Define the active strain tensor as follows:

$$\mathsf{F}_{\mathsf{a}}(\mathbf{X},t) = \begin{cases} \mathsf{I}, & \text{for } \mathbf{X} \in \text{substrate}, \\ \gamma(t)\mathbf{f}_\circ \otimes \mathbf{f}_\circ + \frac{1}{\sqrt{\gamma(t)}}(\mathsf{I} - \mathbf{f}_\circ \otimes \mathbf{f}_\circ), & \text{for } \mathbf{X} \in \text{tissue}. \end{cases} \tag{2.31}$$

Here $\gamma\colon [0,T] \to (0,1]$ dictates the contraction of the muscle fibres, directed along the longitudinal direction, depending on time. The specific functional form of γ on t is irrelevant, because we neglect any viscous effect of the elastic problem and the surrounding environment. In our case, we simply consider a linear function of the time, with a maximum value for $t = 1$ equal to γ_{max}. Another choice, that tries to mimic the dynamic observed during the experiments, reads as follows

$$\gamma(t) = \gamma_{\mathsf{max}}\, t\, e^{-\frac{1}{2}t^2}.$$

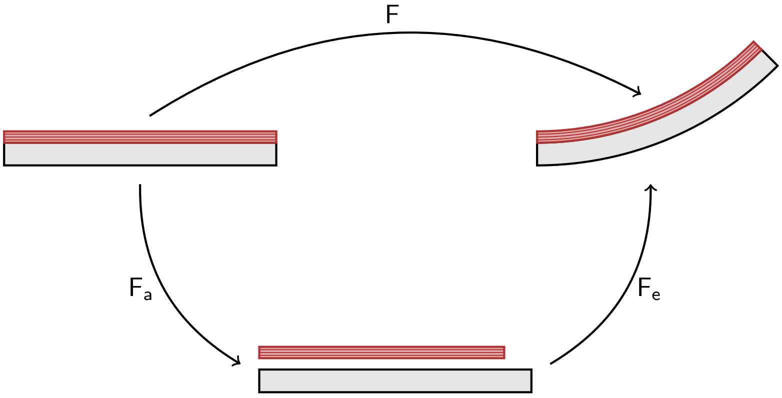

Figure 2.11 Bending of a MTF by means of a strain decomposition.

A sketch of the expected deformation according to our framework is presented in figure 2.11. The activation F_{a} of (2.31) is a shortening of the tissue while keeping the substrate unchanged; the intermediate configuration cannot be compatible, since it is not possible to glue the tissue and the substrate together without an elastic deformation. The latter is then provided by F_{e}.

The strain–energy density function is the sum of two contributions, one for the tissue, the other for the substrate

$$\mathcal{W}(\mathsf{F}_{\mathsf{e}}) = \mathcal{W}_{\mathsf{substrate}}(\mathsf{F}_{\mathsf{e}}) + \mathcal{W}_{\mathsf{tissue}}(\mathsf{F}_{\mathsf{e}}).$$

More specifically, we assume that both the addends are a quasi–incompressible neo–Hookean strain–energy, but with different shear and bulk moduli. The passive behaviour of the fibres is neglected here, since

1. the contribution to the energy of $\mathcal{W}_{\mathsf{tissue}}$ is very small when compared to $\mathcal{W}_{\mathsf{substrate}}$, because the substrate is considerably stiffer, and
2. fibres are under compression, so they would actually be deactivated.

Resuming, we have (for the nomenclature we refer to chapter 1):

$$\mathcal{W}(\mathsf{F}) = \frac{\mu}{2}(\mathcal{I}_1^{\mathsf{iso}} - 3) + \frac{\kappa}{4}(J^2 - 1 - 2\ln J), \qquad \begin{array}{ll} \mu_{\mathsf{tissue}} = 30 \text{ kPa}, & \mu_{\mathsf{substrate}} = 1.5 \text{ MPa}, \\ \kappa_{\mathsf{tissue}} = 3 \text{ MPa}, & \kappa_{\mathsf{substrate}} = 1.5 \text{ GPa}. \end{array}$$

The most significant value is the shear modulus of the substrate, which is directly related to the curvature: the higher $\mu_{\mathsf{substrate}}$, the lower the curvature of the MTF.

Stoney's formula Before proceeding with the numerical analysis of the model, a valuable understanding on the functional dependence of the curvature on the parameters, comes from the Stoney's formula (Stoney, 1909), which provides the relationship between stress σ_{t} and curvature ζ for a thin film deposited on an elastic substrate, in the context of small deformations

$$\sigma_{\mathsf{t}} = \frac{E_{\mathsf{s}} h_{\mathsf{s}}^2}{6 h_{\mathsf{f}} (1 - \nu_{\mathsf{s}})} \zeta,$$

where h is the thickness and the pedix $\cdot_{\mathsf{s}}$ refers to the substrate. The formula applies under strict hypothesis, in particular that $h_{\mathsf{s}} \gg h_{\mathsf{t}}$.

The material parameters E and ν can be easily computed from the shear and the bulk moduli:

$$E = \frac{9\kappa\mu}{3\kappa + \mu}, \qquad \nu = \frac{3\kappa - 2\mu}{2(3\kappa + \mu)}.$$

For infinitesimal strains, the multiplicative decomposition of the deformation gradient rewrites an additive splitting of the strain ε:

$$\varepsilon = \varepsilon_{\mathsf{e}} + \varepsilon_{\mathsf{a}}.$$

Substituting, we obtain the following formula:

$$\zeta = 6 \, \frac{1 - \nu_{\mathsf{s}}}{1 - \nu_{\mathsf{t}}} \frac{E_{\mathsf{t}}}{E_{\mathsf{s}}} \frac{h_{\mathsf{t}}}{h_{\mathsf{s}}^2} \, \gamma.$$

The Poisson's ratios are both close to $\frac{1}{2}$, while $E_{\mathsf{s}} \approx 3\mu = 4.5$ MPa and $E_{\mathsf{t}} \approx 90$ kPa.

2.4.3 Results

The numerical approximation of the bending problem introduces various difficulties to be addressed:

- large aspect–ratio of geometry;
- quasi–incompressibility of the materials;
- very different passive properties between the substrate and the tissue;
- discontinuous tangential stress across the interface.

An optimal solution might be a "segregated strategy", where the problem is iteratively solved: at each iteration, both the materials are separated and solved independently, then the interface condition (continuity of the displacement and the normal stress) is enforced by means of suitable exchange of the boundary conditions (a domain decomposition method with no overlap). In our case, we adopt a simple "monolithic" strategy, where the elastic problems are solved simultaneously.

It is well known that for a bending problem the mesh needs to be very refined in the longitudinal direction; since this dimension is hundreds of times the thickness, we tested different meshes in order to understand which aspect ratio keeps a good accuracy of solution. With quadratic finite element, we found that $128 \div 512$ subdivisions of the longitudinal direction and $8 \div 16$ along the thickness is fine enough to achieve convergence to a mesh–independent solution.

Concerning the boundary conditions, we fix the displacement to zero at the bottom line of left face, and we apply symmetry condition to the left and the back face, i.e. no displacement in the orthogonal direction.

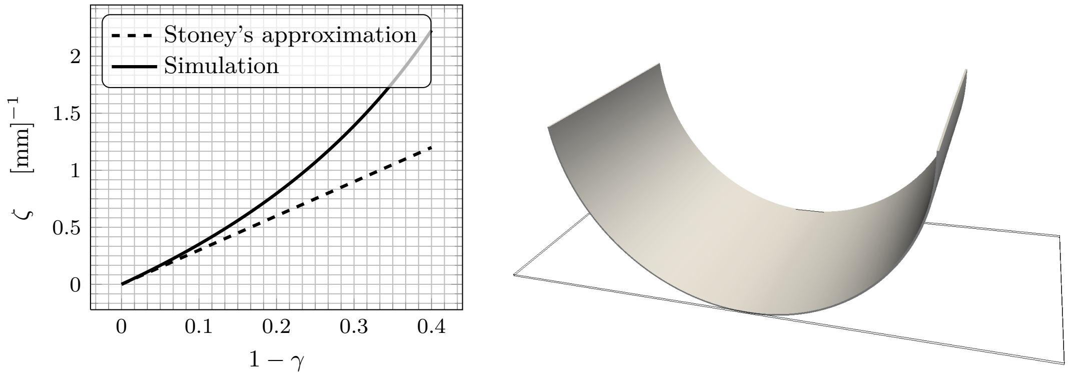

(a) Curvature vs. activation. **(b)** Solution at $\gamma = 0.8$.

Figure 2.12 Simulation of a MTF with thickness of substrate of 18.0 μm.

						Avg.
ζ	0.207	0.227	0.244	0.284	0.324	0.257
γ	0.882	0.910	0.872	0.845	0.872	0.876

Table 2.1 Data from the experiments performed by Shim et al. (2012), with substrate thickness of 14.5 μm and the corresponding fitted values of γ for the activation.

Figure 2.12b shows the final deformation for a 20% shortening of the myocytes; moreover, on the left panel we plot the curvature of the MTF[2] versus activation: for small deformation there is a good accordance with the Stoney's equation, while for large displacements the thin film bends more than its linear counterpart.

Experimental data, taken from Shim et al. (2012), can be found in Table 2.1. The authors perform several experiment, for different thickness of the substrate, and they measure the curvature. Here we match the curvature with the corresponding activation γ, which ranges between about 0.85 to 0.9, with an average of 0.876. This would suggest a physiological shortening range

---

[2] The curvature is computed taking the inverse of the radius of the circle passing through three points at $x = 0$, $x = \frac{L}{2}$ and $x = L$.

of about 10% to 15%, which is compatible to the experiments on isolated myocytes, or just a slightly lower than expected. However, in this context the fibres are not pre–stretched, so it is reasonable to conjecture that the working range of γ in the beating heart is higher (see discussion of section 2.1.2).

2.5 Active contraction of an idealised ventricle

2.5.1 Free contraction

In this section we perform the same simulations illustrated in section 2.3.2 on the idealised ventricle. The geometry is unloaded, so no inner pressure is applied, and we consider an homogeneous contraction of the fibres until a maximum shortening of 10%.

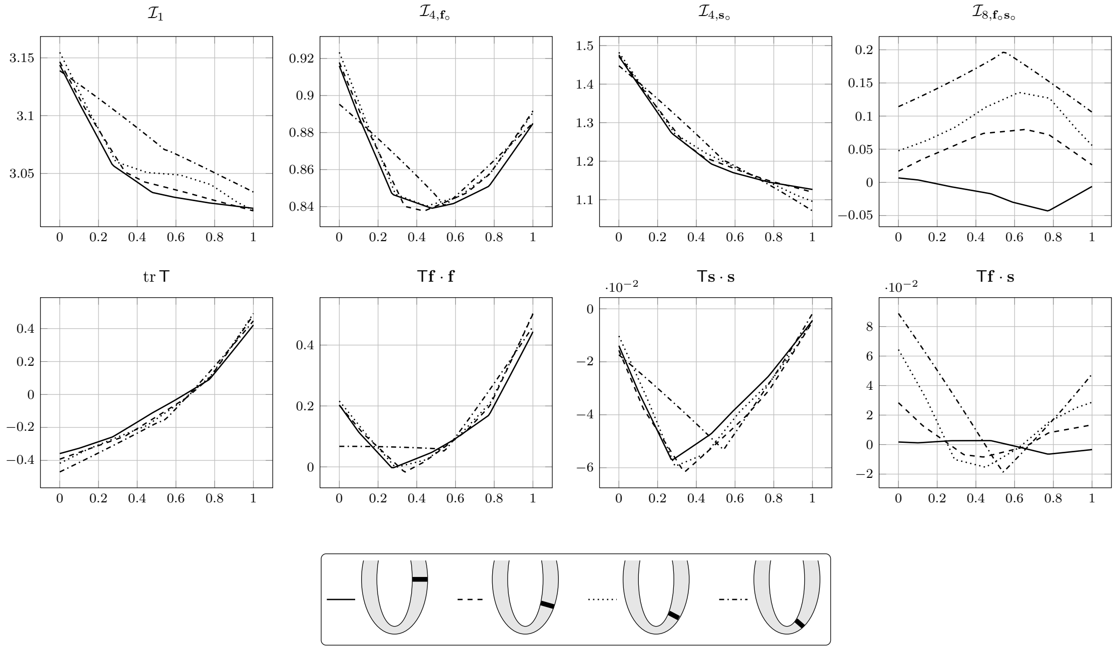

Figure 2.13 Transmural variation of the invariants and stress components for free contraction of the canine geometry. Sections are indicated by the legend, and the abscissa indicates the wall depth. Stresses, measured in N/cm^2, are plotted for $\gamma = 0.9$.

Figure 2.13 provides a snapshot of the mechanical status of the ventricle at the end of the free contraction. The fibres are under compression, since $\mathcal{I}_{4,\mathbf{f}_\circ}$ is always less than the unit, and the shortening, which is exactly the square root of the invariant, ranges from 0.91 to 0.96, with the lower values attained at the mid–myocardium. These values should be compared to the distortion shortening $\gamma = 0.9$: the difference indicates the lack of compatibility of the deformation and so presence of a residual stress.

The sheets are under traction, within the innermost layer, the myocardium being elongated of about 20% while the outermost layer only of 5%. This suggests that the strain–energy term $\mathcal{W}_{4,\mathbf{s}_\circ}$ could play a prominent role during the systole, as opposite of the passive inflation test of the previous chapter, where sheets, when radially distributed, were always under compression and so deactivated. On the other hand, for these tests no inner pressure is applied, which would compress the sheets decreasing the value of $\mathcal{I}_{4,\mathbf{s}_\circ}$.

Finally, the eighth invariant $\mathcal{I}_{8,\mathbf{f}_\circ\mathbf{s}_\circ}$ is higher in the the apical region, indicating the presence of a longitudinal shear stress.

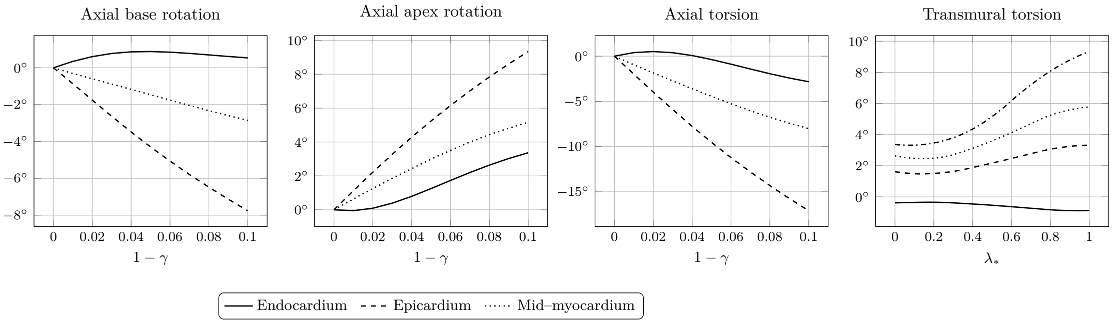

Figure 2.14 Torsion of the canine ventricle during the free contraction. The first three plots shows the axial rotation versus the activation. The last plot shows the transmural rotation for $\gamma = 0.9$ (for the legend refer to figure 2.13).

Concerning the torsion, figure 2.14 highlights a greater rotation of the epicardium with respect to the endocardium in the longitudinal direction: the shortening of the fibres is rather uniform, so the torsion can be explained by the fact that the external fibres have an higher lever arm then the internal ones. This behaviour is totally different from the one observed during the passive inflation (see figure 1.20), where the endocardium rotated much more than the epicardium. Moreover, in the present case, endocardium ($\lambda_* = 0$ of the last panel of figure 2.14) and epicardium ($\lambda_* = 1$) rotate in the same direction.

The volume decreases almost linearly with respect to $1-\gamma$, as showed for instance by figure 2.16. With an activation of 10%, the volume diminishes of about 8 ml, but we expect a reduction of the slope as soon as γ tends to zero, since the residual strain increases. This tendency can be better appreciated from figure 2.19.

Sensitivity analysis

As it has been done for the passive inflation of the ventricle in the previous chapter, we perform several benchmarks to evaluate the sensitivity of the free contraction on the parameters of the model.

Boundary conditions There is no significant difference in enforcing zero vertical displacement of the base with respect to the traction–free case (see figure 2.15), except for the final elongation of the ventricle during the twitch. However, this difference has a little effect on the final volume because the latter is practically dictated by the inner radius, which significantly lower than its reference state.

Fibres distribution The microstructure has a major role on the apparent deformation (cfr. figure 2.16), and this is expected since the activation occurs along the fibres. The most evident difference is in the longitudinal deformation, comparing fibres circumferentially (or almost circumferentially) distributed and a more physiological pattern. Indeed, in the former case there is a large reduction of the thickness of the wall, which yields to a large increase of

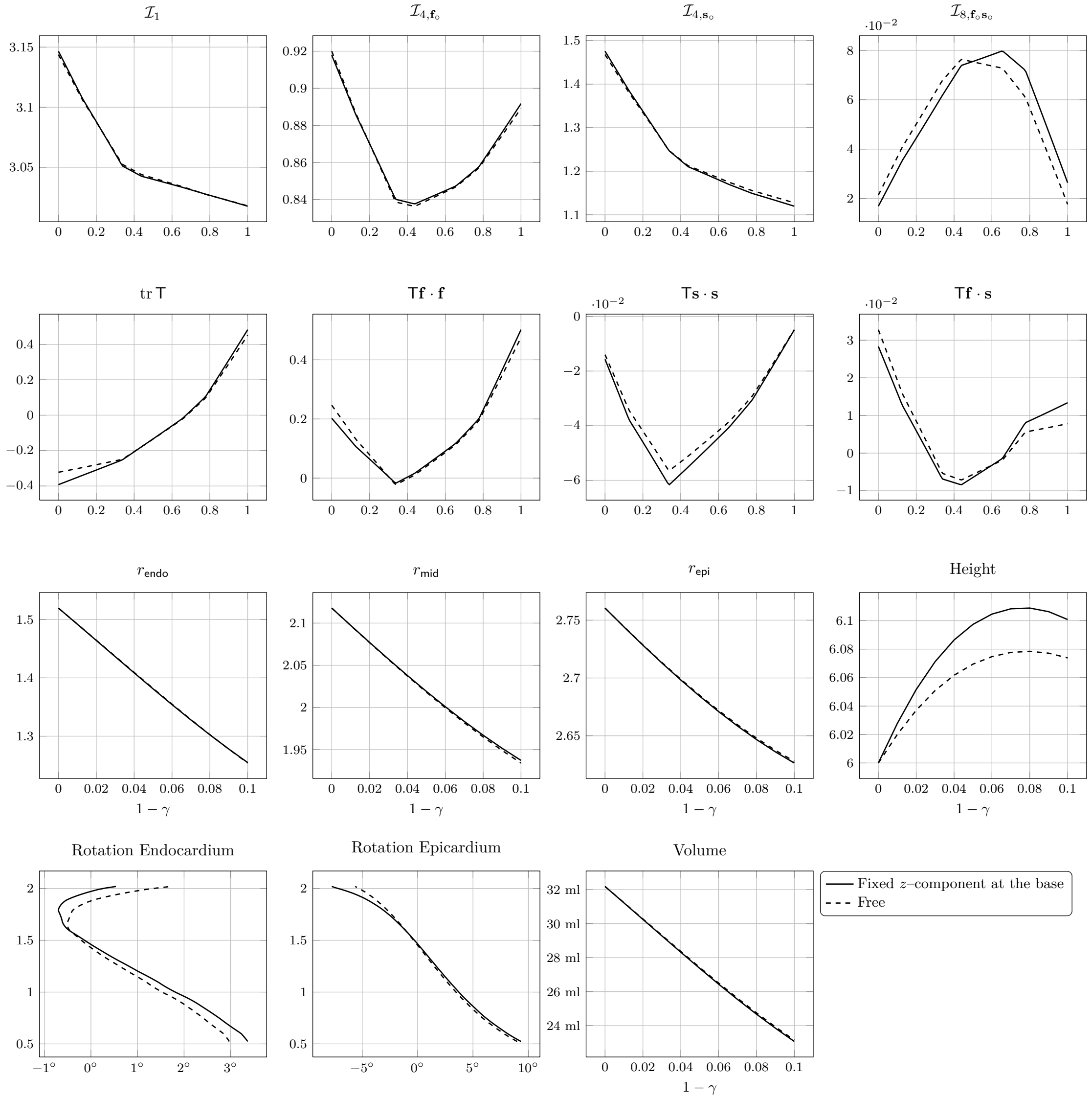

Figure 2.15 Effect of different boundary conditions at the ventricle base on the free contraction test of the canine geometry of the left ventricle. The first two rows show the invariants and the stresses (in $\mathrm{N/cm^2}$) vs. wall thickness λ_* at the height $\mu = \pi/3$ at $\gamma = 0.9$. The third row shows the radius at different wall depths for $\mu = \pi/2$ and the height (base–apex distance) vs. the activation. The last row illustrates the torsion vs. the longitudinal coordinate μ and the volume vs. the activation.

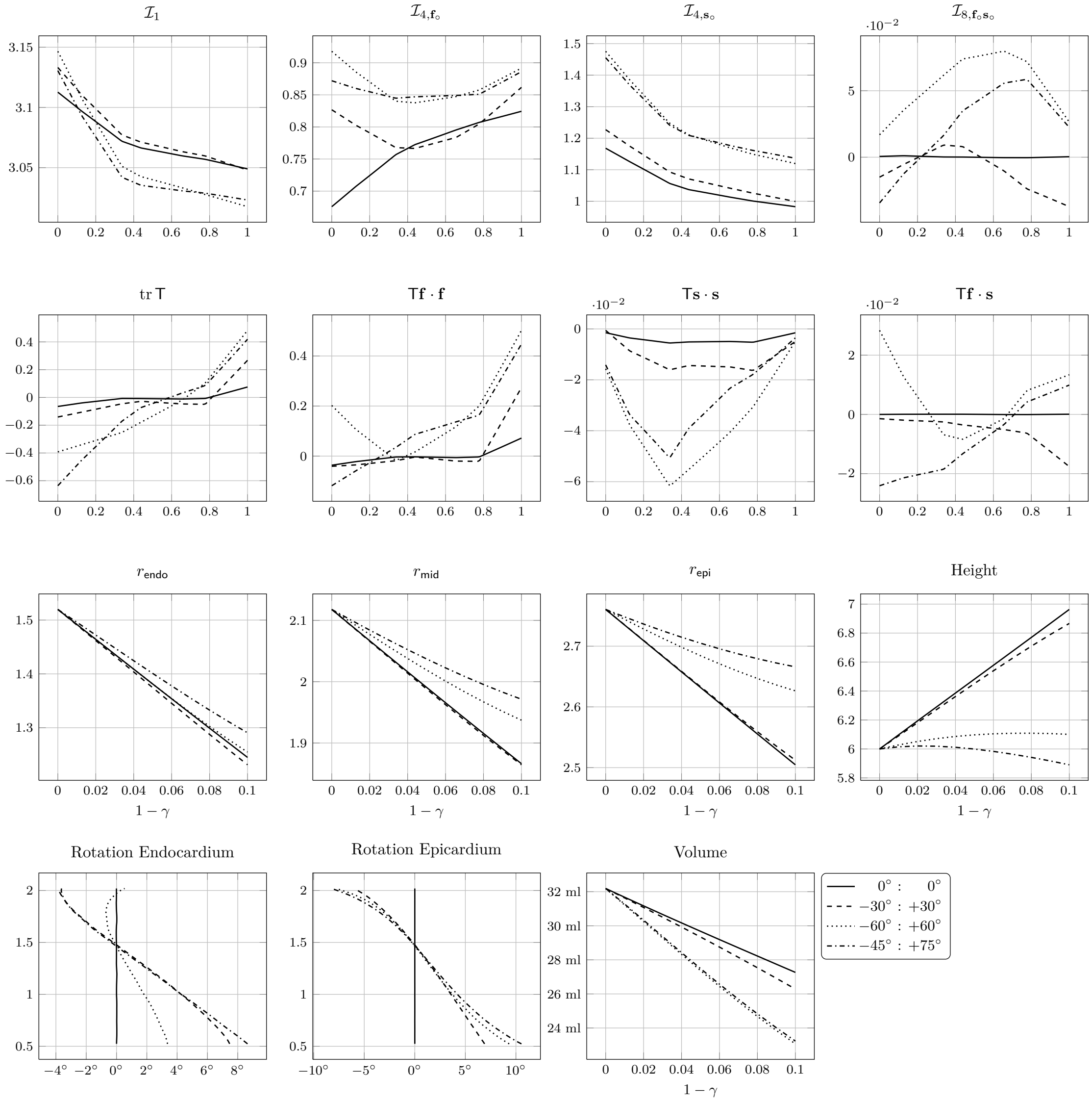

Figure 2.16 Sensitivity of the results to the fibres distribution during the free contraction test of the canine geometry of the left ventricle. The first two rows show the invariants and the stresses (in N/cm^2) vs. wall thickness λ_* at the height $\mu = \pi/3$ at $\gamma = 0.9$. The third row shows the radius at different wall depths for $\mu = \pi/2$ and the height (base–apex distance) vs. the activation. The last row illustrates the torsion vs. the longitudinal coordinate μ and the volume vs. the activation.

the height of the ventricle, since the incompressibility needs to be satisfied. In this simulations we observe an unphysiologically large elongation of the ventricle since no boundary conditions are applied at the epicardium.

We remark that the heart is actually contained in a sac called pericardium, which is filled with a fluid and whose stiffness is rather high. This prevents extremely large displacements of the muscle. Nevertheless, if we had imposed a Robin–type[3] boundary condition to mimic the presence of the pericardium, the stress at the apex would have been particularly high during the twitch. This condition is not optimal from a physiological viewpoint, since the overstressed area would be oxygen starved, and a remodelling would occur at long time–scale (Katz, 2010).

The volume varies linearly with respect to γ, and the slope is higher for a highly variable fibre distribution. This could lead to a physiological advantage, since the ejection would be more effective.

The rotation of the endocardium and the epicardium is similar for all the cases with non–circumferential microstructure, with the only exception of the rotation of endocardium for the $-60^\circ : 60^\circ$ case, which is surprisingly different. This might be related to the angle of the innermost layer of fibres (-60°) which is the lowest when compared to the other cases.

Expect for the “circumferential fibres” case, in terms of torsion there is no evident advantage of a particular distribution over the others. On the other hand, the crucial point is the variability of the fibre angle across the wall, since if it weren’t present, then there would be no torsion at all.

Strain–energy form The results of figure 2.17 enable us to conclude that the sheet–specific strain–energy term $\mathcal{W}_{4,\mathbf{s}_\circ}$ cannot be neglected in the model in an unloaded contraction. Most notably, for this case the ventricle shortens in the longitudinal direction, while in the reference case it elongates: we observe that in the first case the ventricle, during the contraction, shrinks without changing its shape. This could also explain the slightly lower stresses.

The $\boxed{\text{no–fix}}$ test shows that there is no need to deactivate fibres and sheets under compression, and no loss of stability is observed. This seems contradictory since $\mathcal{I}_{4,\mathbf{f}_\circ} < 1$, so a small difference should have been observed. Actually this is correct, because the strain–energy is evaluated with respect to the metric dictated by $\mathsf{F}_\mathsf{a}^\mathsf{T}\mathsf{F}_\mathsf{a}$, indeed $\mathcal{I}^{\mathsf{e}}_{4,\mathbf{f}_\circ} > 1$ since the actual stretch of the fibres is always lower than 10%, due to the lack of compatibility.

Material parameters The difference in the results between the material parameters set it is more marked that the passive inflation case, especially for the longitudinal displacement and, only for the Holzapfel–Ogden set, the torsion at the endocardium (figure 2.18).

Effect of a non–radial sheets distribution The non–uniform distribution of the laminar structure is taken into account in the same way of the previous chapter, to which we refer for further details, varying the angle with respect to the radial direction across the wall.

The effect on the deformations is a longitudinal shortening during the contraction, unlike the case with sheets are radially distributed, where the ventricle elongates (see figure 2.19). This explains why the final volume is lower than the reference case. A secondary effect of the non–uniform laminar structure is an higher rotation of the endocardium. It is also worth noting that the stress distribution is more uniform when an even small variation of the laminar microstructure is taken into account.

---

[3] A traction proportional to the displacement of the boundary itself, like distributed springs.

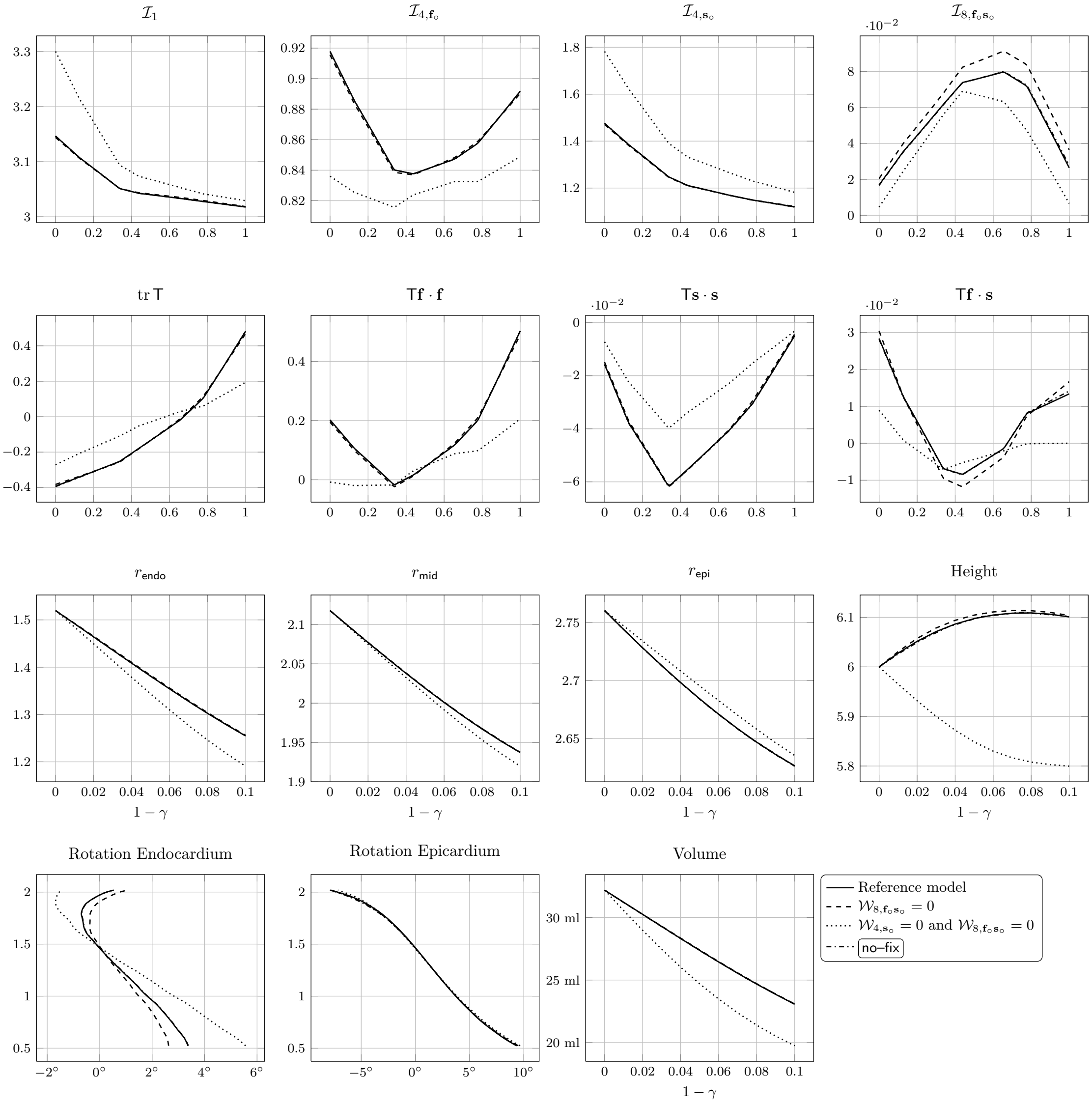

Figure 2.17 Effect of the activation/deactivation of some specific contributions of the strain–energy form on the results of the free contraction test of the canine geometry of the left ventricle. The first two rows show the invariants and the stresses (in N/cm^2) vs. wall thickness λ_* at the height $\mu=\pi/3$ at $\gamma=0.9$. The third row shows the radius at different wall depths for $\mu=\pi/2$ and the height (base–apex distance) vs. the activation. The last row illustrates the torsion vs. the longitudinal coordinate μ and the volume vs. the activation.

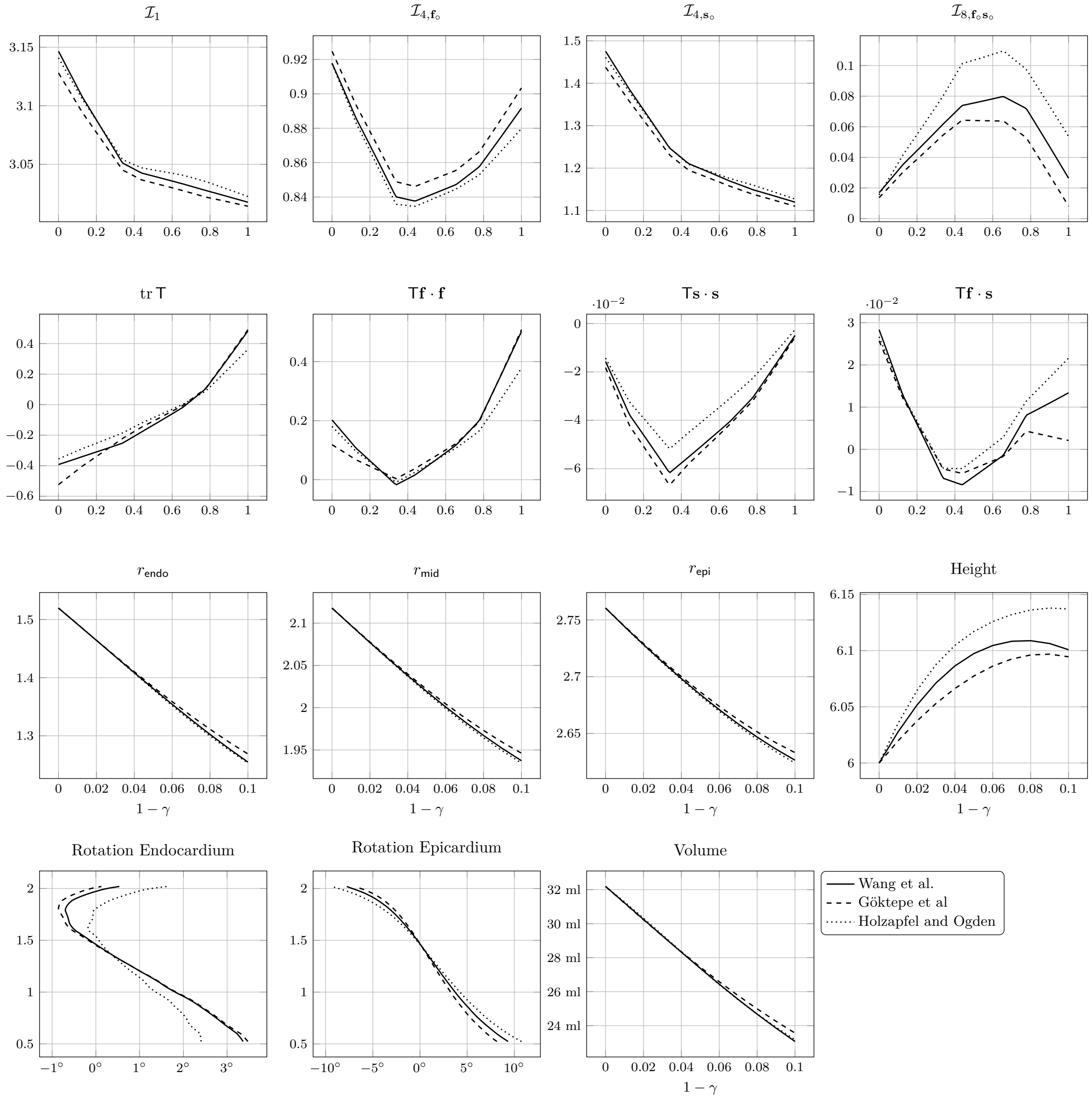

Figure 2.18 Numerical results produced by different material parameters sets for the free contraction test of the canine geometry of the left ventricle. The first two rows show the invariants and the stresses (in N/cm^2) vs. wall thickness λ_* at the height $\mu = \pi/3$ at $\gamma = 0.9$. The third row shows the radius at different wall depths for $\mu = \pi/2$ and the height (base–apex distance) vs. the activation. The last row shows the torsion vs. the longitudinal coordinate μ and the volume vs. the activation.

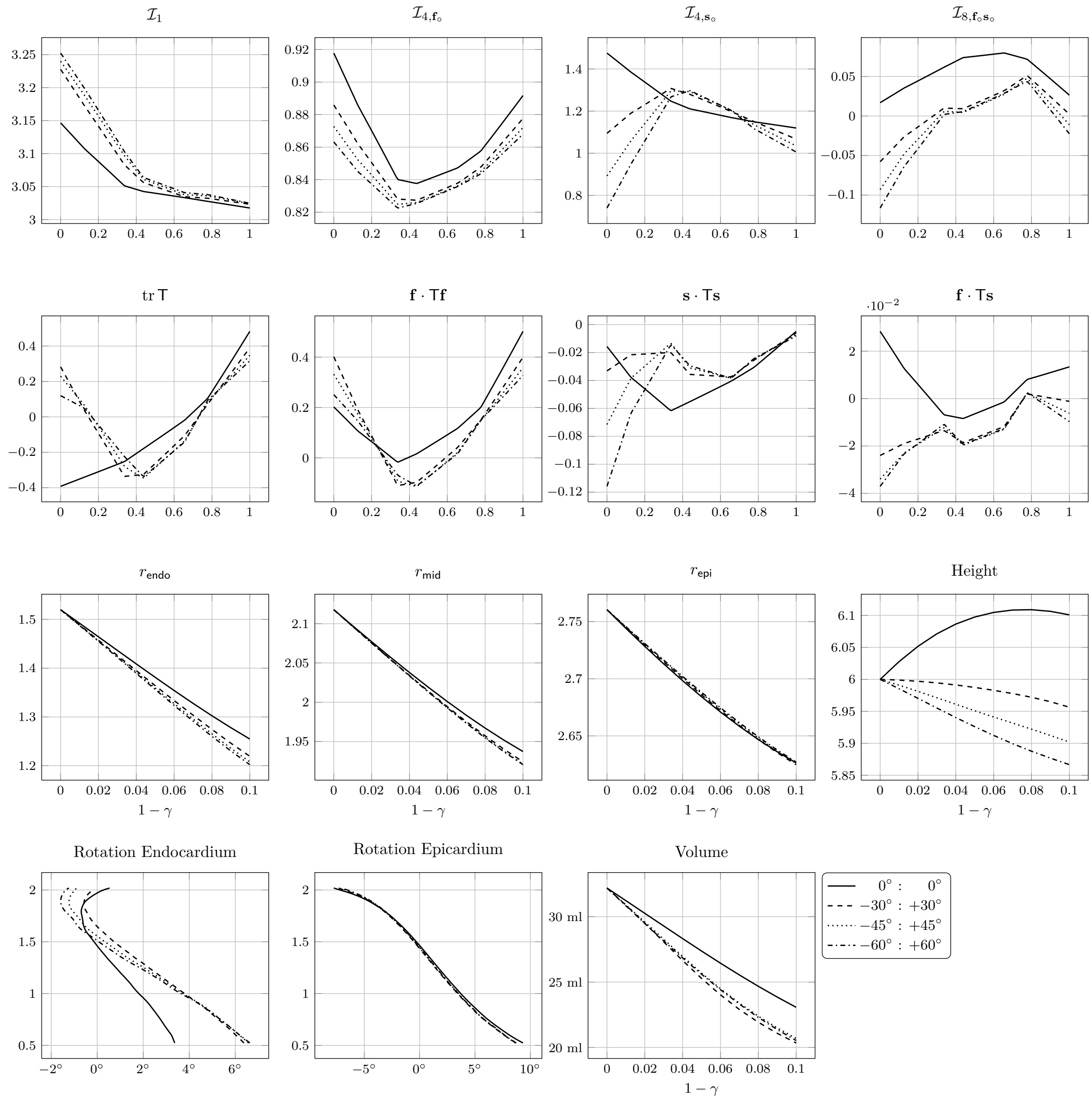

Figure 2.19 Sensitivity of the results on the sheets distribution during the free contraction test of the canine geometry of the left ventricle. Sheets form a non–zero angle with respect the radial direction $\mathbf{e}_\lambda$, as indicated by the legend. The first two rows show the invariants and the stresses (in N/cm^2) vs. wall thickness λ_* at the height $\mu = \pi/3$ at $\gamma = 0.9$. The third row shows the radius at different wall depths for $\mu = \pi/2$ and the height (base–apex distance) vs. the activation. The last row illustrates of the torsion vs. the longitudinal coordinate μ and the volume vs. the activation.

In this respect, we conclude that the sheets are moderately important during the free contraction, and a variable structure could be physiologically advantageous.

2.5.2 Isochoric contraction

In the heart, the systole starts as soon as the electric potential triggers the sarcomeres twitch inside the myocytes. In physiological conditions, this generally happens around the end–diastolic point (EDP), just after the blood has been pushed by the atrial contraction inside the ventricle through the mitral valve. The contraction of the fibres suddenly increases the cavity pressure closing the mitral valve; since also the aortic valve is closed, the ventricle undergoes an *isochoric* contraction, meaning that the chamber volume cannot change during the twich. Indeed, the blood is an incompressible fluid that cannot flow outside because the valves are closed.

During this phase the inner pressure significantly raises from the end–diastolic pressure (which is the *preload*) to the arterial pressure, when the aortic valve opens. Since we have neither a complete description of the fluid dynamics inside the ventricle, nor a characterisation of the valves, we need to enforce the volume constraint in some other ways.

Let $V_{\mathsf{inner}}(t)$ be the inner volume at the (fictitious) time t. During the contraction, we would like to impose the following constraint:

$$\frac{\mathrm{d}}{\mathrm{d}t} V_{\mathsf{inner}}(t) = 0. \tag{2.32}$$

The Lagrangian formulation reads as follows:

$$\mathscr{L}(\boldsymbol{\varphi}, \Theta, p, \xi; \gamma) := \mathcal{F}_{\mathrm{HW}}(\boldsymbol{\varphi}, \Theta, p; \gamma) - \xi V'_{\mathsf{inner}},$$

where $\mathcal{F}_{\mathrm{HW}}$ is the Hu–Washitzu functional (section 1.2.2), and ξ is a scalar Lagrangian multiplier, while $\gamma(t)$ is the given activation. Of course the volume V_{inner} depends on $\boldsymbol{\varphi}$ (see section 1.4), since

$$V_{\mathsf{inner}} = \int_{\Omega_{\mathsf{inner}}} J \,\mathrm{d}V = -\frac{1}{3} \int_{\Gamma_{\mathsf{endo}}} \boldsymbol{\varphi}(\mathbf{X}) \cdot (\operatorname{cof} \mathsf{F}) \mathbf{n}_0 \,\mathrm{d}A.$$

The saddle–point of the functional (2.32) can be characterised taking the variations $(\boldsymbol{\eta}, \Xi, q, \zeta)$ with respect to $(\boldsymbol{\varphi}, \Theta, p, \xi)$:

$$\begin{cases} \langle \mathrm{D}_{\boldsymbol{\varphi}} \mathscr{L}_{\mathsf{HW}}, \boldsymbol{\eta}_0 \rangle = \langle \mathrm{D}_{\boldsymbol{\varphi}} \mathcal{F}_{\mathsf{HW}}, \boldsymbol{\eta}_0 \rangle - \xi \, \langle \mathrm{D}_{\boldsymbol{\varphi}} V'_{\mathsf{inner}}, \boldsymbol{\eta}_0 \rangle = 0, \\ \langle \mathrm{D}_{\Theta} \mathscr{L}_{\mathsf{HW}}, \Xi \rangle = \langle \mathrm{D}_{\Theta} \mathcal{F}_{\mathsf{HW}}, \Xi \rangle = 0, \\ \langle \mathrm{D}_{p} \mathscr{L}_{\mathsf{HW}}, q \rangle = \langle \mathrm{D}_{p} \mathcal{F}_{\mathsf{HW}}, q \rangle = 0, \\ \langle \mathrm{D}_{\xi} \mathscr{L}_{\mathsf{HW}}, \zeta \rangle = -\zeta \, \langle V'_{\mathsf{inner}}, \boldsymbol{\eta}_0 \rangle = 0. \end{cases}$$

Everything is already known expect for $\mathrm{D}_{\boldsymbol{\varphi}} V'_{\mathsf{inner}}$, which can be evaluated as follows:

$$\langle \mathrm{D}_{\boldsymbol{\varphi}} V'_{\mathsf{inner}}, \boldsymbol{\eta}_0 \rangle = \frac{\mathrm{d}}{\mathrm{d}t} \int_{\Omega_{\mathsf{inner}}} \operatorname{cof} \mathsf{F} : \textsc{Grad}\, \boldsymbol{\eta}_0 \,\mathrm{d}V = \frac{\mathrm{d}}{\mathrm{d}t} \int_{\boldsymbol{\varphi}(\Omega_{\mathsf{inner}})} \operatorname{div} \boldsymbol{\eta} \,\mathrm{d}v = \frac{\mathrm{d}}{\mathrm{d}t} \int_{\partial \boldsymbol{\varphi}(\Omega_{\mathsf{inner}})} \boldsymbol{\eta} \cdot \mathbf{n} \,\mathrm{d}a.$$

Comparing with equation (1.24), we observe that ξ is exactly the inner pressure, to be applied in order to keep the volume constant. The only difference is that now the value of the pressure is an unknown of the problem.

The derivative in time can be approximated with a first order finite difference, so that

$$\frac{\mathrm{d}}{\mathrm{d}t} V_{\mathsf{inner}}(t) \approx \frac{V_{\mathsf{inner}}(t_{k+1}) - V_{\mathsf{inner}}(t_k)}{\Delta t}, \qquad t \in (t_k, t_{k+1}),$$

but, since the volume is constant by hypothesis, with can just enforce that the volume at time t is equal to the initial volume

$$V_{\mathsf{inner}}(t) = V_{\mathsf{inner}}(0) = \int_{\Omega_{\mathsf{inner}}} \mathrm{d}V.$$

From an implementation viewpoint, we just consider the inner pressure p_{inner} a variable and we add a new equation that enforce the constant volume. The evolution in time is dictated by γ, which is increased from zero to its maximum value.

Results

In this section we study the isochoric contraction of the ventricle when the initial inner pressure is zero. The final activation γ is 15% of shortening.

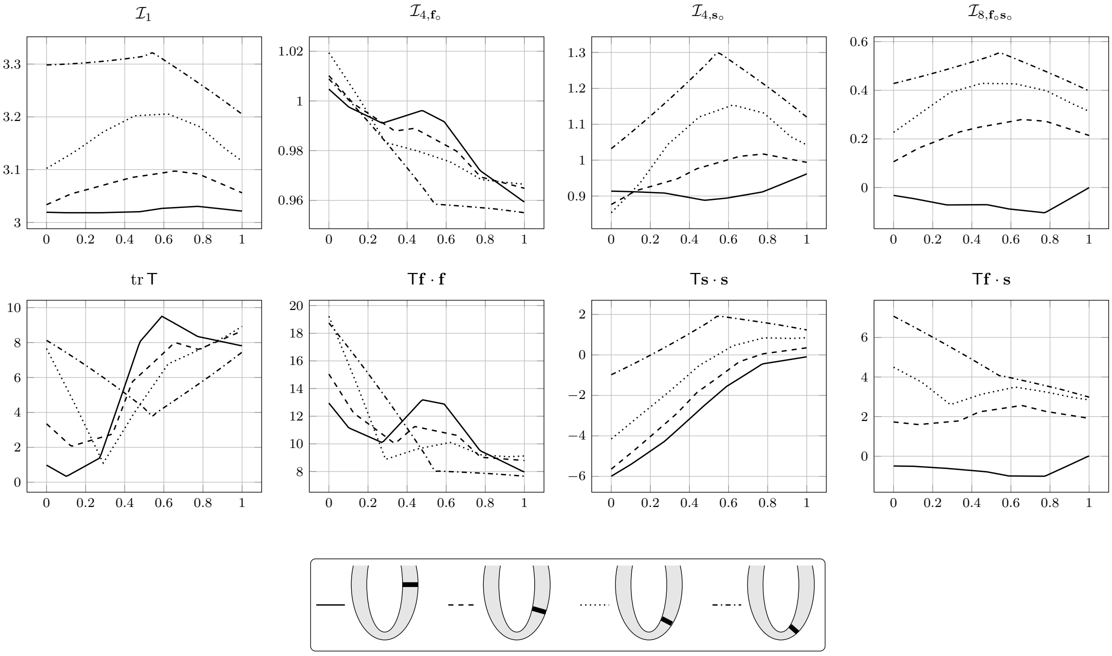

Figure 2.20 Transmural variation of the invariants and the stress components for the isochoric contraction of the canine geometry. Sections are indicated by the legend, and the abscissa indicates the wall depth. Stresses, measured in $\mathrm{N/cm^2}$, are plotted for $\gamma = 0.85$.

First of all, the obtained deformation is completely different from all the one obtained in the previous test case, since now the ventricle only slightly changes its shape. Indeed, the contraction is almost entirely translated into residual stress. Figure 2.20 clearly supports this fact, since the stress is one to two orders of magnitude higher than its counterpart in the free contraction and the passive inflation test cases.

Moving towards the apical region, the invariants become significantly different from zero, since the ventricle elongates, except for the fibre–specific invariant $\mathcal{I}_{4,\mathbf{f}_\circ}$, which remains close to the unity. This is an important aspect, because it means that the contraction of the fibres is very close to be isometric, condition under which a myocyte exerts the maximum active force. In this respect, the deformation is a balance of a free contraction and a passive inflation.

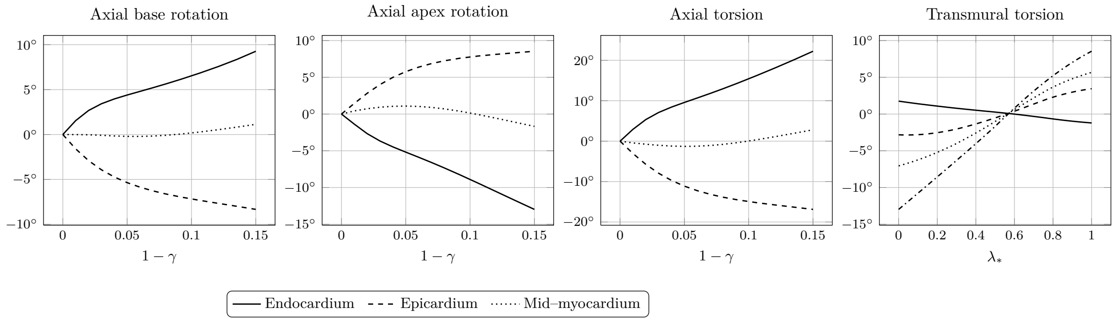

Figure 2.21 Torsion of the canine ventricle during the isochoric contraction. The first three plots shows the axial rotation with respect to the inner pressure. The last plot shows the transmural rotation for $\gamma = 0.85$ (for the legend refer to figure 2.20).

Torsion The torsion is plotted in figure 2.21: there is a large axial rotation of the base with respect to the apex, of about 20° at the endocardium, while it is the opposite at the epicardium. Moreover, there is a significant transmural torsion, that resembles the one from the passive inflation test more than the free contraction case, where there is no torsion but only a rotation of the epicardium and the endocardium in the same direction.

Boundary conditions If no constrain is enforced on the base, this tends to swell outwards, and the deformation induces lower residual stresses, as illustrated by figure 2.22. Since the longitudinal deformation is accommodated by the base swelling, the height of the whole ventricle is less than the "fixed z–component" case, and so the produced pressure, which is 25% lower for $\gamma = 0.85$.

Microstructure Figure 2.23 reveals one of the most important physiological consequences of the microstructure of the ventricle. We distinguish two categories: circumferential or almost circumferential fibres, identified by $0^\circ : 0^\circ$ and $-30^\circ : +30^\circ$ labels, and fibres with a great variability across the wall, symmetric or not with respect to the midwall, represented by $-60^\circ : +60^\circ$ and $-45^\circ : +75^\circ$ cases.

The first category of fibres yields to a unphysiological elongation of the ventricle: indeed, there is no support in the apical region, since the fibres are not very effective. The volume is constrained to remain constant, so the elongation is counterbalanced by a reduction of the inner radius. Most of the deformation is explained by the inelastic activation F_a, so the stored elastic energy is close to zero, since $\mathsf{F} \approx \mathsf{F}_\mathsf{a}^{-1}$. This yields to a negligible residual stress, and it translates in a very low increase of the inner pressure.

On the other hand, with the second category of fibres the deformation is moderate: $\mathcal{I}_{4,\mathbf{f}_\circ}$ is about one, which means that the contraction is isometric. The elongation is modest, and the inner radius remains constant, so almost the totality of the active contraction is stored as elastic strain–energy, since $\mathsf{F} \approx \mathsf{I}$ and so $\mathsf{F}_\mathsf{e} \approx \mathsf{F}_\mathsf{a}$. This is the ideal case, since the inner pressure significantly raises in order to keep the volume constant.

The physiological meaning of these observations is the following: the gap between diastolic and systolic pressure is very high (about 100 mmHg), since the blood needs to flow around the body and come back in the heart without stagnate. A contractile tube, as a primordial heart, with circumferential fibres, cannot produce an high pressure gradient with a moderate contraction. But ellipsoidal ventricle with fibres spanning a wide range of angles can

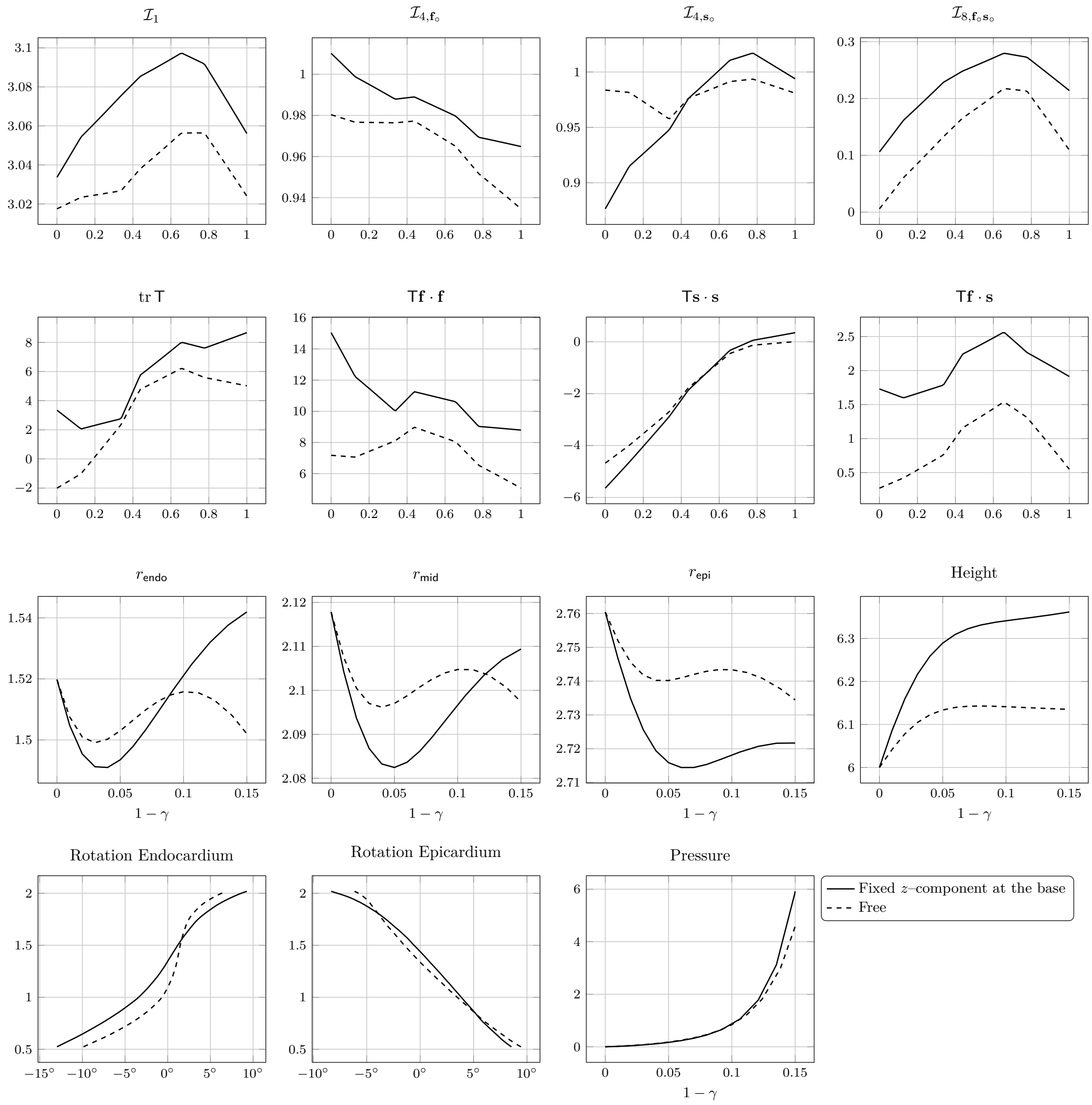

Figure 2.22 Effect of different boundary conditions at the ventricle base for the isochoric contraction test of the canine geometry of the left ventricle. The first two rows show the invariants and the stresses (in $\mathrm{N/cm^2}$) vs. wall thickness λ_* at the height $\mu = \pi/3$ at $\gamma = 0.85$. The third row shows the radius at different wall depths for $\mu = \pi/2$ and the height (base–apex distance) vs. the activation. The last row consists of the torsion vs. the longitudinal coordinate μ and the pressure vs. the activation.

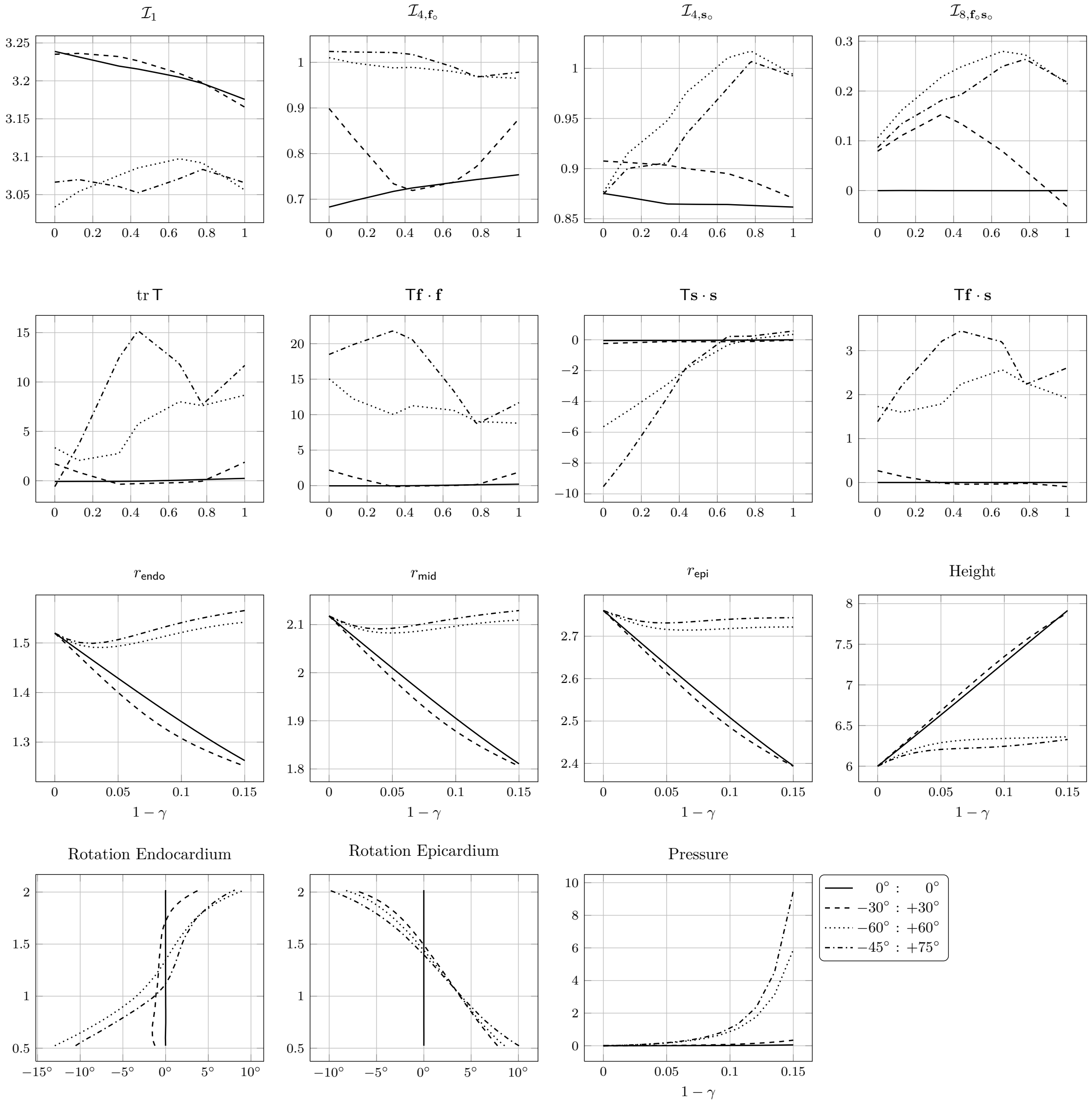
$\mathcal{I}_1$ $\mathcal{I}_{4,\mathbf{f}_\circ}$ $\mathcal{I}_{4,\mathbf{s}_\circ}$ $\mathcal{I}_{8,\mathbf{f}_\circ\mathbf{s}_\circ}$

$\operatorname{tr}\mathsf{T}$ $\mathsf{Tf}\cdot\mathsf{f}$ $\mathsf{Ts}\cdot\mathsf{s}$ $\mathsf{Tf}\cdot\mathsf{s}$

r_{endo} r_{mid} r_{epi} Height

Rotation Endocardium Rotation Epicardium Pressure

Figure 2.23 Sensitivity of the results to the fibres distribution during the isochoric contraction test of the canine geometry of the left ventricle. The first two rows show the invariants and the stresses (in N/cm^2) vs. wall thickness λ_* at the height $\mu = \pi/3$ at $\gamma = 0.85$. The third row shows the radius at different wall depths for $\mu = \pi/2$ and the height (base–apex distance) vs. the activation. The last row consists of the torsion vs. the longitudinal coordinate μ and the pressure vs. the activation.

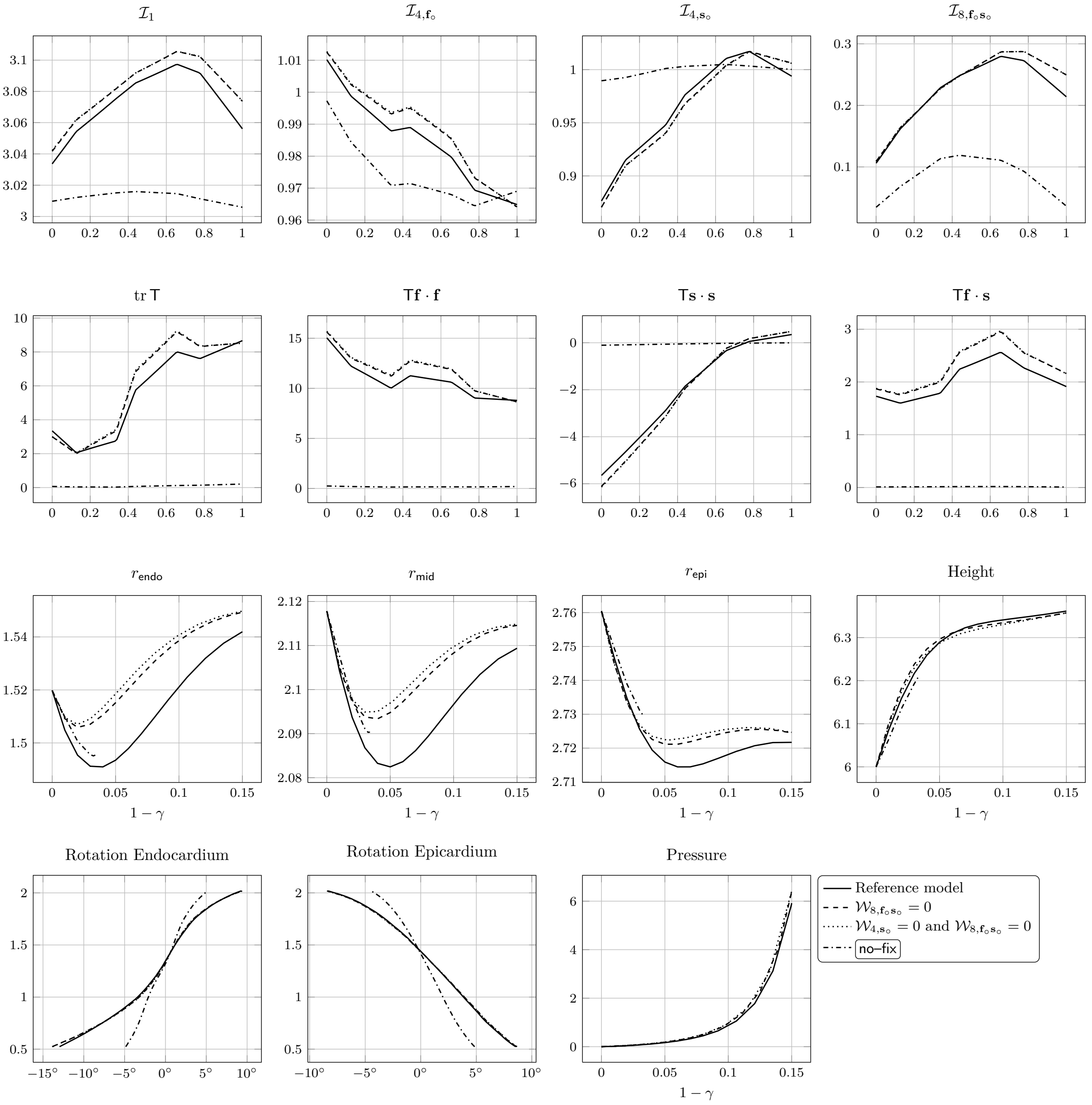

Figure 2.24 Effect of the activation/deactivation of some specific contributions of the strain–energy for the isochoric contraction test of the canine geometry of the left ventricle. The first two rows show the invariants and the stresses (in $\mathrm{N/cm^2}$) vs. wall thickness λ_* at the height $\mu=\pi/3$ at $\gamma=0.85$. The third row shows the radius at different wall depths for $\mu=\pi/2$ and the height (base–apex distance) vs. the activation. The last row consists of the torsion vs. the longitudinal coordinate μ and the pressure vs. the activation.

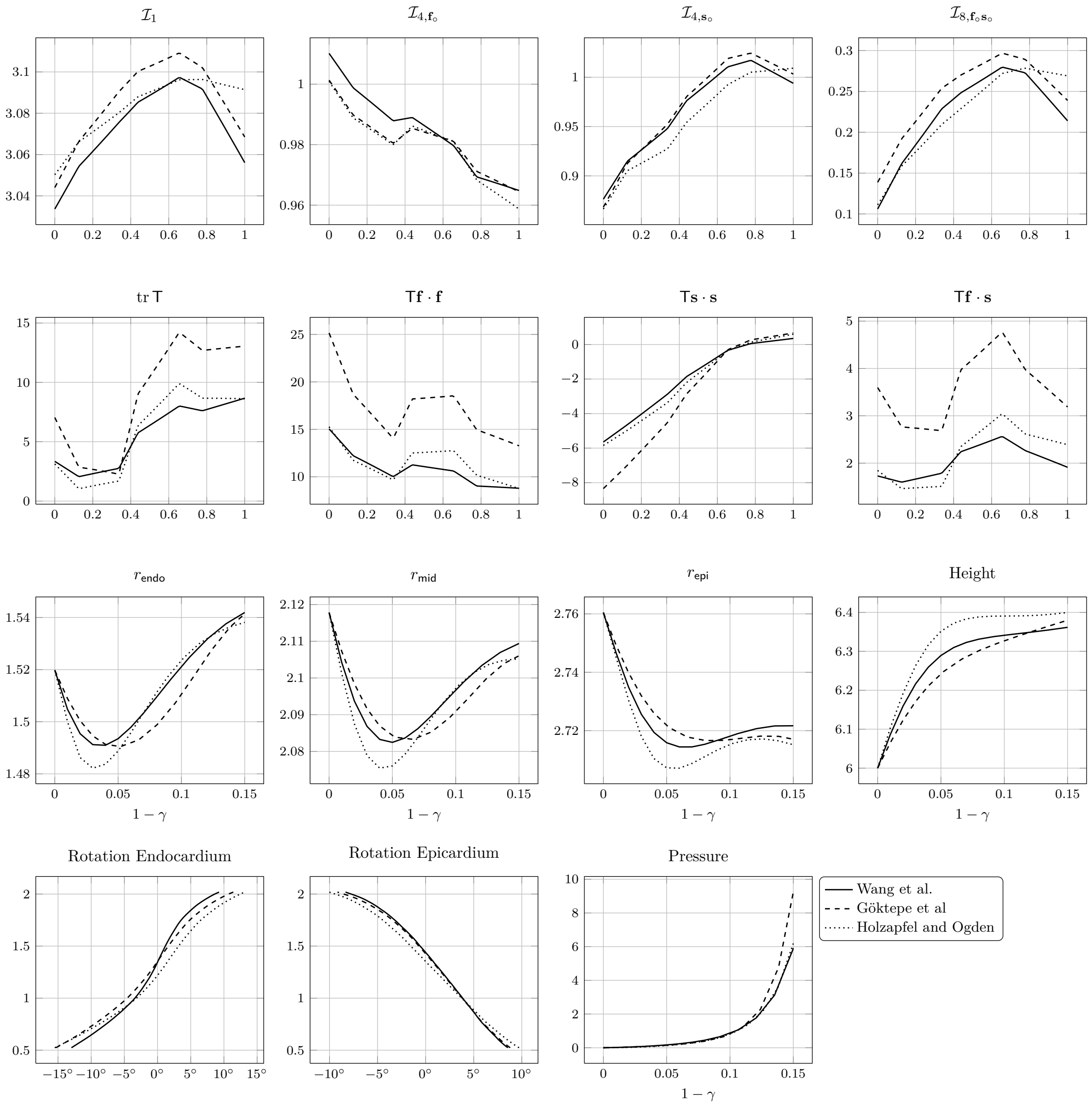

Figure 2.25 Numerical results produced by different material parameters set for the isochoric contraction test of the canine geometry of the left ventricle. The first two rows show the invariants and the stresses (in N/cm^2) vs. wall thickness λ_* at the height $\mu = \pi/3$ at $\gamma = 0.85$. The third row shows the radius at different wall depths for $\mu = \pi/2$ and the height (base–apex distance) vs. the activation. The last row consists of the torsion vs. the longitudinal coordinate μ and the pressure vs. the activation.

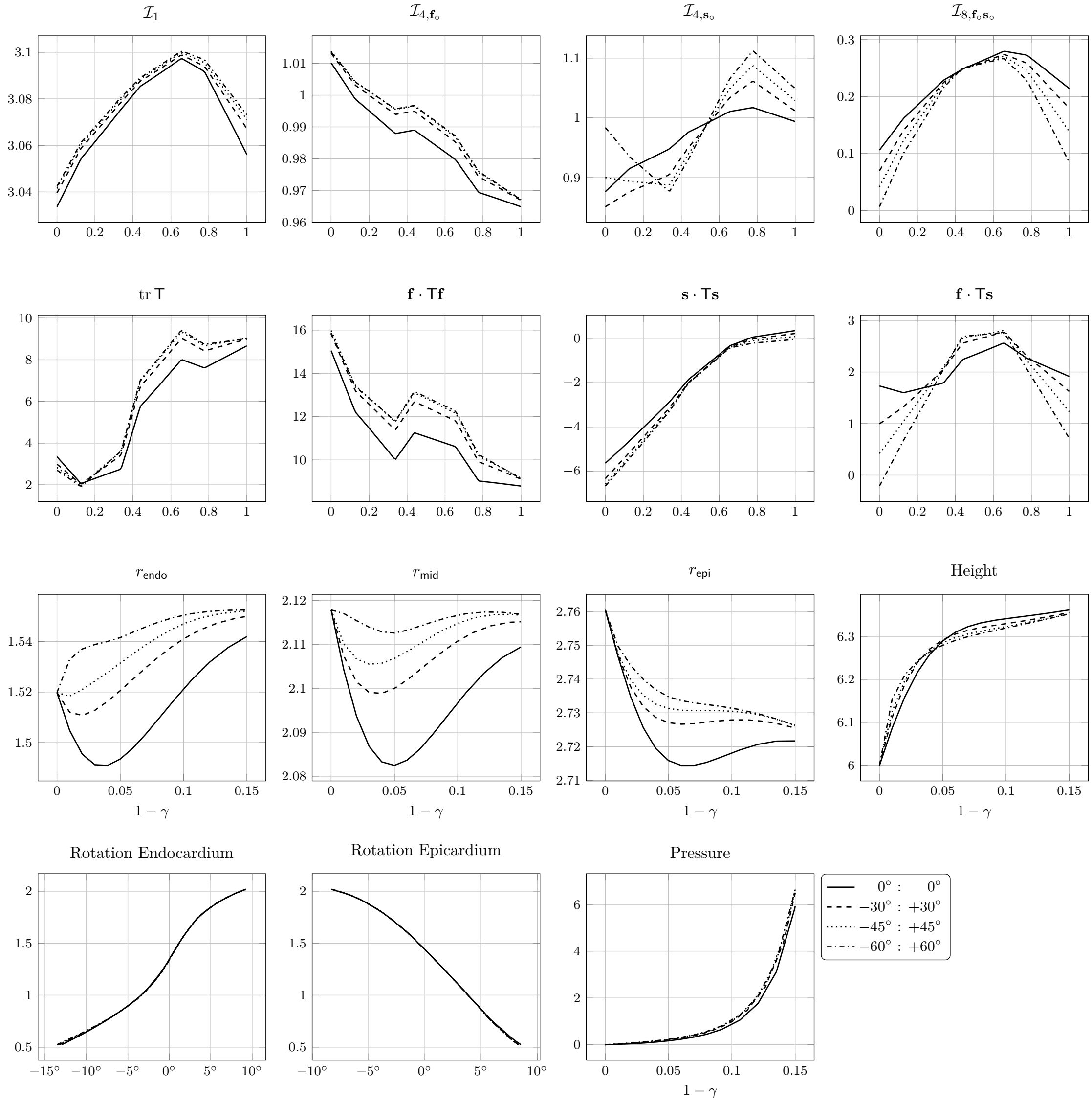

Figure 2.26 Sensitivity of the results on the sheets distribution for the isochoric contraction test of the canine geometry of the left ventricle. Sheets form a non–zero angle with respect the radial direction $\mathbf{e}_\lambda$, as indicated by the legend. The first two rows show the invariants and the stresses (in $\mathrm{N/cm^2}$) vs. wall thickness λ_* at the height $\mu = \pi/3$ at $\gamma = 0.85$. The third row shows the radius at different wall depths for $\mu = \pi/2$ and the height (base–apex distance) vs. the activation. The last row consists of the torsion vs. the longitudinal coordinate μ and the pressure vs. the activation.

be very effective, since even a small contraction (less than 10%) is enough to produce an inner pressure of 100 mmHg.

Observe that also two families of fibres, for instance one with a constant angle of +60° and the other of −60°, would be as effective as a variable distribution across the wall. But in the former case, for symmetry reason, the would be no torsion, which plays a fundamental role in the fluid–dynamics of the chamber.

Strain–energy form As for the passive inflation case, sheets are under compression, so the corresponding strain–energy term is largely deactivated. Figure 2.24 confirms this, since there is no difference between the case with $\mathcal{W}_{8,\mathbf{f}_\circ\mathbf{s}_\circ} = 0$ and the one with also $\mathcal{W}_{4,\mathbf{s}_\circ} = 0$. If the automatic deactivation is not taken into account (`no–fix` version), the simulations fails, since the sheet–specific stress term is negative and it destabilises the whole structure.

Material parameters The parameters from (Wang et al., 2013) and (Holzapfel and Ogden, 2009) perform similarly in term of stress and strain, while the parameters set from (Göktepe et al., 2011) is quite different, since it yields to a significantly higher inner pressure. We conclude that the isotropic contribution to the energy is negligible, so the deformation is not sensitive to the corresponding parameters (we recall that the isotropic shear modulus of the Holzapfel–Ogden parameters set is an order of magnitude lower than the other two sets), while a modest difference in the shear modulus of the fibres is magnified by the isochoric contraction: see table 2.2.

	a (kPa)	b	a_{f} (kPa)	b_{f}	a_{s} (kPa)	b_{s}	a_{fs} (kPa)	b_{fs}
Holzapfel–Ogden	0.059	8.023	18.472	16.026	2.481	11.120	0.216	11.436
Göktepe et al.	0.496	7.209	15.193	20.417	3.283	11.176	0.662	9.466
Wang et al.	0.2362	10.810	20.037	14.154	3.7245	5.1645	0.4108	11.300

Table 2.2 Material parameters comparison.

Effect of a non–radial sheets distribution Figure 2.26 shows that a variable laminar microstructure has a negligible effect of the strain and the stress, expect for $\mathcal{I}_{4,\mathbf{s}_\circ}$, which is greater than one on the outermost layers of the myocardium, and less than one on the innermost layers, i.e. the sheets close to the endocardium are in compressive regime, and it is the opposite for the sheets close to the epicardium.

2.5.3 Approximation of the end–systolic point

The constant–volume contraction ends when the inner pressure is high enough to open the aortic valve and let the blood rapidly flow outside. This stage is called *ejection phase*, and it is delimited by the aortic valve opening (AVO) and the aortic valve closing (AVC).

During the ejection phase pressure and volume of the chamber are related in a complex manner, since the time–variation of the volume depends on the valve geometry, on the compliance of the arterial vessels, on the overall resistence of the circulatory system, and so on. It is not the purpose of the present work to address such phenomena, so we simply fix an end–systolic pressure and compute the volume from the corresponding mechanics.

The only computational issue for this specific test is the valve opening: the idea is to check, during the isochoric contraction, whether the pressure is higher or not than a given threshold p_{avo}, which is the *afterload*. Since the pressure is a Lagrangian multiplier, we can control its value only through the activation γ, which is decreased linearly for one to its minimum value of 0.85 (15% of shortening).

The strategy we have adopted is as follows: as soon as the pressure cross the threshold, we perform a linear interpolation of the pressure with respect to γ, trying to estimate the correct γ the gives exactly p_{avo}:

$$\gamma_{\mathsf{avo}} = \frac{\gamma^{k+1} - \gamma^k}{p^{k+1}_{\mathsf{endo}} - p^k_{\mathsf{endo}}}(p^{k+1}_{\mathsf{endo}} - p^k_{\mathsf{avo}}) + \gamma^k,$$

where k is the iteration counter and p_{endo} is the chamber pressure. Then, we recompute the solution with this new estimate γ_{avo}, starting from the more convenient state between the one above the threshold and the other below.

After this stage, the volume constrain is removed and the ventricle is free to change its internal volume by means of the contraction, which stops when the shortening γ reaches its minimum value. This marks the end–systolic point.

The forthcoming simulations consist of a sequence of all the previous tests, starting from a passive inflation, then an isochoric contraction and eventually a free contraction, but with a remarkable difference: in the present case, during the free contraction the ventricle bears a rather high inner pressure.

Here we do not account for the diastolic phase downstream the systolic one, during which a relaxation occurs: indeed, this phase would be exactly the same of the systolic one, but backwards. Indeed, without a correct description of the valves and the systemic circulation, even with lumped models, it is not possible to relate pressure and volume during the ejection and the passive filling. Another possibility is to directly assign the pressure or the volume, as a function of time, here not adopted for sake of simplicity.

Results

We perform two simulations, one with an canine geometry and radially distributed sheets, and the other with a human geometry (see figure 1.16) and variable laminar microstructure. The material parameters are the one from Wang et al. (2013), fibres rotates from −60° at the endocardium to 60° at the epicardium, and we fix the z–component to zero at the base.

Canine	Volume	Pressure	γ
Initial	32.37 ml	0.0 mmHg	1.0
End–Diastolic Point (EDP)	39.50 ml	7.5 mmHg	1.0
Aortic Valve Opening (AVO)	39.50 ml	116.5 mmHg	0.911
End–Systolic Point (ESP)	26.11 ml	116.5 mmHg	0.85
Human	Volume	Pressure	γ
Initial	136.29 ml	0.0 mmHg	1.0
End–Diastolic Point (EDP)	170.02 ml	7.5 mmHg	1.0
Aortic Valve Opening (AVO)	170.02 ml	116.3 mmHg	0.9
End–Systolic Point (ESP)	124.30 ml	116.3 mmHg	0.85

Table 2.3 Pressure, volume and contraction at key points of the pV–loop.

Table 2.3 resumes the pressure and the volume at different points of the pV–loop. For the canine geometry, the stroke volume, defined as the difference between the end–diastolic and end–systolic volumes, is about 13.4 ml, which yields to an ejection fraction (the stroke volume over the end–diastolic volume) of 34%. This value is rather low, but it depends on several factors and it can be easily increases by changing the contractility or the end–systolic pressure: for instance, with $\gamma = 0.8$ instead of 0.85, thus with a 20% of shortening of the fibres, the ejection fraction becomes 61%, which is within the physiological range for a normal heart. Concerning the human

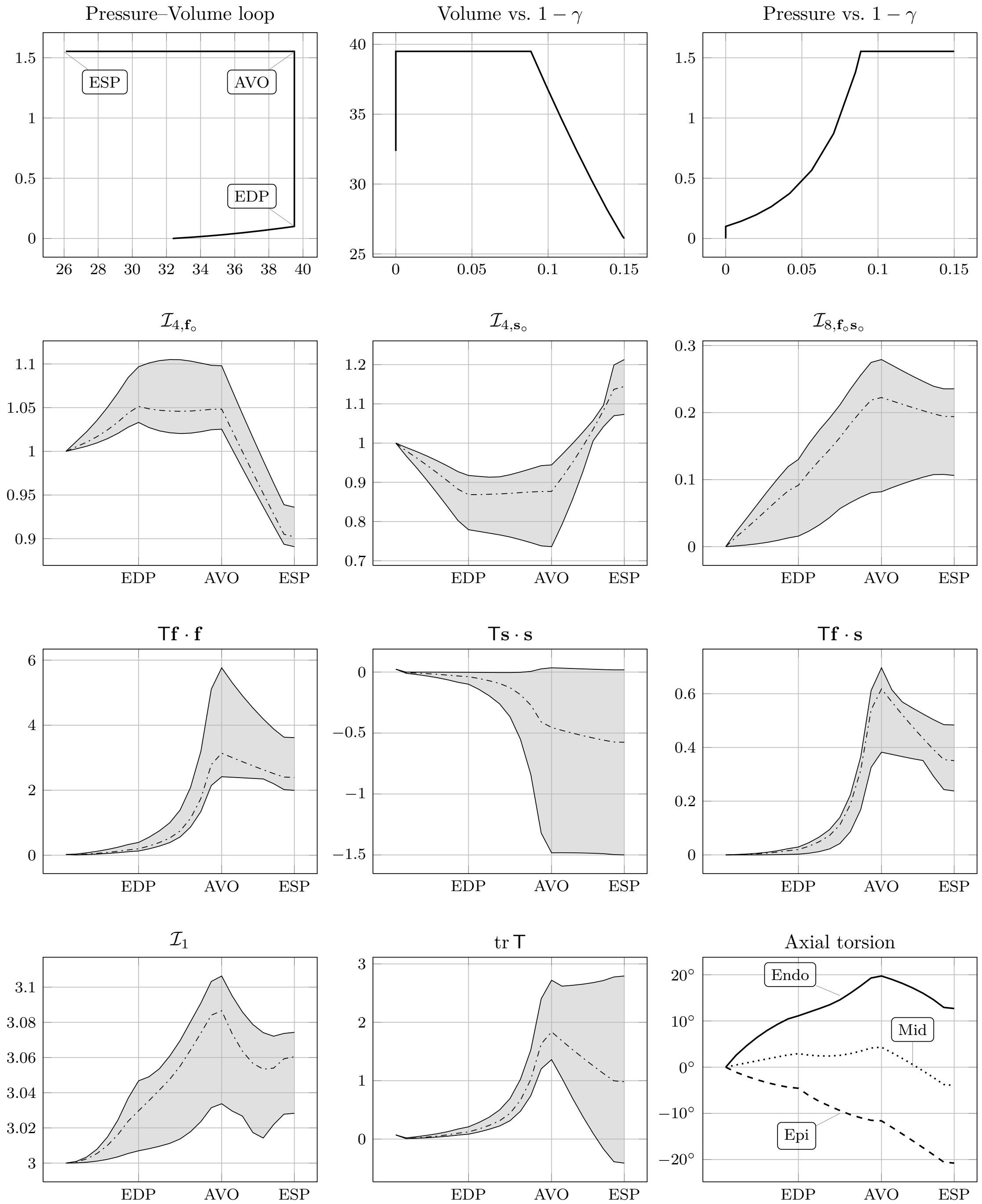

Figure 2.27 Evolution of pressure, volume, torsion, strain and stress during the passive inflation and the subsequent systole on the canine ventricle. Pressure and stresses are in $\mathrm{N/cm^2}$, while the volume is in millilitres. The grey area represent the range of values spanned by the indicated quantity. The time (abscissa) is fictitious so no scale is provided.

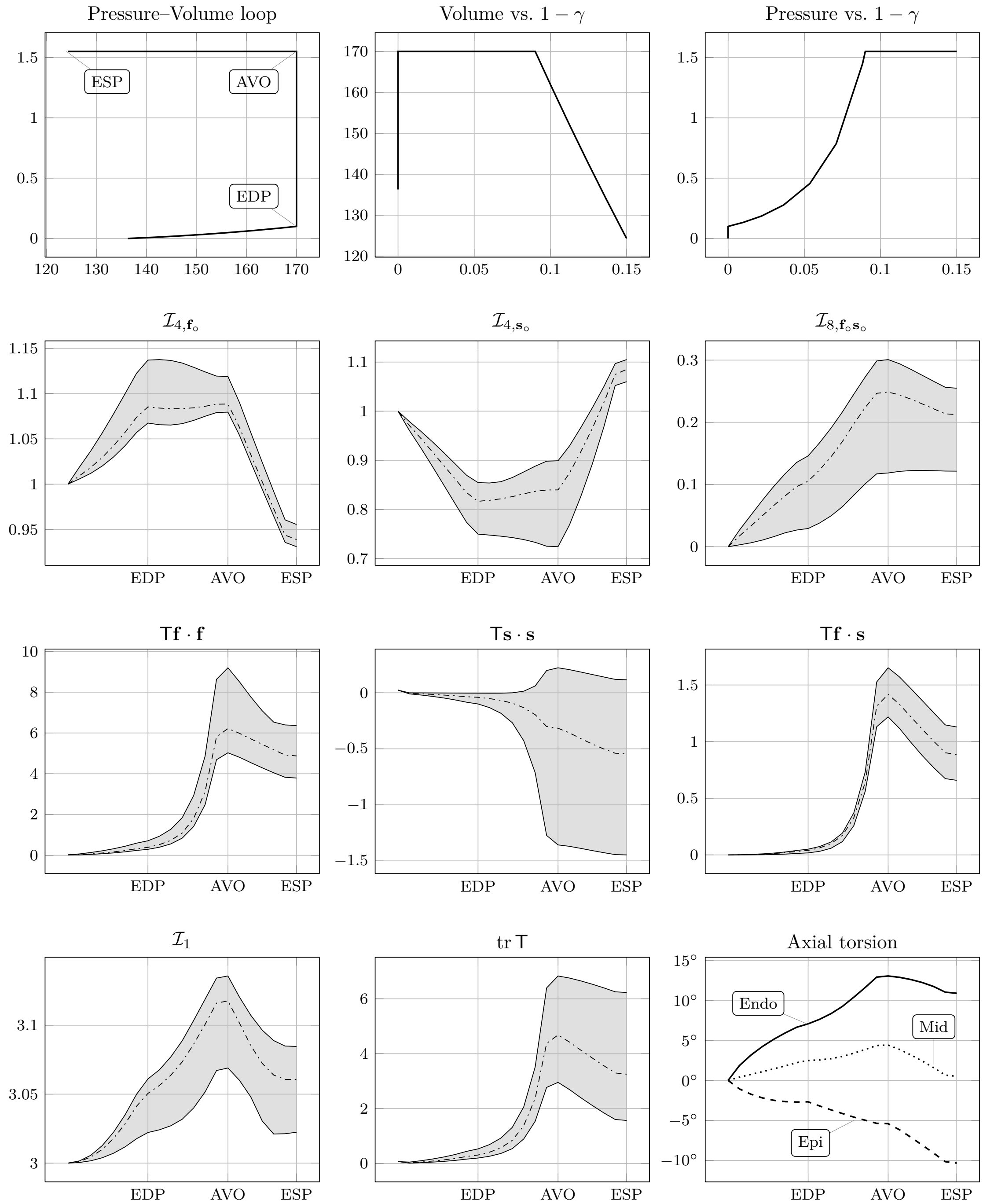

Figure 2.28 Evolution of pressure, volume, torsion, strain and stress during the passive inflation and the subsequent systole on the human ventricle. Pressure and stresses are in N/cm^2, while the volume is in millilitres. The grey area represent the range of values spanned by the indicated quantity. The time (abscissa) is fictitious so no scale is provided.

geometry, the stroke volume is 46 ml while the ejection fraction is 27%, which increases to 52% when $\gamma = 0.8$.

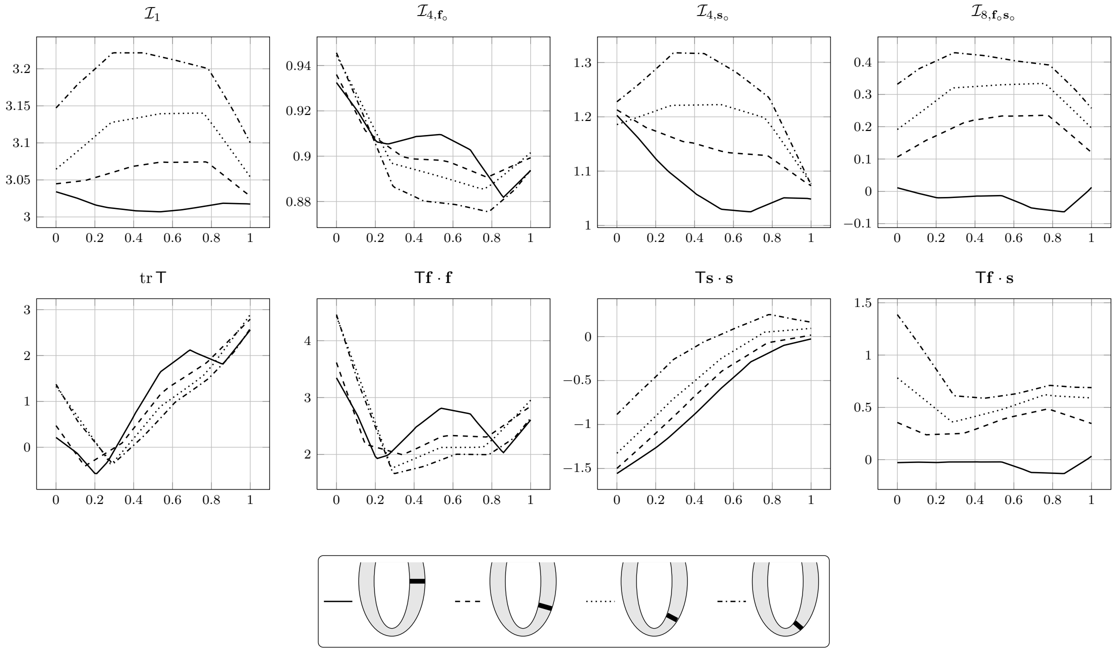

Figure 2.29 Transmural variation of the invariants and the stress components at the end–systolic point of the canine geometry. Sections are indicated by the legend, and the abscissa indicates the wall depth. Stresses, measured in N/cm^2, are plotted for $\gamma = 0.85$.

Figures 2.27 and 2.28 show a detailed view of strain, stress and torsion of the ventricle over the whole deformation history, both for canine and human geometries. Several remarks can be made regarding the results:

- The ventricle undergoes a significant longitudinal torsion during the contraction, with a maximum absolute value of about 20°, which is consistent with the physiological range. The torsion at the endocardium starts to decrease after the aortic valve closing, but this doesn't happen for the torsion at the epicardium: this should be compared with the torsion observed during the free contraction test, in figure 2.14. Indeed, the rotation is more pronounced at the epicardium, probably because the fibres from this layer have a longer lever arm than the fibres in the endocardium.

- The fibres strain is rather low in the first two phases (before the aortic valve opening), since $\mathcal{I}_{4,\mathbf{f}_\circ}$ is only slightly higher than one. More precisely, the square root of $\mathcal{I}_{4,\mathbf{f}_\circ}$ is the strain in the fibre direction, and it ranges between 2% and 4%, confirming the hypothesis that during the isovolumic phase the fibres undergo an isometric contraction. However, in the ejection phase fibres start to shorten until a value of about 6%, with $\gamma = 0.85$.

- Between the passive filling and the isochoric contraction there is no evident discontinuity in the stress variation, since it exponentially grows at the same rate. This is not the case for the strain: $\mathcal{I}_{4,\mathbf{f}_\circ}$ and $\mathcal{I}_{4,\mathbf{s}_\circ}$ change their trend when the mitral valve closes.

- During the ejection phase, the stress across the sheets direction $\mathbf{T}\mathbf{s}\cdot\mathbf{s}$ ranges from 0 N/cm^2 on the epicardium (no external pressure is applied, and the boundary is free), to 1.55 N/cm^2 on the endocardium, which is the inner pressure in the ventricle.
- The eighth invariants raises linearly during the whole simulation, with a change of trend in the last phase. The associated stress $\mathbf{T}\mathbf{f}\cdot\mathbf{s}$ is particularly uniform across the wall, since the maximum and minimum value are very close to each other.

Conclusions

In the first part of this chapter we have addressed the correct mathematical statement of the contractility of a muscle, with a focus on the cardiac system. Mathematical comments have a general validity, the physiological characterization pertains the specific system at hand.

An acceptable mathematical model for the active behaviour of the cardiac muscle should satisfy mathematical and biological requirements.

- Correct biological behaviour: when the effective potential wave activates the muscle, the material should contract in the direction of the fibres. It is experimentally observed that the cardiac wall produces an active stress that grows with the stretch. The dependence between stretch and active stress is linear at a cell level, typically nonlinear at a tissue level, an issue that remains to be better understood.
- The total stress must obey frame invariance and a suitable sign preserving condition (rank–one ellipticity, in the present work).

A constitutive form of the active stress should be prescribed with the due attention to the properties listed above. If the active stress in itself is not at least rank–one elliptic, a condition on the ellipticity of the total stress can arise, typically limiting the maximum admissible strain (Pathmanathan et al., 2010). On the other hand, the active stress can have strong sign–preserving properties, possibly stronger than the ones typically advocated for the standard stress, as the due weakness will be ensured by the standard part of the stress. Provided that the sought mathematical characterization is abided, the active stress approach ensures the flexibility to reproduce the observed physiological behaviour.

The active strain approach is mathematically more robust, as frame invariance and rank–one ellipticity are simply inherited from the corresponding properties of the standard strain energy of the material. Conversely, the analysis of the physiological predictions in terms of dependence of the active force on the stretch is more involved. The active strain approach is more rigid and allows no chance for modelling the physiological behaviour after that the inert properties of the material are prescribed. When a reinterpretation of the active strain in terms of active stress is possible, no new free parameters are to be fitted: the new dynamic contribution naturally arises from the visible stretch, because the kinematics of the microstructure is directly encoded in the equations. While the mathematical derivation of the model is more elegant, as no active stress function is to be tuned, the physiological effectiveness of the obtained model remains to be addressed in the literature, with the exception of a few investigations into the physiological relevance of the multiplicative decomposition which has been done for smooth muscles with promising results, see, e.g., Murtada et al. (2010) and Stålhand et al. (2008).

Therefore, in the second part of the chapter is we have numerically tested the active strain model on basis of physiologically bases geometry, strain–energy and boundary conditions, with the specific aim to benchmark the ability of the model to predict relevant properties such as the pressure–volume loop and the torsion.

The resulting description of the systolic phase of the heartbeat is a complex interaction of several actor: some on them, such as the microstructure or the form of the elastic energy, could have a tremendous impact on the resulting mechanical problem. The active strain approach have provided a robust and physiologically motivated way to test the sensitivity of the systolic phase on perturbations of the parameters.

Simulations show that a non–correct characterisation of the fibres and, at some extent, of the laminar structure of the myocardium could yield to an unphysiological behaviour, especially during the isovolumic contraction, where it is fundamental to convert the active shortening of the myocytes into a pressure high enough to open the aortic valve. Moreover, the variability of the fibres across the wall implies the presence of a torsion, either axial, as a rotation of the base with respect to the apical region, and transmural, i.e. as a sliding of the epicardium and the endocardium. If the fibres are uniformly distributed, or barely variable, the torsion is not very low, and this is disadvantageous from the viewpoint of the fluid dynamics within the chamber.

Final remarks

In this thesis we have investigated the mathematical modelling of the heart, with a focus on the coupling of passive and active behaviour of the cardiac muscle.
The main original results of this work can be resumed as follows:

- The numerical keypoints for an effective numerical implementation of a nonlinear structural model (variational formulation, tangent problem, boundary conditions) have been addressed in chapter 1.
- Numerical simulations in test problems show that the application of the Holzapfel–Ogden strain–energy to cardiac mechanics weakly depends on the specific contribution of the strain of the sheets, while a strong sensitivity of the results on the orientation of the fibres is apparent.
- The active behaviour of the cardiac muscle calls for an appropriate reformulation of the standard hyperelastic theory. In chapter 2 are illustrated the possible strategies in the respect, with a discussion of the pros and cons of an active strain formulation. In particular, the issues of rank–one convexity, frame–indifference and symmetry are pointed out.
- The active bending of a monolayer of cardiomyocytes is used as a benchmark to calibrate the correct value of the active strain parameter.
- The active deformation of sample geometries and a prolate ellipsoid representing a prototype of the left ventricle (including the microstructure) demonstrate the efficacy of the approach illustrated in the thesis. In particular, the correct volume variation, transmural shear and apex–base torsion of the left ventricle are numerically reproduced *without* any further parameters fitting.

References

Alford, P. W., A. W. Feinberg, S. P. Sheehy, and K. K. Parker. 2010. *Biohybrid thin films for measuring contractility in engineered cardiovascular muscle*, Biomat. **31**, 3613–3621.

Aguado–Sierra, J., A. Krishnamurthy, C. Villongco, J. Chuang, E. Howard, M. J. Gonzales, J. Omens, D. E. Krummen, S. Narayan, R. Kerckhoffs, and A. D. McCulloch. 2011. *Patient–specific modeling of dyssynchronous heart failure: a case study*, Progress in biophysics and molecular biology **107**, no. 1, 147–155.

Ambrosi, D. and F. Guana. 2007. *Stress-modulated growth*, Math. Mech. Solids **12**, no. 3, 319–342.

Ambrosi, D., G. Arioli, F. Nobile, and A. Quarteroni. 2011. *Electromechanical coupling in cardiac dynamics: the active strain approach*, SIAM J. Appl. Math. **71**, no. 2, 605–621.

Antman, S. S. 2005. *Mathematical foundations of elasticity*, Springer.

Baker, M. and J. L. Ericksen. 1954. *Inequalities restricting the form of the stress-deformation relations for isotropic elastic solids and Reiner-Rivlin fluids*, J. Wash. Acad. Sci **44**, 33–35.

Böl, M., O. J. Abilez, A. N. Assar, C. K. Zarins, and E. Kuhl. 2012. *In vitro/in silico characterization of active and passive stresses in cardiac muscle*, Int. J. Multiscale Comput. Eng. **10**, no. 2.

Bovendeerd, P. H. M., T. Arts, J. M. Huyghe, D. H. Van Campen, and R. S. Reneman. 1992. *Dependence of local left ventricular wall mechanics on myocardial fiber orientation: a model study*, J. Biomech. **25**, no. 10, 1129–1140.

Boyett, M. R., J. E. Frampton, and M. S. Kirby. 1991. *The length, width and volume of isolated rat and ferret ventricular myocytes during twitch contractions and changes in osmotic strength*, Exp. Physio. **76**, no. 2, 259–270.

Campbell, K. B., A. M. Simpson, S. G. Campbell, H. L. Granzier, and B. K. Slinker. 2008. *Dynamic left ventricular elastance: a model for integrating cardiac muscle contraction into ventricular pressure–volume relationships*, J. Appl. Phys. **104**, 958–975.

Chadwick, R. S. 1982. *Mechanics of the left ventricle*, Biophys. J. **39**, 279–288.

Cherubini, C., S. Filippi, P. Nardinocchi, and L. Teresi. 2008. *An electromechanical model of cardiac tissue: constitutive issues and electrophysiological effects*, Prog. Biophys. Mol. Biol. **97**, 562–573.

Costa, K. D., J. W. Holmes, and A. D. McCulloch. 2001. *Modeling cardiac mechanical properties in three dimensions*, Phil. Trans. R. Soc. Lond. A **359**, 1233–1250.

Demiray, H. 1976. *Stresses in ventricular wall*, J. Appl. Mech. **98**, 194–197.

Destrade, M., M. D. Gilchrist, D. A. Prikazchikov, and G. Saccomandi. 2008. *Surface instability of sheared soft tissues*, J. Biomed. Engng. **130**.

Destrade, M., J. G. Murphy, and G. Saccomandi. 2012. *Simple shear is not so simple*, Int. J. Nonlin. Mech. **47**, 210–214.

DiCarlo, A. and S. Quiligotti. 2002. *Growth and balance*, Mech. Res. Commun. **29**, 449–456.

Dokos, S., B. H. Smaill, A. A. Young, and I. J. LeGrice. 2002. *Shear properties of passive ventricular myocardium*, Am. J. Physiol. Heart Circ. Physiol. **283**, no. 6, H2650–H2659.

Downey, J. M. 2003. *The mechanical activity of the heart* (L. R. Johnson, ed.), Essential medical physiology, 3rd edition, Elsevier.

Feinberg, A. W., A. Feigel, S. S. Shevkoplyas, S. Sheehy, G. M. Whitesides, and K. K. Parker. 2007. *Muscular thin films for building actuators and powering devices*, Science **317**, no. 1366.

Feinberg, A. W., P. W. Alford, H. Jin, C. M. Ripplinger, A. A. Werdich, S. Sheehy, A. Grosberg, and K. K. Parker. 2012. *Controlling the contractile strength of engineered cardiac muscle by hierarchal tissue architecture*, Biomat. **33**, 5732–5741.

Gilbert, S. H., A. P. Benson, P. Li, and A. V. Holden. 2007. *Regional localisation of left ventricular sheet structure: integration with current models of cardiac fibre, sheet and band structure*, Eur. J. Cardio–Thorac. **32**, no. 2, 231–249.

Göktepe, S. and E. Kuhl. 2010. *Electromechanics of the heart: a unified approach to the strongly coupled excitation–contraction problem*, Comput. Mech. **45**, 227–243.

Göktepe, S., S. N. S. Archarya, J. Wong, and E. Kuhl. 2011. *Computational modeling of passive myocardium*, Int. J. Numer. Biomed. Engng. **27**, 1–27.

Guccione, J. M., K. D. Costa, and A. D. McCulloch. 1995. *Finite element stress analysis of left ventricular mechanics in the beating dog heart*, J. Biomechanics **28**, no. 10, 1167–1177.

Helm, P. A., H. Tseng, L. Younes, E. R. McVeigh, and R. L. Winslow. 2005. *Ex vivo 3D diffusion tensor imaging and quantification of cardiac laminar structure*, Magnet. Reson. Med. **54**, no. 4, 850–859.

Hibbitt, H. D., P. V. Marcal, and J. R. Rice. 1970. *A finite element formulation for problems of large strain and large displacement*, Int. J. Solid Structures **6**, 1069–1086.

Holzapfel, G. A. and R. W. Ogden. 2009. *Constitutive modelling of passive myocardium: a structurally based framework for material characterization*, Phil. Trans. R. Soc. A **367**, 3445–3475.

Horgan, C. O. and J. G. Murphy. 2011. *Simple shearing of soft biological tissues*, Proc. R. Soc. A **467**, no. 2127, 760–777.

Humphrey, J. D., R. K. Strumpf, and F. C. P. Yin. 1990. *Determination of a constitutive relation for passive myocardium: II. — Parameters estimation*, J. Biomech. Engng. **112**, 340–346.

Hunter, P. J., M. P. Nash, and G. B. Sands. 1997. *Computational electromechanics of the heart* (A. V. Panfilov and A. V. Holden, eds.), Computational biology of the heart.

Hunter, P. J., A. J. Pullan, and B. H. Smaill. 2003. *Modeling total heart function*, Annu. Rev. Biomed. Eng. **5**, no. 1, 147–177.

Iribe, G., M. Helmes, and P. Kohl. 2007. *Force–length relations in isolated intact cardiomyocytes subjected to dynamic changes in mechanical load*, Am. J. Physiol. Heart Circ. Physiol. **292**, H1487–H1497.

Iyer, R. K., L. LY. Chiu, L. A. Reis, and M. Radisic. 2011. *Engineered cardiac tissues*, Curr. Opin. Biotech. **22**, no. 5, 706–714.

Katz, A. M. 2010. *Physiology of the Heart*, Lippincott Williams & Wilkins.

Klotz, S., I. Hay, M. L. Dickstein, G. H. Yi, J. Wang, M. S. Maurer, D. A. Kass, and D. Burkhoff. 2006. *Single–beat estimation of end-diastolic pressure–volume relationship: a novel method with potential for noninvasive application*, Am. J. Physiol. Heart Circ. Physiol. **291**, no. 1, H403–H412.

Kuznetsov, Y. A. 1998. *Elements of Applied Bifurcation Theory*, Springer.

LeGrice, I., P. Hunter, A. Young, and B. Smaill. 2001. *The architecture of the heart: a data–based model*, Phil. Trans. R. Soc. Lond.A **359**, 1217–1232.

Liu, I-Shih. 1982. *On representation of anisotropic invariants*, Int. J. Engng. Sci. **20**, no. 10, 1099–1109.

______. 2002. *Continuum mechanics*, Springer.

Marsden, J. E. and T. J. R. Hughes. 1983. *Mathematical foundations of elasticity*, Dover Pubblications.

Mesin, L. and D. Ambrosi. 2011. *Spiral waves on a contractile tissue*, Eur. Phys. J. Plus **126**, no. 2, 1–13.

Merodio, J. and R. W. Ogden. 2006. *The influence of the invariant I_8 on the stress–deformation and ellipticity characteristics of doubly fiber–reinforced non–linearly elastic solids*, Int. J. Non–Lin. Mech. **41**, 556–563.

Murtada, S., M. Kroon, and G. A. Holzapfel. 2010. *A calcium–driven mechanochemical model for prediction of force generation in smooth muscle*, Biomech. Model. Mechanobiol. **9**, 749–762.

Nardinocchi, P. and L. Teresi. 2007. *On the active response of soft living tissues*, J. Elast. **88**, 27–39.

Nardinocchi, P., L. Teresi, and V. Varano. 2011. *A simplified mechanical modeling for myocardial contractions and the ventricular pressure–volume relationships*, Mech. Res. Comm. **38**, no. 7, 532–535.

Nardinocchi, P., P. E. Puddu, L. Teresi, and V. Varano. 2012. *Advantages in the torsional performances of a simplified cylindrical geometry due to transmural differential contractile properties*, Eur. J. Mech. A **36**, 173–179.

Nawroth, J. C., H. Lee, A. W. Feinberg, C. M. Ripplinger, M. L. McCain, A. Grosberg, J. O. Dabiri, and K. K. Parker. 2012. *A tissue–engineered jellyfish with biomimetic propulsion*, Nature **30**, 792–797.

Needleman, A. 1977. *Inflation of spherical rubber balloons*, Int. J. Solid and Struct. **13**, 409–421.

Nielsen, P. M., I. J. Le Grice, B. H. Smaill, and P. J. Hunter. 1991. *Mathematical model of geometry and fibrous structure of the heart*, Am. J. Physiol. Heart Circ. Physiol. **260**, no. 4, H1365–H1378.

Nobile, F., A. Quarteroni, and R. Ruiz–Baier. 2012. *An active strain electromechanical model for cardiac tissue*, Int. J. N. Meth. Biomed. Engng. **28**, no. 1, 52–71.

Panfilov, A. V., R. H. Keldermann, and M. P. Nash. 2005. *Self–organized pacemakers in a coupled Reaction–diffusion–mechanics system*, Phys. Rev. Lett. **95**.

Pathmanathan, P., S. J. Chapman, D. J. Gavaghan, and J. P. Whiteley. 2010. *Cardiac electromechanics: the effect of contraction model on the mathematical problem and accuracy of the numerical scheme*, Q. J. Mechanics Appl. Math. **63**, 375–399.

Redaelli, A. and R. Pietrabissa. 1997. *A structural model of the left venricle including muscle fibres and coronary vessels: mechanical behaviour in normal conditions*, Meccanica **32**, 53–70.

Rodriguez, E. K., A. Hoger, and A. D. McCulloch. 1994. *Stress–dependent finite growth in soft elastic tissues*, J. Biomech. **27**, 455–467.

Rossi, S., R. Ruiz–Baier, L. F. Pavarino, and A. Quarteroni. 2012. *Orthotropic active strain models for the numerical simulation of cardiac biomechanics*, Int. J. N. Meth. Biomed. Engng. **28**, no. 6-7, 761–788.

Simo, J. C. and R. L. Taylor. 1991. *Quasi–incompressible finite elasticity in principal stretches. Continuum basis and numerical algorithms*, Comput. Methods Appl. Mech. Eng. **85**, 273–310.

Smith, N. P., D. P. Nickerson, E. J. Crampin, and P. J. Hunter. 2004. *Multiscale computational modelling of the heart*, Acta Numer., 371–431.

Schmid, H., M. P. Nash, A. A. Young, and P. J. Hunter. 2006. *Myocardial material parameter estimation — a comparative study for simple shear*, J. Biomech. Engng. **128**, 742–750.

Schröder, J. and P. Neff. 2003. *Invariant formulation of hyperelastic transverse isotropy based on polyconvex free energy functions*, Int. J. Solids Struct. **40**, 401–445.

Sengupta, P. P., A. J. Tajik, K. Chandrasekaran, and B. K. Khandheria. 2008. *Twist mechanics of the left ventricle*, Cardiov. Imag. **1**, no. 3.

Shariff, M. H. B. M. 2012. *Nonlinear orthotropic elasticity: only six invariants are independent*, J. Elast.

Sharifimajd, B. and J. Stålhand. 2012. *A continuum model for skeletal muscle contraction at homogeneous finite deformations*, Biomech. Model. Mech., 1–9.

Shim, J., A. Grosberg, J. C. Nawroth, K. Kit Parker, and K. Bertoldi. 2012. *Modeling of cardiac muscle thin films: Pre-stretch, passive and active behavior*, J. Biomech. **45**, no. 5, 832–841.

Stålhand, J., Klarbring A., and Holzapfel G. A. 2008. *Smooth muscle contraction: Mechanochemical formulation for homogeneous finite strains*, Prog. Biophys. Mol. Biol. **96**, 465–481.

Streeter, D. D., H. M. Spotnitz, D. P. Patel, J. Ross, and E. H. Sonnenblick. 1969. *Fiber orientation in the canine left ventricle during diastole and systole*, Circ. Res. **24**, no. 3, 339–347.

Stoney, G. G. 1909. *The tension of metallic films deposited by electrolysis*, Proc. R. Soc. A **82**, no. 553, 172–175.

Taber, L. A. 1991. *On a nonlinear theory for muscle shells: part II — Application to the beating left ventricle*, J. Biomech. Engng. **113**, no. 63.

Taber, L. A. and R. Perucchio. 2000. *Modeling Heart Development*, J. Elast **61**, 165–197.

Taber, L. A. 2008. *Theoretical study of Beloussov's hyper–restoration hypothesis for mechanical regulation of morphogenesis*, Biomech. Model. Mechan. **7**, no. 6, 427–441.

———. 2009. *Towards a unified theory for morphomechanics*, Philos. Trans. R. Soc. London, Ser. A **367**, 3555–3583.

Takeuchi, M., Y. Otsuiji, and R. M. Lang. 2009. *Evaluation of left ventricle function using left ventricular twist and torsion parameters*, Current Cardiology Reports **11**, no. 3, 225–230.

Tallarida, R. J., B. F. Rusy, and Loughnane M. H. 1970. *Left ventricular wall acceleration and the law of Laplace*, Cardiovasc. Res. **4**, 217–223.

Trayanova, N., W. Li, J. Eason, and P. Kohl. 2004. *Effect of stretch-activated channels on defibrillation efficacy*, Heart Rhythm **1**, no. 1, 67–77.

Usyk, T. P., R. Mazhari, and A. D. McCulloch. 2000. *Effect of laminar orthotropic myofiber architecture on regional stress and strain in the canine left ventricle*, J. Elast. **61**, no. 1-3, 143–164.

Vendelin, M., P. H. M. Bovendeerd, J. Engelbrecht, and T. Arts. 2002. *Optimizing ventricular fibers: uniform strain or stress, but not ATP consumption, leads to high efficiency*, Am. J. Physiol. Heart Circ. Physiol. **283**, no. 3, H1072–H1081.

Wakatsuki, T., M. S. Kolodney, G. I. Zahalak, and E. L. Elson. 2000. *Cell mechanics studied by a reconstituted model tissue*, Biophys. J. **79**, 2353–2368.

Wang, H. M., H. Gao, X. Y. Luo, C. Berry, B. E. Griffith, R. W. Ogden, and T. J. Wang. 2013. *Structure–based finite strain modelling of the human left ventricle in diastole*, Int. J. Numer. Meth. Biomed. Engng. **29**, 83–103.

Weise, L. D. and A. V. Panfilov. 2013. *A Discrete Electromechanical Model for Human Cardiac Tissue: Effects of Stretch-Activated Currents and Stretch Conditions on Restitution Properties and Spiral Wave Dynamics*, PLOS ONE **8**, no. 3, e59317.

Weiwad, W. K., W. A. Linke, and M. H. Wussling. 2000. *Sarcomere length–tension relationship of rat cardiac myocytes at lengths greater than optimum*, J. Mol. Cell. Cardiol. **32**, no. 2, 247–259.

Winfree, A. T. 1989. *Electrical instability in cardiac muscle: phase singularities and rotors*, J. Theor. Biol. **138**, no. 3, 353–405.

Yavari, A. and A. Goriely. 2012. *Riemann–Cartan geometry of nonlinear dislocation mechanics*, Arch. Ration. Mech. An. **205**, no. 1, 59–118.

Yin, F. C. P., R. K. Strumpf, P. H. Chew, and S. L. Zeger. 1987. *Quantification of the mechanical properties of noncontracting canine myocardium under simultaneous biaxial loading*, J. Biomech. **20**, 577–589.

Yin, F. C. P., C. C. Chan, and R. M. Judd. 1996. *Compressibility of perfused passive myocardium*, Am. J. Physiol. Heart Circ. Physiol. **271**, H1864–H1870.

Young, A. A. and B. R. Cowan. 2012. *Evaluation of left ventricular torsion by cardiovascular magnetic resonance*, J. Cardiov. Magn. Reson. **14**, no. 49.

Zienkiewicz, O. C., R. L. Taylor, and J. Z. Zhu. 2005. *The Finite Element Method: Its Basis and Fundamentals*, Butterworth-Heinemann.